Development of digital models of the High Frequency Instrumen t(HFI) of Planck needed for its operation

Andrea Catalano

Observatoire de Paris

ECOLE DOCTORALE
ASTRONOMIE ET ASTROPHYSIQUE
D'ILE-DE-FRANCE

PhD in Astronomy and Astrophysics

Author

Andrea Catalano

Title:

Development of digital models of the High Frequency Instrument (HFI) of Planck needed for its operation

Tutor

Jean-Michel LAMARRE

Jury

Chairman :	Daniel	ROUAN
Rapporteurs :	Marco	BERSANELLI
	François-Xavier	DESERT
Examiners :	Jan	TAUBER
	Michel	PIAT
Invité:	Etienne	POINTECOUTEAU

Observatoire de Paris

ECOLE DOCTORALE
ASTRONOMIE ET ASTROPHYSIQUE
D'ILE-DE-FRANCE

Doctorat en Astronomie et Atrophysique

Auteur

Andrea Catalano

Titre:

Développement de modèles numériques de l'Instrument Haute Fréquence (HFI) de Planck nécessaires à son exploitation

Thèse dirigée par:

Jean-Michel LAMARRE

Jury

Président :	Daniel	ROUAN
Rapporteurs :	Marco	BERSANELLI
	François-Xavier	DESERT
Examinateurs :	Jan	TAUBER
	Michel	PIAT
Invité:	Etienne	POINTECOUTEAU

I'm trying to bring heaven in my head
but the Moon seems to know
with all her fairplay
the sky is too high.

Contents

Introduction

Planck est le troisième satellite consacré à l'étude du Fond Cosmologique Micro-onde (FCM), après, COBE et WMAP. Il réalisera un relevé complet dans 9 bandes couvrant le domaine spectral compris entre 25 GHz et 1 THz. Planck fournira la mesure ultime des anisotropies en température du FCM jusqu'à des échelles d'environ 5 minutes d'arc, avec une sensibilité limitée principalement par le bruit de photons et par sa capacité à soustraire les avant-plans. Il mesurera aussi sa polarisation, les modes scalaires (modes E) devant largement sortir du bruit alors que la détection des modes tensoriels (modes B), où l'on peut espérer trouver la signature d'ondes gravitationnelles produites pendant l'inflation, n'est pas assurée. La mesure des avant-plans fournira une riche moisson de données de plusieurs composantes de l'émission du ciel, par exemple des milliers de galaxies et d'amas de galaxies ou le milieu diffus de notre propre galaxie. Le lancement de Planck et de son compagnon Herschel est attendu en d'Avril 2009.

A bord de Planck, l'instrument haute fréquence HFI (High Frequency Instrument) comportera 52 bolomètres refroidis à 100mK. Cet instrument très ambitieux est réalisé par un consortium international piloté par la France (PI : Jean-Loup Puget IAS/Orsay). Mon travail de thèse est consacré essentiellement à l'étalonnage et au réglage, au sol et en vol, de l'instrument HFI. Il comprend d'un côté une partie expérimentale, c'est-à-dire la réalisation de séquences d'étalonnage au sol et le traitement des données obtenues pendant la campagne d'étalonnage PFM (Proto-Flight-Model), et de l'autre un travail de simulation de l'instrument pour interpréter ces données et pour prédire et comprendre son comportement pour la campagne future de réglage et d'étalonnage en vol. Des modèles numériques spécialisés de l'instrument HFI ont été développés, en particulier en ce qui concerne la détermination de sa réponse photométrique et de sa réponse dynamique, qui est essentielle du fait du mode d'observation par balayage du ciel à grande vitesse (6 Deg/s). Ces modèles sont élaborés à partir d'une description physique de l'instrument et de ses composants. Cela concerne par exemple la transmission totale de l'optique, le rayonnement de l'instrument sur ses propres détecteurs et le

comportement des bolomètres, la réponse statique et dynamique des chaines de mesure. Ils sont ajustés grâce à des séquences d'étalonnage particulières. Ce mémoire présente le satellite Planck et l'instrument HFI. Il décrit les sequences de calibration auxquelles j'ai personnellement participé. Il détaille des méthodes des mesures originales qui ont été développées pour Planck comme la mesure expérimentale des défauts de linéarité des détecteurs. Je présenterai aussi une avancée dans la théorie des bolomètres, qui permet de prédire la réponse et le bruit d'un bolomètre polarisé en courant alternatif.

Parallèlement à ce travail très instrumental, j'ai développé un travail purement astrophysique sur les amas de galaxies. Il concerne la physique des composantes dans le milieu intra-amas. Les observations en optique et proche infrarouge ont montré la présence, en plus du gaz baryonique et de la matière noire, d'une composante stellaire intra-amas. Cette population stellaire est fort probablement associée à une composante diffuse de poussière, qui doit être un vecteur de refroidissement et/ou de chauffage, mais qui reste à quantifier. En collaboration entre Antonio da Silva, Centro de Astrofisica da Universidade do Porto et Etienne Pointecouteau, Ludovic Montier, Martin Giard du CESR de Toulouse, nous avons exploité un modèle numérique de formation des structures, incluant le refroidissement radiatif et de la poussière dans le milieu intra-amas. Mon travail a consisté à analyser le résultat de ces simulations numériques en comparant les propriétés statistiques (relations Lx-M, Y-M et S-M) de la population d'amas simulés dans les cas d'un modèle gravitation+refroidissement radiatif et gravitation+refroidissement radiatif+poussière. On a montré que le refroidissement radiatif a un effet significatif et que sa prise en compte permet d'améliorer l'accord entre les modèles et les observations.

Introduction

Planck is the third satellite devoted to the study of the Cosmic Microwave Background (CMB) after COBE and WMAP. It will measure the whole sky in 9 spectral bands between 25GHz and 1THz. Planck will provide the definitive measurement of the CMB temperature anisotropies down to 5' angular scales with a sensitivity mainly limited by the photon noise and by the contamination of foregrounds. Planck will also measure the polarisation of the sky. The scalar modes (E modes) of the CMB will be measured with a large signal to noise ratio, and the tensor modes (B modes) that should contain signatures of gravitational waves generated during inflation, may be detected. The measurements of the foregrounds will provide a wealth of data on astrophysical components observable in the submillimetre range, such as thousands of galaxies, The Sunyaev-Zeldovich effect of thousands of clusters, or the diffuse emission of our own galaxy. The launch of Planck and its companion satellite Herschel is expected in April 2009.

The High Frequency Instrument of Planck (HFI), with its 52 bolometers cooled at 100 mK, has been designed and developed by a international consortium headed by France (PI Jean-Loup Puget IAS/Orsay). This work is dedicated to the calibration and the optimal tuning of the HFI on ground and in flight. It reports two types of complementary activities: One is the operation and calibration of the proto-flight model (PFM), including the optimization of the instrument settings, the reduction and the interpretation of the data. The second one is the development of numerical models representing the physics of the instrument to understand and predict its response in a large variety of situations. Specialized models have been developed to describe its photometric response and its dynamical behaviour, which is a key point in relation with the chosen observation strategy, based on a 6 Deg/s scanning speed. These models are based on a description of the physical phenomena that take place inside the instrument, especially its self-radiation on its receivers and the physics of the bolometers and their readout electronics. This document presents the Planck project and the HFI instrument. It describes the calibration sequences to which I directly contributed. It details

original measurements methods that we have developed, such as the accurate measurement of the linearity of HFI bolometers. It presents also a breakthrough in the theory of the response and noise of bolometers mounted in a Alternating Current (AC) biased electronics.

In parallel to this experimental work, a study on clusters of galaxy has been developed. It regards the physics of the intra-cluster medium components. The optical and infrared observations have shown the presence of an intra-cluster stellar component in addition to baryon gas and dark matter. This stellar population is probably related to a spread dust component so it has to be related to cooling and/or heating processes in the cluster medium. In collaboration with Antonio da Silva, Centro de Astrofisica da Universidade do Porto et Etienne Pointecouteau, Ludovic Montier, Martin Giard (CESR, Toulouse), we have utilized a digital model of structure formation, including the radiative cooling of the dust in the intra-cluster medium. My work consisted in analysing results of these digital simulations and in comparing the statistical properties (Lx-M, Y-M and S-M relations) of the cluster population for different models of structure formation (gravitation+radiative cooling and gravitation+ radiative cooling+ dust cooling models). We have shown that the radiative cooling has a tangible effect and that accounting for this effect improves the agreement between models and observations.

Chapter 1

The Planck Satellite and its Science

The Precision Cosmology Era

Cosmology is the astrophysical study of the origin, structure, composition and evolution of the Universe.

All peoples from prehistory to present day have asked to themselves the reason why there is something instead of nothing, and when and where the first object formed. The technological challenge in answering these questions during past centuries has been too great to provide all but a purely philosophical argument.

The birth of a *Scientific Cosmology*[1] could be set as the work of Alexander Friedmann in 1922 [1] on the cosmological solution of General Relativity for the case of Isotropy and Homogeneity. From this through to the 1950s, many improvements and some observations have been made in order to to make this model a satisfactory representation of reality. This Mathematical framework is based on four principles and a set of equations[2]:

The Dicke Principle: Gravity is a metric phenomenon and the geometry of the Universe is determined by its matter and energy contents;

The Newtonian Paradigm of Dimensions: We live in a universe with three space-like and one time-like dimensions;

[1] Considering as *Scientific* a speculation following the Galilean scientific method

[2] This section has been written thanks to the notes I took from the lectures of Prof. Francesco Melchiorri in 2003.

The Conditional Cosmological Principle: The Universe is Isotropic. If space is analytic, then Isotropy implies Homogeneity[3];

The Fluidity Principle: The Universe is filled by one or more ideal fluids (such as a perfect gas) governed by a simple equation of state: $P = \omega\rho$ where the *state parameter* ω is a function of time only, and the speed of light $c = 1$;

The Einstein Field Equations: The equations of General Relativity relate the properties of the cosmic fluids to that of the space-time geometry;

$$R_{\mu\nu} - \frac{1}{2}g_{\mu\nu}R - \Lambda g_{\mu\nu} = 8\pi G T_{\mu\nu} \tag{1.1}$$

where $g_{\mu\nu}$ is the metric, $T_{\mu\nu} = diag(\rho, p, p, p)$ is the momentum-energy tensor, ρ is the energy density, p is the pressure of the fluid and $R_{\mu\nu}$ is the Riemann tensor (and R its related scalar) and Λ is a component, as Einstein originally did in his formulation of general relativity, called the *Cosmological Constant*, which is not diluted with the expansion of the universe. The Riemann tensor depends on the second derivatives of the metric and contains information about the considered space curvature.

In general, under the assumptions of Homogeneity and Isotropy allowed by the first two principles, we can obtain the Friedmann-Robertson-Walker metric which can be expressed as:

$$d^2s = d^2t - a^2(t)[\frac{d^2r}{1 - kr^2} + r^2(d^2\theta + \sin^2\theta d^2\varphi)] \tag{1.2}$$

where k can be equal to $0, \pm 1$ and fixes the space-time metric, and $a(t)$ is the scale factor.

At the beginning of the 1950s, George Gamow, by interpreting Hubble's observations [2] of the recession of galaxies[4], added physics to the model of Mathematical Cosmology, assuming that the primordial Universe was in a phase of high temperature where light elements (H, He-4, He-3, D, Li, Be) were synthetized [3]; this new idea was called *Big Bang* Cosmology by Fred Hoyle and opened the Era of *Modern Cosmology.*

[3]The term *Conditional* takes into account the possibility of a fractal Universe which can be Isotropic but not Homogeneous.

[4]This shift in frequency called $Redshift$, is proportinal to the distance to the galaxies and it points to the expanding nature of the Universe.

Filling the metric in the general relativity equation we obtain the dynamic equation for a Homogeneous and Isotropic Universe (Friedmann equations):

$$\left(\frac{\dot{a}}{a}\right)^2 = \frac{8G\pi}{3}\rho - \frac{k}{a^2} + \frac{\Lambda}{3} \tag{1.3}$$

$$\frac{\ddot{a}}{a} = -\frac{4\pi}{3}G(\rho + 3p) + \frac{\Lambda}{3} \tag{1.4}$$

where $\dot{a} = Ha$ is the *Hubble Law* (in its linearised form).

Matter and radiation depend on the scale factor in a different ways: in case of matter the number of particles is preserved so the scale factor decreases as $\frac{1}{R^3}$ [5]. For radiation (photons and massless neutrinos) results $\frac{1}{R^4}$[6].

In order to solve the Friedmann equations we have to specify the matter density of the Universe. The Friedmann equations become:

$$\left(\frac{da}{adt}\right)^2 = H_0^2[\Omega_{R_0}(\frac{a_0}{a(t)})^4 + \Omega_{M_0}(\frac{a_0}{a(t)})^3 + (1-\Omega_0)(\frac{a_0}{a(t)})^2 + \Omega_\Lambda] \tag{1.5}$$

where $\Omega_0 = \Omega_{R_0} + \Omega_{M_0} + \Omega_\Lambda = \frac{\rho}{\rho_c}$ and ρ_c is the critical density at which the expansion (of the universe) is constant.

For these reasons the history of the Universe is roughly divided in two eras[4]: the *Radiation Era* and the *Matter Era*. The Radiation Era dominated the first 10^5 years; the following $\sim 10^{10}$ years, the Matter Era, are characterised by the prevalence of matter. At the beginning of the radiation era, a few minutes after initial singularity, the temperature of the Universe and the baryonic density were high enough to allow the nucleosynthesis of light elements to take place. At earlier times the physics of the Universe is almost unknown. It is assumed that the Universe underwent a phase of accelerated expansion, known as *Inflation*[5]. At redshift equal to 1100 the radiation de-coupled from the matter (de-coupling era). This is the era of the surface of last scattering (LSS) in which the photons are de-coupled from the matter and were free to move in a transparent Universe , eventually to become the present day Cosmic Microwave Background (CMB) radiation. The Big Bang model was strongly supported by the discovery of CMB in 1965 by Arno Penzias and Robert Wilson [6].This discovery evidenced that the Universe at very large scale is isotropic and homogeneous.

[5] $R \equiv \chi a(t)$ is the product between the comoving distance χ and the scale factor parameter $a(t)$.

[6] The energy density decreases for two reasons: a factor $\frac{1}{R^3}$ (as for matter) and a factor $\frac{1}{R}$ due to the wavelength stretching.

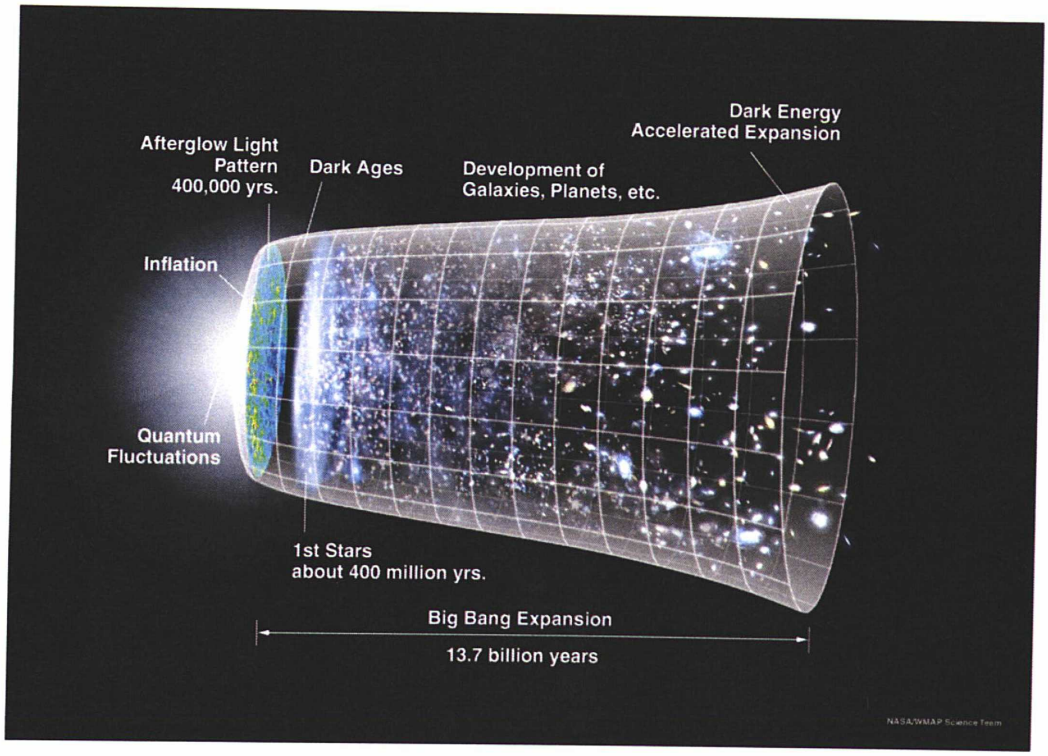

Figure 1.1: *Events in the history of the Universe as it evolved from the Big Bang (http://www.jwst.nasa.gov/firstlight.html).*

In recent times (two decades) a new era of *Precision Cosmology* started. It happened particularly due to the technological improvements of the instruments used to observe the far distance galaxies and the CMB. It is nevertheless necessary to stress that the word *Precision* is motivated by fact that the final precision depends only on the sensitivity of the instrument rather than on the difficulty of interpreting the results. In fact, the simplicity of the physical situation makes the interpretation of the data straightforward. Nevertheless, the Big Bang theory is characterized by a small number (approximately 11) of free parameters at early times, but the complexity of the present Universe would require an enormous number of parameters to describe. This is why the cosmologists concentrate their efforts in describing the universe at early times rather than trying to understand the evolution and the origin of the Universe starting from present time.

Some scientists (see for example [7]) conclude that precision cosmology is essentially a χ^2-based cosmology. Parameter estimation requires two conditions being fulfilled: the data set must be free from systematic errors, and

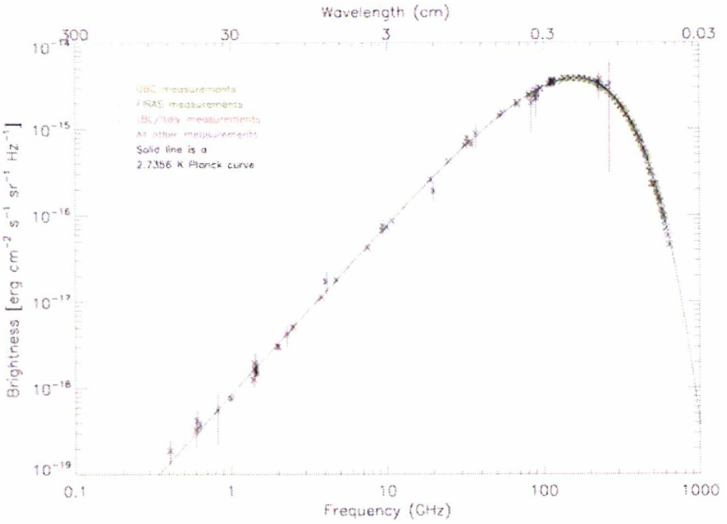

Figure 1.2: *Photometric data from Cobe Satellite compared with a blackbody at T=2.275 ± 1mK [9].*

the fitted model must be physically correct. In our cosmology it may be that the fitted data are not clean enough, and that a different set of physical laws applied to a different cosmology would fit the same data set equally well. For this reason an appropriate set of tests must be identified and performed to verify the basic hypotheses. These tests have to be model-independent. That is, independent of the values of the cosmological parameters involved. A very important source of model-independent tests is the CMB. For instance, we can check the scaling of the temperature of the CMB with redshift, which is independent of both the matter density and energy content of the Universe [8].

In the following sections I will introduce the CMB and its theoretical framework. In section 1.2 I will describe space-borne missions to observe the CMB prior to the Planck Surveyor Planck satellite which represents the main subject of my PhD thesis.

1.1 The Cosmic Microwave Background

The History of the Universe evolution as it has been presented in the last section, is essentially a thermal history because it is determined by the mean energy of the photons through the different epochs and consequently their

different interaction with matter.

The expansion of the Universe is an adiabatic process[7] in which the temperature decreases as $T \propto a(t)^{-1}$. Before redshift $z \sim 1100$ the temperature of the Universe was such that protons and electrons were de-coupled and free to move in a primordial plasma. Compton scattering (Fig 1.5) of electrons, which are in turn linked to the protons through Coulomb interactions, strongly couples the photons to the baryons and establishes a photon-baryon fluid.

Photon pressure resists compression of the fluid due to gravitational infall and sets up acoustic oscillations. During this epoch the temperature falls low enough to permit electrons and protons to recombine. The photon Compton cross-section with electrons decreases rapidly. At redshift $z \sim 1100$, recombination produces neutral hydrogen and the photons last scatter. Regions of compression and rarefaction at this epoch represent hot and cold spots respectively. Photons also suffer gravitational redshifts from climbing out of the potentials on the last scattering surface. The resultant fluctuations appear to the observer today as anisotropies on the sky (Last Scattering Surface LSS). This epoch corresponds to a temperature of 3000K which means, in relation to the standard scaling with the a parameter, that our Universe is permeated by a radiation of a blackbody at a temperature of $T = 2.725$ [10]. From this result, using the standard cosmological model we can extrapolate the temperature of the CMB at any z through the law:

$$T_{CMB} = 2.725(1 + z) \tag{1.6}$$

Note that the location of the LSS depends on the validity of the above redshift law. On the other hand, the precise location of the LSS is important because the angular extent of the horizon at LSS is a crucial quantity, related to the matter content of the Universe.

The CMB is the most perfect blackbody in nature. Nevertheless, a level of anisotropy in the CMB is necessary in such a way that it could evolve into the strongly non-homogeneous structures we observe in the present Universe.

The origin of the anisotropies is found in the fluctuations of the quantum inflationary field. This would result in fluctuation in the primordial plasma when radiation and matter were tighly coupled. Small differences of the CMB temperature in different directions are due to several phenomena:

• Photon and matter temperature differences on the LSS lead to differences in the observed CMB temperature as a function of the position on the sky;

[7] we neglect exothermic matter processes such as electron-positron annihilations. In these cases the temperature increases but not the a parameter.

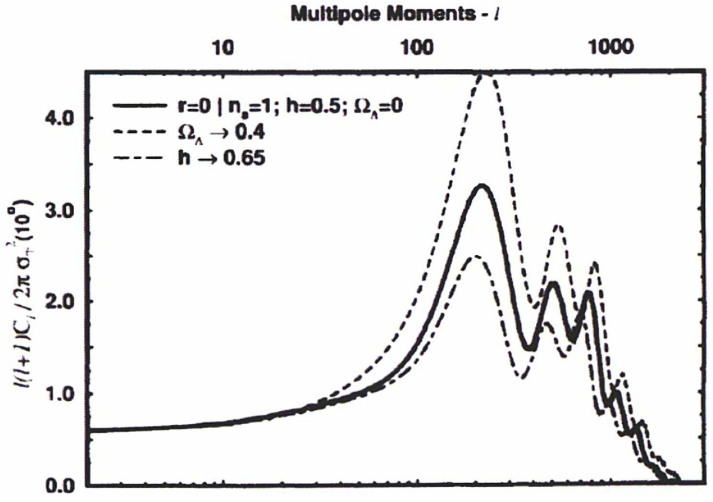

Figure 1.3: *Power spectra as a function of I for scale-invariant models, with various values given to the cosmological constant ($\Omega_\Lambda = 0; 0.4$), Hubble constant ($h = 0.5$ and 0.65) [11].*

• The same density differences lead to gravitational potential differences: if photons "climb" a potential well to get to us, they get redshifted (and vice versa), and this decreases the observed temperature (gravitational potential redshift);

• Gravitational potential differences create forces that cause motions, these motions create shifts in frequency due to the doppler effect;

• If the gravitational potentials are changing with time, the energy of photons changes along the way, leading to the so called integrated Sachs-Wolfe (ISW) effects.

Since CMB is projected onto the sky it is usual to develop the sky maps in spherical harmonics Y as:

$$\frac{\Delta T}{T_0} = \sum_{l=2}^{\infty} \sum_{m=-l}^{+l} a_{lm}^T Y_{lm}^T(\theta, \varphi) \tag{1.7}$$

where the coefficients a_{lm} are random variables with an average equal to zero.

For gaussian fluctuations, the statistical content is encapsulated in the

two point temperature correlation function, or equivalently, its angular decomposition into Legendre moments C_l.

$$\langle \left(\frac{\Delta T}{T_0}\right)^2 \rangle = \frac{1}{4\pi} \sum_{l=1}^{\infty} (2l+1) C_l^{TT} \tag{1.8}$$

where we set:

$$\langle a_{lm}^T \cdot a_{l'm'}^T \rangle = C_l^{TT} \delta_{ll'} \delta_{mm'} \tag{1.9}$$

In Fig.1.3, we show typical predictions for the Intensity anisotropy power spectrum C_l for different models of Cosmology.

CMB anisotropies and the derived angular power spectrum, can be used to fix the values of many of the key parameters that define our Universe, in particular its geometry, age, and composition.

1.1.1 The Dipole Anisotropy

The study of CMB anisotropies shows a dipole term associated with the peculiar motion of the observer with respect to the local cosmological standard of rest. This amplitude of distortion can be represented by the following law:

$$T = T_0(1 + \beta cos\theta) \tag{1.10}$$

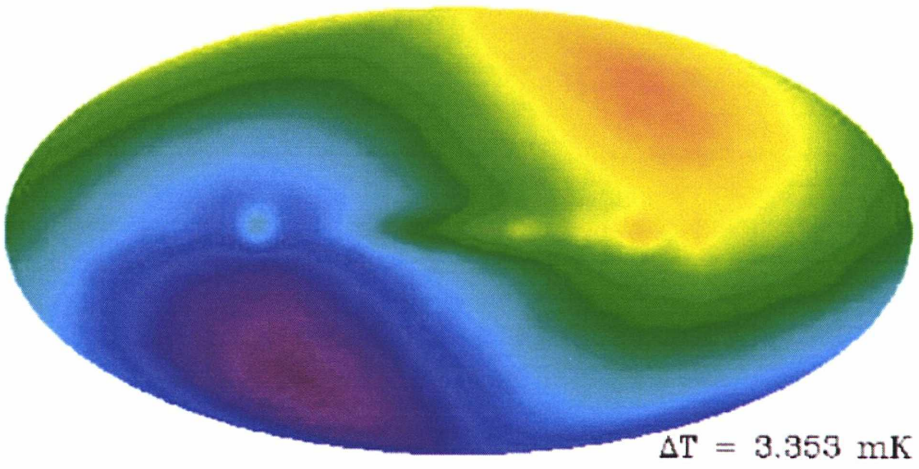

Figure 1.4: *Dipole maps from FIRAS*

where T_0 is the mean temperature of the CMB over the sky, $\beta = v/c$ is the velocity of the observer with respect to the LSS at redshift $z = 1100$ and θ is the angle between the direction of observation and that of motion. It produces a fluctuation of the order of 3.3mK with a direction (in galactic coordinates) of $l = 264.4$ and $b = 48.4$.

The dipole fluctuation is composed of several terms: the peculiar motion of the Sun (sum of the peculiar velocity of the Local Group of galaxies and the velocity of the Sun with the rotation of our galaxy)[8], the Earth velocity in its orbit around the Sun and the specific motion of the observer with respect to the earth (the orbital motion of the satellite, for example). The main term (and the most uncertain) is due to the peculiar motion of the Local Group. The second is a sinusoidal term dominated by the Earth orbital motion. It is a perfectly known in amplitude and direction and corresponds to about 15% of the first term in amplitude.

The kinetic explanation of the dipole requires a peculiar velocity of the observer, which can be explained only as the result of a gravitational acceleration integrated in time. We know that the Local Group of galaxies has a peculiar velocity with respect to LSS. From the COBE (see section 1.3) measurements we find $v_{LG} = 627 \pm 22$ toward $l = 276 \pm 3$ and $b = 30 \pm 3$ degrees. The most probable cause for this motion is gravitational instability.

An open question is over which distance do density fluctuations contribute to the gravitational field that defines the Local Group motion. This seems to be around 100-200Mpc, as suggested by optical and X-ray studies.

The measurement of the Dipole Anisotropy is a key point for CMB observations: this signal could be used as the best photometric calibrator for extended sources in the microwave domain([12]). In fact, if it is possible to measure very accurately the CMB Dipole in the whole sky (for instance, over a period of a year), we can use that part of the anisotropy associated with the orbital motion of the Earth around the Sun which is the best known component of the Dipole signal. At the same time we can improve the determination of the peculiar motion of the solar system using the Plankian nature of the CMB ([13]).

1.1.2 The Polarisation of CMB

That the CMB anisotropies are polarised is a consequence of the gravitational instability paradigm. Under this paradigm, the small fluctuations of the early Universe grow into the large scale structure we can see today. If the

[8]This is the only term taken into account to produce a fluctuation of the order of 3.3mK

primordial fluctuations are partially polarised at last scattering they would polarise the CMB anisotropies up to us [14].

Observations of CMB polarisation (CMBP) provide important tools for reconstructing the model of the fluctuations from the observed power spectrum:

• Different sources of temperature anisotropy (scalar, vector and tensor) give rise to different patterns in polarisation. Thus, by including polarisation information, one can provides information complementary to the temperature power spectrum. This could break parameter degeneracy;

• The polarisation spectrum is sensitive to the presence of gravitational waves at a wider angular scale range than the temperature spectrum. Inflationary theory predicts in fact the existence of a stochastic gravitational-wave background with a nearly-scale-invariant spectrum. CMB polarisation would thus allow in some way to study the inflationary model and to investigate the primordial plasma before the LSS;

• The level of polarisation is a direct measurement of the duration of the last scattering surface period;

We detail the basic argument of generation of CMBP. Thompson scattering of the photons with plasma depends directly on their level of polarisation (Fig1.5). The cross-section of this process is:

$$\frac{d\sigma_T}{d\Omega} = \frac{3\sigma_T}{8\pi} \mid \varepsilon^{'} \cdot \varepsilon^{''} \mid^2 \tag{1.11}$$

Where σ_T is the total Thompson cross-section, and $\varepsilon^{'}$, $\varepsilon^{''}$ represent the incident (scattered) polarisation directions.

Thompson scattering does not produce circular polarisation because of its rotational symmetry. Heuristically the incoming radiation shakes an electron in the direction of its electric field vector $\overrightarrow{E}$ causing it to radiate with an outgoing polarisation parallel to that direction. However, since the outgoing polarisation $\overrightarrow{E}^{'}$ must be orthogonal to the outgoing direction, incoming radiation that is polarised parallel to the outgoing direction cannot scatter, leaving only one polarisation state. If the intensity were completely isotropic the missing polarisation state is supplied by radiation incoming from the direction orthogonal to the original one. In an isotropic context contributions of polarised radiation scattered by LSS electrons cancel out two by two, leaving

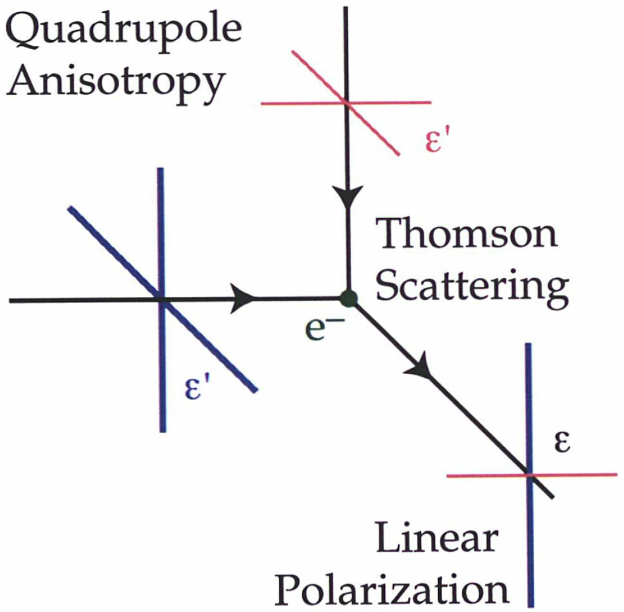

Figure 1.5: *Thompson Scattering : if the incoming radiation has a quadrupole component the outgoing radiation has a linear polarisation [14].*

only a quadrupole distribution of intensity as the possible source of polarised (linear) radiation. In particular, the polarisation is oriented along the cold axis of the quadrupole moment in the transverse plane.

In order to better clarify Thompson scattering it is necessary to introduce the *Stokes Parameters*.

Consider a plane wave propagating along z with a frequency of ω_0. The electric field is:

$$E_x(z,t) = E_{0x}\cos(\tau + \delta_x) \tag{1.12}$$

$$E_y(z,t) = E_{0y}\cos(\tau + \delta_y) \tag{1.13}$$

with $\tau = \omega_0 t$. If any correlations between these two components occur the plane wave is defined to be polarised. Stokes parameters are defined by the time averages:

$$I = \langle E_{0x}^2 \rangle + \langle E_{0y}^2 \rangle \tag{1.14}$$

$$Q \equiv \langle E_{0x}^2 \rangle - \langle E_{0y}^2 \rangle \tag{1.15}$$

$$U \equiv \langle 2E_{0x}E_{0y}\cos(\delta_x - \delta_y) \rangle \tag{1.16}$$

$$V \equiv \langle 2E_{0x}E_{0y}\sin(\delta_x - \delta_y) \rangle \tag{1.17}$$

where I is the intensity of the radiation, Q and U the linear polarisation (horizontal and vertical at ± 45 degrees), and V the circular polarisation. In the case of a non-polarised wave Q, U and V are equal to zero.

Coming back to Thompson scattering, from a mathematical point of view, after scattering the output Stokes parameters of the re-radiated field is given by:

$$I = \frac{3\sigma_T}{16\pi}[\frac{8}{3}\sqrt{\pi}a^I_{(00)} + \frac{4}{3}\sqrt{\frac{\pi}{5}}a^I_{(20)}] \tag{1.18}$$

$$Q = \frac{3\sigma_T}{4\pi}\sqrt{\frac{2\pi}{15}}Real(a^I_{(22)}) \tag{1.19}$$

$$U = -\frac{3\sigma_T}{4\pi}\sqrt{\frac{2\pi}{15}}Im(a^I_{(22)}) \tag{1.20}$$

$$V = 0 \tag{1.21}$$

Both Q and U are generated by the radiation process, but they are due to the quadrupole of the incident radiation. V is not generated through this process, although it can be generated through other processes.

Temperature perturbations have three geometrically distinct sources: the scalar (compressional), vector (vortical) and tensor (gravitational wave) perturbations. The scalar perturbations represent perturbations in the density of the primordial plasma at LSS and are the only fluctuations which can form structure through gravitational instability. Vector perturbations represent vortical motions of the matter. There is no associated density perturbation and the vorticity is damped by the expansion of the Universe as are all the motions that are not enhanced by gravity.

Tensor fluctuations are transverse perturbations to the metric, which can be viewed as gravitational waves. A plane gravitational wave perturbation represents a quadrupolar stretching of space in the plane of the perturbation.

In order to expand the polarisation pattern in spherical harmonics, it is useful to decompose it into E modes and B modes (scalar and pseudo-scalar components). This comes from a linear combination of $Q \pm iU$ and allows to describe polarisation using two quantities completely determined by linear polarisation which are rotationally invariant:

$$\frac{P_{(ab)}}{T_0}(\theta,\varphi) = \sum_{l=2}^{\infty}\sum_{m=-l}^{l}[a^E_{lm}Y^E_{lm(ab)}(\theta,\varphi) + a^B_{lm}Y^B_{lm(ab)}(\theta,\varphi)] \tag{1.22}$$

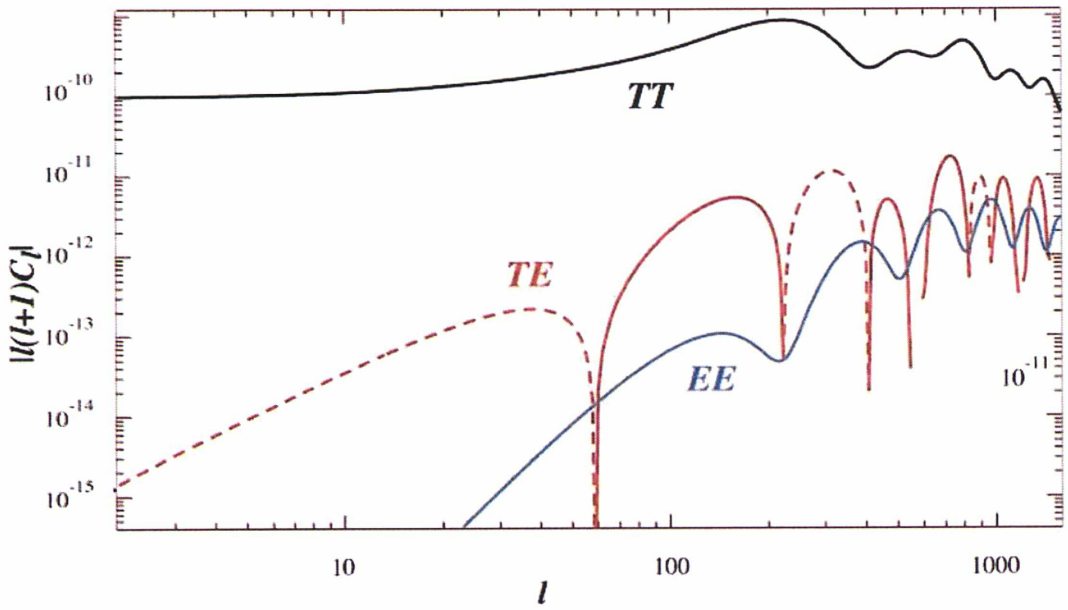

Figure 1.6: *Power spectra for scalar perturbations only (Temperature TT, E-modes EE and correlation spectra TE): the polarisation power spectrum is about 90% smaller then the temperature power spectrum at high l [14].*

From Eq. 1.22 it is possible to deduce five different spectra:

$$\langle a^E_{lm} \cdot a^E_{lm} \rangle = C_l^{EE} \delta_{ll'} \delta_{mm'} \tag{1.23}$$

$$\langle a^B_{lm} \cdot a^B_{lm} \rangle = C_l^{BB} \delta_{ll'} \delta_{mm'} \tag{1.24}$$

$$\langle a^T_{lm} \cdot a^E_{lm} \rangle = C_l^{TE} \delta_{ll'} \delta_{mm'} \tag{1.25}$$

$$\langle a^T_{lm} \cdot a^B_{lm} \rangle = C_l^{TB} \delta_{ll'} \delta_{mm'} \tag{1.26}$$

$$\langle a^E_{lm} \cdot a^B_{lm} \rangle = C_l^{EB} \delta_{ll'} \delta_{mm'} \tag{1.27}$$

Due to their origin, temperature fluctuations are expected to be well correlated with $E - modes$ while $B - modes$ power spectrum is expected to be not correlated with temperature. While the temperature power spectrum peaks at the same angular scale of the horizon, the polarisation spectrum peaks at angular scales smaller than the horizon at last scattering due to the casuality. Furthermore, the polarised fraction of the temperature anisotropy is small since only those photons that last scattered in an optically thin region could have possessed a quadrupole anisotropy. The fraction depends on the duration of the last scattering. For a standard thermal history, it is expected to be between 5% and 10% on a characteristic scale of tens of arcminutes.

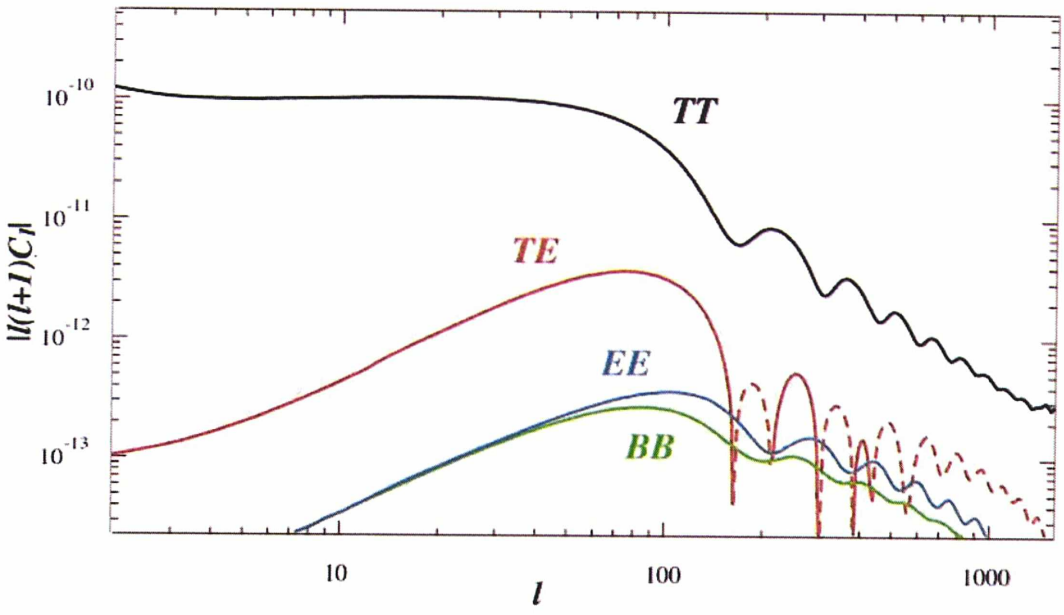

Figure 1.7: *Power spectra for the case of pseudo-scalar perturbations only [14].*

1.1.3 The Secondary Anisotropies

Fluctuations generated at the recombination epoch are said to be *Primary Anisotropies*. After recombination, photons of the CMB travel into a transparent universe until they reach us. Nevertheless, some level of anisotropies can be generated in this phase. These induced anisotropies are said to be *Secondary Anisotropies*. This definition are not ambiguous for small-scale anisotropies but it becomes unsatisfactory for large-scale anisotropies for which the light travel time across a perturbation is of the order the age of the Universe.

Secondary Anisotropies contain a large amount of cosmological information (and information on physical process in general) hard to study in any other way. The following is a short list of the principal sources of secondary anisotropies.

• *The Thermal Sunyaev-Zel'dovich Effect :* CMB photons passing through a cluster of galaxies can have a spectral distortion caused by inverse Compton scattering with hot electrons of the ICM (Intra-cluster Medium) in the direction of the cluster (Sunyaev and Zel'dovich 1972). The S-Z effect appears as

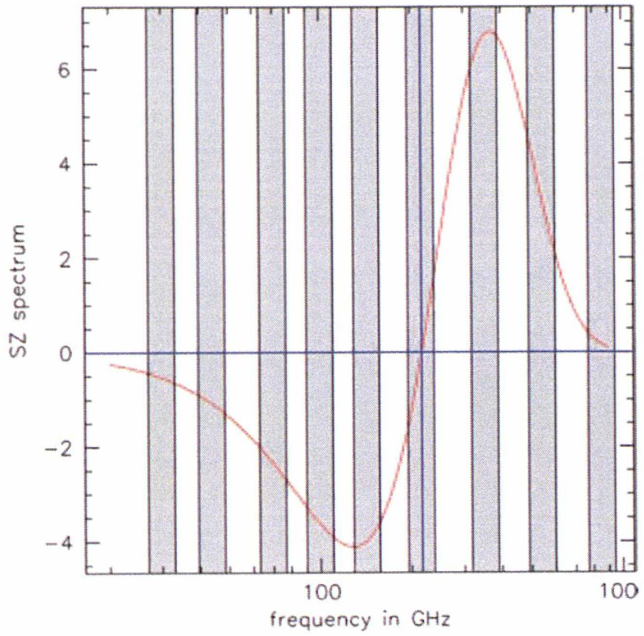

Figure 1.8: *Thermal S-Z effect (red line): the spectral bands of Planck Satellite are over plotted.*

an intensity decrease at frequencies lower than $\sim 217GHz$ and an increase at higher frequencies (Fig1.8). Because of its spectral signature, the thermal S-Z effect can be separated from the primary CMB anisotropies using observation at several frequencies.

The S-Z effect recovers many astrophysical and cosmological informations: first, we can perform a survey of the cluster versus redshift in the sky using CMB. We can recover CMB temperature at cluster redshift in order to check the brighness-redshift equation 1.6. Finally, CMB observation of clusters can be combined with X-ray observations to derive independently the principal cosmological parameters.

• *Gravitational Lensing :* The General Theory of relativity says a photon follows a geodesic paths rather than a straight line. These geodesic paths in fact represent the shortest line between two points in a gravitationally distorted space-time. Since the Universe today is strongly non-homogeneous, the CMB photons can be used to trace out the large-scale matter distribution thanks to this secondary gravitation effect.

Figure 1.9: *The Galaxy Cluster Abell 2218 (NASA): the Gravitational Lensing effect is present by distortion of the galaxies of the cluster.*

• *The Integrated Sachs-Wolfe Effect :* The Sachs-Wolfe effect is caused by the gravitational redshift (or blueshift) of the CMB photons climbing out of (or falling into) an over-density. If the effect occurs at the surface of the last scattering , it is considered to be a component of the primary anisotropy (Non-Integrated Sachs-Wolfe).
If the same effect occurs between the surface of last scattering and the observer, so it is not part of the primordial CMB and is called The integrated Sachs-Wolfe effect (ISW). It occurs when the density of the Universe is dominated by something other than matter. If the Universe is dominated by matter, then large-scale gravitational potential wells and hills do not evolve significantly. If the Universe is dominated by radiation, or by dark energy, though, those potentials do evolve, subtly changing the energies of the photons passing through them. There are two contributions to the ISW effect. The "early-time" ISW occurs immediately after the (non-integrated) Sachs-Wolfe effect produces the primordial CMB, as photons course through density fluctuations while there is still enough radiation around to affect the Universe's expansion. Although it is physically the same as the late-time ISW, for observational purposes it is usually lumped in with the primordial CMB, since the matter fluctuations that cause it are in practice undetectable. The "late-time" ISW effect arises quite recently in cosmic history, as dark energy, or the cosmological constant, starts to govern the Universe's expansion. This linear part of the effect entirely vanishes in a flat universe with only matter,

but dominates over the higher-order part of the effect in a universe with dark energy. The full nonlinear (linear + higher-order) late-time ISW effect, especially in the case of individual voids and clusters, is sometimes known as the Rees-Sciama[2] effect, since Martin Rees and Dennis Sciama elucidated the following physical picture. Accelerated expansion due to dark energy causes even gentle large-scale potential wells and hills to decay over the time it takes a photon to travel through them. A photon gets a kick of energy going into a potential well (a supercluster), and it keeps some of that energy after it exits, after the well has been stretched out and shallowed. Similarly, a photon has to expend energy entering a supervoid, but will not get all of it back upon exiting the slightly squashed potential hill. A signature of the late-time ISW is a non-zero cross-correlation function between the galaxy density (the number of galaxies per square degree) and the temperature of the CMB, because superclusters gently heat photons, while supervoids gently cool them. This correlation has been detected at moderate to high significance.

1.1.4 Foregrounds

Foregrounds are all the astrophysical sources cause a spurious effect in the CMB observations. In particular, the characterization of polarised foregrounds is a key point for a successful mission. In case of a space mission we do not have to deal with foregrounds coming from the atmosphere.

The main astrophysical foregrounds are $free - free$, *synchrotron* and *dust* emission.

Free-Free Emission

Thermal bremsstrahlung from an ionized hydrogen cloud (HII region) is often called free-free emission because it is produced by free electrons scattering off ions without being captured. The electrons are free before the interaction and remain free afterwards. The emission is proportional to:

$$T_{Br} \propto \nu^{-2.15} \tag{1.28}$$

Free-Free emission is intrinsically unpolarised but it can be partially polarised by Thomson scattering within the HII region.

The emission is larger at low frequencies but it is not expected to dominate the polarisation at any frequency.

Synchrotron Emission

A charged particle moving in a magnetic field radiates energy. At non-relativistic velocities, this results in cyclotron radiation while at relativistic

velocities it results in Synchrotron radiation. Synchrotron radiation is typically generated by galaxies, where relativistic electrons spiral (and hence change velocity) through magnetic fields.

The Synchrotron emission follows the power law:

$$I_{sincro} = C\nu^{\beta} \tag{1.29}$$

where C and β are determined by the density and energy of electrons and the intensity of the magnetic field in the considered region.

This non-thermal radiation contains a percentage of polarised emission:

$$P = \frac{3\beta + 3}{3\beta + 1} \tag{1.30}$$

with $\beta \leq -1$. Depending from the observed region on the sky, Synchrotron emission can be polarised from 10% to 75%. The r.m.s. fluctuation of Synchrotron emission corresponds to a change in temperature of about $50\mu K$. Synchrotron emission and its polarisation is the dominant source of foregrounds at frequencies lower than 100GHz (see Fig 1.10).

Dust Emission

Dust emission is due to the thermal emission from small particles and grains in a local medium. Part of this emission is polarised by its local magnetic field which acts to align elongated grains so that they spin with their long axes perpendicular to the field.

At low Galactic latitudes, thermal emission from dust particles dominates the IR spectrum. In general, depending on the shape and the alignment of dust particles, emission from dust can be polarised from 2% to 10% [15]. At frequencies higher than 200GHz, dust is the dominant foreground.

This emission results in a linear polarisation that can be also used to measure the direction of the magnetic field.

Due to the different spectral indices, the minimum in the foreground polarisation, as with the temperature, is near 100GHz (Fig.1.10). For full sky measurements, because synchrotron emission is more highly polarised than dust, the optimum frequency at which to measure intrinsic (CMB) polarisation is slightly higher than for anisotropy. Over small region of the sky where one or the other of the foregrounds is known a priori to be absent the optimum frequency would clearly be different. However, as with anisotropy measurements, with multifrequency coverage, polarised foregrounds can be removed.

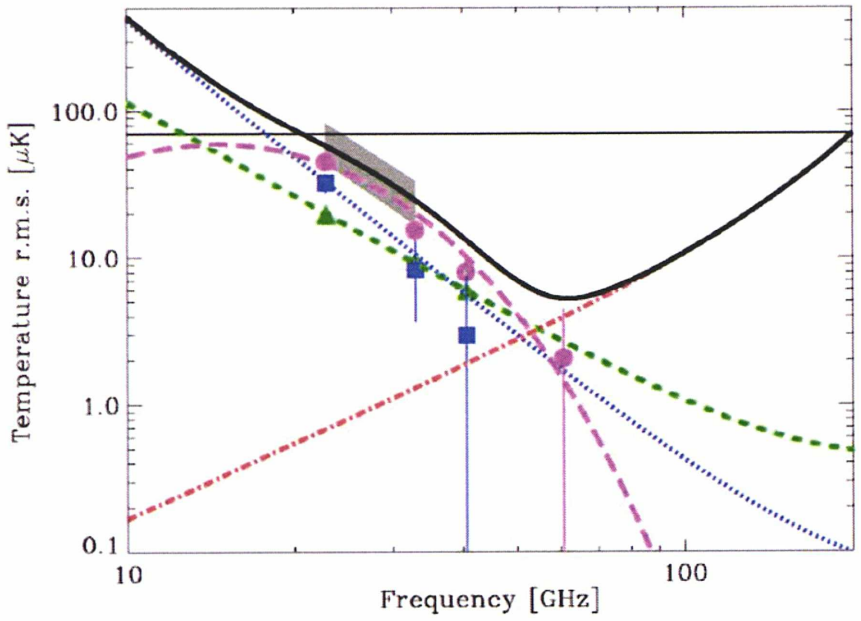

Figure 1.10: *r.m.s. fluctuation spectra (thermodynamic temperature units) of foreground components at 1 degree resolution (Davies et al 2006). Synchrotron (blue square), free-free (green triangle) and anomalous dust-correlated emission (magenta circles) co-add to the dust (red dotdashed line). CMB is shown at 70 mK r.m.s. Total foregrounds (black solid curve) show a clear minimum around 70 GHz.*

It also interesting to consider how the spatial as well as the frequency signature of the polarisation can be used to separate foregrounds. Using angular power spectra for the spatial properties of the foregrounds is a simple generalisation of methods already used in anisotropy work. For instance, in the case of synchrotron emission, if the spatial correlation in the polarisation follows that of the temperature itself, the relative contamination will decrease on smaller angular scales due to its diffuse nature. Furthermore, the peak of the cosmic signal in polarisation occurs at even smaller scales than for temperature anisotropy [16].

1.2 The Challenge of Precision Cosmology: Three Generations of Satellites

As many scientists say, we live in the precision cosmology era. This is possible thanks to experiments (space-borne and ground-based) which permitted (as COBE and WMAP) and will permit (Planck) measurements to increased precision. The next section is a short review of the principal CMB experiments prior to the Planck satellite.

1.3 First Generation of Precision Cosmology: COBE

The Cosmic Background Explorer (COBE), launched in November 1989 on a Sun-synchronous orbit, included two microwave experiments. Both instruments have unveiled, with an angular resolution of 7 degrees, an image of the microwave sky nearly uncontaminated by the radiation from the Earth or from other sources in the sky. The Far Infrared Absolute Spectrophotometer (FIRAS) has measured the sky radiation between 30 GHz and 600 GHz with a spectral resolution of 30 GHz ([17]). The measured CMB spectrum ((Figure 1.2) is near to that of a blackbody at (2.725 ± 0.001) K ([18]). Deviations from a perfect blackbody are less than 50 parts per million of its peak emission. This very pure spectrum ruled out a number of alternative theories developed to explain the CMB without a Big Bang. COBE has revealed that the observable Universe is uniform at very large scales, which has strong theoretical implications.

The spectrum of the dipole has been measured by FIRAS and its shape is consistent with the assumption that it is produced by a Doppler shift of the monopole. Its value of (3.372 ± 0.007) mK implies that the Sun's peculiar speed with respect to a comoving frame is (371 ± 1) km/s. Further contrast enhancement reveals a very small but significant random *anisotropy*, i.e., deviations from uniformity, with rms amplitude of $(29 \pm 1)\ \mu K$ at the angular resolution of 10 degrees ([19]). Such anisotropies were keenly expected as a major sign that we understood the nature and the origin of the CMBR. They were expected to be the remnants of quantum fluctuations during the first moments of the Big Bang. And without them, it would have been very difficult to understand how such an extremely uniform source could have produced the highly structured Universe that we can observe now in our neighbourhood. J. Mather and G. Smoot received the 2006 Nobel Prize of Physics for the results of the COBE spacecraft. Although its angular

resolution was only 7 degrees and the signal to noise only 2 per beam on anisotropies, COBE has produced a wealth of major discoveries.

1.4 Second and Third Generation: from Ground Based Experiments to the Planck Satellite

Even before the discovery of the CMB anisotropies by COBE, it was understood that high sensitivity measurements could be and had to be made by new types of instruments.

The critical data is the C(l), i.e., the power spectrum of the anisotropy map, that must be measured at moments l of the spherical harmonics ranging from zero (mean brightness of the sky) to about 3000 (features smaller than 7'), and at sensitivity of a few microkelvins. A first view of the C(l) was obtained through a number of remarkable ground based and balloon-borne experiments. This was a huge improvement with respect to COBE.

The Boomerang ([20]), Maxima ([21]) and Archeops ([22]) balloonborne experiments have shown images of the CMB on fractions of the sky with good signal to noise ratio. Ground based experiments, such as CBI ([23]; [24]), ACBAR ([25]; [26]), VSA ([27]), and DASI ([28]) have unveiled the highresolution part of the CMB spectrum.

The stationary part of the noise from an instrument can be evaluated by powerful statistical tools, but its non-Gaussian and non-stationary parts, and the other sources of systematics are much more difficult to evaluate and to remove from the data. Their levels have to be reduced as much as possible. This difficulty has been considered as the major design driver of CMB experiments. In addition, an optimal interpretation of the C_l will rely on full sky maps with a pixel size of less than 0.1 degrees. All these requirements can be met properly only with a space mission with adapted design and mission profile, although very significant observations can be achieved from the ground.

This has been undertaken by NASA and ESA with the spacecrafts WMAP ([19]) and Planck (The Planck consortia 2005). Both experiments had benefited from a formal positive decision in the spring 1997, a similar date in very different programmatic contexts: NASA favouring immediate start and early launch, while the ESA was looking for synergy between Planck and Herschel and therefore a later launch. Consequently, they illustrate very different strategies. The Wilkinson Microwave Anisotropy Probe (WMAP) intended to take advantage of the available and proven technology to get major new

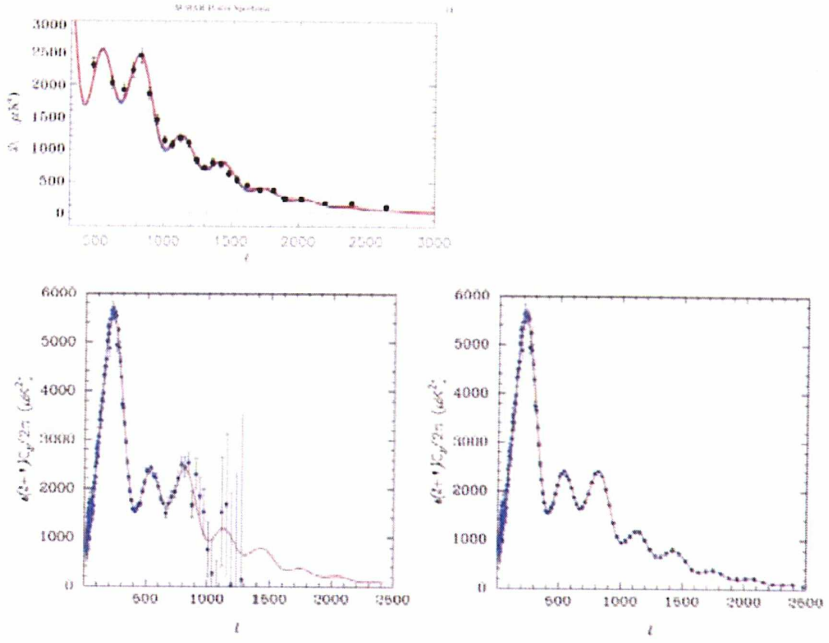

Figure 1.11: *Accurately measuring the C(l) curve should be achieved in the first decade of the 21st century, as shown by the 3-years WMAP results (Spergel et al 2007) (lower left), the ACBAR measurements (Reichardt et al 2008) from the South Pole (upper left) and a simulation of the Planck data (lower right), with a launch expected end 2008.*

results as soon as possible, while Planck was designed to perform at the limits set by physics, which required more risky and longer development. In the following subsections I will detail separately the two instruments in terms of orbits and general configuration.

1.4.1 The Wilkinson Microwave Anisotropy Probe (WMAP)

The Wilkinson Microwave Anisotropy Probe (WMAP Fig.1.12), developed by NASA, was launched on June 30, 2001, and has been mapping the temperature and polarisation anisotropies on the full sky in 5 microwave bands (22, 30, 41, 60, 94GHz).

The satellite observes at the Lagrange 2 (L_2) point, where emission and magnetic fields of the Earth do not affect the satellite. The differential measurements with many scans in different orientations per pixel significantly suppress undesired $1/f$ noise and noise correlations between pixels.

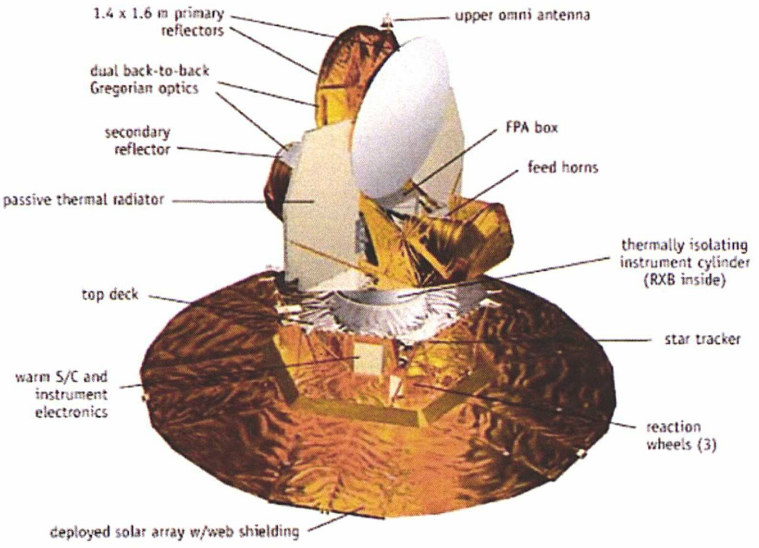

Figure 1.12: *View of the WMAP satellite*

The recivers are HEMT1.16 (High Electron Mobility Transistors) cooled down to about 90 K by passive cooling, taking advantage of the favourable conditions and exceptional stability offered by the L2 orbit, intended to reduce systematic effects of thermal origin to a minimum. Temperature fluctuations are induced only by the annual variation of the distance to the Sun and by bursts of solar activity.

The principal specifications of WMAP are presented in Table1.13 and compared to the Planck specifications.

	WMAP	*PLANCK*
Orbit	Halo Orbit - Lagrange point L2	Halo Orbit - Lagrange point L2
Sky coverage	Full sky	Full sky
Optical system	Back-to-Back Gregorian, 1.4 m x 1.6 m primaries	Gregorian, 1.5 m x 1.8 m primary
Scan angle	±70° from rotation axis	85° from rotation axis
Detection HEMT amplifiers	HEMT amplifiers	HEMT amplifiers + 100 m bolometers
Polarization sensitive	I, Q, U Stokes parameters	I, Q, U Stokes parameters (not at 545 GHz and 857 GHz)
HEMT Radiometric system	Sky/sky pseudo-correlation differential	Sky/4 K load differential
Spin Modulation	≈ 7.57 mHz spacecraft spin	≈ 16.6 mHz spacecraft spin
Precession Modulation	≈ 0.3 mHz spacecraft precession	No precession
Calibration In-flight	Amplitude from dipole modulation	Amplitude from dipole modulation
Beam knowledge	Calibration on Jupiter	Calibration on planets
Required temperature	About 90 K	Telescope 50 K ; HEMT 20 K ; Bolometers 0.1 K
Cooling system	Passive cooling	Passive + H2 J-T + He J-T + 0.1 K Dilution
Attitude control	3-axis controlled, 3 wheels, gyros, sta trackers, sun sensors	Spin controlled, thrusters, star trackers, gyros
Power	419 W	2000 W
Mass	840 kg	1450 kg
Launch	Delta II 7425-10 on 30 June 2001 at 3:46:46.183 EDT	Ariane 5 dual launch (with HSO) - Planned Dec 2008
Orbit	Orbit 1° to 10° Lissajous orbit about second Lagrange point, L2	Lissajous orbit about second Lagrange point, L2
Trajectory	3 Earth-Moon phasing loops, lunar gravity assist to L2	Direct way to L2 orbit
Design Lifetime	27 months = 3 month trajectory + 2 yrs at L2	17 months = 3 month trajectory + 14 months at L2

Figure 1.13: *Main features of WMAP and Planck spacecrafts.*

W=*WMAP*	W	W	W	W	W									
P=*Planck*						P	P	P	P	P	P	P	P	P
(LFI/HFI)						L	L	L	H	H	H	H	H	H
HEMT amps.	x	x	x	x	x	x	x	x						
Bolometers									x	x	x	x	x	x
Centre Freq. (GHz)	23	33	41	61	94	30	44	70	100	143	217	353	545	857
Bandwidth (GHz)	5.5	7.0	8.3	14	20	6	8.8	14	33	47	72	116	180	283
Nb. of Unpol. Dets	0	0	0	0	0	0	0	0	0	4	4	4	4	4
Nb of Polarised Dets	2	2	4	4	8	4	6	12	8	8	8	8	0	0
Angular Resolution (FWHM, arcmin)	53	40	31	21	13	33	29	14	9.5	7.2	5	5	5	5
Average $\Delta T/T^*$ per pixel ($\mu K/K$)						2.5	3.0	5.2	2.5	2.2	4.8	15	NA	NA
System temp. (K)	29	39	59	92	145	11	16	29						
RJ Sensitivity per freq. band ($\mu K\ s^{1/2}$)	800	800	500	600	400	110	120	130	14	12	10	8	10	7

* for a 14 months mission

Figure 1.14: *Channels of WMAP and Planck*

1.4.2 The Planck Mission

The Planck Mission [29], named in honor of the German scientist Max Planck (1858-1947), is a mission of the European Space Agency (ESA) developed in partnership with the European scientific community. It is planned to launch Planck on an Ariane 5 rocket toghther with the Hershel Space Observatory (see http://www.rssd.esa.int/Hershel) in March 2009. Planck is a part of ESA's *Cosmic Visions* 2020 programme.

The Planck Satellite comprises a Telescope, two instruments High Frequency Instrument *HFI* and Low frequency Instrument *LFI* and a Spacecraft. The HFI is inserted into and attached to the frame of the LFI focal plane unit (see Fig.1.16) The two instruments cover 9 bands from 30 to 857GHz (30-44-70GHz for LFI and 100-143-217-353-545-857GHz for HFI). The characteristics of the two instruments are summarised in Tab1.21 and Tab1.14 in comparison with those of WMAP. It is clear that the two instruments alone are very sensitive, but with the combination of the data sets together it will be possible to achieve the very hard goals of the mission.

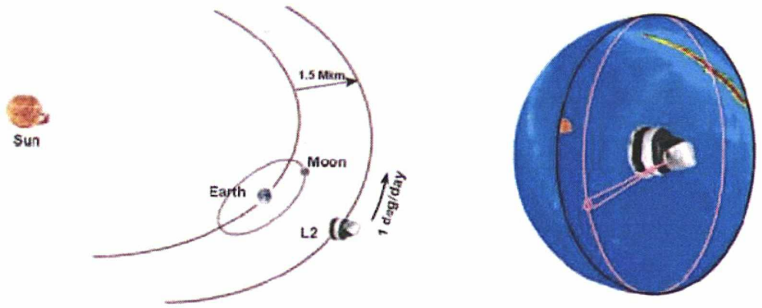

Figure 1.15: *Planck Orbit at L_2 lagrangian point*

After a transit phase lasting 3-4 months, the Planck Satellite will be inserted into a Lissajous orbit[9] around the second Lagrange point of the Earth-Sun system (see Fig1.15). The spacecraft will spin at $\sim 1rpm$ around an axis offset by 85% from the telescope boresight, so that the observed sky patch will trace a great circle on the sky. From L_2 the spin axis can be

[9]In orbital mechanics, a Lissajous orbit is a quasi-periodic orbital trajectory an object can follow around a colinear libration point of a two-body system without requiring any propulsion.

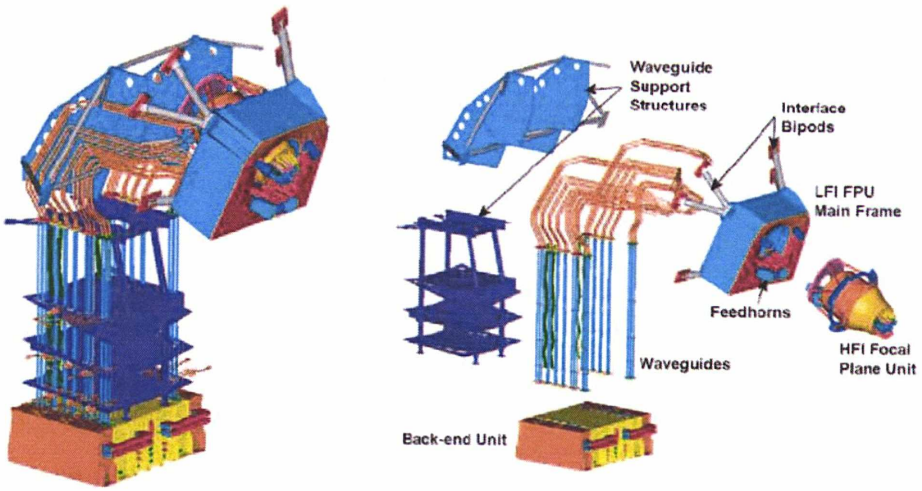

Figure 1.16: *The LFI radiometer array assembly (left) with details of the all units (right): the HFI is inserted into the focal plane unit of LFI.*

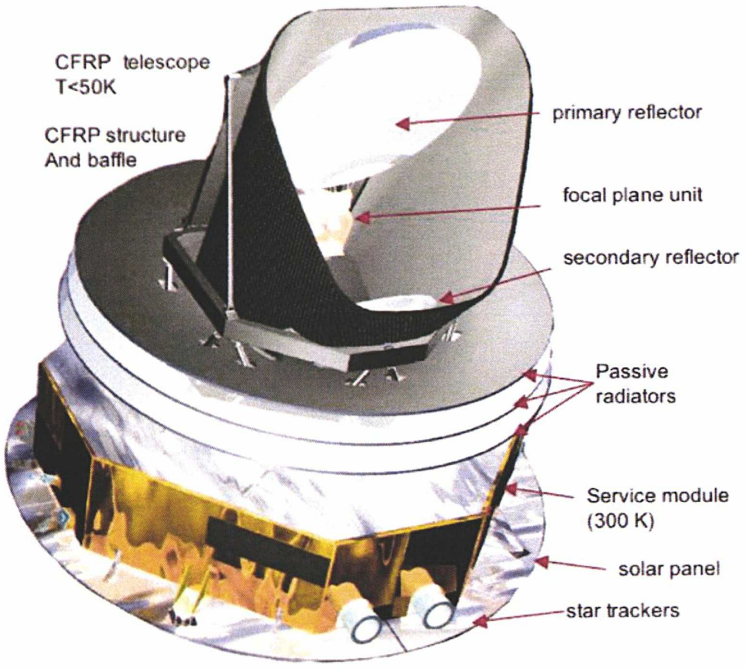

Figure 1.17: *Conceptual view of the Planck Spacecraft with the Planck Telescope*

continuously pointed in the anti-Sun direction and the satellite itself used to shield the payload from solar illumination. This strategy will minimise confusing signals due to the thermal fluctuations and straylight entering the detectors through the far side lobes. It also enables aggressive use of passive radiative cooling to cool the payload, a key feature in the overall thermal design of Planck. As the spin axis follows the Sun the circle observed by the instrument sweeps through the sky at a rate of few per cent day^{-1}. The whole sky will be covered in a little more than 6 months; this operation will be repeated at least twice during the lifetime of the cryogenic system.

The spacecraft

The spacecraft consists of a telescope, a baffle, V-grooves (these three elements constitues the Planck Optical System) and the Service Module Houses.

The Planck Telescope consists of two ellipsoidal mirrors with a Gregorian-Dragone-Mitsugushi configuration of 1.5m and 0.64m (circular projected aperture) and the supporting structures and the surrounding baffles. The Telescope unit includes the structure in witch both LFI and HFI instrument

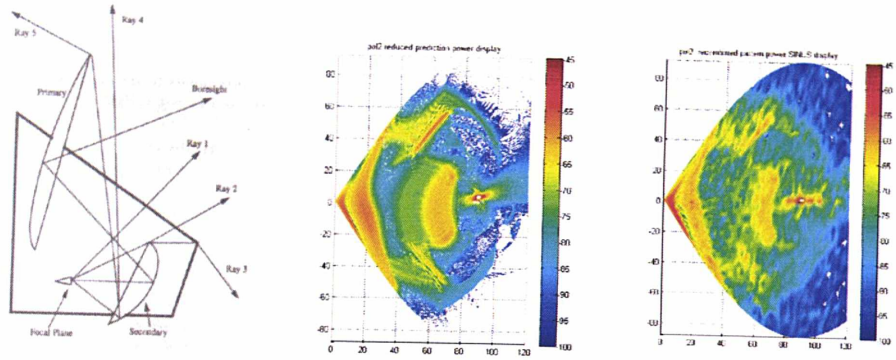

Figure 1.18: *Straylight incoming in focal plane unit: on the left a geometrical study from the horn to the sky. This study shows the possibility for straylights to come into the horns from 4 different directions. In the centre and on the right simulations and measurements of signal from straylight respectively. In these plots the level of saturation corresponds to* $-45dB$ *in gain.*

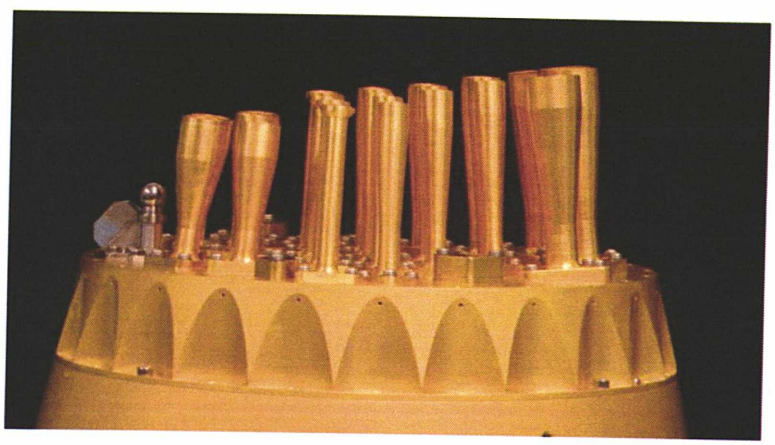

Figure 1.19: *Focal Plane Units (FPU) of the HFI instrument. The position of the Horns is optimazed taking into account the distortion of FPU due to the design of the Telescope. The size of the HFI FPU corresponds to 4 degrees in the sky*

are mounted(Fig1.17). All the structures and baffles provide to the telescope a stable thermal environment, protect the telescope from sun and earth direct irradiation and contribute to reduct the radiative power that reaches a detector when it is not originated from a source in the far fields of the beam (*Straylights*).

In Fig1.18 the distribution of the power of the straylight in the detected

signal is presented. The Planck Telescope is designed as an off-axis tilted system offering the advantage of an unblocked aperture. The Telescope line of sight lies in the Z,X plane of the spacecraft coordinate system and is at an angle of 85 degrees from the spacecraft's axis. It operates at a temperature between 40K and 65K and it is optimized to work in a range of frequency between 25 and 1000 GHz. The useful field of view for all the horns of Planck HFI is equal to 4 degrees in the sky.

The image of the sky in the focal plane of the telescope has a typical distortion produced by the design of the mirrors, that is the reason why the position in space of the horns in the FPU is optimized taking into account this effect (Fig1.19).

The design of the telescope was based on these criteria :

• Angular resolution should cover the useful range of multipole moment, i.e. provide an angular resolution of 5 arcmin.

• The design should minimize the straylight, which means
- No diffracting obstruction (an off-axis Gregorian-like design)
- providing the resolution with a extremely low edge taper (-20 to -30 dB) to minimize spillover.
- Having a low emissivity and a low temperature. Ref.. ([30])

• fitting in the volume allocated inside the compartment allocated in the Ariane V shroud, that must also accommodate Herschel and the structure supporting it. This requirement is in contradiction with the two previous ones, which led to painful compromises. They resulted in the distorting optical design, whose effect on science may have been underestimated.

I will detail the Planck optical system in the chapter 2 on section 2.1.

The Service Module houses consists of warm electronics , the ancillary equipment of the spacecraft (Telecommunications units, solar panels and batteries, attitude control, propellant tanks etc...). It is an octagonal box built around a conical tube which supports the satellite loads. The propellant tanks and the tanks containing cryogenic fluids for HFI coolers are located inside the tube. Most other units are located outside the tube, mounted on side panels of the octagonal box, allowing them to radiate to space.

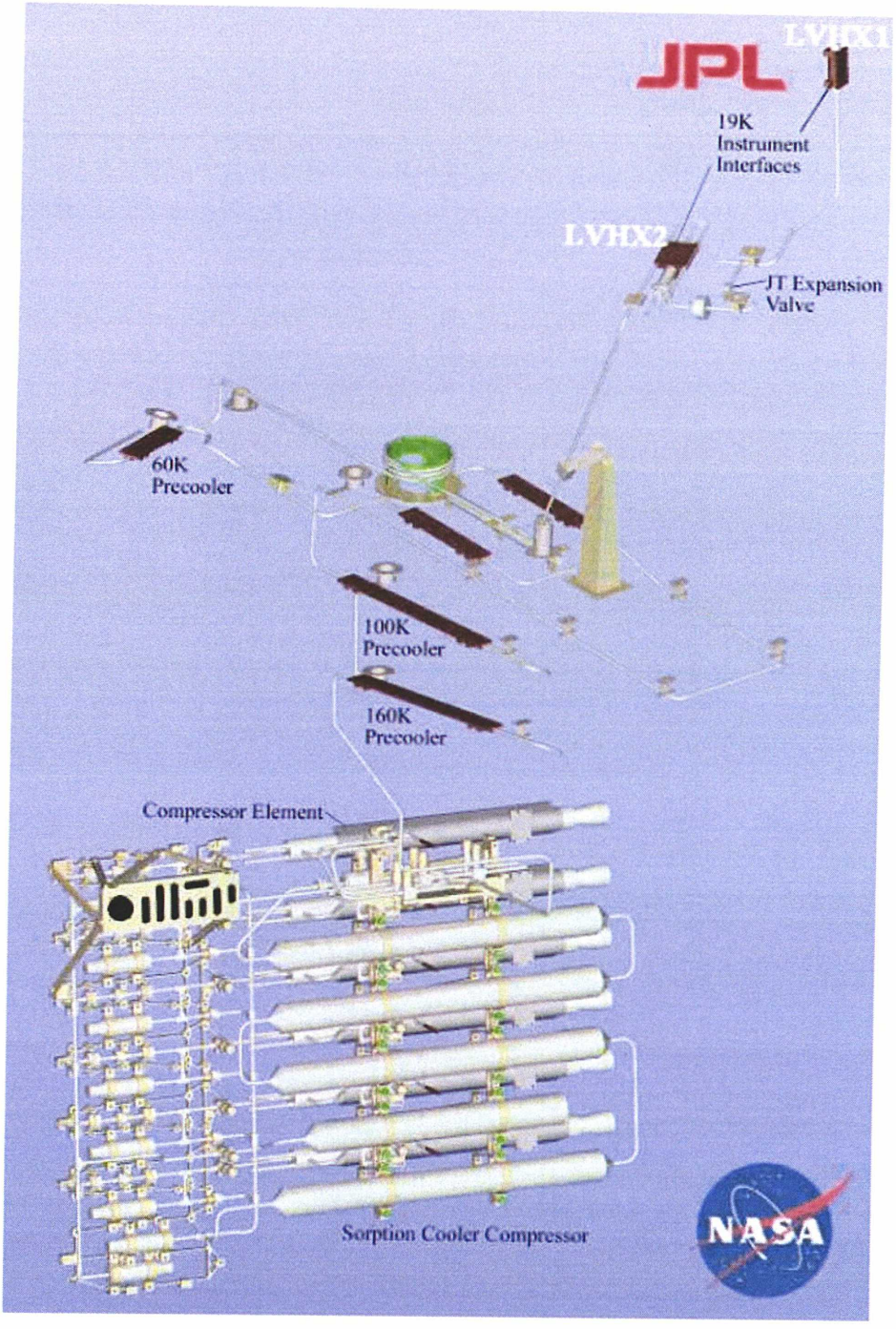

Figure 1.20: *Design of Sorption Cooler by JPL*

Sorption Cooler

The sorption cooler provides the cooling of LFI instrument with the controlling of the interface HFI-LFI flange temperature and the cooling of the HFI 18K stage on which the Helium of the $4K$ cooler is pre-cooled.

The working principle of this absorption compressor is based on the properties of hydride $LaNi_{4.78}Sn_{0.22}$. This hydride can absorb a large quantity of Hydrogen molecules when it has a low pressure and temperature thanks to the high ratio between surface and volume of the solid. The compressor injects hot gas with constant pressure in the Joule-Thompson circuit. This Hydrogen gas is pre-cooled by three V-grooves of the satellite. Then the gas expands thanks to a Joule-Thompson expansion[10] in a valve mounted on the top of the two warm excenge pipes LVHX1 and LVHX2. Finally the fluid Hydrogen at a temperature of 18K and 20K respectively circulates into two exchangers before coming back to a cold tank of compressor to restart the whole cycle (see Fig 1.20).

To make the Sorption Cooler working the satellite has to produce a electrical power of 300W with a period of 940sec (Nominal values derived from PFM Calibration campaign). The Temperature of LVHX1 is critical for the whole HFI cryogenic chain. So it is necessary to check the fluctuation of this plate. During the test in CSL a r.m.s. fluctuation of $420mK$ has been measured. This is acceptable for HFI. The duration of life is fixed by the wear and tear of the Hydride chamber. With the nominal specification of Sorption cooler (power and period) the duration of life of the whole cryogenic chain is not limited by the sorption cooler.

The Sorption cooler are integrated in a complex way in the spacecraft. It relies on the passive cooling provided by the 3 V-grooves and the warm radiator which radiates into deep space the power of the sorption cooler. The sorption coolers have been extensively tested at JPL and then in an integrated test with the payload, the warm radiator and a representative spacecraft in the FM1 test at CSL.

The LFI Instrument

The Low Frequency Instrument (Fig.1.16) of the Planck satellite represents an improvement in technology and sensitivity with respect to the WMAP satellite. Because of the similar technology used, the two instruments are readily comparable. The LFI consists of a 22 channel array of differential

[10]The Joule-Thomson effect describes the increase or decrease in temperature of a real gas when it is allowed to expand freely at constant enthalpy (which means that no heat is transferred to or from the gas, and no external work is extracted).

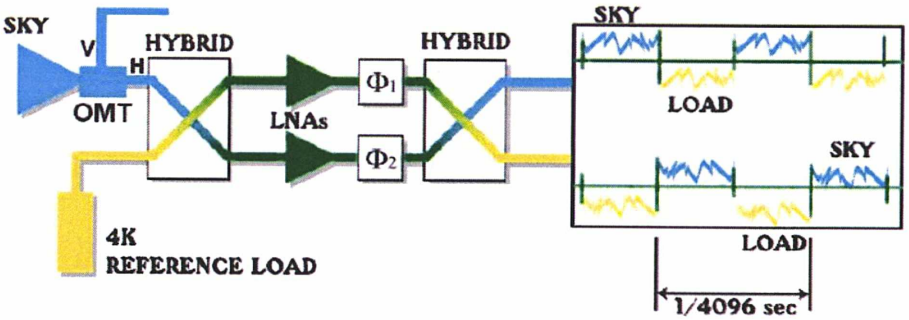

Figure 1.21: *Schematic view of LFI front-end radiometer.*

receiver. observing in three spectral bands (30-44-70 GHz). The focal plane unit is cooled to 20K in order to minimise power dissipation and to increase sensitivity. The 20K temperature is achieved by a *Sorption Cooler* (see previous section). The receivers are high-electron-mobility transistors (HEMTs) based on Indium-phosphide (InP) with ultra-low-noise amplifiers.

They potentially have the lowest noise at frequencies below 100 GHz, when cryogenically cooled. We have designed monolithically integrated InP millimeter-wave low-noise amplifiers (LNAs). The Planck design goal for noise temperature is 35 K at the ambient temperature of 20 K. The operation bandwidth is over 20% at 70 GHz. The maximum allowable power consumption for a Planck low-noise amplifiers (LNA) (gain 20 dB) is P_{be} =5 mW at 20 K. The chosen foundry for these LNA's was DaimlerChrysler Research, Ulm, Germany.

The LFI receivers are sensitive to polarisation. The ratio between the sensitivity to fluctuations in intensity and polarisation is $\sqrt{2}$ because the number of channels per polarisation is half that for intensity. The principal role of LFI is the characterisation the foreground (polarised and un-polarised) such as the synchrotron emission and polarised Galactic foreground components which are expected to have a strong emission in the LFI spectral bands.

In order to eliminate as much as possible the contribution of $1/f$ noise a differential pseudo-correlation scheme is adopted. In this scheme the signal from the sky is combined with a blackbody reference load by a hybrid coupler. The two signals are amplified, in two independent amplifier chains and then separated by a second hybrid. Because the two signals have been amplified with the same gain through the two amplifiers, the true sky power can be recovered. The control of the $1/f$ noise and the recovery of the fluctuation

of the sky signal is performed by switching phase shifters at 8kHz in each amplifier. The choice of the reference signal to be used, was made in order to minimise the effects of other systematics by adopting a source as close as possible in temperature to the sky input signal. For this reason the chosen source was the signal emitted by the 4k stage of the HFI (see section 2.2).

The HFI Instrument

A detailed description of the HFI instrument is postponed to chapter 2.

Chapter 2

The HFI Instrument

Introduction

The HFI consists of the focal plane unit, the readout electronics, the Data Processing Unit, the coolers (and their electronics), harness and tubes linking the various subsystems (see Fig2.1). It is designed to use bolometers cooled at 0.1K, that are the most sensitive detectors for wide band photometry in the HFI spectral range (100GHz-1THz).

Cooling the detectors at 0.1K in space is a major requirement that drives the architecture of the HFI. This is achieved, starting from the passively cooled 50K/60K stage of the payload module, by a four-stage cooling system (18K-4K-1.6K-0.1K) detailed in section 2.5. The 18K cooler is common to the HFI and the Low Frequency Instrument (LFI).

In this chapter we shall present a general view of the instrument from HFI cold optics to the scientific signal in digital units.

2.1 The Cold Optics

The coupling of the FPU with the telescope is done by naked corrugated horns (devoid of windows), designed to minimise the energy taken from outside the telescope (Spill-Over) and to optimise the angular resolution. This horn is attached to the 4K stage and coupled to a back horn by a wave guide section that constitutes the only radiative coupling between the outside and the inside of the 4K box. Filters are attached on the 4K, 1.6K stage, and bolometers on the 0.1K stage, which corresponds to an optimal distribution of heat loads on the different stages.

Since most sources of spurious radiation have a steep spectrum, a high spectral rejection is mandatory. In addition, the radiation of the filters them-

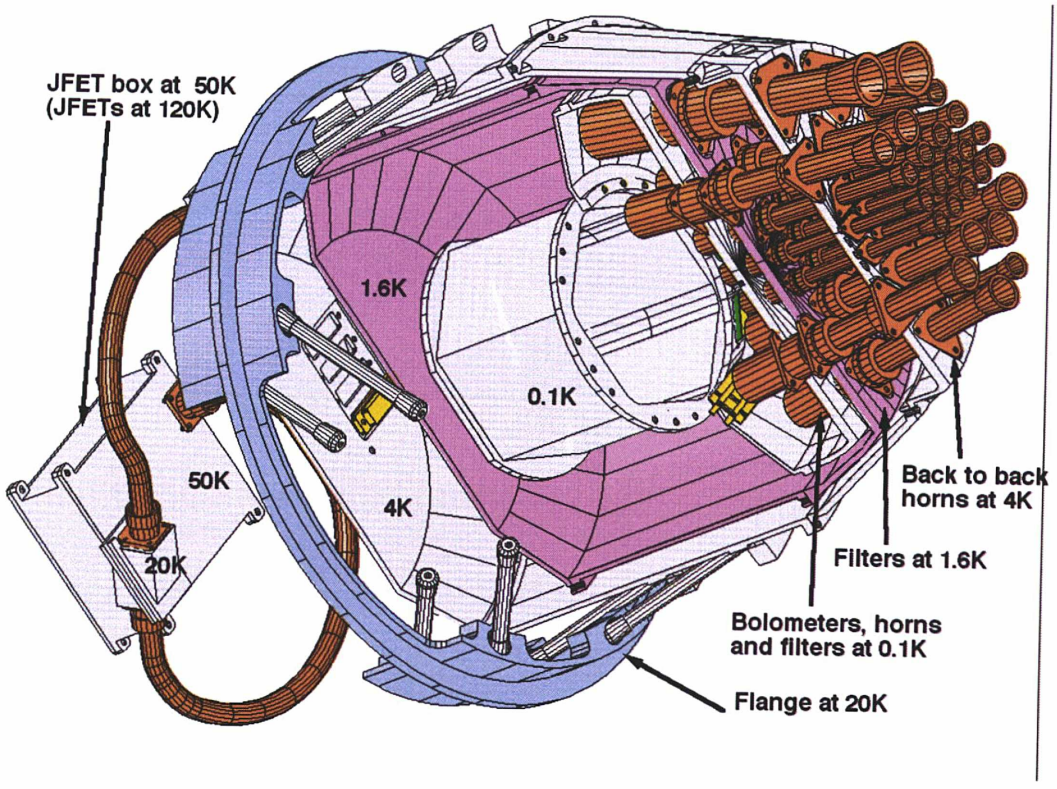

Figure 2.1: *A general view of Planck HFI instrument.*

selves on the detectors and the load from warm parts on the cryogenic stages must be kept small (<100 nW on the 0.1K stage). Complying with these requirements is achieved by high performance interference filters and by this original architecture tightly coupling optical and cryogenic designs (see Fig 2.1). By using back to back horns at 4K, a beam waist is produced at the 1.6K level where spectral filters are placed to define the detected band. A third horn concentrates the radiation onto the bolometric detector. This design naturally offers thermal breaks between the 100mK detectors, the warmer 1.6K filters and the focal plane horns at 4K. In some channels, an additional lens on the 1.6K stage has proven to minimise the losses of the optical chain (see Fig 2.3).

Pixel Layout

Figure 2.2 shows a schematic view of the HFI focal plane. The limitation of the number of horns comes from a thermal and mass limitation imposed by

the cooler and from the requirement to share the focal plane with the LFI.

The number of detectors at the same frequency is determined by the cross scan sampling requirement, the need to measure polarisation and the goal of maximum redundancy. In fact in order to measure polarisation we must have at least a measurement of three polar directions at the same point of the sky. For redundancy and because polarisation sensitive bolometer (PSB) can be made by pair, it has been chosen to measure 4[31].

The location of the different pixel at different frequencies is determined by the requirement to minimise the effect of focal plane aberration, and to measure at short time intervals the different polarisations of a given source on the sky by detectors on the same scan path. The problems to find a sufficient sampling issue is detailed in the chapter 5.

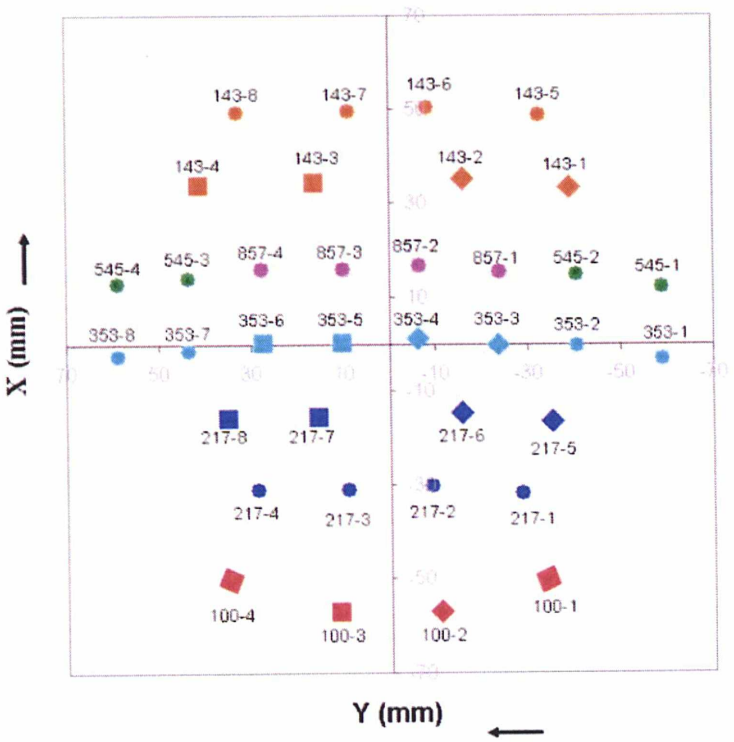

Figure 2.2: *Diagram of HFI Horn Position and PSB orientation on the RDP (Reference Detector Plane).*

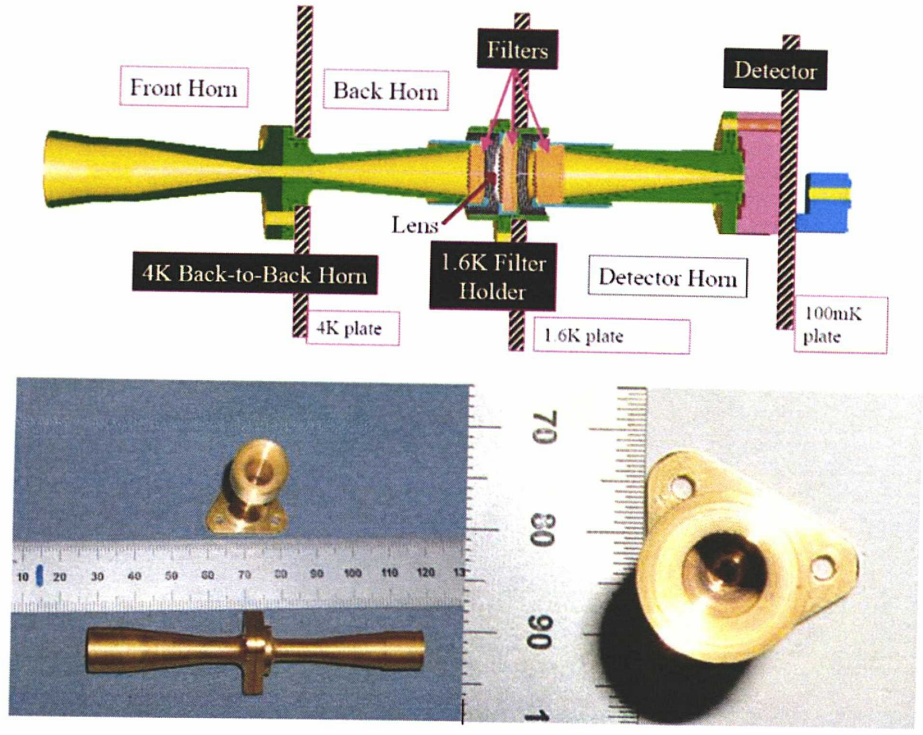

Figure 2.3: *On the top: optic of one channel of the FPU. On the bottom: example of 143 HFI back-to-back horn with a top view of the front horn in the back-to-back horn.*

Coupling to the Planck Telescope: Horns

To obtain the necessary resolution with low spillover properties, a flared shaped corrugated horn design has been chosen for the feeds.

In general horn antennas are the conventional types of feed used in heterodyne systems where one coherent mode (single-moded horns) couples to the mixer normally located in the waveguide at the back of such horns. On the other hand the corrugated horns designed for the HFI feed incoherent bolometric detectors.

Both polarisations of the radiation can propagate through the circular waveguide filters and can be detected by a conventional bolometer.

The 100, 143, 217, and 353GHz horns are single moded, and so produce coherent diffraction limited beam patterns. The details of the sidelobe structure, and thus the spillover levels as a function of edge taper, depends on the phase error $d^2/(8\lambda L)$ across the horn aperture (d is the horn diameter

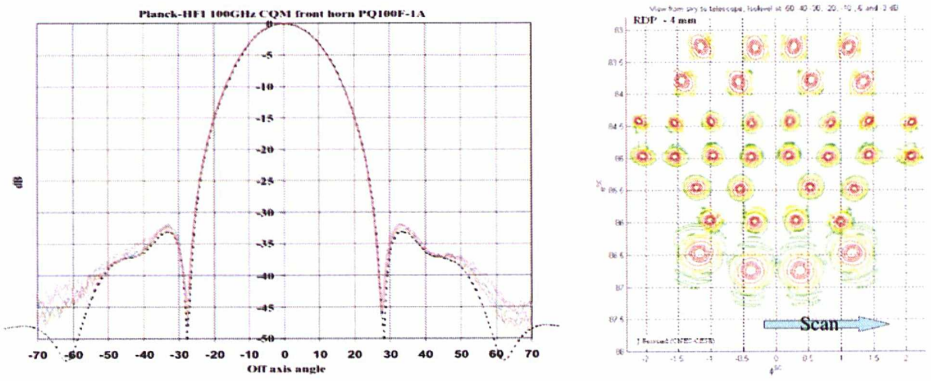

Figure 2.4: *On the left measurement and simulations superposed of a typical beams of HFI. Noise is limiting accuracy under -35dB. On the right beam positions in the SC reference frame and scanning direction.*

and L the horn axial length). However, because of mass restrictions and the limited field of view in the telescope focal plane, sizes of the horns have to be minimised. For the higher frequencies (545GHz and 857GHz) the angular resolution requirement does not demand diffraction limited operation for the required spillover levels. *Few moded* horns have been designed for these cases to increase the throughput and coupling to a 5 arcmin beam on the sky[32]. Few moded operation is obtained by increasing the waveguide diameter and allowing higher-order waveguide modes to propagate.

the table hereafter shows the nominal resolution for each HFI band:

Frequency (GHz)	100	143	217	353	545	857
Resolution (Arcmin)	9.4	7.1	5.0	5.0	5.0	5.0

The Spectral and geometrical properties of the horns have been measured individually. A typical measurement of beam with the comparison with the model is presented on Fig2.4.

Spectral band Selection: Filters

The selection of the observation band of each detector is obtained by a sequence of filters that guarantee the spectral purity of the final measurements.

The spectral bands are defined by a combination of the high pass (cut-on) effect of the waveguide of the back-to-back horns and a low pass metal mesh

filter (cut off). Four additional low pass edge fillters minimise the harmonic leaks, which makes an overall rejection factor that exceeds 10^{10} at higher frequencies. This scheme also allows some flexibility to choose where the unwanted thermal power is dumped (i.e. 4K, 1.6K or 100mK cryogenic stages).

The interferometric mesh filters are using low-loss metallic grids that provide a very high transmission and a very sharp cut. They produce the effective band selection of HFI Channels. The working principle of this filter is based on reflection of the unwanted radiation (not on absorption as yoshinaga filters). This provide a very low level of backgroung from instrument itself [34].

The HFI metal mesh interference filters have been developed by Univer-

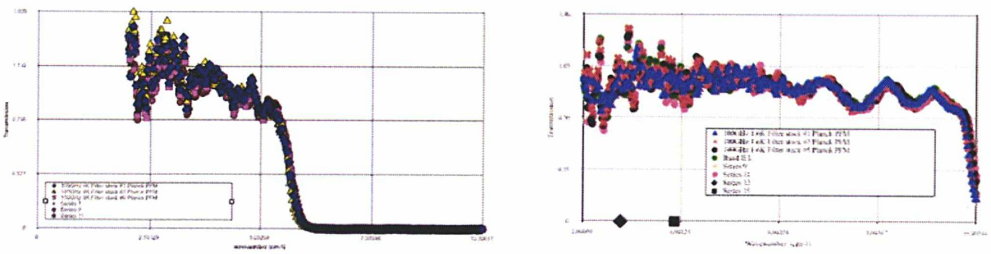

Figure 2.5: *Characterisation of the stack of mesh filters in 4K and 1.6K stage*

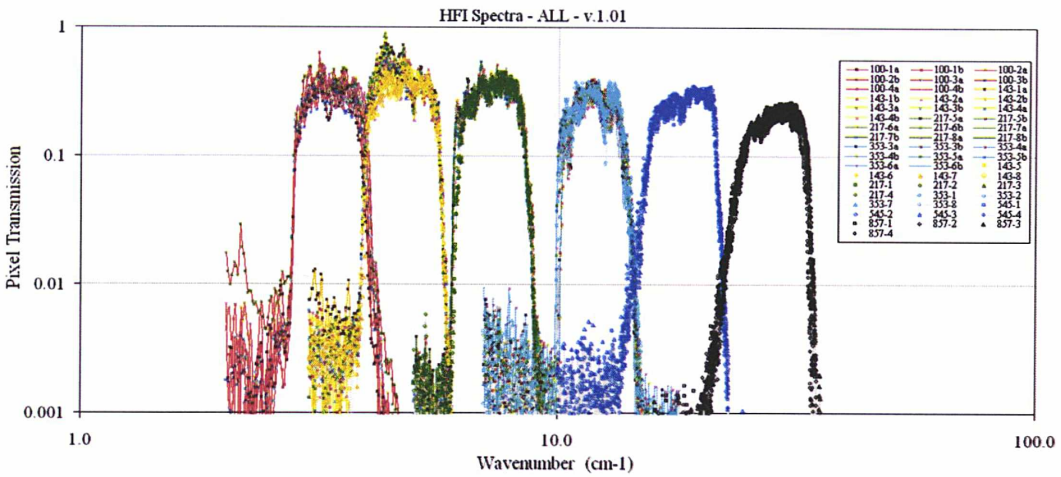

Figure 2.6: *In-band spectral transmission mesured during PFM calibration on all the 52 channels of HFI [33]*

sity of Cardiff. They have been shown to be durable (embedded in polypropylene) and lightweight (self-supporting) and have been qualified for space use by NASA.

To minimise the thermal loading on the 100mK stage the first low pass filter is placed at the exit of the back-to-back horn pair where there is a beam waist and the incident radiation is at near normal angles to the filter. This ensures that most of the unwanted power (wavelength lower band edge) is kept at the 4K stage level. Equally important, this location has been shown to eliminate the enhanced side lobe response that occurs if the filters are placed in a converging beam in front of the feeds.

The spectral transmission of each HFI channel is derived from PFM calibration [33]. In Fig 2.6 the total spectral transmission normalised to 1 for all 52 channels of HFI is presented. The normalisation factor is one of the measurements performed by LERMA (EFF sequence) and it is showed in Chapter 4.

2.2 The Detectors

The Planck HFI bolometric detectors must have inherent NEPs less than or equal photon noise of the background together with a speed of response fast enough to preserve all of the signal information at the 1 rpm scan rate of the satellite. This is achieved by the CalTech/JPL (California Institute of Technology, Jet Propulsion Laboratory, Pasadena, USA) spiderweb bolometers.

Bolometers are broadband thermal detectors optimized to the work from far infrared to the microwave domain. At wavelength larger than $200\mu m$, photoconductors lose their efficiency . On the other hand in this range of frequency, coherent detectors are not sensitive enough to be preferred to bolometers (see Fig2.7).

Spiderweb bolometers are manufactured using metal meshes and a doped (NTD) germanium with a resistance strongly dependent on the temperature. The size of meshes is adapted to operate in 6 spectral band of frequency between 100-900 GHz. A detailed theory of a bolometer is postponed to chapter 3. Polarisation Sensitive Bolometers (PSB) are implemented in all CMB channels (100GHz, 143GHz, 217GHz, 353GHz, 545GHz, 857GHz).

The choice of the spiderweb technology is due to the necessity to reduce the noise produced by cosmic rays. The use of an absorber with a spider web shape in fact reduces strongly the cross section (of the order of 90%less) for all the particles coming from the sky. Because of the size of the aperture

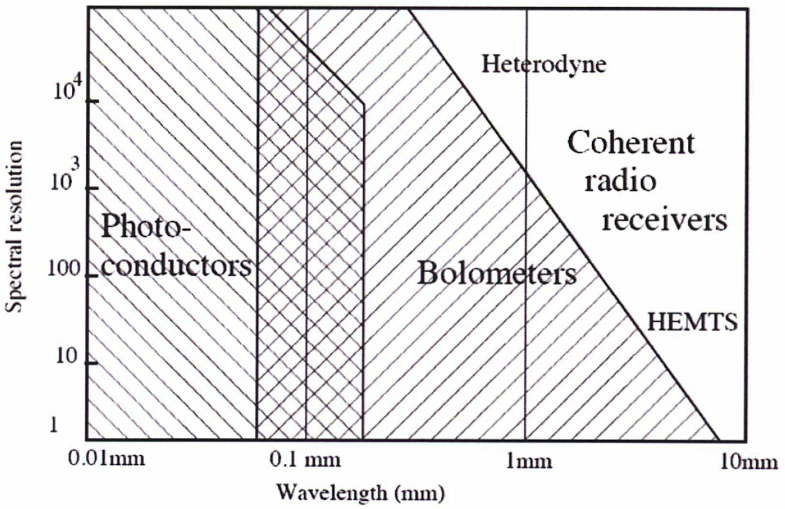

Figure 2.7: *Domain of interest of bolometers for astrophysical observations. The spectral resolution versus wave length is plotted [35]*

of the spiderweb mesh, the bolometer have an effect of a low frequency pass filter on the incoming radiation.

Because the mechanical resonant frequency of the micromesh bolometers is high ($\sim$ 50 kHz), the devices are insensitive to the relatively low frequency vibrations encountered during the launch and operation. This type of bolometer has been tested under vibrations 10 times in excess of the expected level. No degradation in the noise performance has been observed

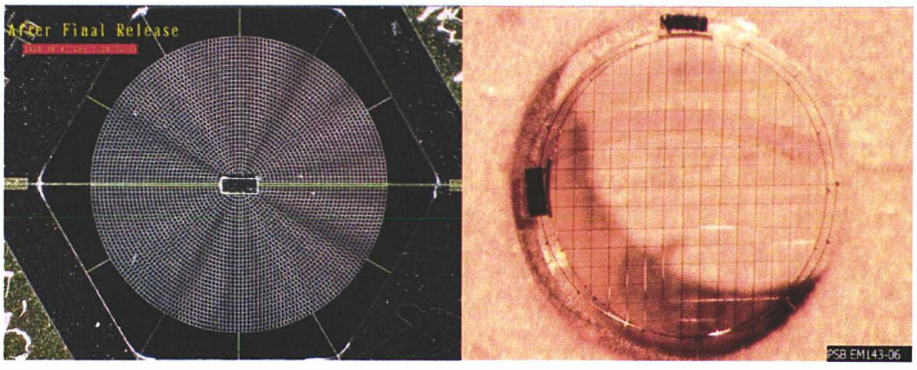

Figure 2.8: *Image of a typical HFI spiderweb and a PSB (polarised sensitive bolometer)*

after vibration.

2.3 Readout Electronics

The readout electronics (REU) is designed to measure the impedance of the temperature sensitive element of the bolometer. This is done by injecting a current, and therefore deposing some power in the bolometer which changes its temperature. In consequence, the bolometer response and performance strongly depend on the design of the readout electronics.

The classical method is: a bolometer is polarised with a DC bias voltage through a load resistance R_L, and the voltage V_b is measured thanks to an amplifier with an high input resistance. The advantage of this architecture is the use of a well established theory of bolometer [36], [37]. The optical power W_{opt} absorbed by the bolometer and the response of the bolometer can be directly computed.

On the other hand a DC bias polarisation increases the level of low frequency noise like fliker noise making impossible the detection of a faint and slowly varying optical signal. In addition the Johnson noise produced by the load resistance obliges to put this element on the coldest cryogenic stage.

The Electronic chain implemented in HFI instrument initially proposed by A. Benoit [38], is a evolution of the AC readout developed by Rieke et al., known to improve the law frequency stability of bolometers [39]. In the Fig2.9 a scheme of the principles of read-out system is presented.

Here the load resistor is replaced by two simetric capacitors in order to equilibrate an AC bias polarisation system. The capacitance does not produce any significant heat and is not a source of Johnson noise so it is not more necessary to put this element in the coldest cryogenic stage with any significant advantage in terms of thermal budget and lifetime of the instrument. In addition the capacitance has a large input impedance (for $4.7pF$ the value of the impedance at 100Hz is equal to $\sim 4.7G\Omega$ against a typical value of $40M\Omega$ for a load resistance).

A Second original feature of this new system is that the AC bias applied is the sum of two differents signals. The capacitance is polarized by a triangular wave voltage which produces a square wave current into the capacitor. A second square bias voltage which produces transient currents is added in order to correct for the capacitive of the cables (stray capacitance). A third square voltage (V_{bal}) in opposition of phase is added to $V_{bolometer}$ to balance the signal, that is to keep its amplitude well inside the range accepted by the amplification and demodulation electronics.

The amplitude of these three voltages are controlled by three 12 bit DACs

(Digital to Analogical Converter) with a reference voltage of 2.5 Volts. The amplitude of square balance and transient voltage and the slope of triangular bias voltage are (Montier private communications):

$$V_{Bal} = V_{alim} \frac{T_{bal}}{4095 \cdot GPAU_{200}} \tag{2.1}$$

$$V_{Tran} = 2V_{alim} \frac{R_{50}}{R_7 + R_{50}} \frac{T_{bal} T_{tran}}{4095^2} \tag{2.2}$$

$$V_{Tri} = V_{alim} \frac{R_7}{R_7 + R_{50}} \frac{t_{mod}/2}{R_{22}(C_5 + C6)} \frac{T_{bias}}{4095} \tag{2.3}$$

where T_{bal}, T_{tran}, T_{bias} represent the telecomand expressed in digit controlled by a software, V_{ref} is the reference voltage, t_{mod} is the time period, ,4095 is the range in digit of the DAC and:

$$V_{alim} = V_{ref} \frac{R_{21} + R_{17}}{R_{21}}$$

$$V_{ref} = 2.5Volt$$

$$R_{21} = 5.6kOhm$$

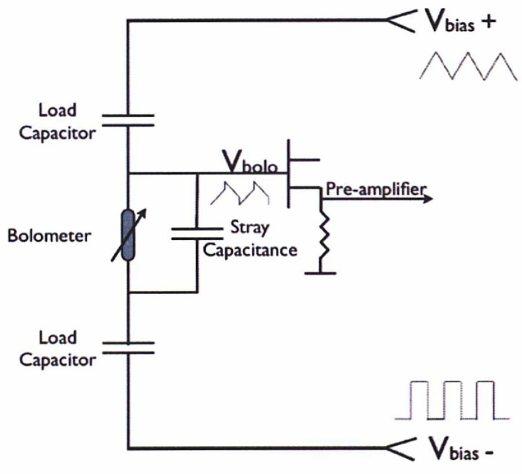

Figure 2.9: *Scheme of the HFI AC bias (sum of two signals) with a capacitive load and a stray capacitance in parallel with the detector*

$$R_{17} = 10kOhm$$
$$R_{50} = 10kOhm$$
$$R_{7} = 20kOhm$$
$$R_{22} = 240kOhm$$
$$GPAU_{200} = 200$$
$$C_{5} = 10nF$$
$$C_{6} = 10nF$$

The output signal is amplified in the Pre-Amplification Unit (PAU), and V_{bal} is substracted. After that the signal is amplified a last time according to the programmable gain of amplification Gamp (set to 0.33, 1, 3 or 7.6) and filtered by a band pass filter (5-600 HZ). Finally the signal is converted into digital signal, called *Raw-Signal* S by a 16 bit ADC. This signal is expressed in ADU, from 1 to 65535, and centered around 32768.

The scientific signal (DSN) is given as the sum of the raw-signal S on each half-periods:

$$DSN^{+} = \sum_{+} S(i)$$
$$DSN^{-} = \sum_{-} S(i)$$

with DSN^{+} the scientific signal on the first half-period and DSN^{-} on the second half-period.

The computation of DSN depens on 2 parameters:

N_{sample} = number of points per half-period ($N_{sample=}$ 36, 40 and 45).

S_{phase} = is the rank of the first high frequency sample to be co-added to form a DSN.

They are computed according to the following expressions :

$$\sum_{+} = \sum_{S_{phase}}^{N_{sample}-1+S_{phase}}$$
$$\sum_{-} = \sum_{0}^{S_{phase}-1} + \sum_{N_{sample}+S_{phase}}^{2N_{sample}-1}$$

2.3.1 Stray Capacitance

Any two adjacent conductors can be considered as a capacitor, although the capacitance will be small unless the conductors are close together or long. This (unwanted) effect is called *stray capacitance*. Stray capacitance can allow signals to leak between otherwise isolated circuits (an effect called crosstalk), and it can be a limiting factor for proper functioning of circuits at high frequency. Let us consider here the effect of the stray capacitance in the readout circuit.

It is possible to calculate analytically the stray capacitance of the circuit by making some simple assumptions: If we consider a stray capacitance in parallel with the bolometer, the equation of the circuit is:

$$V_b = \frac{Z_p Z_b}{Z_p Z_b + (Z_p + Z_b) Z_l} V_0 \tag{2.4}$$

where Z_p, Z_l and Z_b are the impedances of stray capacitance, the load capacitance and the bolometer. V_0 is the total input voltage (triangular plus square voltage).

To compute how the transient step of V_0 is propagated to V_b the bolometer impedance can be considered as very large with respect to that of capacitors C_p and C_L. In this case we obtain from Eq 2.4:

$$\frac{V_b}{V_0} = \frac{C_L}{2C_p + C_L} \tag{2.5}$$

In this case $V_0 = V_{Tran}$; from Eq 2.1 and Eq 2.2 we obtain:

$$V_{Tran} = 2\frac{R_{50}}{R_7 + R_{50}} \frac{T_{Tran}}{4095} \cdot GPAU_{200} V_{bal} \tag{2.6}$$

In the readout electronics is balanced it must happen:

$$V_b = V_{Bal} \tag{2.7}$$

So it is possible to calculate the stray capacitance from 2.5 as:

$$C_p = \left(\frac{\frac{2GPAU_{200}}{R_{50}} T_{Tran}}{(R_7 + R_{50})4095} - 1\right)\frac{C_l}{2} \tag{2.8}$$

For a typical bolometer if $C_L = 4.7$pF and $T_{Tran} = 2000$ (that is nearly the value of the transient during PFM ground calibration) we obtain:

$$C_p = 150.6pF$$

The interaction between the bolometers and the REU is therefore complex. We address in the next chapter various approaches taken to model this interaction and the response of the instrument.

2.4 Sensitivity

The quantity that takes in account the sensitivity of the instrument is the Noise Equivalent Power (NEP). It represents the power producing a signal in a post detection bandwidth of 1Hz integrated for 0.5 sec equal to standard deviation of the noise. This quantity takes into account the response and the noise of the detector (see section 3.2.5). All the sources of noise add quadratically the corresponding NEP to produce the total NEP.

In the case of Planck HFI we can separate three type of contributions in terms of noise:

$$NEP^2_{tot} = NEP^2_{Photons} + \sum_{i=1}^{N} NEP^2_{bolo(i)} + \sum_{i=1}^{N} NEP^2_{others(i)} \tag{2.9}$$

where $\sum_{i=1}^{N} NEP^2_{bolo(i)}$ corresponds to the contribution in NEP of the noise coming from the bolometer (Johnson noise, phonon noise principally), and $\sum_{i=1}^{N} NEP^2_{others(i)}$ is the contribution of the rest of source of noise[1] (Preamplifier noise principally but also microphone, cross-talk, shot noise and electronic noise). $NEP^2_{Photons}$ is determined by the corpuscular nature of photon following the Bose-Einstein statistic. So in the best conditions the contribution of Photon noise is the limit of sensitivity of the instrument and it is taken as a reference for the other ones.

In case of Planck HFI the goal NEP has been defined:

$$NEP_{GOAL} \leq 2 * NEP_{Photons} \tag{2.10}$$

To make this happens it has been fixed as nominal specification:

$$\sum_{i=1}^{N} NEP^2_{bolo(i)} \leq NEP^2_{photon} \tag{2.11}$$

and

$$2 \cdot \sum_{i=1}^{N} NEP^2_{others(i)} \leq NEP^2_{photon} \tag{2.12}$$

As a guideline for the design of the instrument, it has been required that the proper source of noise of each sub-system had to be less than 0.3 time photon noise.

$$NEP_{sub-system} \leq 0.3 NEP_{photon} \tag{2.13}$$

So that the impact on the total NEP is less than 5%.

[1] A detailed discussion on principal sources of noise is posponed to section 3.2.5

In the table 2.4 measurements of the NEP are presented for typical channels of HFI. The table shows that the nominal requirements for sensitivity are reached.

Bolo	I_{bias} [nA]	NEP_{tot} [$attoWatt/\sqrt{Hz}$]	NEP_{phot}	NEP_{phon}	NEP_{john}	NEP_{fet}	NEP_{comp}
PSB100	0.262	14.4	10.6	4.9	6.6	2.9	4.3
PSB143	0.293	17.5	13.7	5.0	7.5	3.1	5.3
SWB143	0.343	19.5	13.6	5.7	10.3	4.5	5.9
PSB217	0.283	18.4	14.6	5.1	7.6	3.3	5.6
SWB217	0.374	26.3	21.3	7.2	10.3	3.5	7.9
PSB353	0.277	25.3	21.9	5.3	8.0	2.8	7.6
SWB353	0.337	28.7	25.3	4.5	8.7	3.7	8.7
SWB545	0.666	47.9	38.4	14.3	18.6	7.2	14.4
SWB857	0.690	78.4	69.8	14.6	20.5	7.8	23.6

Table 2.1: *Principal contributions of the NEP (photon, phonon, johnson, Jfet and compression) of typical HFI bolometers for nominal bias current. Total NEP is also presented. ([40], [41])*

2.5 The HFI Cryogenic System

The sensitivity of the HFI critically depends on the temperature of the detectors.

It has been shown [42] that 100mK or less were needed for the Planck mission called COBRAS/SAMBA at this time.

To obtain such a low temperature, it is necessary to surround the coldest stage with different cryogenic stages at different temperatures. In addiction, in order to decrease the photon noise level of the instrument itself, several cryogenic levels are used to cool down the hornes and the mesh filters witch selects the spectral bands (see section 2.3).

A basic technique to reach cryogenic temperatures is to put the detector in thermal contact with a fluid (or a solid) with a low boiling temperature (or sublimation temperature). The evaporation latent heat permits to keep the normal boiling temperature as a constant even in presence of an heat input from a warm environment, of course wasting part of the fluid.

In the case of Planck HFI the use of cryogenic fluids like Helium or Nitrogen to make the dilution cooler system working has not been considered as feasible. It has been chosen to use a Joule-Thompson mechanical cooling technique[2], in which the reliability depends only on mechanics of cooling system and so it provides a considerable cost reduction and an increase in lifetime.

The cooling scheme that allows to cool at 0.1K the 52 bolometers and their filters is based on technical solutions that have been successfully tested in space borne, balloon borne and ground based instruments. Each cooling system takes advantage of the previous one.

The HFI cryogenic system is composed by a dilution cooler and a 4K cooler. The dilution cooler is based on dilution of ^3He into ^4He. It has been developped by CRTBT (Centre de Recherche sur les Très Basses Températures), IAS and Air Liquide. The dilution cooler must work in an environmental temperature less than 4.8K. In order to insure this working temperature we use a Joule-Thompson cooling system based on ^4He expansion principle developped by RAL (Rutherford Appleton Laboratory) and Astrium. In its turn this cooling system works in an environmental temperature less than $18K$. This is obtained by Joule-Thomson expansion of hydrogen and a closed loop sorption/desorption pumps developed by JPL (Sorption Cooler). The Sorption Cooler (see section 1.4.2) fluids have to be pre-cooled to about 50K,

[2]The Joule Thomson effect describes the increase or decrease in temperature of a real gas when it is allowed to expand freely at constant enthalpy (which means that no heat is transferred to or from the gas, and no external work is extracted). The compression of specific gas is realised thanks to an absorption compressor.

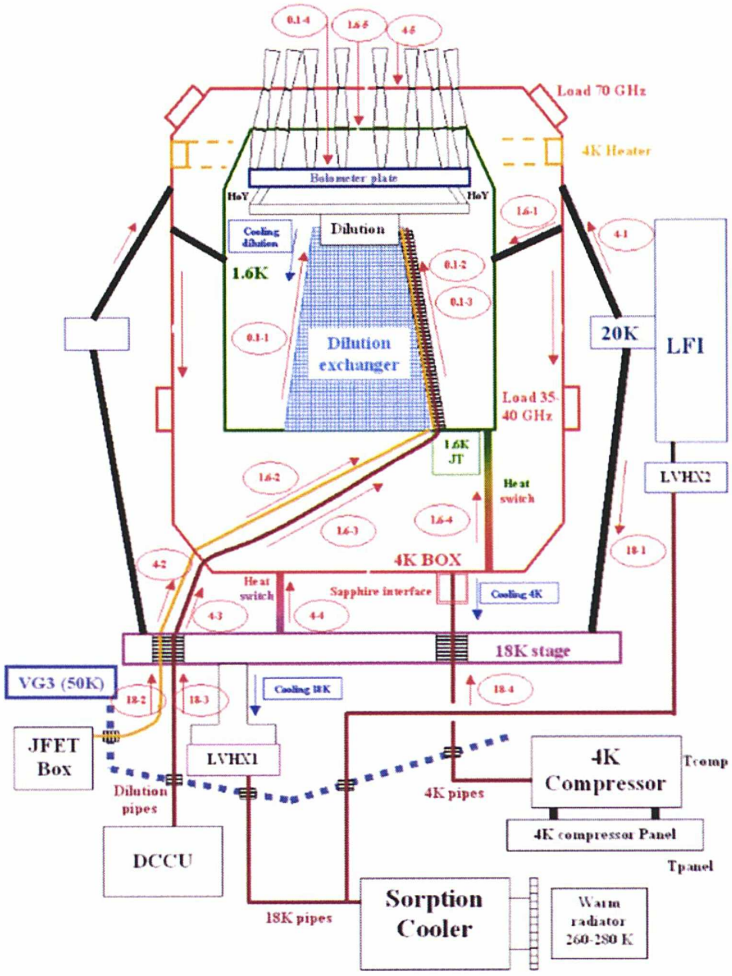

Figure 2.10: *HFI Thermal Path Summary*

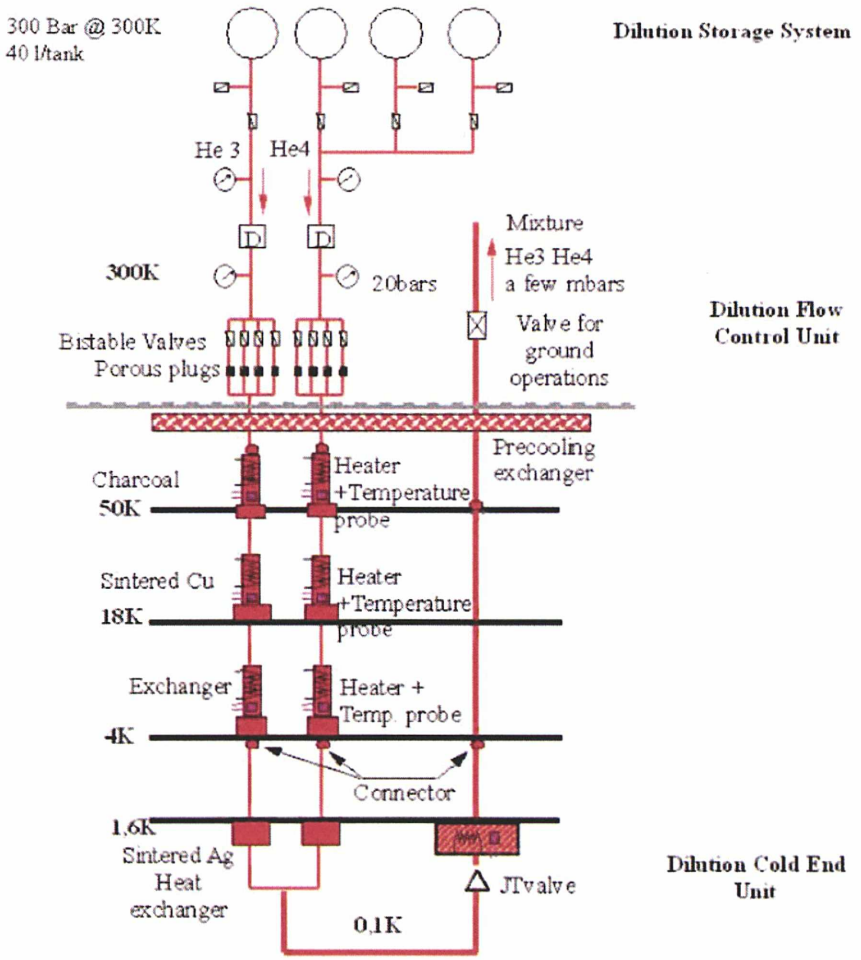

Figure 2.11: *Schematic view of dilution cooler of Planck HFI*

which is made by a passive cooling architecture. This is the characteristic V-Groove radiator that separates the service module from the science payload.

The overall architecture and pointing strategy of Planck are oriented towards an effective cryogenic operation.
The whole cryogenic chain (see Fig 2.10) attends the temperature of 100mK in approximately 34 days. Here a general description of the two sub systems.

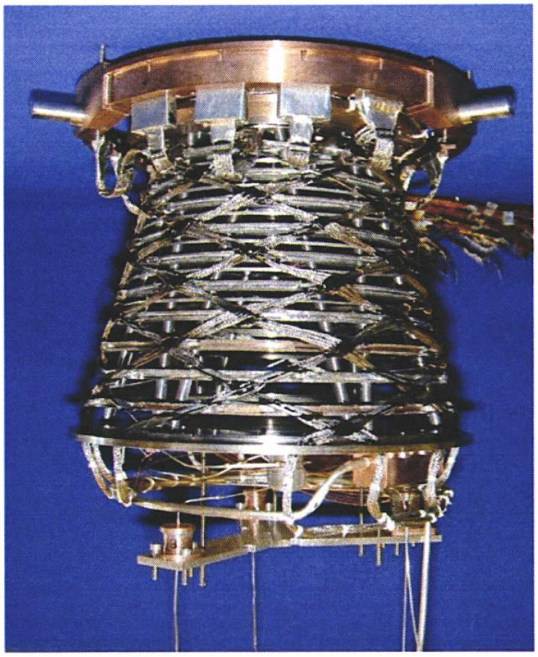

Figure 2.12: *The dilution cooler*

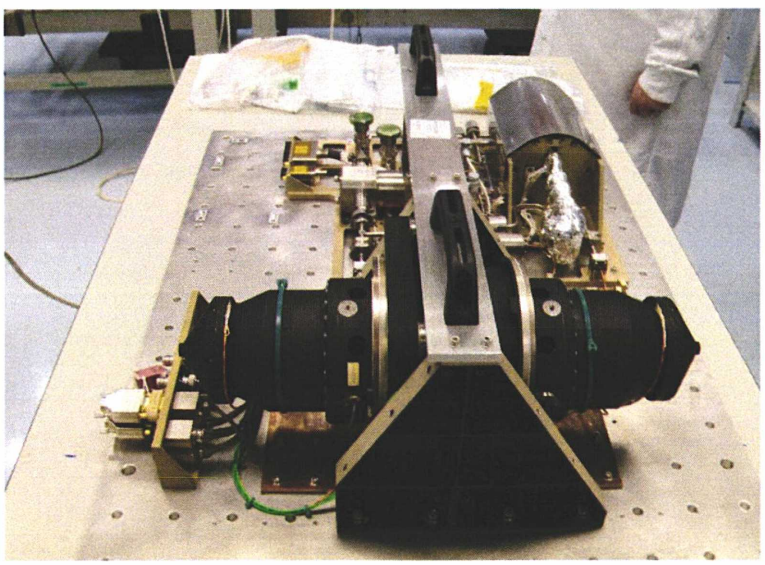

Figure 2.13: *The 4K cooler*

2.5.1 100mK Dilution Cooler

The principle of cooling via dilution of ^3He in ^4He atoms is based on the fact that Van der Waals forces between ^3He and ^4He atoms are higher than between a pair of ^3He or a pair of ^4He atoms. When we mix of these two isotopes they absorb heat to build stronger bonds ([43]). This commercially available technology uses gravity to mix and separate the ^3He rich and ^4He dilute phases. Alain Benoit and Serge Pujol have invented an original method that allows to use the same principle in a micro-gravity environment ([44]). Mixing ^3He and ^4He in small capillary tubes in an open cycle has proven to work in any gravity condition testable on the ground.

In the dilution cooler, it is possible to distinguish a low temperature part in contact with the bolometers plate and a warm part where the gas is stored and its flow controlled (see Fig 2.11).

The low temperature part of the dilution cooler is linked to the plate that supports 52 bolometer, 2 blind bolometers, their horns and filters, thermometers. Three pipes are used to mix the two isotopes: the first two for isotopes injection and the last one to retrieve the mixture.

The dilution is performed in this pipe and it is used to cool down the 100mK head.

The ^3He ^4He mixture delivers its full cooling power to the incoming fluids along a heat exchanger wound-up in a spiral along the conical support. The base of this support is cooled at 1.4K by Joule-Thomson expansion of the mixture.

The duration of life of this open loop system limits the duration of the whole mission. The nominal specifications indicate at minimun a life of 14 months (2 surveys) for the dilution system.

2.5.2 4K Cooler

A 4K stage is required for cooling the dilution refrigerator and the focal plane unit. Fig 2.14 shows a schematic plot of the major components of the 4K system. This system has been developed at the Rutherford Appleton Laboratory ([45]) and constructed by Astrium. This cooler uses a mechanical compressor to realize a Joule-Thompson cycle of ^4He gas which is able to cool the cryostat down to a temperature of 4K. The Helium gas is pre-cooled at 18K by the LVHX1 stage of the Sorption cooler.

The main components of the 4K system for Planck are:

• The JT compressors which give two stages of compression from about 1 bar to 10 bar.

• Ancillary plumbing which contains part of the gas purification system, a filter, a flow meter and a valve for the JT by pass system.
•The cold temperature plumbing which incorporates countercurrent heat exchangers between the stages and filters and gas purifiers on the stages. The 4K stage contains a reservoir for liquid helium.
• Low vibration drive electronics.

The 4K cooler cold head cools down the FPU 4K box. The temperature of this box, and thus of the HFI feed horns, affects the photon noise coming from the emission of the feed horns and filters.

The exact value of the temperature is not critical since the HFI bolometer noise is dominated by the background photon noise and by the detector chain noise from the sources and the telescope. The 4K cold head pre-cools the 3He and 4He gas of the dilution cooler. The intermediate 1.6 K stage is cooled by a Joule-Thompson expansion of Helium and the dilution of the two isotopes provides the 100mK cooling.

The FM 1.6 K JT has a gas flow impedance lower than the one which would give an optimal operation. It was decided not to change this JT as it was shown in FM HFI calibration that the required performances were obtained even at the maximum temperature of 5K. Nevertheless at this pre-

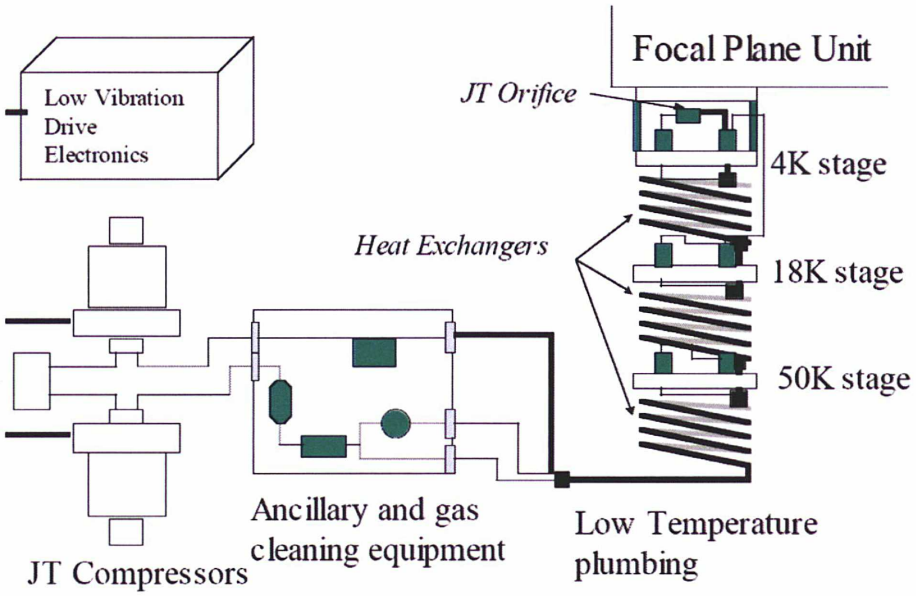

Figure 2.14: *Schematic view of the 4K cooler system.*

cooling temperature, the 1.6 K JT is then operated in a rather marginal mode implying to use a higher isotope flow rate than the one required by the dilution part. Thus the preferred 4K pre-cooling temperature is below 4.7K which brings the 1.6-100 mK dilution cooler in the normal regime where the dilution is setting the isotope flow requirement.

The electrical power needed to operate the 4K cooler is 100W. The duration of life is fixed by the lifetime of the power supply of about $5\dot{1}0^5$ hours.

2.5.3 Thermometers

There are 16 sensitive NTD germanium thermometers on HFI in order to analyse and attenuate the temperature fluctuations of the three active coolers. They are placed at all the cryogenic levels.

The performances in $NE\Delta T$ are presented in the next table: ([40])

	Thermo Signal	μK/sqrt(Hz)
0	HFI_90_THER_100MK1_T3_K_C	0.00795
1	HFI_A2_THER_100MK2_T3_K_C	0.00996
2	HFI_92_THER_PID1N_100MK_T3_K	0.01137
3	HFI_B1_THER_PID1R_100MK_T3_K	0.00928
4	HFI_91_THER_PID2N_100MKPLATE	0.01502
5	HFI_B0_THER_PID2R_100MKPLATE	0.00908
6	HFI_94_THER_1_6K1_T1_K_C	0.31711
7	HFI_B2_THER_1_6K2_T1_K_C	0.28181
8	HFI_93_THER_PID1_6N_T1_K_C	0.26963
9	HFI_A3_THER_PID1_6R_T1_K_C	0.32137
10	HFI_A4_THER_4KH1_T1_K_C	18.69691
11	HFI_B4_THER_4KH2_T1_K_C	15.63974
12	HFI_A5_THER_4KL1_T1_K_C	13.60169
13	HFI_B5_THER_4KL2_T1_K_C	13.48751
14	HFI_95_THER_PID4N_T1_K_C	17.66817
15	HFI_B3_THER_PID4R_T1_K_C	14.38034

Six thermometers Cernox type (with other six for redundancy) are implemented on each cryogenic stage (50K, 18K, 4K, 1.6K, 0.1K, and in the thermal switch 4K-1.6K) in order to follow the cooling of the instrument. A measure is recorded each 70 seconds for each cernox.

In order to attenuate the fluctuation in temperature of the cryogenic 4K, 1.6K and 100mK stages it has been implemented an active regulation of the temperature. This system is based on three elements: a thermometer, a heater and a Proportional Integral Derivated algorithm (PID) coded in the REU.

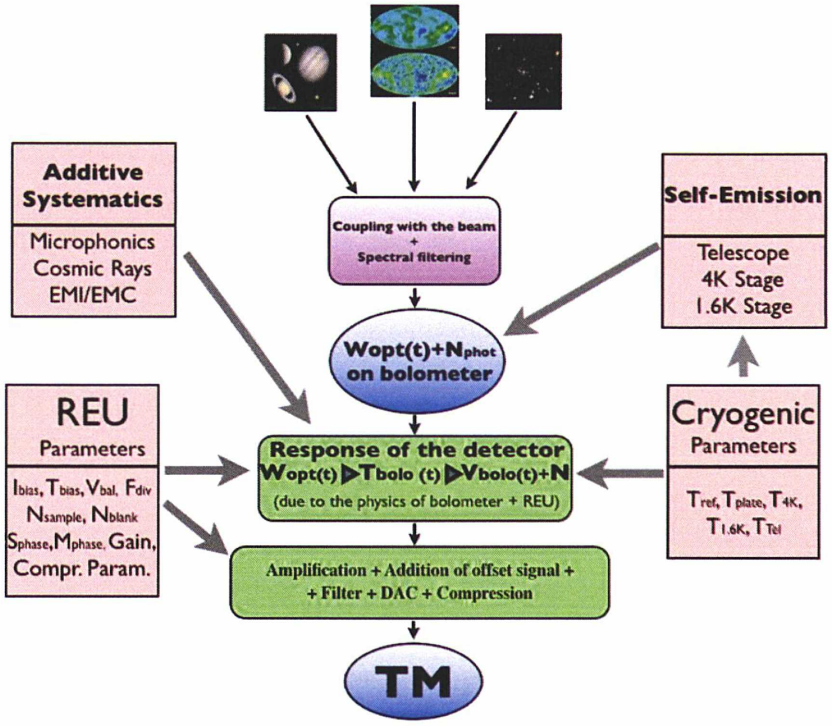

Figure 2.15: *Logic of formation of the signal in HFI.*

2.6 Role of the Calibrations and Instrument Model

To calibrate an instrument is to determine its response by comparison with standards. In Astrophysics, this means characterising in detail the selection of photons (geometry and energy) by the instrument, the detection of these photons and their transformation to data that can be ingested by a computer. In addition it means identifying and characterizing the spurious signals added in this process.

The way of HFI transforms brightness in digital data depends on many environmental and REU parameters. This is presented in the idealised view in figure 2.15. First, the optical chain applies spatial and spectral filtering: the image of the sky is convolved with the beam of the system made by the telescope, the horn and the internal optics including the bolometers. Photons are also selected in frequency by stacks of interference metal mesh filters at different cryogenic temperatures and by the spectral transmission of the waveguide sections of the horn systems. This produces a timeline of optical power in watts ($W_{opt}(t)$) to which a nearly constant self-emission

signal is added, produced by the thermal emission of the telescope and the cryogenic stages. Optical power is absorbed by the bolometer and its statistical fluctuations produces the photon noise N_{phot}. The temperature changes of the bolometer are detected as a voltage with corresponding noises in the bolometer itself and in the readout electronics. Then the signal is amplified, digitised, compressed and delivered to the telemetry system. This makes a very complex process with a large number of free parameters. Prediction of the instrument response and of optimal tuning of the readout is not likely to be accurate enough for our scientific goals. The logic has been to develop numerical models to assist instrument tuning and data reduction, to validate these models during the ground based calibrations and to rely on a fine calibration based on in-flight observation of known sources. Once this point is clear, let me underline also that a flight calibration cannot answer alone to all the scientific needs. For instance, the shape of the spectral bands cannot be measured in flight. This measurement is important in order to remove efficiently the contribution of the foregrounds from the cosmological signal since the two signals have different spectral indices. So it is necessary during ground calibration, to test every single component making use of a physical model in order to understand the physical processes involved. Then, to check the performances of the instrument as a whole, verify the numerical model of the instrument and determine its unknown parameters.

Chapter 3

Modelling the Response of HFI

The Models of HFI

The interpretation of the CMB maps that will be obtained by Planck will rely on an accurate knowledge of the transformation of the information operated in the instrument. Important quantities describing the instrumental functions will be calibrated in flight: photometric response to CMB calibrated on the dipole. Effective beams will be calibrated on planets. Others important quantities can be measured on the ground (i.e. spectral bands).

In order to support this calibration activity, numerical models describing the physical processes that take place in the instrument have been developed.

They are mainly:

Model of optics: they describe the propagation of waves from the sky to the receivers. They are using classical optics, physical optics or dedicated theories, depending on which one is the most adapted. They are used to describe the beams outside of the domain of measurement (far side lobes).

Thermomechanical distortion model of the telescope: The telescope cooling down from 300K to 50K deforms its mechanical characteristics. Different models takes into account these changes and predict the variation of perfomances.

Thermal Models: It is needed to define the settings for all the coolers, to monitor their evolution in flight and to anticipate changes in the tuning. It permits to predict the telecommand to set the working point of PID. It also permits to predict fluctuations of temperature of different cryogenic stages and their propagation to eliminate parasitical effects (like for instance the

effect of the temperature of the sorption cooler on the LFI and HFI detectors).

Simulation of the Optical Signal (SOS): It is the model wich permits to calculate the integrated optical power incident on the bolometer. This model has been developed at LERMA using models and results from PFM calibrations. I report details in the next section.

Response of the instrument: Different models have been developed in order to simulate the response of the instrument. An analytical model has been developed at LERMA in order to check rapidly different static behaviours of the HFI. The time response of the bolometer to a varying optical power is simulated by two similar models: the SEB IDL Models (developed by CESR and LERMA) and the SimHFI labview model (developed by Rashmi Sudiwala from University of Cardiff): Both models solve the differential thermal and electronics equations of bolometers and include a functional description of the whole readout system (see section 3.2.11).

The HFI response models have been presented at the Instrument Science Verification (ISVR) on September 2008 in charge to cover the following tasks:

• To predict the optimal tuning of the instrument.

• To predict the effect of any action that we would have to take in-flight.

• To simulate the response of the instrument in a credible way for end-to-end test.

• To correct for the effects of some variations that could happen while the data is being taken for in-flight calibration (e.g. changes of T_{100mK}, W_{bg}).

• To extend empirical calibrations outside of the measured range.

• To replace empirical calibration data in domains where the model is believed to be more accurate.

• To interpret some complex test data, such as the Bias Step Low Frequency Response (LFR) measurement.

• To validate the good health of the instrument by showing that the instrument behaves as expected and as shown before.

In this chapter I shall present a description of the models that I contributed to develop: the SOS model , the analytical static model and the SEB model. A general description of the modelling AC biased bolometers is also described.

3.1 SOS Model

The output of this model is the optical power absorbed by bolometers.

Considering the background generated by the instrument itself and a source (planets, our galaxy or laboratory sources), the incident power absorbed by detectors is:

$$W_{opt} = \frac{1}{1+P}\left(\int_0^\infty A\Omega(\nu)\tau_{4K}(\nu)\epsilon_{4K}(\nu)BB(T_{4K},\nu)d\nu + \right.$$

$$+\int_0^\infty A\Omega(\nu)\tau_{1.6K}(\nu)\epsilon_{1.6K}(\nu)BB(T_{1.6K},\nu)d\nu + \int_0^\infty A\Omega(\nu)\epsilon_{Tel}(\nu)BB(T_{Tel},\nu)d\nu$$

$$\left. +\int_0^\infty A\Omega(\nu)\tau_{Tel}(\nu)\epsilon_{Tel}(\nu)BB(T_{Tel},\nu)d\nu + \int_0^\infty A\Omega(\nu)\tau_{Tot}(\nu)(\nu)S(T_S,\nu)d\nu\right) \tag{3.1}$$

Where τ_{xx} and ϵ_{xx} are the transmission from the source considered to the detector and the emissivity of the considered cryogenic level respectively and τ_{Tot} is the total optical transmission of the instrument. P is the polarisation factor (P=1 for PSBs, P=0 for SWBs).

Equation 3.1 is not easy to use: all the transmissions and emissivities have to be measured versus optical frequency in the HFI spectral bands. This implies spectral measurements of the emission of each cryogenic stage and a knowledge of the emission of the telescope which depends on the dust deposited on the mirrors during lunch. For these reasons the equation implemented in the model is obtained with some simplifying hypothesis taking into account the PFM calibration results. The equation implemented in the model is presented in chapter 4 (see section 4.4.7)

The parameters that can be varied in the current SOS model are:

- Incoming Source (Background, CMB, Planets, sinus, square or a linear combination of them)
- Temperature of the Telescope
- Temperature of the 4K stage
- Temperature of the 1.6K stage

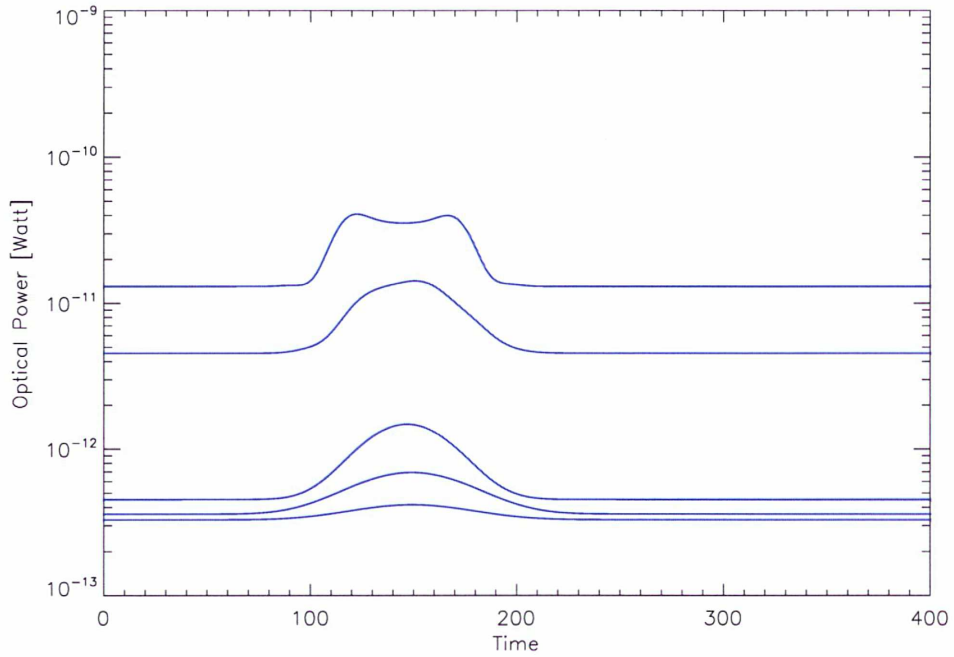

Figure 3.1: *Outputs of SOS model: a Jupiter scan is calculated for typical deterctors of Planck HFI (100GHz, 143GHz, 217GHz, 353GHz, 545GHz, 857GHz) with a nominal background*

- Emissivity of the Telescope

The fixed parameters in the model are:

Total spectral transmission of the optical chain
Thermal emission of 4K stage (from PFM LERMA measurements)
Thermal emission of 1.6K stage (from PFM LERMA measurements)
Effective number of modes in multi-moded channels (from B.Maffei)
Shape of the spectral transmission (from G. Savini)
Beam of the Instrument (from F. Noviello)

In Fig. 3.1 results produced by the SOS model are presented.

The model has been used as part of *Level S* simulations. Data representing a complete survey by Planck are produced with a Sky model and all the perfomances and systematics of the instruments. The contribution of SOS model was to characterise the emission of background from the telescope and

the various cryogenic stages.

3.2 Modelling the response of AC Biased Bolometers

The use of bolometers for astrophysical measurements has dramatically developed during these last decades, which can be explained by the fast improvement of their sensitivity and the emergence of new techniques allowing the production of large arrays of bolometers ([46], [47], [20], [21], [22], [48], [49], [50]). They are now the most sensitive devices for photon detection in wide domains of the electromagnetic spectrum. In the same time, the theory of bolometers was refined and updated to follow the emergence of new technologies and the exploration of new domains of bolometer temperatures ([51], [52]). The readout electronics for semi-conductor bolometers experienced a radical change about two decades ago. Most of them are now using a modulated bias current in order to get rid of low frequency noises that plague DC bias and amplification systems [39].

The interaction of AC biased readout electronics with semi-conductor bolometers is rather different from that of DC readout polarising the detectors through a load resistor RL as analysed in the founding paper by Jones ([36]). Such differences were evidenced during the calibration of the bolometer instrument of the project Planck, although the readout electronics had been designed ([38]) to mimic, as far as possible, the operation of a DC biased bolometric system. This chapter results from the need to be able to predict the real behaviour of AC biased semi-conductor bolometers in an extended range of working parameters. It reports for the first time new results obtained by the LERMA team on this issue.

3.2.1 Model of Bolometers

As pointed out in chapter 2 Planck bolometers are thermal detectors manufactured using metal meshes and a doped semiconductor resistance strongly dependent on the temperature.
The dominant conduction mechanism in the germanium thermometer is the variable range hopping between localised sites and the resistance of the device varies with both applied voltage and temperature. The relation between the resistance and the temperature of the bolometer is set from the variety of the doped semiconductors:

$$R(T,E) = R_* e^{(\frac{T_g}{T})^n - \frac{eEL}{K_b T}} \tag{3.2}$$

where T_g is a characteristic parameter of the material, R_* is a parameter depending on the material and the geometry of the element, L is related to the average hopping distance and E is the electric field across the device.
In absence of electrical non-linearities and other effects such as electron-phonon decoupling, the thermistor resistance depends only on temperature:

$$R(T) = R_* e^{(\frac{T_g}{T})^n} \tag{3.3}$$

At first order the thermal model of a bolometer can be described in the following the way (see Fig 3.2): the incoming optical power is absorbed by the mesh and thermalizes the whole bolometer sensitive element including the thermometer. $C(T)$ is the total heat capacity of the bolometer and $G(T)$ is the thermal conductance to a heat sink at reference temperature ($100mK$ in case of HFI). The absorbed optical power will determine a change in the temperature of germanium thermometer; if the detector is mounted in an appropriate circuit and polarized with a bias current, we can measure a variation of voltage at the end of the bolometer. The total power dissipated in the bolometer is $W = P + Q$ where Q is the absorbed radiant power and $P(t) = V(t)I(t)$ is the electrical power.

In static conditions the balance equation for a bolometer is:

$$G_s(T_b - T_0) = P + Q \tag{3.4}$$

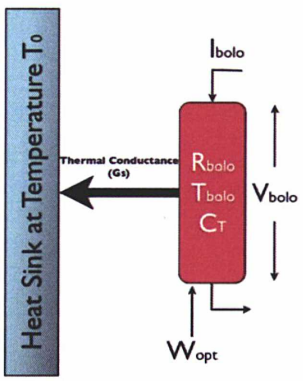

Figure 3.2: *Schematic diagrams of a bolometric detector*

G_s can be rather well represented in our case by:

$$G_s = G_{s0}(T/T_0)^{\beta}$$

where G_{s0} is the static thermal conductance at temperature T_0.

In astrophysical applications, bolometers work in non-equilibrium conditions, the signal from the sky in fact produces a small varying change in temperature on bolometer. So it is useful to deduce the non-equilibrium theory of a bolometer assuming a small variation in temperature dT

$$C\frac{dT_b}{dt} + G_e(T_b - T_0) = Q(t) \tag{3.5}$$

Where $G_e = G_s + \frac{dG_s}{dT}(T - T_0) - \Gamma(R_b, Z_L, ...)$ is the dynamic thermal conductance. Γ is a function depending on the used REU. In Section 3.2.2 I will derive the Γ function for a classical DC biased bolometer and an AC biased bolometer with a load capacitance in series with the detector.

In Eq 3.5 the thermal capacity C is equal to:

$$C = \gamma T + A(\frac{T}{\delta})^3 \tag{3.6}$$

where δ is the Debye temperature (phonon contribution), γ is the Sommerfeld constant of the considered material (electronic contribution) and A is a scaling constant.

Eq3.5 represent a first-order thermal model of a bolometer. Its dynamical response is that of a first-order low-pass filter with a time constant equal to C/G_e. Its transfer function will be:

$$TF_{bolo}(f) = \frac{1}{1 + 2j\pi f\tau} \tag{3.7}$$

and a cut-off frequency equal to $f_c = 1/(2\pi\tau)$.

For a range of frequencies between 1mHz and 1Hz we expect a flat response. An accurate knowledge of this range of frequency is very important for in-flight calibrations on the CMB dipole (see chapter 5).

Unfortunately, as showed by PFM ground calibrations, a first order thermal model is not sufficient to reach the level of accuracy fixed for scientific goals. Measurements showed an evidence of a low frequency excess response (see section 4.6.2). More complex models (empirical and physical) are being developed in order to fit properly experimental data taken during PFM Calibrations and CSL tests. (see section 4.6.3).

3.2.2 Electrical model of readout circuit

To make a bolometer work it is necessary to connect it to a readout circuit. An important characteristic of a bolometer plus Readout Electronics is the relation between a variation of the incident optical power and the voltage measured at the ends of the bolometer that is to say the Responsivity of the detector ($\Re$). The derivative versus the absorbed optical power of the voltage is the Electrical Responsivity $\Re = \frac{dV}{dW_{opt}}$. The optical responsivity is defined as:

$$\Re_{opt} = \eta \Re_{el} \tag{3.8}$$

where η is the absorption efficiency of the radiation of the bolometer.

We shall derive in the next subsections formulae giving the Responsivity in the cases of a classical DC (Direct Current) model and of a AC (Alternating Current) model.

3.2.3 Responsivity of a DC Biased Bolometer

A typical DC bias circuit is schematized in Fig 3.3. It consists of a voltage generator producing a constant voltage V_0 and a bias current I_b in a load resistor of impedance R_L in series with the bolometer.

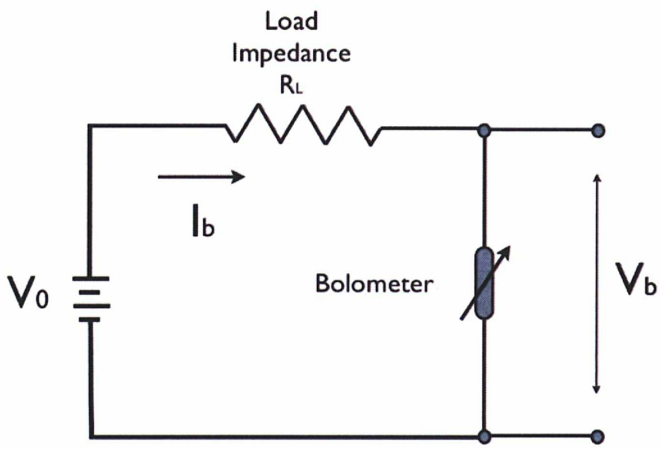

Figure 3.3: *DC bias circuit*

In static conditions we have:

$$V_b = V_0 \frac{R_b}{R_b + R_L} \tag{3.9}$$

We can express the Responsivity as:

$$\Re = \frac{dV_b}{dW_{opt}} = \frac{dV_b}{dR_b}\frac{dR_b}{dT_b}\frac{dT_b}{dW_{opt}} \tag{3.10}$$

From Eq3.9, we obtain:

$$\frac{dV_b}{dR_b} = I_b \frac{R_L}{R_L + R_b} = I_b \cdot \varphi_{DC} \tag{3.11}$$

We can also define α by:

$$\frac{dR_b}{dT_b} = \alpha \cdot R_b \tag{3.12}$$

Where α is the temperature coefficient of resistance of the bolometer. Using Eq3.4 together with Eq3.11 and Eq3.12, we can calculate the differential element $\frac{dT_b}{dW_{opt}}$:

$$\frac{dT_b}{dW_{opt}} = \tilde{G} - \Gamma_{DC}(R_b, Z_L, Z_C, I_b) \tag{3.13}$$

Where:

$$\Gamma(R_b, Z_L, Z_C, I_b) = \alpha R_b I_b^2 (2\varphi_{DC} - 1) \tag{3.14}$$

and:

$$\tilde{G} = G_s + \frac{dG_s}{dT}(T - T_0) \tag{3.15}$$

So the Responsivity of a classical DC biased bolometer becomes:

$$\Re = \frac{\alpha \varphi_{DC} R_b I_b}{G_e^{DC}} \tag{3.16}$$

Which is nothing else than the Zwerdling's formula of the responsivity ([53])

Where in this case the dynamic thermal conductance is equal to:

$$G_e^{DC} = \tilde{G} - \alpha R_b I_B^2 (2\varphi_{DC} - 1) \tag{3.17}$$

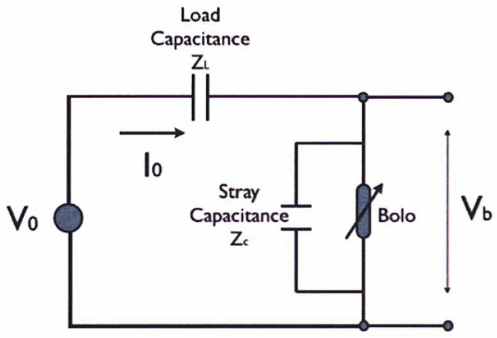

Figure 3.4: *AC bias circuit*

3.2.4 Responsivity of an AC Biased Bolometer

We consider a AC bias circuit as presented in Fig3.4. The voltage at the ends of bolometer is:

$$V_b = V_0 \cdot \frac{R_b Z_s}{Z_L Z_s + R_b(Z_L + Z_s)} \tag{3.18}$$

Let us assume that AC bias frequency F_{mod} is much higher than the bolometer cut-off frequency ($F_{mod} >> \frac{G_e}{2\pi C}$). Then we can consider only the average electrical power and a steady state response and neglect short term variation. We can derive a modified Zwerdling's formula for the responsivity by following the method used in the previous section for a DC biased bolometer:

$$\Re = \frac{\alpha \varphi_{AC} R_b I_b}{G_e^{AC}} \tag{3.19}$$

where AC the dynamic thermal conductance is equal to:

$$G_e^{AC} = G_s + \frac{dG_s}{dT}(T - T_0) - \alpha R_b I_B^2 (2\varphi_{AC} - 1) \tag{3.20}$$

Here the φ_{AC} factor is:

$$\varphi_{AC} = \frac{Z_L Z_s}{Z_L Z_s + R_b(Z_L + Z_s)} \tag{3.21}$$

If we consider the module of the φ factor we can plot (Fig3.5) a responsivity versus bias current for a DC and AC sine biased bolometers. For an

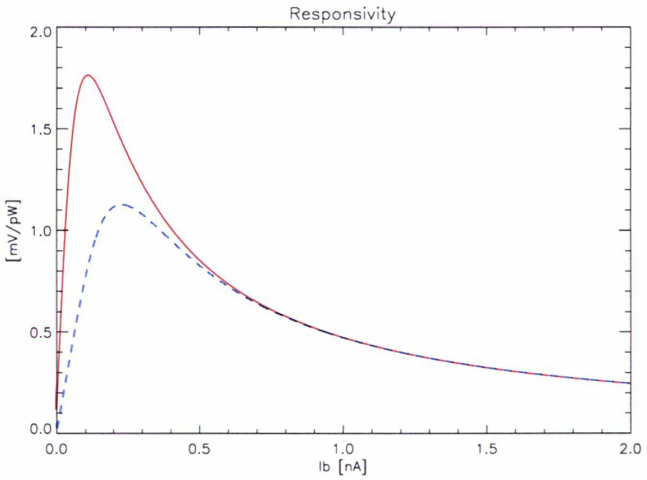

Figure 3.5: *Responsivity versus bias current for DC (blue curve) and AC sine (red courve) bias currents. For AC model we consider a sine polarisation with a stray capacitance of* $C_p = 150pF$ *and plot the responsivity versus the r.m.s. value of the bias current . The bias corresponding to the maximum of the Responsivity are different and equal to* $I_{best}^{DC} = 0.12nA$ *and* $I_{best}^{AC} = 0.22nA$

AC model the max of Responsivity is lower and is obtained for higher bias current in the bolometer. This is the effect of the stray capacitance on performances of an AC biased bolometer: this capacitance is put in parallel with the bolometer and a ΔR_b has an effect on the total impedance (resulting from the parallel) less than ΔR_b ($\Delta Z_T/Z_T < \Delta R_b/R_b$)

3.2.5 Noise of the Bolometer

All the detectors add a noise superposed to the signal. In addition the incoming radiation has a fluctuation due to the fact that the photons following the Bose-Einstein statistic.
The parameter describing the noise is the Noise Equivalent Power (NEP). It is defined as the power producing a signal equal to the noise in a post-detection bandwidth of 1Hz.

$$NEP(f) = \frac{< \Delta S^2(f) >^{0.5}}{\Re(f)} \tag{3.22}$$

where ΔS^2 is the power spectral density of the signal fluctuation and $\Re$ is the responsivity of the detector. NEP is measured in $[Watt/\sqrt{Hz}]$.

In this model we take into account all the principal sources of noise in bolometric detection:

Johnson noise: Johnson noise is the electronic noise generated by the thermal agitation of electrons inside a bolometer at equilibrium. It has a white noise spectrum. The NEP for DC biased bolometers is [37]:

$$NEP_{Johnson} = \sqrt{4k_B T_b R_b I_b^2} \frac{|Z_b + R_b|}{|Z_b - R_b|} \tag{3.23}$$

Where R_b is the bolometer resistance and Z_b is its dynamic impedance.
Let us notice with Mather [37] that Johnson noise does not depend on load impedance. Let us assume here that it does not depend on stray capacitance in the case of AC biased bolometers. Hereafter, we shall use Eq 3.23 indifferently with a DC model or an AC Model.

Phonon noise: The parameters of the bolometer are strongly dependent on the temperature, so small variations in temperature inside the bolometer produce a voltage variation at the ends of the detector with a white noise spectrum.

It results [37]:

$$NEP_{Phonons} = \sqrt{4k_B G T^2} \tag{3.24}$$

This result is independent from the REU.

Photon noise: The Photon noise comes from the fluctuations of the incident radiation due to the Bose-Einstein distribution of the photon emission. The NEP is [54]:

$$NEP_{Photons} = 2\int_{\Delta nu} h\nu Q_\nu d\nu + (1+P^2)\int_{\Delta\nu} \Delta(\nu) Q_\nu^2 d\nu \tag{3.25}$$

Where Q_ν is the absorbed optical power per unit of frequence, $\Delta(\nu)$ is the coherence spacial factor (equal to number of the modes^{-1} = 1 if diffraction limited) and P is the polarisation degree (0 non-polarised 1 polarised).

Preamplifier noise: it results from the impossibility to amplify a signal without adding noise, which results itself directly from the Heisemberg indetermination principle. It depends also on the available components and on the design of the amplifier. We assume that the power spectrum of signal fluctuation is constant for all the bolometers and equal to:

$$\sqrt{<\Delta S^2>_{pre}} = 6.5 \cdot 10^{-9} [V/\sqrt{Hz}] = \sigma_{PA}$$

So the NEP_{pre} results from Eq3.22 as:

$$NEP_{pre} = \frac{\sigma_{PA}}{\Re} \tag{3.26}$$

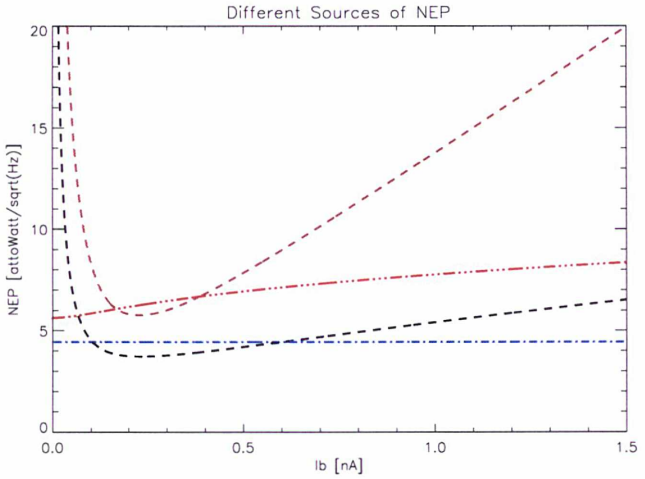

Figure 3.6: *NEP of the 4 considered sources of noise for a PSB100GHz bolometer with a sine AC electronic modulation: NEP Johnson (dashed black curve), Pre-amplificator NEP (dashed brown curve), Photon NEP (blue dash-dot curve) and Phonon NEP (red dash-dot-dot curve)*

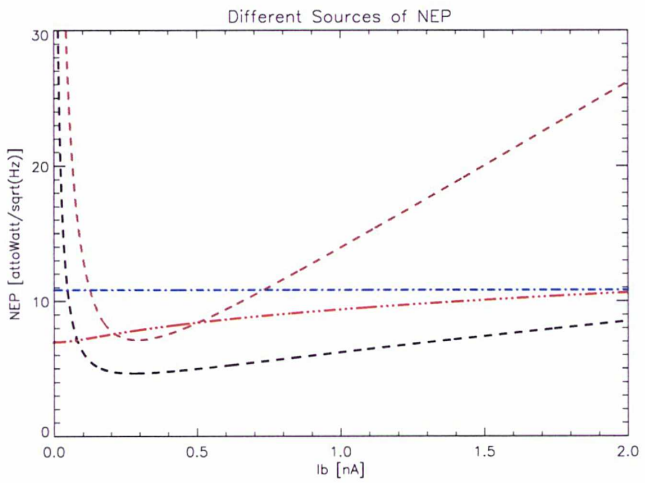

Figure 3.7: *NEP of the 4 considered sources of noise for a PSB353GHz bolometer with a sine AC electronic modulation: NEP Johnson (dashed black curve), Pre-amplificator NEP (dashed brown curve), Photon NEP (blue dash-dot curve) and Phonon NEP (red dash-dot-dot curve)*

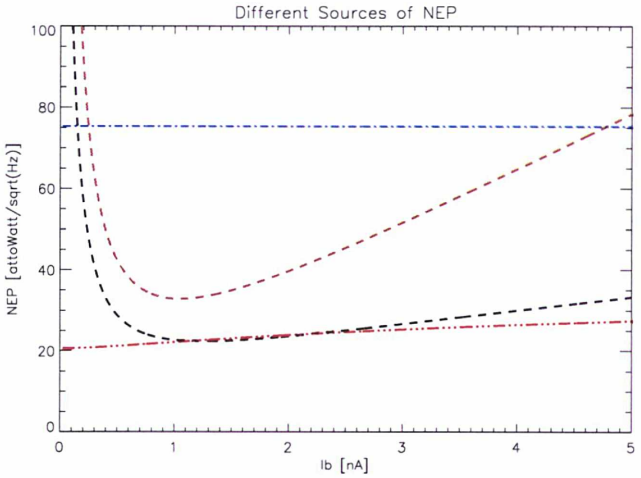

Figure 3.8: *NEP of the 4 considered sources of noise for a 857GHz bolometer with a sine AC electronic modulation: NEP Johnson (dashed black curve), Pre-amplificator NEP (dashed brown curve), Photon NEP (blue dash-dot curve) and Phonon NEP (red dash-dot-dot curve)*

3.2.6 AC Biased Static Model

In this section we shall establish the performances of two type of AC bias readouts that is sine AC model and a square AC model, used in HFI. I will derive the responsivity, the NEP and how the NEP depends on the parameters of the REU (bias current, stray capacitance, modulation frequency and plate temperature) for three typical HFI bolometer (100GHz, 353GHz and 857GHz). In the last subsection the performances of the two model are compared in order to establish the most useful in terms of NEP.

3.2.7 Computing the Response with a Sine Bias

Let us consider the bias circuit of Fig3.4 with a stray capacitance in parallel to the bolometer and a load capacitance in series. The value of the load capacitance is fixed to $C_b = 4.88 \cdot 10^{-12}$ which is the typical value in HFI.
Let's consider a range of temperatures starting from the temperature of the plate (100mK for example) up to an arbitrary value. For each temperature we can calculate the Impedance R_b of the bolometer and its total power using the Eq3.3 and 3.4. In this simulation we assume that the parameters of the bolometers (R_*, T_g, β, etc.....) are the ones of HFI measured by JPL.
If the optical background is constant in this run of simulations the dissipated

electrical power in the bolometer is:

$$W_{elec} = W_{tot} - W_{opt} \tag{3.27}$$

So the r.m.s. Voltage at the ends of the bolometer results:

$$V_b = \sqrt{R_b W_{elec}} \tag{3.28}$$

And the r.m.s. bias current passing through the bolometer is:

$$I_b = \frac{V_b}{R_b} \tag{3.29}$$

In general for a quadrupole we have:

$$F(V_b) = TF(\omega, R_b, C_p) \cdot F(V_0) \tag{3.30}$$

where F indicate the Fourier transform and $TF(\omega, R_b, C_p)$ is the transfer function of the quadrupole. The module of the transfer function is:

$$|TF(\omega, R_b, C_p)| = \frac{R_b \omega C_b}{\sqrt{1 + \omega^2 R_b^2 (C_b + C_p)^2}} \tag{3.31}$$

So the r.m.s. input voltage is:

$$V_0 = \frac{V_b}{|TF(\omega, R_b, C_p)|} \tag{3.32}$$

In order to calculate the optical Responsivity let us consider a small step in temperature for each in temperature of the bolometer. If we keep V_0 unchanged, the step in temperature is due to a change of the optical backgroung that can be computed:

$$W_{opt1} = W_{tot1} - W_{elec1} \tag{3.33}$$

where W_{tot1} is calulated from the new temperatue T_b1 and W_{elec1} is derived from:

$$W_{elec1} = \frac{V_{b1}^2}{R_{b1}} \tag{3.34}$$

and where V_{b1} is equal to:

$$V_{b1} = V_0 \cdot |TF1(\omega, R_{b1}, C_p)| \tag{3.35}$$

assuming V_0 not varying, and $TF1$ calculated from R_{b1}

The Responsivity will be:

$$\Re = |\frac{V_{b1} - V_b}{W_{opt1} - W_{opt}}| \tag{3.36}$$

Thanks to Responsivity and NEP equations of the previous section it is possible to calculate the total NEP for the three sample bolometers (Fig3.9), with a typical (HFI-like) $Wopt$ depending on the bolometer (100GHz=0.3pW, 353GHz=0.5pW, 857GHz=10pW). The values of the REU parameters used are the nominal ones ($Cp = 150pF$, $Fmod = 90Hz$) and the temperature of the plate is $100mK$

It is interesting to study the variations of the best achievable performances with the REU parameters and the temperature of the plate. In Fig3.10, Fig3.11 and Fig3.12 the per cent variation of NEP versus the plate temperature, the stray capacitance and the modulation frequency is plotted. In all cases these parameters on the NEP have a stronger effect in the 100GHz bolometer. This comes from a different ratio of photon NEP to Pre-ampli

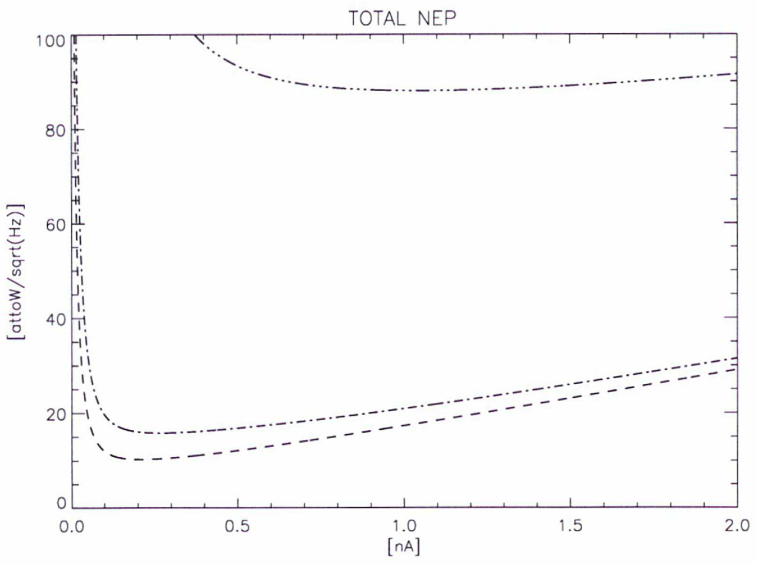

Figure 3.9: *Total NEP for three different HFI bolometer at 100GHz (dashed line), 353GHz (dash-dot line) and 857GHz (dash-dot-dot line) for an AC sine modulation*

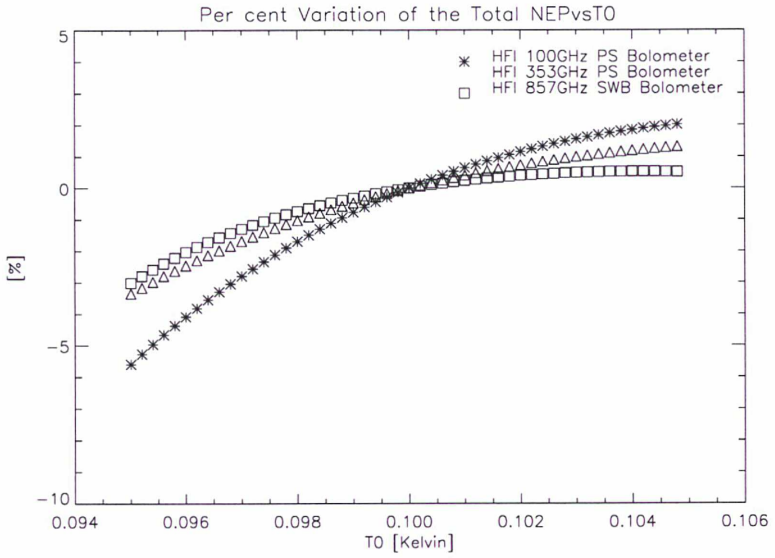

Figure 3.10: *Relative variation of the total NEP versus the bolometer plate temperature from 95mK to 105 mK for three typical bolometer of HFI with a AC sine bias*

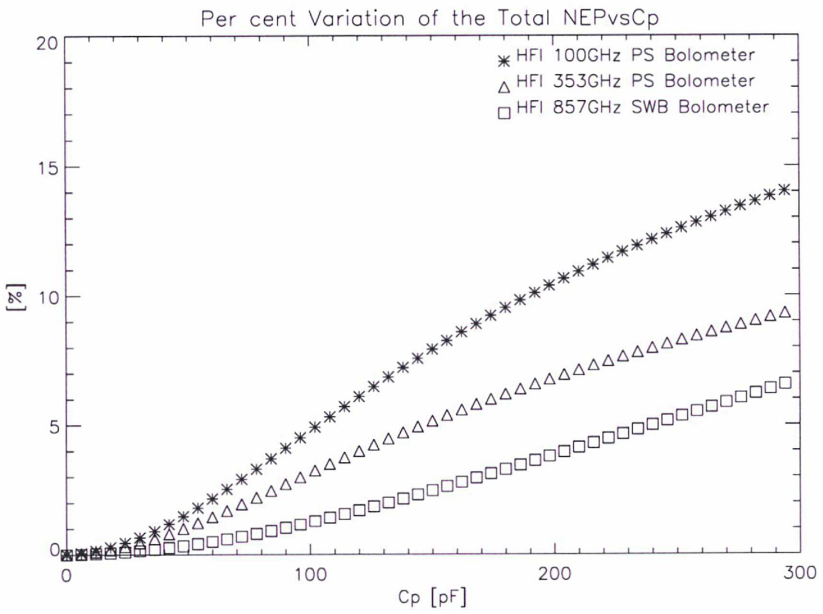

Figure 3.11: *Relative variation of the total NEP versus stray capacitance from 0 to 300pF for three typical bolometer of HFI with an AC sine bias*

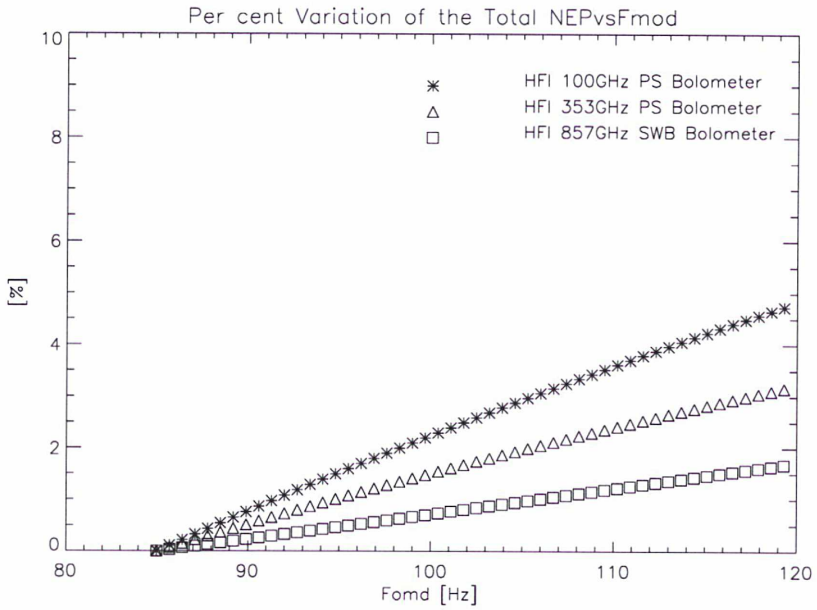

Figure 3.12: *Relative variation of the total NEP versus modulation frequency of the AC sine from 85Hz to 120Hz for three typical bolometer of HFI.*

NEP: the photon NEP increases more rapidly than Pre-ampli NEP from 100GHz to 857GHz (see Fig3.6, Fig3.7, Fig3.8).

3.2.8 Computing the Response with a Square Bias

With the same bias circuit (Fig3.4) it is possible to derive the performaces of a REU in which a square wave voltage applied to the bolometer as in HFI. Let us assume that if the REU is *balanced*, a perfect square wave bias is passing through the bolometer even in presence of a stray capacitance. In HFI this is achieved by using a triangular wave plus a square wave (see section 2.3 in chapter 2).

A square wave can be decomposed as:

$$V_b(\omega) = acos(\omega t) + \frac{a}{3}cos(3\omega t) + \frac{a}{5}cos(5\omega t) + ... =$$

$$= \sum_{n=0}^{\bar{n}} \frac{a}{2n+1}cos((2n+1)\omega t)$$

The r.m.s. V_b is equal to:

$$V_b = \sqrt{\sum_{n=0}^{\bar{n}} (\frac{a}{\sqrt{2}(2n+1)})^2} \tag{3.37}$$

If the temperature of the bolometer is given and the optical power is constant we can calculate the r.m.s. V_b as we did for the sine bias case (Eq3.28 and Eq3.27). So we have:

$$a = \sqrt{W_{elec}R_b} \cdot \sum_{n=0}^{\bar{n}} 2(2n+1)^2 \tag{3.38}$$

The r.m.s. Voltage is equal to:

$$V_b = a \cdot \sum_{n=0}^{\bar{n}} \sqrt{2}(2n+1) \tag{3.39}$$

And the r.m.s. bias current passing through the bolometer is:

$$I_b = \frac{V_b}{R_b} \tag{3.40}$$

Now let's derive the Responsivity. As for the sine AC case, so we can calculate the R_{b1}, W_{tot1}, the $TF1$ starting by a small step in temperature due to an incoming optical signal.

On the contrary we cannot derive the electrical power following the same logic: if we keep the same set up of the REU, after a little step in temperature

the bias passing through the bolometer is not a square wave anymore so the Eq3.37 is not applicable. We have to correct each term of the sum as follow:

$$W_{elect1} = \frac{a^2}{R_{b1}} \sum_{n=0}^{\bar{n}} 2(2n+1)^2 \cdot \Upsilon((2n+1)\omega, R_b, R_{b1}, C_p) \tag{3.41}$$

where

$$\Upsilon((2n+1)\omega, R_b, R_{b1}, C_p) = \frac{TF((2n+1)\cdot\omega, R_b, C_p)}{TF1((2n+1)\cdot\omega, R_{b1}, C_p)} \tag{3.42}$$

In Fig3.13, 3.14, 3.15, 3.16 the total NEP and the study of changing performances versus REU parameters and plate temperature are presented.

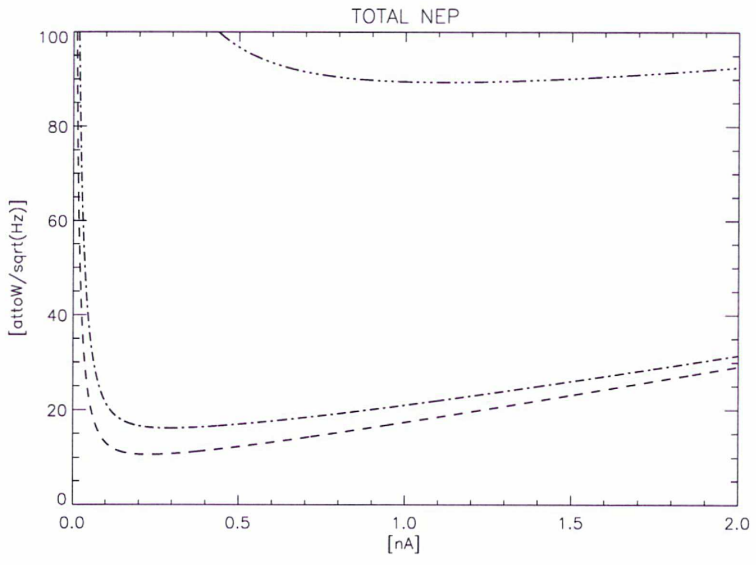

Figure 3.13: *Total NEP for three different HFI bolometers at 100GHz (dashed line), 353GHz (dash-dot line) and 857GHz (dash-dot-dot line) for an AC square modulation*

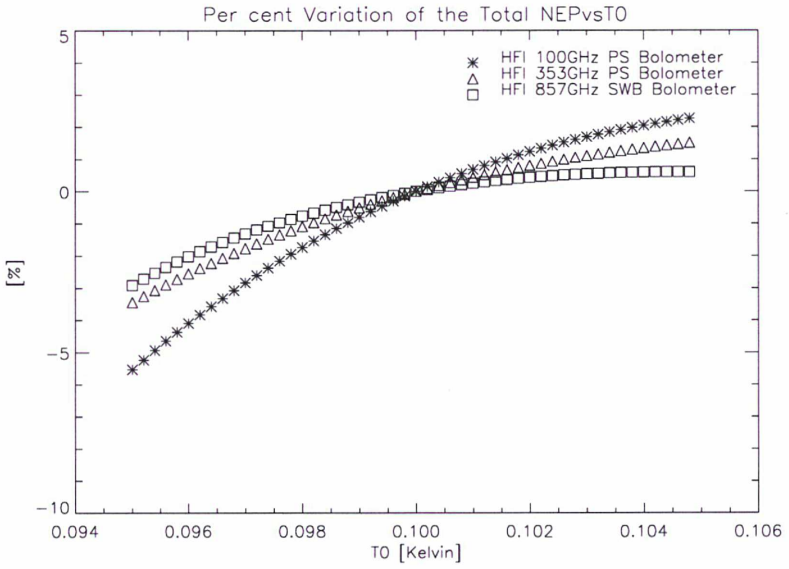

Figure 3.14: *Relative variation of the total NEP versus bolometer plate temperature from 95mK to 105 mK for three typical bolometers of HFI with an AC square bias*

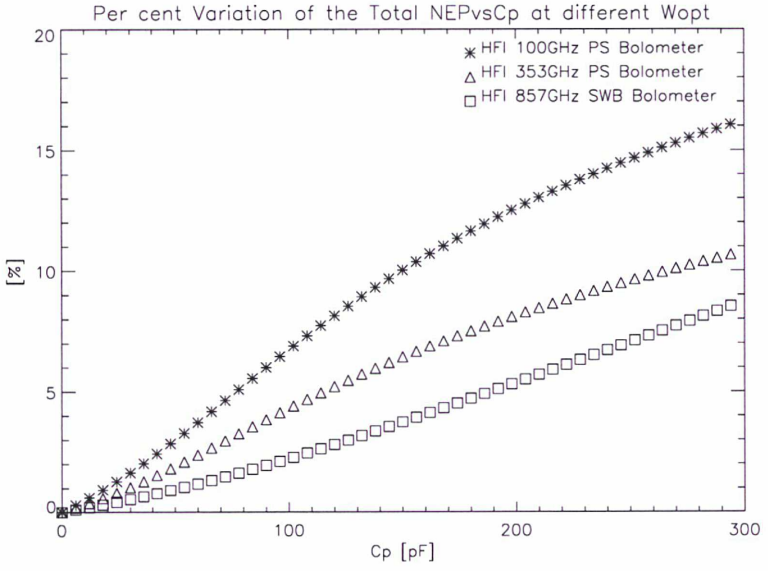

Figure 3.15: *Relative variation of the total NEP versus stray capacitance from 0 to 300pF for three typical bolometers of HFI with an AC square bias*

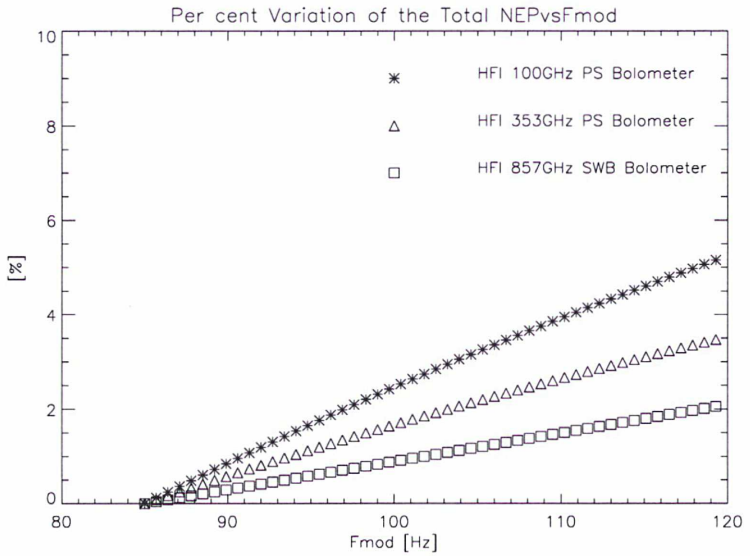

Figure 3.16: *Relative variation of the total NEP versus modulation frequency of the AC square mode from 85Hz to 120Hz for three typical bolometers of HFI.*

3.2.9 Impact on HFI

The consequences of these results on HFI are:

• The bias current corresponding to the minimum of NEP (best bias) with the square AC modulation is of the order of two times larger than the one calculated in a DC model; so the optimisation of this parameter has to be done taking into account the AC square model.

• A stray capacitance as measured in HFI ($\sim 150pF$) gives a loss of NEP in the worst case (100GHz bolometer) of 10%. In the best case the loss of NEP is equal to 4% (857GHz bolometer).

• If we consider as nominal a modulation frequency of 90Hz, the losses of NEP are between 0.8 and 2% from 100GHz to 857GHz bolometers with respect to the minimum frequency of 86Hz.

• The scheduled mission is expected to last 30 months. Let the scientific goals be completely fulfilled if during this period the plate temperature of the bolometers is set at 100mK. With a linear approximation we find that for a 100GHz bolometer, a change of the plate temperature of 1mK gives a

change in NEP of 0.8 %. This means a change of about 6 days in the duration of the mission is needed to reach the same sensitivity than the one we had at 100mK. A longer observational time has the advantage of improving the redundancy of the data. Both criteria (the final S/N and the redundancy) seem to favour the F_{min^2} option (defined as the Helium lowest flow option of the dilution).

3.2.10 Comparison between the two modulation techniques

In Fig3.17 and Fig3.18 The total NEP and the responsivity of the sample bolometers with a sine AC model and a square AC model are over plotted for the three sample bolometers. All the curves are plotted considering an HFI-like set of parameters (Fmod=90Hz, Cp=150pF, T0=100mK).

In all the cases the performances of a sine AC model are better than the square model. This is more obvious in the Responsivity (better by about 10%) than in the total NEP(better by about 4%). So we can conclude that at NEP level a bolometer connected to a sine AC biased REU would be more sensitive for a static signal.

Let us remark that the advantage in NEP is modest. Let us also notice that an AC sine bias would induce important variations of the temperature of the fastest Planck bolometers, bringing them in a non-linear regime. Therefore the simple model would not be accurate for an AC sine Planck case.

On the other hand, the square bias deposits a nearly constant power in the bolometers, that deviate from their mean temperature only by small amounts. This make the simple model an adequate modelling tool to predict the static response of HFI.

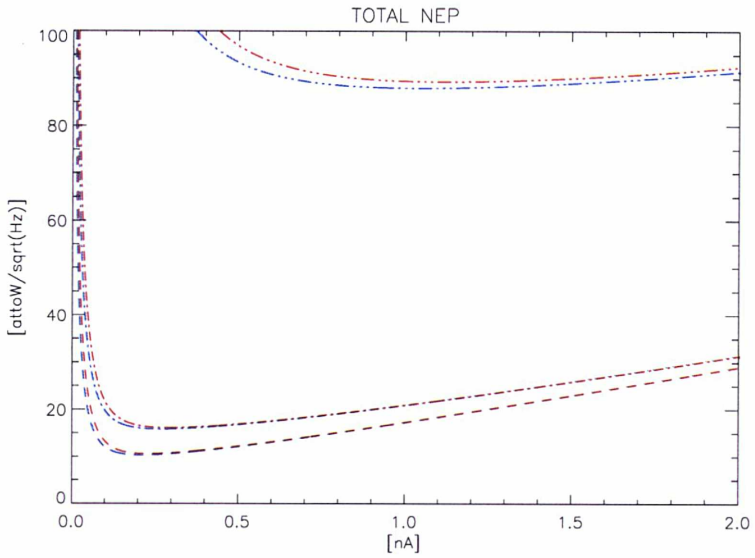

Figure 3.17: *Responsivity of the three sample bolometers in case of an AC sine model (blue curves) and a square AC model (red curves)*

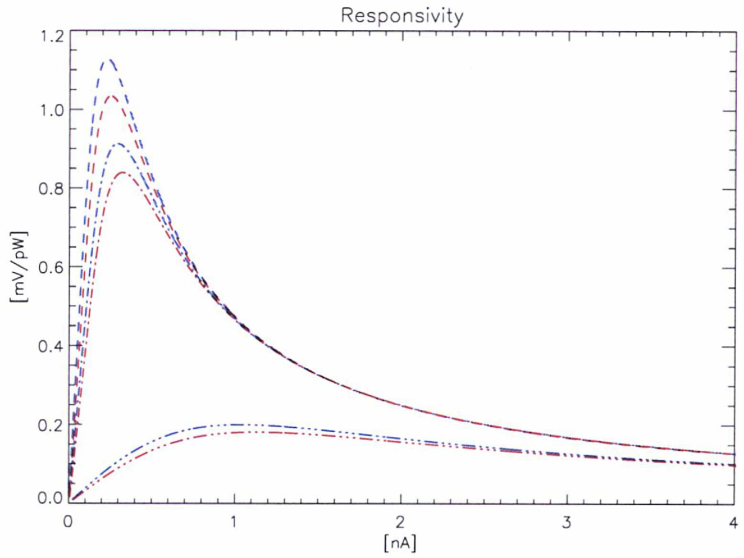

Figure 3.18: *Total NEP of the three sample bolometers in case of an AC sine model (blue curves) and a square AC model (red curves)*

3.2.11 Modelling the dynamic response: the SEB Model

The SEB (Simulation Electronique et Bolomètre) is a brute force model developed under IDL.

The SEB model is based on thermal equation of bolometer (Eq3.5) and the electronic equation of the REU (Eq3.18) with an input voltage calculated by solving the electronic chain on the generation of the signal box. The equations implemented in the model in a differential form are:

$$\frac{dV_b}{dt} = \frac{C_L}{C_L + 2C_p}\frac{dV_0}{dt} - \frac{2}{R_b(C_L + 2C_p)}V_b \tag{3.43}$$

$$\frac{dT_b}{dt} = \frac{1}{C_0 T_b^{\gamma}}\left(\frac{V_b^2}{R_b} - \frac{G_{so}T_{ref}}{\beta+1}\left(\left(\frac{T_b}{T_{ref}}\right)^{\beta+1} - \left(\frac{T_0}{T_{ref}}\right)^{\beta+1}\right) + W_{opt}\right) \tag{3.44}$$

where γ is an empirical parameter which determine the trend of the thermal capacity with the temperature. T_0 is the effective plate temperature, and T_{ref} is equal to 100mKelvin ([55]).

The SEB model engine integrates these two equations versus time by a 4th order Runge-Kuta method. After the model of the response of the bolometers, SEB model provides a simulation of the whole electronic chain to produce as output a signal in scientific units (ADU). This is done using calibration measurements performed at CESR.
The parameters that can be varied in the current SEB model are:

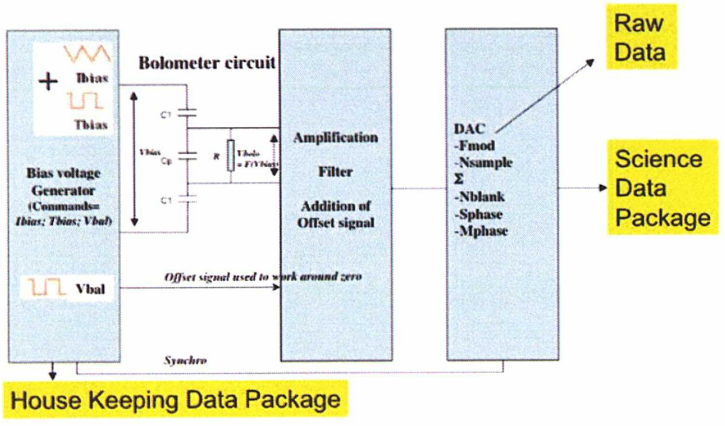

Figure 3.19: *Principle of the readout electronics. It consists of a signal generator and a measurement section delivering digital data.*

- I_{bias}: bias current command in digit

- T_{bias}: bias transient command in digit

- V_{bal}: bias square compensation command in digit

- F_{div}: parameter defining frequency modulation of the electronic ($F_{mod} = \frac{F_{base}}{22N_{sample}(128+F_{div})2}$ where $F_{base} = 4 \cdot 10^7 Hz$)

- G_{PAU} REU modifiable gain

- N_{blank}: Number of blanked point at the beginning of each half period

- S_{phase}: Number of points defining the phase shift to compute DSN

- M_{phase} optional phase shift (of $\frac{\pi}{2}$)

- C_p: stray capacitance

- T_0: the bolometer plate temperature

The main validations of the SEB model until now have been done on static optical signals. On the raw signals taken during sequences of PFM calibrations. In Figure 1 the comparison of the measured raw signals with SEB predictions for Belt 0 Channel 3 is presented. The relative fit quality is of the order of 2 % when the bolometer is implied in the test (I_{bias} and T_{trans}) and of the order of a few tenths of percent when only the warm electronics is tested (V_{bal}).

Another static validation was perfomed in terms of prediction of the best bias current to be used during PFM calibration with a good agreement with measurements. Details are presented on Chapter 4.
One of the objectives in developping the SEB model was to predict the non linear part of the scientific signal response (in ADUs) to the variations of the optical flux (in pW). Another was to model transfer function of the instrument. These kinds of measurement are very difficult to perform in flight so validated models are needed.

My contributions to the SEB have been in particular to make is usable for predicting the time response. Currently the SEB model predictions are not yet accurate enough to be used to describe the instrument performances for

data reduction. Work to improve the model and the accuracy of its input is going on.

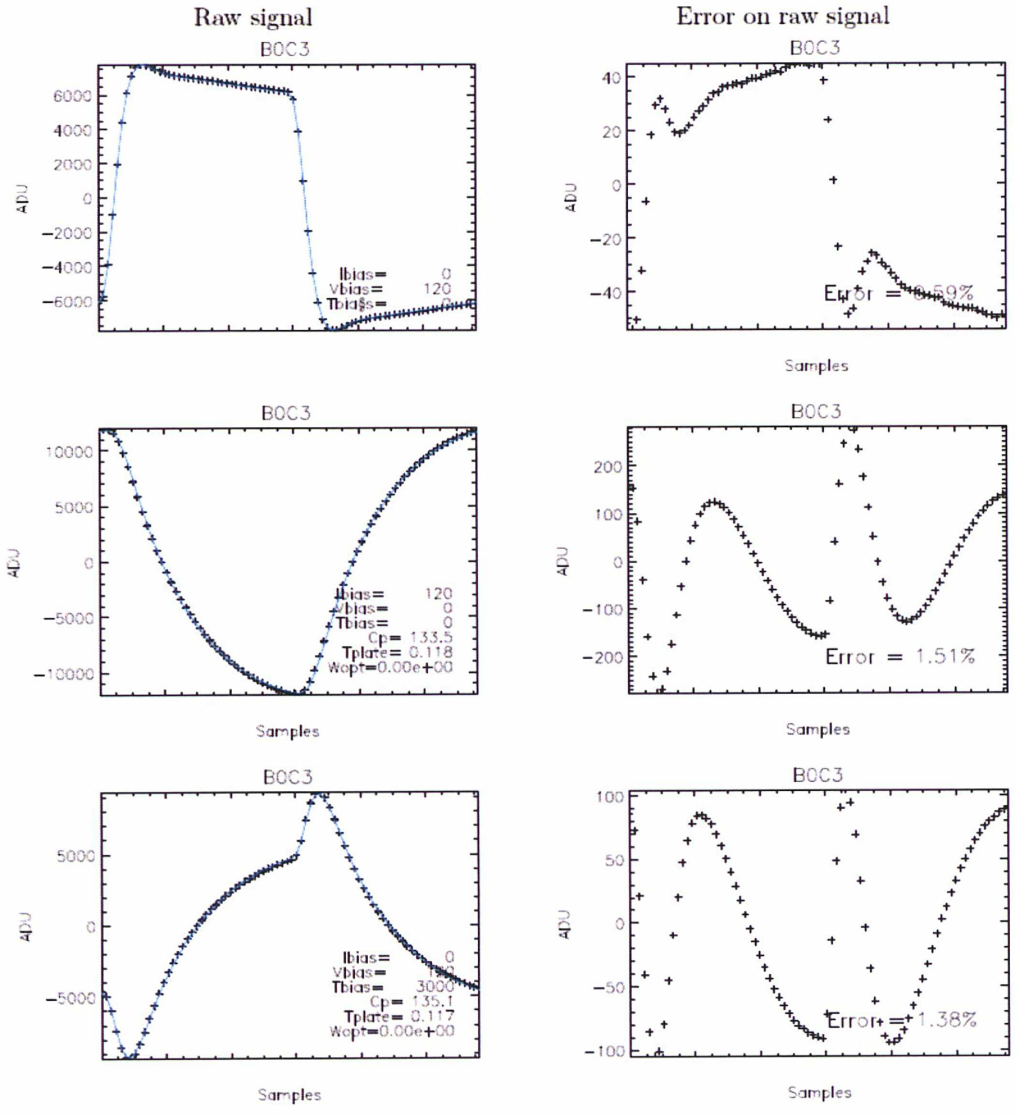

Figure 3.20: *Comparison of the measured raw signals with SEB predictions for Belt 0 Channel 3 [56].*

Chapter 4

Ground Calibration of the HFI Instrument

Introduction

The HFI Ground calibration is a combination of measurements obtained during both the manufacturing of the single components and the test of the instrument as a whole. On the ground all parameters which cannot be measured in-flight will be determined with the appropriate level of accuracy to their final values. All parameters which can be measured in-flight with the needed level of accuracy will be determined only to preliminary values, with a level of accuracy compatible with the verification of the instrument performances. The ground calibration is constituted of measurements related to components and sub-systems, and of a global calibration of the Focal Plane Unit (FPU). The global FPU calibration has taken place at IAS in the Saturne cryostat (4.2).

The Proto Flight Model (PFM) was calibrated in June and July 2006. In this chapter I will detail the calibration sequences to which I personally contributed. PFM calibration represents the last scientific ground calibrations with the instrument as a whole after CQM (Calibration of Qualification Model) and PFM-Characterization. In the next section I will list all the test the instrument needs to be ground-calibrated. On section 4.2 I will detail the experimental setup used in Orsay during PFM calibration. Starting to section 4.3 I will show the measurements and results of all the sequences in which I have been involved. In particular Optimisation of some REU parameters (I_{bias}, S_{phase}, F_2), Measure of the Emissivity of the CS1 source, Measure of the thermal emission of 4K and 1.6K cryogenic stages, measure of

the total optical transmission of the HFI instrument, measure of the static response function (check for non-linearities) and the dynamical response (time response).

4.1 HFI PFM Ground Calibration

Calibration of HFI as a whole could be separated in 4 principal parts after a first phase of optimisation of the tuning parameters . Here the list of all the principal tasks of PFM calibration with the laboratories in charge of each one.

- **Optimisation of the thermal and REU parameters** (CESR - LERMA)
- **Optical Response :**
  - Characterisation of the horn pattern (CARDIFF)
  - Spectral response (CARDIFF - IAS)
  - Optical Polarisation (LAL)
  - Total Optical Transmission (LERMA)
  - Background characterisation (LERMA)
- **Static Response**
  - Detector characterisation (V-I curves) (GRENOBLE)
  - Absolute Response (Static function) (LERMA)
  - Linearity characterisation (LERMA)
  - Responsivity (GRENOBLE)
- **Dynamic Response :**
  - Characterisation of the transfer function in the frequency range of interest (LERMA - LAL - CALTECH - JPL)
- **Detection Noise :**
  - Characterisation of the total power spectral density of HFI (GRENOBLE)
  - Characterisation of the Cross-talk (electrical and optical) (CESR)
  - Response to particles (CESR - LAL - GRENOBLE)

4.2 Calibration Facility

The Saturne cryostat (Fig 4.1 on the left) consists in a vacuum chamber (1600 mm high, 1604 mm diameter). The vacuum chamber is attached to

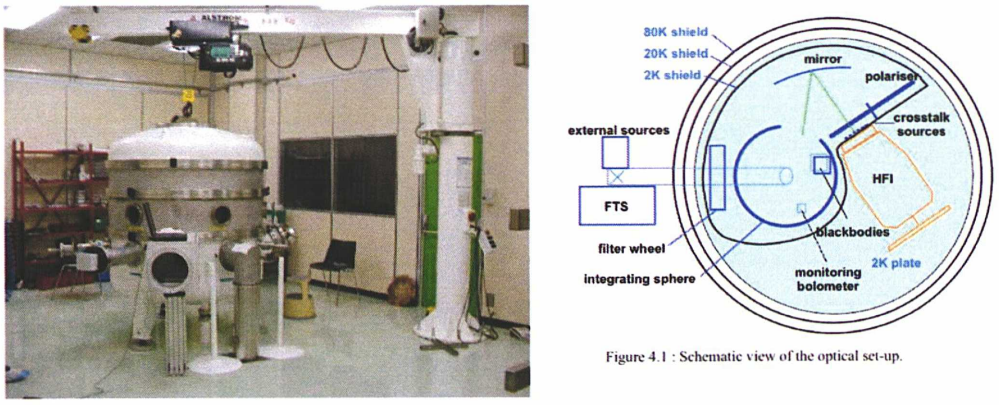

Figure 4.1 : Schematic view of the optical set-up.

Figure 4.1: *On the left: view of the Saturne cryostat in the IAS clean room. On the right: schematic view of the optical setup*

the ground by three legs. All the utilities and all the leak proof interfaces are on the bottom of the vacuum chamber. The specified autonomy for the HFI calibration is 24 h whithout transfer from the 4K storage to the 2K plate. The regulated temperatures are the 2 K plate (LHe bath at low pressure - MKS regulator), the 4 K HFI interface (LHe bath + heater) and the 20 K HFI interface (Helium Gas + heater). In addition, an auxiliary of gas He circuit will be provided for the pre-cooling of HFI.

The optical system on the 2 K plate was designed using optical simulation (figure 4.1 on the right) taking into account the constraints of the cryostat. It consists on a 2K plate which the HFI FPU and several optical components are mounted.

Integrating sphere

An Integrating sphere is an optical component consisting of a cavity with its interior with a high diffuse reflectivity. The shape of the cavity is spherical. Its relevant property is a uniform scattering or diffusing of light. Light rays incident on any point on the inner surface are, by multiple scattering reflections, distributed equally to all other such points and effects of the original direction of such light are minimized. An integrating sphere may be thought of as a diffuser which preserves the total power but destroys spatial information. In the calibration facility the integrating sphere is used to couple optical sources with the HFI instrument. It is thermally coupled to the cold plate. On the top of the sphere two *Mickey ears* appears in order to contain the CS2 source (see below) and the reference bolometer volumes.

Sources

In the calibration facility it is possible to use several optical source:

- *CS1 (Cold Source 1):* it is attached to the integrating sphere in order to simulate the background produced by Planck telescope. It consists of an annular blackbody (with a throughput of $1000 mm^2 sr$) changing from about 50 K and the temperature of the cavity (source turned-off).

- *CS2 (Cold Source 2):* it is a chopped blackbody feeding the integrating sphere. Operation temperature is between 2 K and 20 K.

- *External Sources:* they are coupled to the integrating sphere by the FTS line. It consists of a Fourier Transform Spectrometer and chopped sources. The Fourier Transform Spectrometer used to measure the spectral response of the instrument is obtained from a commercial model (Sciencetech) with a spectral range from 2 to 100 cm^{-1} a resolution as good as 0,015 cm^{-1} (60 cm optical travel) and a minimum scanning speed slower than 0.02 $cmsec^{-1}$. This FTS will be equiped with a wide band beam splitter (polariser type interferometer), and an internal bolometer detection system on a dedicated output port (for tests and system monitoring).

These sources are monitored by an absolute bolometer and a reference bolometer: except for the cavity in thermal equilibrium with all the source inside, the calibration facility does not include any absolute source. Therefore, it must be calibrated itself with an absolute detector : we will use a bolometer with well known beam characteristics and response, called the absolute bolometer. The absolute bolometer will be operated at 300 mK to be able to measure signals in the dynamic range of HFI. The readout electronics is identical to one channel of the HFI readout. In order to control the reproducibility of the sources, a bolometer system will monitor the flux inside the integrating sphere during caracterisation and use of the calibration facility. This is the reference bolometer.

Mirror

The mirror conjugates the sphere output and the FPU focal plane with a magnification of about 1.2. The mirror diameter is 320 mm, spherical with a radius of 180 mm. The mirror is made of aluminium with a smooth surface in order to insure a reflectivity greater than 0.98 in the HFI wavelength

range. The mirror must be strongly coupled to the cold plate to keep it at 2 K.

Polariser

A polarizer is a device that converts an unpolarized beam (coming from integrating sphere) into a beam with a single polarization state. In Calibration facility a 140 mm diameter polariser from MICRONIC company with a grid step of $40\mu m$ has been used. The polariser is placed in a converging beam in front of the horns thanks to a support that can take three positions: one with a rotative polariser in the beam, one with the crosstalk sources in the beam, and one with nothing in the beam.

4.3 Optimization of the REU Parameters

The strategy of ground calibrations as it has been estabilished, is to fix the REU parameters (exept F_{mod} and temperature of bolometer) and to measure the relation volt versus optical power for a set of fixed parameters close to those we will have in flight, so we can deduce the model with a polynominal fit with the experimental data and the responsivity with its derivative. With this approach it is necessary to find a way to fix the REU parameters.

We discuss in this section the optimisation of the bias current, S_{phase} parameter and the calibration of the F_2 parameter.

4.3.1 The Bias Current

The bias current tuning test is a key point in optimisation of the HFI performance. Both the static and dynamic response strongly depend on the bias current. The level of noise is also affected by changing it. We need to optimise this parameter taking into account all these effects and in a range of realistic flight backgrounds.

The starting point is the use of SEB and SOS simulators (see section related) to perform static simulations of the HFI instrument with an appropriate background.

The method used to determine the optimal bias current was [57]:

- Estimation of the range of possible backgrounds and calculation of the signal to noise ratio (SN) for a source of 1mK. This calculation has been made using SEB model and SOS model.

- Determination of an empirical law between time constant and bias current using JPL data.

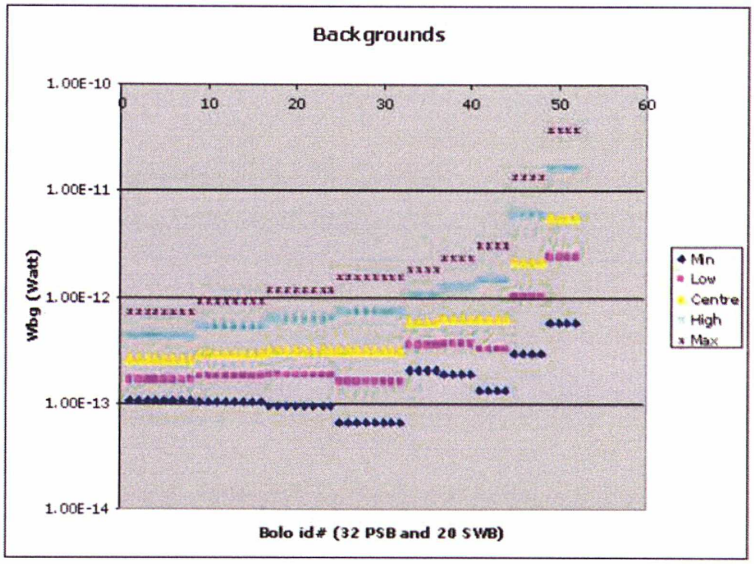

Figure 4.2: *Range of backgrounds: incident power on the HFI bolometers for max, high, central, low and min backgorunds.*

- Extension of the results in the domain of optical modulation frequencies.
- Calculation of the best bias current (using a toy model of noise).
- Extension of the calculation at different temperatures of the bolometers.

Characterization of backgrounds

Let us define 3 cases by playing with all the parameters that determine the background by using the SOS simulator.

	$T_{Telescope}[K]$	Telescope Emis. [%]
LOW Background	40	0.6
CENTRAL Background	45	1
HIGH Background	50	2

Table 4.1: *Variation of telescope parameters to compute three different backgrounds*

After the electrical and optical tests performed at JPL and Cardiff, many parameters have been tested at first order (total optical efficiency, spectral

transmission etc.). The telescope is the most uncertain and variable object in the optical chain, because its emissivity is unknown. It depends mainly on dust deposited during launch. It will also change during flight (micrometeorites and aging of coating). In addition its temperature can change with of the distance to sun and solar activity.

For these reasons let us neglect the uncertainties on backgrounds coming from 4K and 1.6K cryogenic stages, and define three backgrounds (low, central, high) by changing the parameters (temperature and emissivity) of the telecope. In this way it is reasonably sure that all possible backgrounds are covered in flight (Tab 4.1).

Time Constant

The physical model of the bolometers (chapter 3) shows that the bias current affects strongly their time constant. In this case, an empirical solution has been preferred rather than a theoretical model using the knowledge of the bolometers from the JPL and Cardiff tests.

Let us use the experimental points of time constant versus bias current fitting the data with the next empirical law:

$$\tau(I_b) = C_1 + \frac{C_2}{I_b + C_3} \tag{4.1}$$

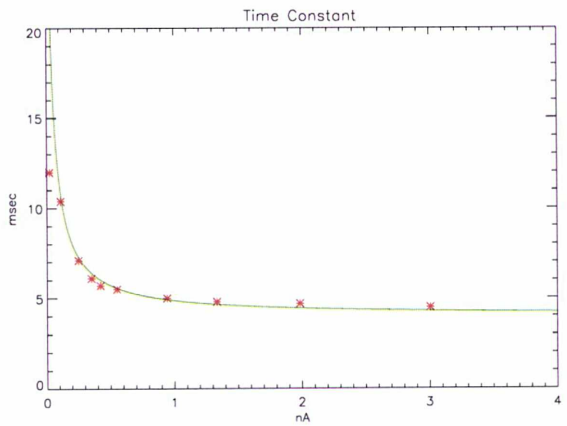

Figure 4.3: *Bolometer PSB100GHz 36J12. Time Constant empirical model (continuous line) and experimental points from JPL versus bias current.*

Optical Modulation Frequency

To measure properly the best bias current we have to respect as well as possible the flight condition during the mission so it is necessary to take into account the optical modulation frequency (angular speed of satellite around his spin axis) in order to understand the range of interest in frequency for each channel of HFI.
We know that the FWHM changes versus HFI channels. So the maximum frequency of interest is given by the relation:

$$f \sim \frac{v_{ang}}{\alpha(FWHM)} \tag{4.2}$$

Channel [GHz]	100	143	217	353	545	857
FWHM [Arcmin]	9.2	7.2	5	5	5	5
Optical freq max [Hz]	40	50	72	72	90	90

The frequency of optical modulation is related to the momentum l of the spherical harmonics:

$$f \geq \frac{l}{60} \tag{4.3}$$

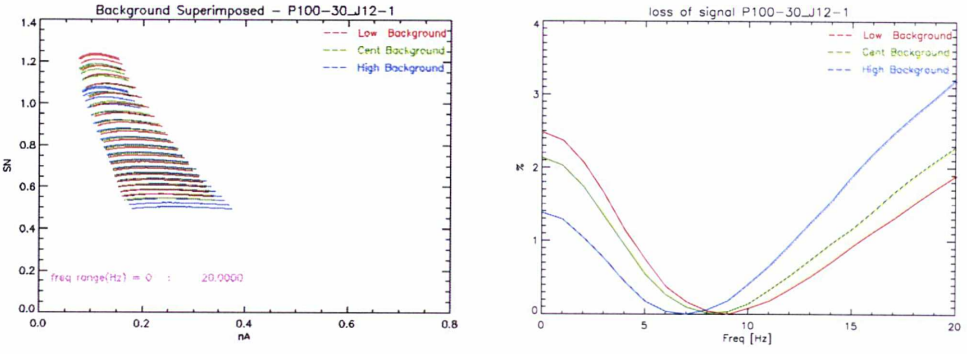

Figure 4.4: *On the left the Signal to noise ratio (for a source of 1mK RJ at a bolometer temperature of 100mK) versus bias current is plotted for the bolometer PSB 100GHz (position in the focal plane 3A): we present the intersection between the three different background and we take account of the dependance of the optical modulation frequencies. The best bias current for this bolometer is 0.22 nA. On the right the percentual loss of energy versus the optical modulation frequency is plotted.*

The optical modulation frequency changes (worse) the signal to noise ratio. If we consider a flat noise (early in the project), we have:

$$SN(I,f) = \frac{SN(I)}{\sqrt{1+(2\pi\tau(I)f)^2}} \tag{4.4}$$

All the optical modulation frequencies are possible up to the limit set by the beam size and the angular speed of the satelite.

The best Bias Current Calculation

In the figure 4.4 the signal to noise ratio for the different backgrounds is presented. To compute the best bias current let us consider the intersection between backgrounds and into this set the bias current is calculated where the sum of the SN for the different backgrounds is maximum. For the $100GHz$ channel we consider a range of 0-20 Hz, which corresponds to the range of effective l accessible with the 9.2 arcmin beam.

Temperature

The nominal value of the temperature during the work conditions will be $100mK$. We have shown the variation of the NEP versus plate temperature on chapter 3 (see Fig.3.14). We have also iterated the process for different temperatures for two reason:

- The cryogenic system may not work perfectly during the mission so we have to be able to predict the response of the instrument at different temperatures.
- A temperature slightly different from $100mK$, even though it reduces the sensitivity on a single measure, could increase a lot the lifetime of the cryogenic system. It can increase the sensitivity of the mission. This will be known better after calibration and finalised once flight background are known.

Measuring Optimal Bias Current

During PFM calibration campaign we performed a test sequence "best bias" looking for a validation of the predicted value. This test had a twofold goal: first it is a way to test the model of the instrument SEB and SOS. Second this test provides the real value to be used during all the tests as nominal best bias current at the temperature of the bolometers. The model if validated will be used to extrapolate best bias for other temperatures [58].

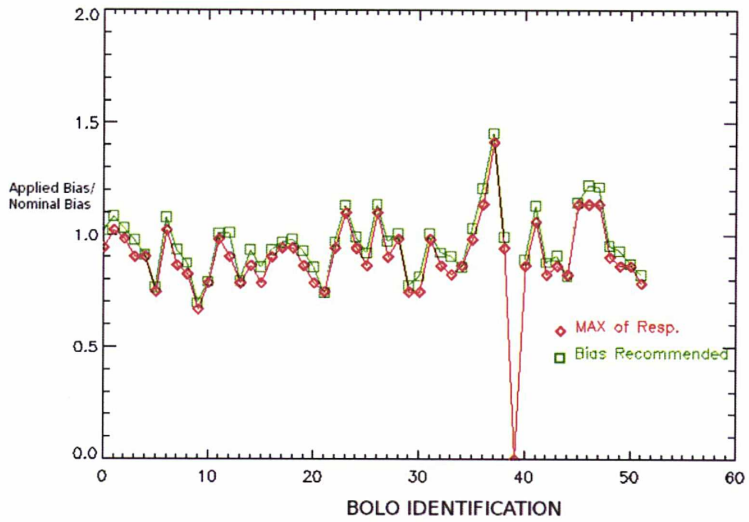

Figure 4.5: *Measured and recommended bias current (normalized by the preliminary setting) for the 52 bolometers of HFI*

The sequence consists of checking the response to the fibre source CSM versus bias current The maximum responsivity has been measured with approximate background conditions (CS1=30K and T platform=2.0K see section 4.4.4).

In Fig 4.5 results of the sequence are presented. Red points represent the bias current values giving to the max of response for the considered bolometer (the value is normalised by the preliminary set derived from simulations). As expected, maximum response happens generally for normalized applied bias slightly less than one because the effect of time constant is not taken into account in the measurements. The green curve is calculated considering the effect of time constant of bolometers taking into account the measurement from JPL with the same procedure than simulations. A few measurements were not successful due to incorrect settings of the Vbal and Tbias. The optimal bias was recommended by analogy with bolometers of the same kind.

Full data reduction of noise and response measurements (cite by FX Desert et al) confirmed that the chosen Ibias values were providing a near to optimal signal to noise with the most probable background expected in flight.

The Recommended best bias currents for a temperature of the platine of 100mK are presented in table 4.2

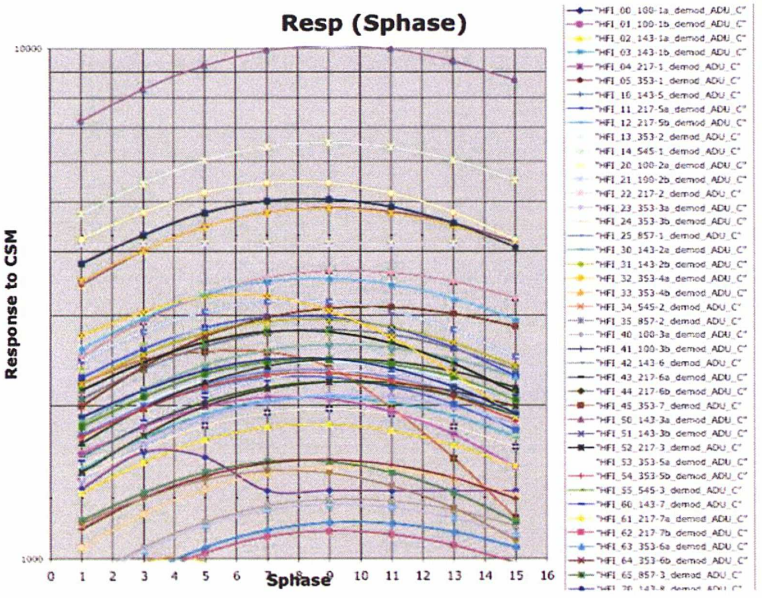

Figure 4.6: *Response to the CSM fibre source versus Sphase. Some channels give neaningless results due to incorrect Tbias and Vbal settings.*

4.3.2 Optimising the S_{phase} Parameter

The S_{phase} parameter has been defined in Cap2. We performed a test in order to optimise S_{phase} to get the maximum response [58].

The response to the carbon fibre CSM source modulated at 2.5Hz has been measured under background conditions that approximate the guessed in-flight conditions (CS1=30K and T platform=2.0K). The modulation frequency was 86.09 Hz (Fdiv=136 and Ns=40). Sphase has been varied from 1 to 15 by steps of 2. An *Optimization* of the REU was performed after every phase change, which was the only way we found to obtain acceptable operation with grouped TC (Fig 4.6). A channel *Autobalance* or *Optimisation* is an automated procedure that adjusts the transition compensation of the bias voltage so that the bias current is as near an possible of a square wave (see 2.3).

The results were fitted with a 4th order polynomial and the optimal Sphase value was derived. Some channels give responses obviously wrong, which was expected because they were known not to converge when "optimized". For these channels we forced results to a regular value. The predictions of the SEB model prove to be accurate, and can be a basis to set

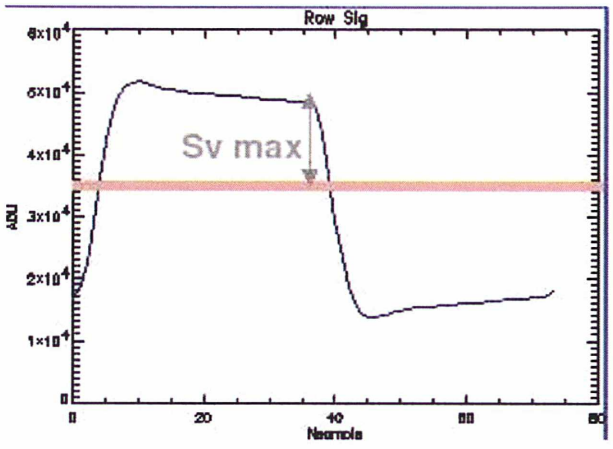

Figure 4.7: *Definition of F_2 parameter: it represents the amplitude of the square signal calculated at the end of each half period*

Sphase for these channels.

The Results have been used during all the PFM calibration campagn as nominal S_{phase} parameters and are listed in table 4.2.

4.3.3 Measurement of the F_2 parameter of the IMO function

The Instrument Model Database (IMO) contains few thousand parameters describing in detail a simplified representation of the instrument for data

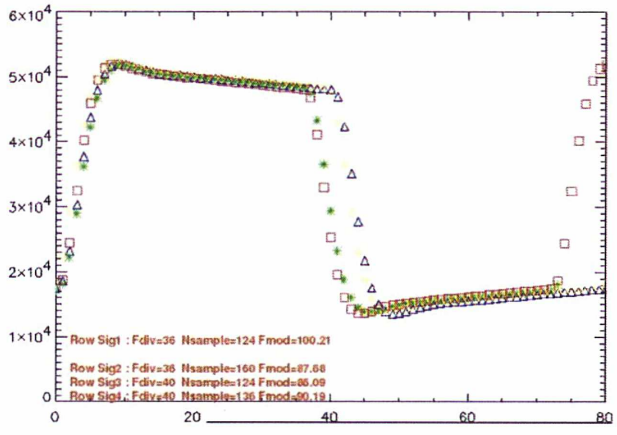

Figure 4.8: *Overplotted Raw signals of Fmod sequence for the four steps.*

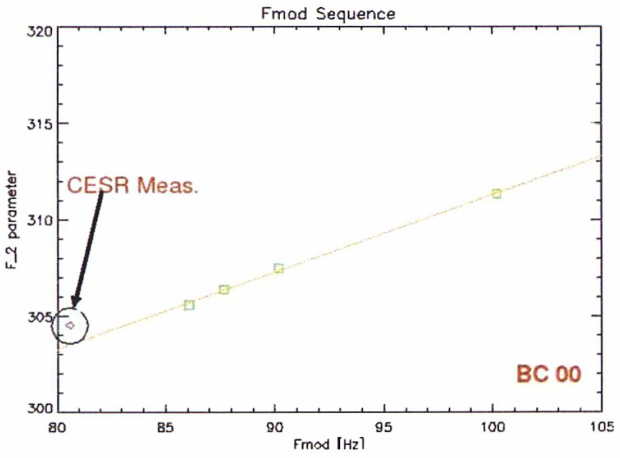

Figure 4.9: *F_2 linear fit for the particular case of belt-channel 00. We add the CESR point taken at 80.6Hz*

processing. A Function implemented in the IMO (derived from calibration of the REU) permits to calculate Volts from the DNS:

$$V_b = -\frac{(\frac{DSN}{N_{sample}} - 32768)(\frac{G_{calib}}{G_{REU}}) - \frac{F_2 \cdot V_{bal}}{2}}{F_1} \tag{4.5}$$

where:
N_{sample} is the total number of sampled points in an half period.
G_{REU} represents the programmable gain of REU, G_{Calib} is the one used during REU calibration in CESR.
V_{bal} is the square compensation voltage.
F_1 is another calibration parameter. It represents the amplitude of the voltage applied to the bolometer for a given (and single) I_{bias} command, and a given impedance of the bolometer.

F_2 parameter represents the ratio between delivered signal from REU [ADU] and digit parameter in case of only use of a compensation square in the electronic chain (Fig4.7).

$$F_2 = -2\frac{S_{vmax}}{V_{bal}}[ADU/Digit]$$

At PAU level a pass-band filter (5-600Hz) is present so F_2 could be affected by a changing of modulation frequency (F_{mod}). At this moment in the IMO instrument function (Eq(4.5)) F_2 parameter is a constant for each bolometer.
The sequence consists in checking the raw signal instrument response versus

modulation frequency for all the bolometric belt-channels of HFI [59]. During the sequence there is no current on the bolometer ($I_{bias} = 0$ and $T_{bias} = 0$ V_{bal}= 100). We perform the sequence setting F_{mod} from 86.09Hz to 100.21Hz according to four different steps fig(4.8) (86.09Hz, 87, 68Hz, 90, 19Hz, 100.21Hz). I fit results with a slope as:

$$F_2(f) = a_1 + a_2 \cdot f \tag{4.6}$$

Same strategy of analysis used by CESR [60] is performed in order to calculate F_2.
The data from 87,68Hz are not reliable because of command problems during the sequence. After data analysis we can remark that in general if we set F_{mod} at 100Hz the F_2 corrections calculated can be up to 3% (Fig(4.9)).
These results show that we have to correct the F_2 parameter in the instrument equation with a vector of values depending on the F_{mod} we use.

In tab 4.2 we present the results of the linear fit coefficients.

Belt-Channel	Best Bias (Meas) $[nA]$ (at 100 mK)	Best Bias (Sim) $[nA]$ (at 100 mK)	Best S_{phase} $[digit]$	a_1 $[ADU/dig]$	a_2 $[ADU/(dig \cdot f)]$
0 0	0,271	0.25	10	271.060	0.402457
0 1	0,306	0.24	10	269.113	0.414250
0 2	0,297	0.27	9	270.562	0.404969
0 3	0,288	0.28	9	268.908	0.415777
0 4	0,397	0.43	8	268.976	0.416219
0 5	0,346	0.40	7	271.662	0.399113
1 0	0,356	0.31	10	271.125	0.401986
1 1	0,329	0.33	8	269.763	0.408334
1 2	0,292	0.31	9	267.794	0.422606
1 3	0,342	0.48	7	268.864	0.413432
1 4	0,649	0.78	8	267.830	0.424019
1 5	-	-	-	269.089	0.408524
2 0	0,270	0.27	9	270.808	0.405827
2 1	0,297	0.28	9	270.448	0.404649
2 2	0,417	0.50	9	271.863	0.383817
2 3	0,306	0.30	9	271.884	0.400512
2 4	0,298	0.33	8	270.602	0.405490
2 5	0,761	0.76	8	270.219	0.406297
3 0	0,287	0.27	9	269.574	0.411966
3 1	0,298	0.28	9	271.018	0.401803
3 2	0,292	0.28	9	268.932	0.416161
3 3	0,295	0.34	8	270.314	0.409169
3 4	0,664	0.89	7	269.559	0.412629
3 5	0,682	0.65	9	270.305	0.406522
4 0	0,279	0.22	9	270.137	0.404928
4 1	0,251	0.25	9	270.691	0.403013
4 2	0,370	0.34	8	271.111	0.398881
4 3	0,295	0.25	9	270.969	0.399043
4 4	0,282	0.29	8	271.596	0.401397
4 5	0,394	0.37	9	269.477	0.415201
5 0	0,314	0.37	9	267.270	0.441982
5 1	0,297	0.36	6	268.557	0.425540
5 2	0,407	0.35	9	269.447	0.415496
5 3	0,297	0.31	8	270.379	0.405400
5 4	0,284	0.32	8	269.552	0.409669
5 5	0,645	0.69	8	270.311	0.403043
6 0	0,363	0.32	10	268.989	0.415372
6 1	0,283	0.24	10	269.996	0.411739
6 2	0,280	0.17	10	267.032	0.443202
6 3	0,348	0.35	9	269.786	0.414935
6 4		0.32	8	269.148	0.418552
6 5	0,730	0.75	8	270.805	0.404634
7 0	0,356	0.30	10	267.084	0.443582
7 1	0,291	0.33	8	266.100	0.445994
7 2	0,289	0.29	9	268.442	0.424953
7 3	0,659	0.80	8	273.415	0.375547
7 4	0,647	0.56	6	268.071	0.428543
7 5	-	-	-	266.321	0.445826
8 0	0,266	0.21	9	265.933	0.449745
8 1	0,276	0.22	10	270.222	0.405870
8 2	0,283	0.27	9	269.989	0.407632
8 3	0,279	0.29	9	269.067	0.415956
8 4	0,381	0.45	8	269.875	0.409462
8 5	0,389	0.46	8	268.725	0.418329

Table 4.2: *Summari zing table: Best bias measured and simulated Best S_{phase} and linear fit coefficients for F_2 calculation are presented.*

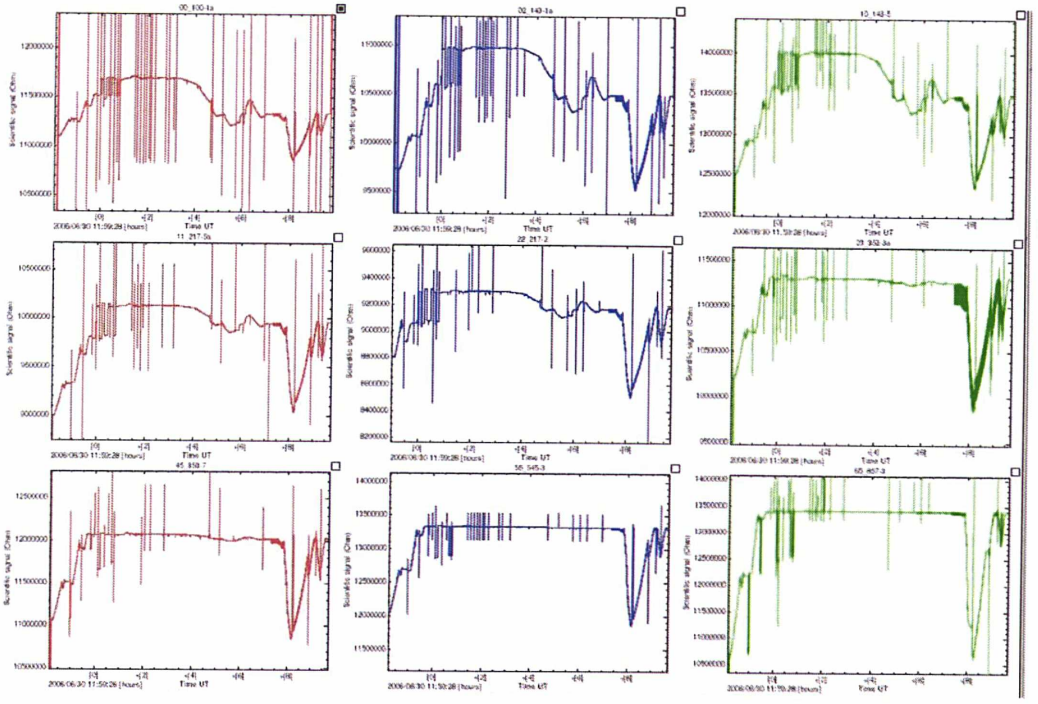

Figure 4.10: *EFF sequence during 30th of june for one bolometer each frequency*

4.4 Photometric Characterisation: EFF Sequence

During PFM Calibration campaign one of the task of LERMA was the characterisation of the photometric response of the HFI (EFF sequence) [61]. The EFF calibration sequence consisted in changing the temperature of the source and evaluating the power absorbed in the detectors by balancing the REU (see definition in section 4.3.2) and applying the IMO function. When autobalanced, the bias current absolute value is nearly constant and the steady state temperature of the bolometer is similar to that of a DC biased bolometer. So to recover the power absorbed in the bolometers we can use a DC biased model of a bolometer. The *sources* have been CS1, the whole optical cavity of the Saturne Cryostat and the 4K and the 1.6K stage emission.
The calibration facility was used to measure the various terms of the photometric equation of HFI.

4.4.1 Principles of the EFF calibration sequence

If we consider a nominal top-hat spectral band of 33% with respect the central frequency, the optical power absorbed by the bolometers is given by:

$$W_{Opt} = \frac{n}{1+P} \cdot [\tau_{Tot} \int_{\Delta\nu} \lambda^2 \cdot BB_\nu(T_{Sat}, \nu) d\nu + \cdot \tau_{Tot} \epsilon_{CS1} \int_{\Delta\nu} \lambda^2 \cdot BB_\nu(T_{CS1}, \nu) d\nu +$$
$$+ \tau_{4K} \epsilon_{4K} \int_{\Delta\nu} \lambda^2 \cdot BB_\nu(T_{4K}, \nu) d\nu + + \tau_{1.6K} \epsilon_{1.6K} \int_{\Delta\nu} \lambda^2 \cdot BB_\nu(T_{1.6K}, \nu) d\nu]$$

where:

$BB(T_X, \nu)$ is the blackbody radiation function of the considered extended source
$n\lambda^2$ is the beam throughput. For the multi-moded channels the λ^2 is multiplied to the equivalent numbers of modes. We use 3.4 for 545GHz, 8.3 for 857GHz and 1 for the others.
T_X is the temperature of the considered spread source (Saturne, CS1, 4K and 1.6K stage)
$\Delta\nu$ represents the nominal top-hat spectral band.
P is Polarisation factor. We consider HFI bolometers as ideal bolometers with $P = 1$ if PSB and $P = 0$ if SWB.
τ_{Tot} is the total efficiency of the optical system including the bolometer efficiency.
ϵ_X is the emissivity of the considered source.
τ_{4k} and $\tau 1.6K$ are the applicable effective transmission for the cryogenic stages.

Note that τ_{4k} is not the transmission of the 4K stage but the transmission of the colder stages. It is the same for $\tau_{1.6K}$. All the efficiencies and transmissions are considered as constant in the band of frequencies of each channel.

Based on the CQM (Cryo-Qualification Model) data analysis, it has been found that the straylight in the calibration facilities is very low ([62]): so in the EFF data analysis we do not consider this contribution. Because τ_{4K} and ϵ_{4K} cannot be measured separately, from now we define this product as the *Coupling parameter*. The same for $\tau_{1.6K} \cdot \epsilon_{1.6K}$ product.

$$coup_{4K} = \tau_{4K} \cdot \epsilon_{4K}$$
$$coup_{1.6K} = \tau_{1.6K} \cdot \epsilon_{1.6K}$$

The Goal of EFF sequence is to measure the τ_{Tot}, $coup_{4K}$, $coup_{1.6K}$, ϵ_{CS1} parameters.

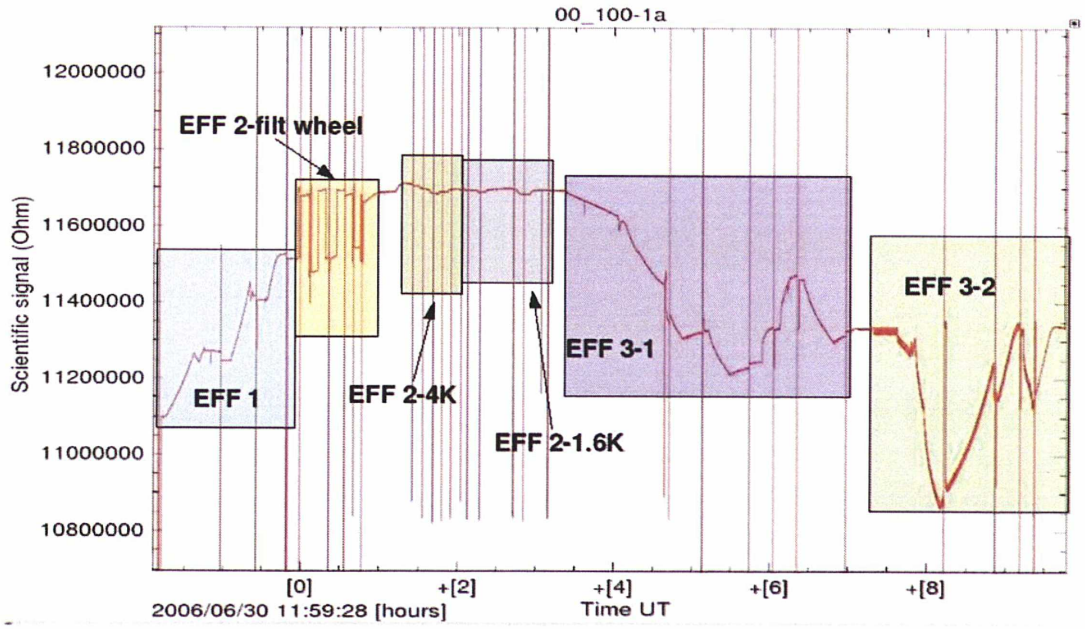

Figure 4.11: *Detailed plot for 100GHz bolometer bc=00 of EFF sequence*

4.4.2 General Procedure

The basic measurement sequence is common for all the photometric sequencies:

- Variation of the temperature of the source.

- After stabilization in temperature of the source, we perform an autobalance in order to calculate the optical power on the bolometer with a classical bolometer model (biased in a DC mode).

$$W_{Opt} = \frac{G_0}{T_{ref}^{\beta}(\beta+1)}(T_b^{\beta+1} + T_{100mK}^{\beta+1}) - R_b I_b^2$$

where:
G_b is the thermal conductance between the bolometer and the heat sink, T_{100mK} is the real temperature of the 100mK stage, T_{ref} is the reference temperature (100mK in our case), β is an experimental parameter, I_b is the bias current on the bolometer and T_b R_b are the temperature and resistence derived from the IMO.

- Using data from two different stabilized temperatures we calculate ΔW_{opt}

• When the temperatures of the other background sources are constant, ΔW_{opt} only depends on the temperature variation of the studied source.

• We calculate the optical parameter comparing ΔW_{opt} to the difference of two black bodies at the same temperatures.

$$\Theta_{EFF} = \frac{\Delta W_{opt}^{Meas}}{\frac{1}{1+P^2}\int_{\Delta\nu} n\lambda^2 \Delta B B_\nu(T,\nu)d\nu}$$

Where Θ_{EFF} represents the generic optical parameter.
There was a temperature drift of the $2K$ platform during the $1.6K$ and $4K$ sequence so we have to correct the general procedure taking into account these deviations.

In Fig 4.11 a detailed plot of the impedance timeline of the whole EFF sequence is presented for a 100GHz bolometer:

• *EFF1*: measure the emissivity of the CS1 source.

• *EFF2-Filter Wheel*: measure of the low frequency response using the response to Heavyside steps produced by opening and closing the cryogenic filter wheel (see section 4.6.1).

• *EFF2-4K*: Measure of the coupling factor of the 4K cryogenic stage.

• *EFF2-1.6K*: Measure of the coupling factor of the 1.6K cryogenic stage.

• *EFF3-1*: Measure of the total efficiency of HFI.

• *EFF3-2*: Measure of the Steady state response function of HFI (see section 4.5)

4.4.3 Background Conditions

During the calibration run the temperature of the $100mK$ stage was very stable ($\sim 2\mu K/h$). We report in Fig(4.12) the history of the cryogenic stage

The REU Autobalance procedure is quantised and it introduces some noise (for example no change of parameters where one is expected)(Fig4.13). This could introduce some systematics in the sequences where the signal to noise ratio is small.

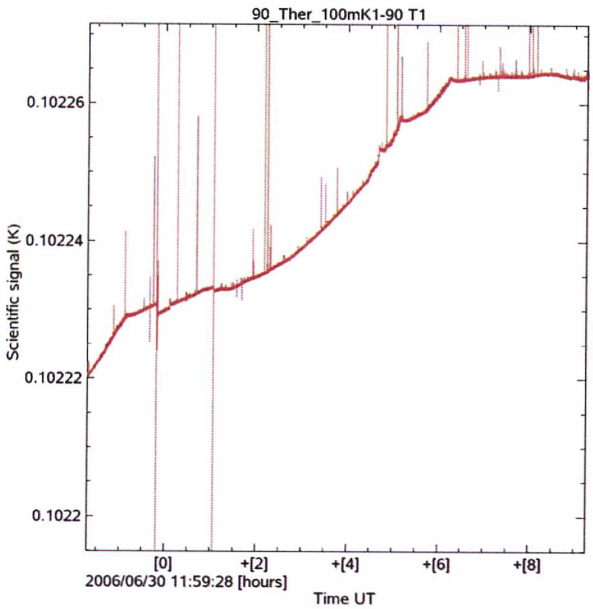

Figure 4.12: *Time evolution of temperature of the100mK stage from the thermometer bc=90 during the first day of the EFF sequence*

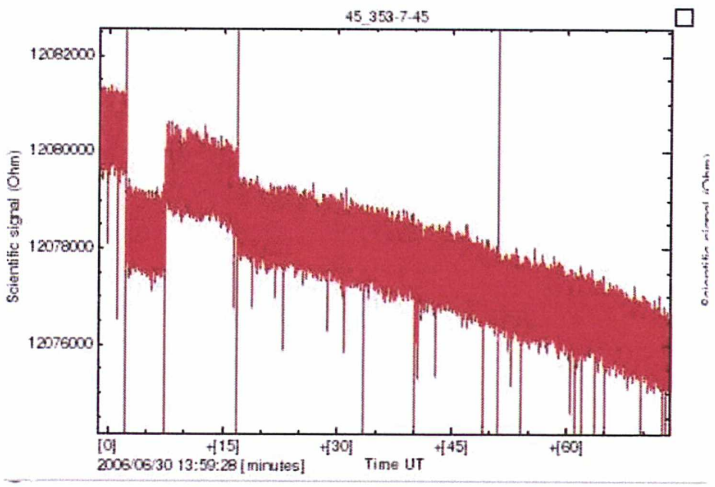

Figure 4.13: *Exemple of the intrinsic noise in the autobalance procedure: Bolometer 353-7 bc=45 during thermal signal from 1.6K stage sequence. The optical power on the bolometer does not change but when we perform an autobalance the level of the signal changes. We can conclude that there is an intrinsic noise in autobalance procedure of the order of magnitude of the quantisation step of the bias transient commands.*

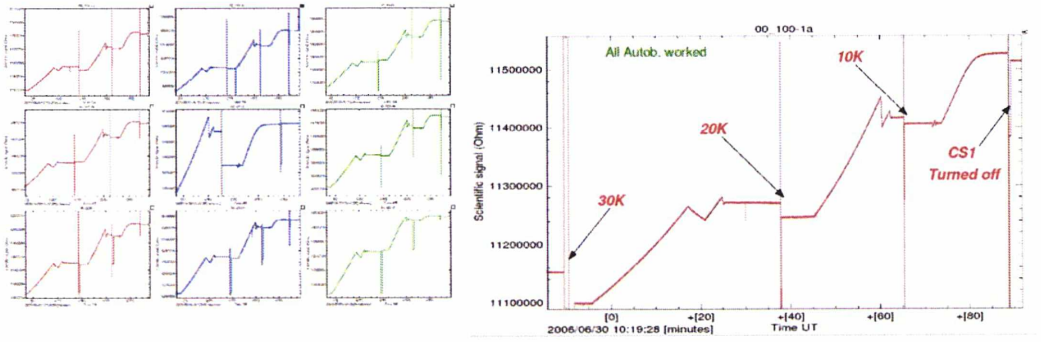

Figure 4.14: *EFF1 sequence (one bolometer of each kind) and detailed plot for 100GHz bc=00*

4.4.4 Measuring the Emissivity of the CS1 source

The goal of this sequence is to measure the effective emissivity of CS1 in the intensity of CS1 in the integrating sphere, and to compute which temperature of CS1 gives the flux most representative of the telescope emission. The expected temperature and emissivity of the telescope are:

$$T_{Tel} = 45K$$

and

$$\epsilon_{Tel} = 1\%$$

CS1 is a black body embeded in the cavity. Its brightness is diluted in the integration sphere. We can consider therefore CS1 as a *grey body* with a characteristic emissivity.
In Fig(4.14) we present the signal for one bolometer for each family of detectors. We performed a temperature change of CS1 from $30K$ to $2K$ (temperature in which CS1 is switched off and thermalized with the platform).
Let us remark that during this sequence the temperature drifts from the background sources were negligible with respect to the signal to noise ratio, so for this analysis we use the general procedure to analyse the data.
In Fig(4.15) and table we present the results for the CS1 efficiency detected by all the 52 bolometers of HFI. For 4 bolometers the autobalance procedure did not work. It means that these bolometers worked in saturation conditions so the results for these 4 bolometers are not significant.
To calculate the best temperature to set CS1 source in order to simulate the background from the telescope, we perform a χ^2 test to minimize the differ-

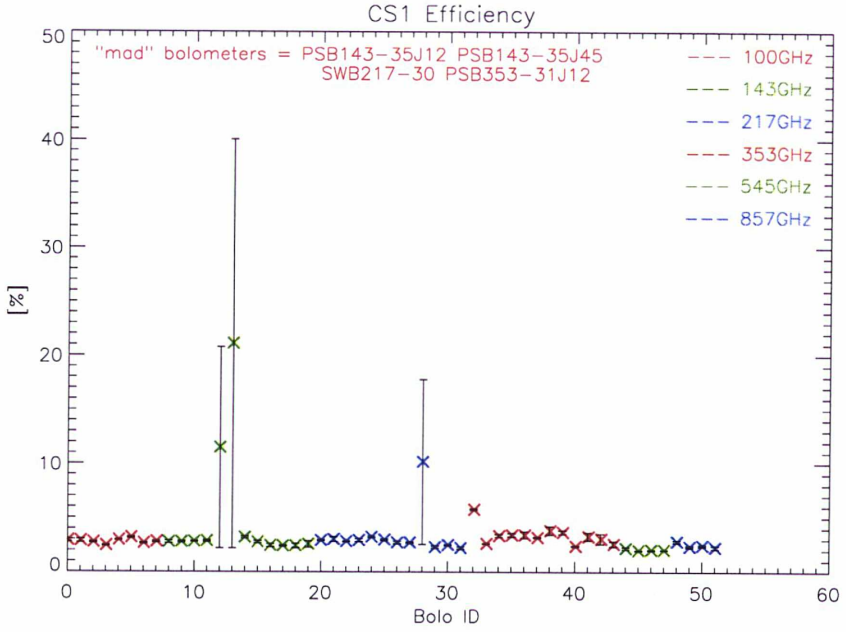

Figure 4.15: *Results from EFF1: emissivity of CS1 source measured by all 52 HFI bolometers. During this sequence the autobalance procedure for four detectors did not work.*

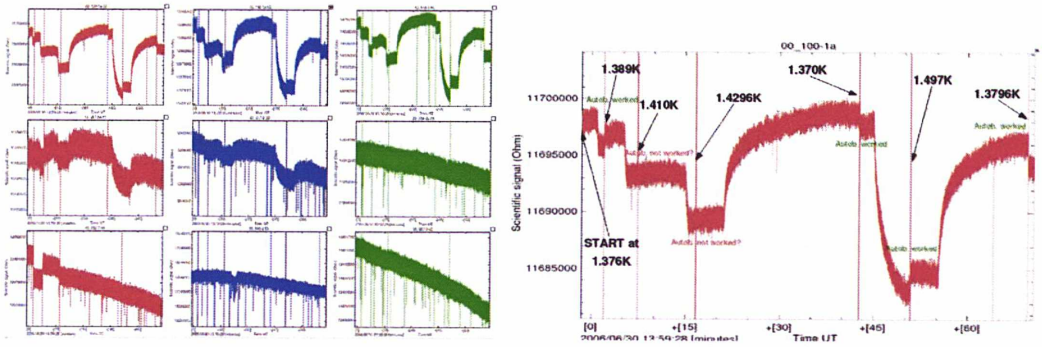

Figure 4.16: *EFF2-1.6K sequence (one bolometer of each kind) and Detailed plot for 100GHz bc=00*

ence between the signal from the telescope ($T = 42K$ $\epsilon Tel = 1\%$) and a *grey body* with an optical efficiency as calculated for CS1 for a range of different temperatures. The result of this simulation give a temperature of 26K.

4.4.5 Thermal emission of the 4K and 1.6K stage

The thermal emission of the 4K and 1.6K stages of the FPU is a constitutive part of the background power absorbed by the bolometers. They also constitute a potential source of additional low frequency noise, if the temperature of these stages is not stable enough.
A drift in temperature of the platform induced a difficulty in interpreting the thermal emission sequence during the calibration run.
To compensate the drift we consider the sequence corresponding to the absolute calibration (see 4.4.6) and in particular the relation between the signal of the bolometers and the temperature of the platform during this sequence. Let us consider they have a linear relation.

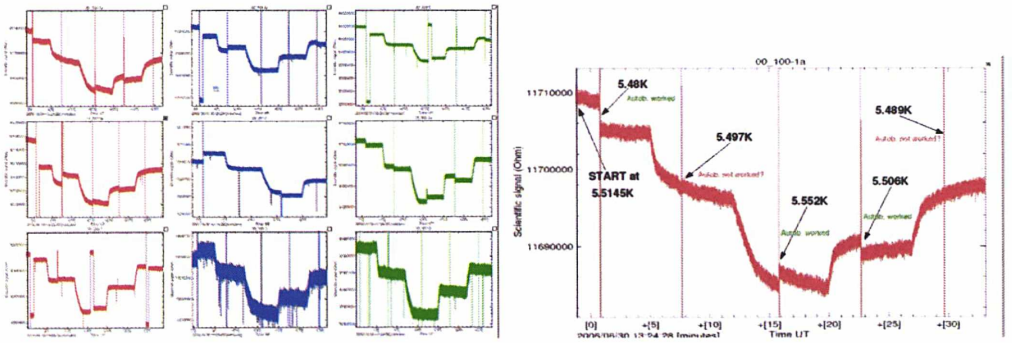

Figure 4.17: *EFF2-4K sequence (one bolometer of each kind) and Detailed plot for 100GHz bc=00*

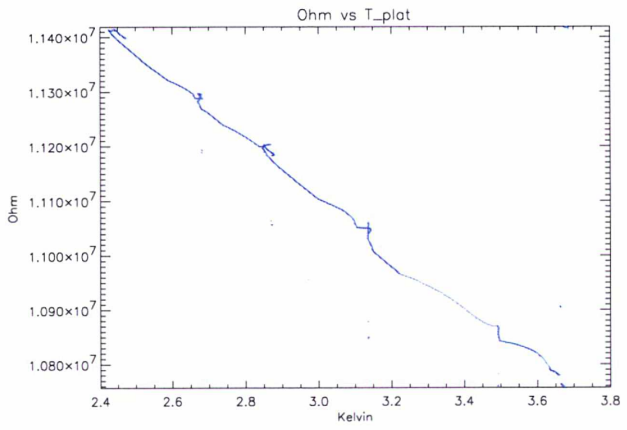

Figure 4.18: *Trend between signal and temperature of 2K platform. With this relection we calculate the β parameter*

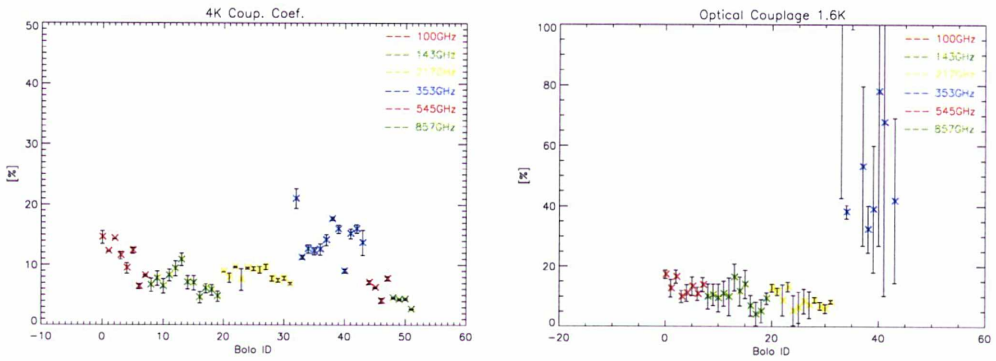

Figure 4.19: *Results from thermal emission sequence: on the right thermal emission from 4 K stage is plotted. On the left plot thermal emission from 1.6K stage is plotted: the high frequency channels are not sensitive (the optical coefficient is about 0%*

We define a new signal as:

$$SIG_{new} = SIG_{old} - \beta T_{plat}$$

where β is the slope between signal and the platform temperature during absolute calibration sequence. In Fig(4.18) we present the analysis for one detector (100GHz bc=00).
We performed this analysis for all bolometers and in both sequences, the results are summarized in Fig(4.19).
In the $1.6K$ sequence the results show that high frequency channels are not sensitive (a tiny emmission from 1.6K stage at high frequency).

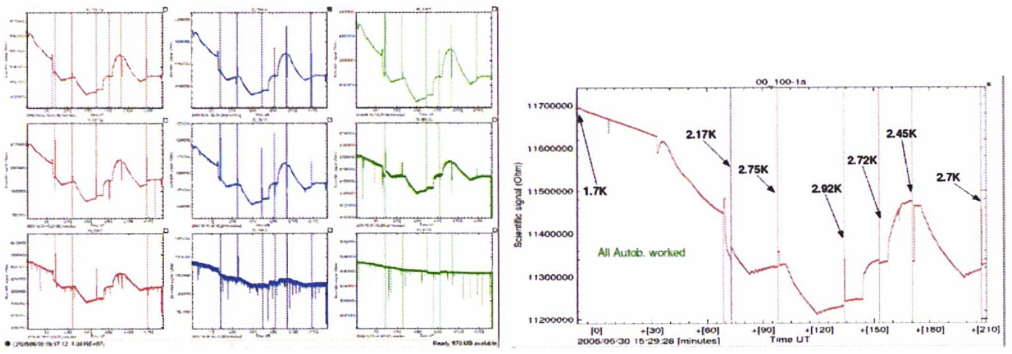

Figure 4.20: *EFF3-1 efficiency sequence (one bolometer of each kind) and Detailed plot for 100GHz bc=00*

4.4.6 Total Efficiency

We used the whole Saturne cavity as a blackbody (all sources are OFF for temperature uniformity) to measure the absolute response of the instrument. The range of temperature was from 2K to 3.7K.

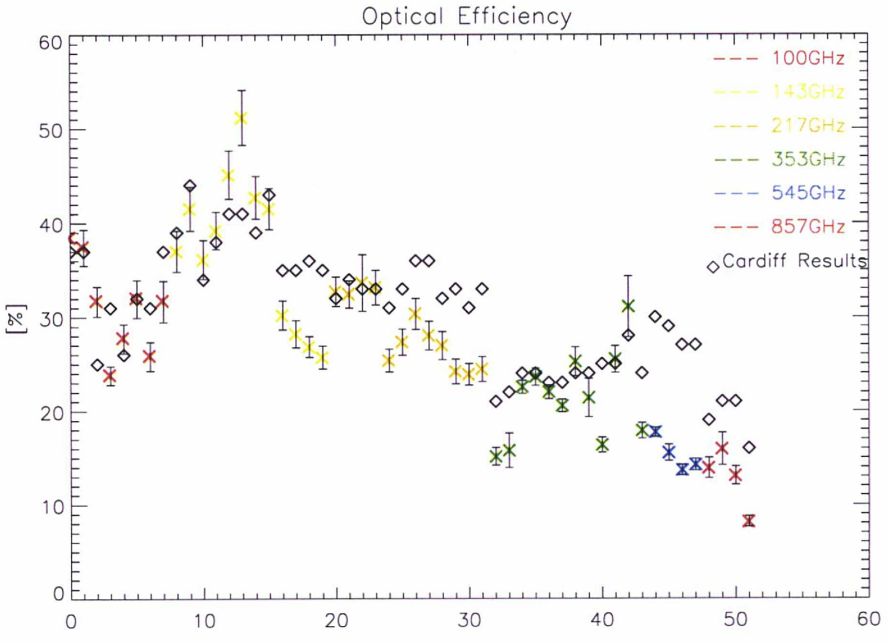

Figure 4.21: *Results from EFF3-1 sequence: total optical efficiency calculed with a nominal top-hat band. A comparison with Cardiff Results (black points) is performed.*

The optical efficiency measured with the EFF sequence should be different from those measured at Cardiff with quasi-RJ sources. In Fig 4.21 We present results of the analysis performed using nominal top-hat spectral bands.

The most important differences between calibration run and Cardiff measurements appear for the high frequency channels (Fig 4.17). One possible explanation is a different spectral index between used sources.

In the table 4.3 the total efficiency is presented

4.4.7 HFI Photometric Equation implemented in the IMO

The total optical efficiency as derived in section 4.4.6, represents the physical Total efficiency of the instrument if we use top-hat nominal bands. The spectral bands has been derived with interferometric measurements during PFM calibration [33] as a product of the real shape of the spectral bands and the beam throughput of the instrument. All the beams have been normalised to one at their maximum point. In this case, according to the general procedure presented in the section 4.4.2, we have:

$$PAR_{EFF} = \frac{\Delta W_{opt}^{Meas}}{\frac{1}{1+P}\int_0^\infty n\lambda_0^2 \chi(\nu)\Delta BB_\nu(T_{Sat},\nu)d\nu} \tag{4.7}$$

where:

$n\lambda_0$ is the beam throughput at central frequency of channel

$\chi(\nu)$ is the spectral transmission of the optical chain (normalised to 1 on the pick).

PAR_{EFF} parameter does not represent the physical total efficiency of the instrument but it is a normalisation parameter that takes in account the integrated power in the spectral bands. In Fig 4.22 results of this analysis are presented.

In this case the photometric equation is:

$$W_{Opt} = \frac{n}{1+P}\cdot[\lambda_0^2 PAR_{EFF}\int_0^\infty \chi(\nu)\cdot BB_\nu(T_{Source},\nu)d\nu + coup_{4K}\int_{\Delta\nu}\lambda^2\cdot BB_\nu(T_{4K},\nu)d\nu + \\ + coup_{1.6K}\int_{\Delta\nu}\lambda^2\cdot BB_\nu(T_{1.6K},\nu)d\nu] \tag{4.8}$$

B-C	Opt ID	CS1eff [%]	C_{4K}[%]	$C_{1.6K}$[%]	τ_{Tot}[%]	PAR_{EFF}[%]
0 0	100-1a	2.43 ± 0.11	11.53 ± 1.2	11.14 ± 2.73	24.62 ±1.61	39.29 ± 0.65
0 1	100-1b	2.73 ± 0.15	14.32 ± 0.12	17.83 ± 2.99	32.83 ±1.83	57.52 ± 1.3
0 2	143-1a	2.77 ± 0.041	7.730 ± 2.3	12.70 ± 4.97	42.94 ±2.25	66.45 ± 1.3
0 3	143-1b	2.76 ± 0.039	6.673 ± 2.1	12.46 ± 5.77	38.52± 2.07	57.58 ± 0.83
0 4	217-1	2.28 ± 0.024	7.425 ± 0.53	9.19 ± 4.06	24.96± 1.14	40.79 ± 0.77
0 5	353-1	3.28 ± 0.067	15.18 ± 1.6	-	26.24±0.83	51.44 ± 0.84
1 0	143-5	2.41 ± 0.058	5.836 ± 1.7	7.477 ± 5.43	27.87 ± 1.52	38.65 ± 0.59
1 1	217-5a	3.00 ± 0.070	7.878 ± 1.5	15.16 ± 5.96	33.53± 1.02	53.94 ± 0.93
1 2	217-5b	2.90 ± 0.11	8.851 ± 0.098	15.90 ± 4.44	33.82 ± 1.39	59.67 ± 0.94
1 3	353-2	3.07 ± 0.063	15.98 ± 1.3	-	32.02±1.02	60.49 ± 3.8
1 4	545-1	2.00 ± 0.041	6.247 ± 0.20	-	15.98 ±0.61	32.03 ± 0.86
1 5	DARK	-	-	-	-	-
2 0	100-2a	2.86 ± 0.077	12.21 ± 0.025	14.44 ± 4.06	38.8 ±2.06	52.89 ± 0.82
2 1	100-2b	2.89 ± 0.093	14.57 ± 0.021	18.15 ± 1.92	39.8±1.97	58.21 ± 1.8
2 2	217-2	-	7.706 ± 0.85	10.97 ± 3.04	27.8 ± 3.11	45.23 ± 0.75
2 3	353-3a	3.67 ± 0.097	15.96 ± 1.3	-	22.0 ±0.81	39.62 ± 1.3
2 4	353-3b	3.82 ± 0.10	17.67 ± 0.49	-	25.9± 0.91	45.03 ± 1.7
2 5	857-1	2.44 ± 0.14	4.348 ± 0.24	-	13.3 ± 0.54	25.45 ± 0.88
3 0	143-2a	2.76 ± 0.037	7.004 ± 2.3	16.79 ± 6.46	42.9± 2.07	64.63 ± 1.7
3 1	143-2b	3.19 ± 0.19	7.082 ± 2.1	14.52 ± 6.62	44.1±2.29	62.98 ± 1.7
3 2	353-4a	3.19 ± 0.29	14.14 ± 1.8	-	21.1± 1.25	42.00 ± 0.83
3 3	353-4b	3.42 ± 0.047	12.57 ± 1.8	-	22.6± 1.02	40.50 ± 0.69
3 4	545-2	2.19 ± 0.21	7.093 ± 0.54	-	18.1± 0.81	31.63 ± 0.47
3 5	857-2	2.82 ± 0.048	4.545 ± 0.14	-	14.1± 0.51	24.44 ± 1.1
4 0	100-3a	3.16 ± 0.14	12.33 ± 0.95	15.18 ± 4.22	33.1± 1.73	50.19 ± 0.92
4 1	100-3b	2.93 ± 0.068	9.433 ± 1.7	12.79 ± 3.83	28.7 ±1.95	41.62 ± 0.79
4 2	143-6	2.44 ± 0.061	4.615 ± 1.8	9.004 ± 4.81	31.2 ±2.03	44.97 ± 0.73
4 3	217-6a	2.70 ± 0.11	9.658 ± 0.91	10.66 ± 7.35	28.9± 1.53	44.22 ± 0.71
4 4	217-6b	2.71 ± 0.044	9.189 ± 1.1	12.12 ± 7.50	31.3± 1.27	50.85 ± 0.95
4 5	353-7	2.39 ± 7.61	9.006 ± 0.62	-	16.8± 1.56	31.72 ± 0.61
5 0	143-3a	-	10.85 ± 1.5	19.00 ± 6.18	53.0± 2.54	93.31 ± 1.6
5 1	143-3b	-	9.394 ± 1.2	14.48 ± 10.0	46.7± 2.76	71.08 ± 1.3
5 2	217-3	2.48 ± 0.10	7.776 ± 0.67	8.072 ± 3.84	24.6 ± 0.97	40.55 ± 0.64
5 3	353-5a	3.41 ± 0.072	12.29 ± 1.1	-	24.2± 1.08	37.75 ± 0.28
5 4	353-5b	3.34 ± 0.0085	12.65 ± 1.3	-	23.1± 0.96	34.57 ± 0.48
5 5	545-3	2.04 ± 0.13	4.065 ± 0.76	-	13.9± 0.44	25.01 ± 0.44
6 0	143-7	2.41 ± 0.16	6.085 ± 1.5	6.548 ± 5.63	29.1± 1.43	41.63 ± 0.68
6 1	217-7a	2.96 ± 0.29	9.355 ± 0.62	9.797 ± 7.71	28.2± 1.22	41.01 ± 0.64
6 2	217-7b	3.22 ± 0.029	9.444 ± 0.25	8.391 ± 7.11	26.2± 1.31	41.93 ± 0.61
6 3	353-6a	2.61 ± 0.36	11.24 ± 0.69	-	16.2± 3.57	28.59 ± 0.62
6 4	353-6b	-	21.01 ± 0.7	-	15.6±3.58	28.90 ± 0.64
6 5	857-3	2.34 ± 0.023	4.266 ± 0.20	-	16.1± 0.48	29.40 ± 0.34
7 0	143-8	2.55 ± 0.35	4.804 ± 1.6	10.49 ± 2.63	26.6± 1.28	39.83 ± 0.74
7 1	217-8a	2.92 ± 0.46	7.572 ± 3.5	16.27 ± 4.36	34.2± 1.88	52.50 ± 0.67
7 2	217-8b	2.81 ± 0.23	9.636 ± 0.23	11.88 ± 7.25	34.6± 1.95	63.28 ± 3.4
7 3	545-4	2.03 ± 0.11	7.713 ± 0.64	-	14.6±0.94	26.95 ± 0.37
7 4	857-4	2.26 ± 0.026	2.685 ± 0.18	-	8.7± 0.55	14.18 ± 0.59
7 5	DARK	-	-	-	-	-
8 0	100-4a	2.79 ± 0.035	8.199 ± 0.32	15.25 ± 3.19	32.8±2.12	43.73 ± 0.81
8 1	100-4b	2.64 ± 0.020	6.390 ± 0.70	12.21 ± 3.04	26.7± 1.92	37.73 ± 0.61
8 2	143-4a	2.85 ± 0.10	8.254 ± 1.9	13.37 ± 5.74	40.1±1.71	51.13 ± 0.80
8 3	143-4b	2.81 ± 0.076	6.472 ± 2.3	12.21 ± 6.36	37.4±1.86	51.94 ± 1.1
8 4	217-4	2.21 ± 0.077	6.888 ± 0.35	10.26 ± 3.00	25.2±1.15	39.60 ± 0.65
8 5	353-8	2.59 ± 0.15	13.67 ± 4.1	-	18.4± 0.82	35.93 ± 0.67

Table 4.3: *Summarizing table: Bolo Identification and optical parameters are presented. The parameter PAR_{EFF} is calculated with real spectral bands.*

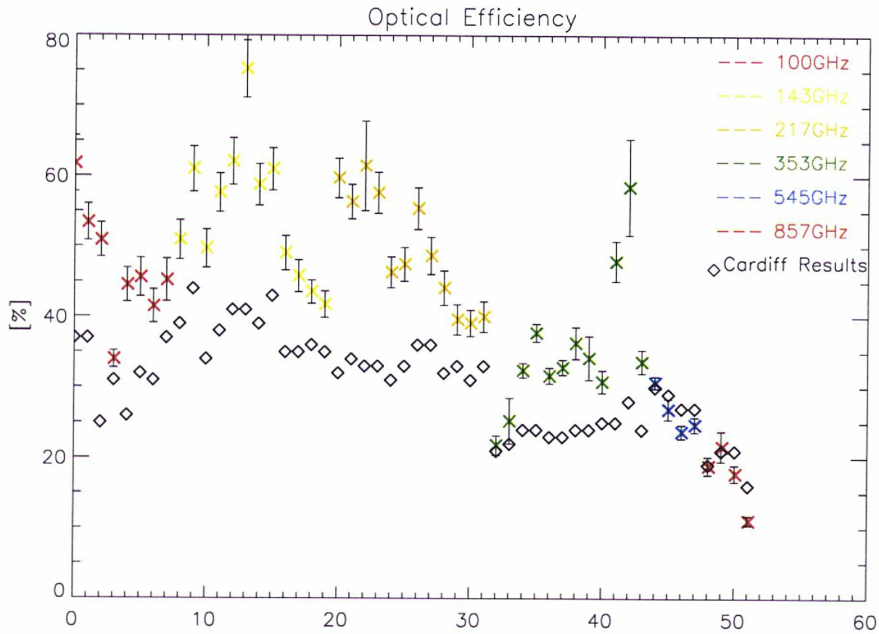

Figure 4.22: *Normalisation parameter calculed with the real spectral band. A comparison with Cardiff results is performed (Black points)*

This equation is the one implemented in the IMO and in the SOS model.

4.4.8 Conversion Factor $W_{RJ} - W_{stage}$

It is useful to quantify the optical power produced by cryogenic stages with respect an optical RJ source using results from EFF sequences [63].

The optical power absorbed by the bolometers, for the different cryogenic stages and for the RJ source, is represented here by a simplified model (the emissivity and transmission are constant in each spectral band):

$$W_{4k} = \frac{1}{1+P}\left[n \cdot coup_{4K} \int_{\Delta\nu_{4K}} \lambda^2 \cdot BB_\nu(T_{4K}, \nu) d\nu\right]$$

$$W_{1.6k} = \frac{1}{1+P}\left[n \cdot coup_{4K} \int_{\Delta\nu_{1.6K}} \lambda^2 \cdot BB_\nu(T_{1.6K}, \nu) d\nu\right]$$

$$W_{RJ} = \frac{1}{1+P}\left[n\lambda_0^2 \cdot PAR_{EFF} \int_0^\infty \chi(\nu) BB_\nu(T_{RJ}, \nu) d\nu\right]$$

where:
PAR_{EFF} is the Normalised factor coming from the absolute calibration sequence.
$\chi(\nu)$ is the normalized spectral transimission
$BB_\nu(T,\nu)$ is the blackbody radiation function
$BB_\nu(T_{RJ},\nu)$ is the RJ blackbody function ($BB_{RJ} = \frac{(2\nu^2)}{c^2} kT_{RJ}$)
$A\Omega$ is the beam throughput
T_{RJ} is the temperature of the RJ source
$coup_X$ is the product between emissivity and transmission of the considered cryogenic stage.

The basic calculation corresponding to a variation of 1mK for both RJ and cryogenic stage, is:

$$Factor = \frac{\Delta W_{RJ}}{\Delta W_{stage}}$$

The results are presented in table 4.4.

Belt - Channel	Factor(4K)	Factor(1.6K)
0 0	3.2603670	5.3749381
0 1	3.9391137	4.8830234
0 2	9.6272322	13.536259
0 3	9.3161862	11.955983
0 4	8.4868726	34.968610
0 5	9.8938011	-
1 0	9.1649904	20.201117
1 1	11.295206	28.794500
1 2	10.647343	27.660199
1 3	11.472524	-
1 4	44.265453	-
2 0	15.379843	25.823870
2 1	15.926464	24.033604
2 2	19.221434	74.283205
2 3	6.5489347	-
2 4	6.3209959	-
2 5	348.65420	-
3 0	71.724422	75.145708
3 1	64.880013	82.150096
3 2	7.0975526	-
3 3	7.7417330	-
3 4	44.481461	-
3 5	353.61491	-
4 0	35.991761	52.704187
4 1	50.467107	68.869179
4 2	94.564368	134.83750
4 3	42.252579	230.94184
4 4	52.412841	233.97753
4 5	10.727145	-
5 0	8.4552581	10.796830
5 1	8.0672579	14.753680
5 2	7.9981327	40.040096
5 3	9.3888035	-
5 4	7.8787447	-
5 5	59.988668	-
6 0	21.512498	69.167244
6 1	15.210974	93.797560
6 2	15.022314	111.75411
6 3	6.8671300	-
6 4	3.1895440	-
7 0	432.69001	-
7 1	77.309363	85.371911
7 2	63.665617	149.43119
7 3	55.402297	250.40364
7 4	32.930486	-
7 5	353.75490	-
8 0	53.682351	50.372252
8 1	69.347135	65.634791
8 2	57.510024	91.204085
8 3	60.101094	85.446861
8 4	46.387478	161.32676
8 5	7.7145274	-

Table 4.4:

4.4.9 Discussion on Photometric Results

Looking at results of EFF sequence we find that the coupling coefficients between two PSB of the same pair are different. The same effect occurs on total efficiencies. This seems strange since the pair of PSB has exactly the same optical chain in front of it. In fact optical transmission depends on both the optical chain and the quantic coupling of a photon with the bolometer itself. This cross section is a function of manufacturing material of the bolometer and of its position in the cavity at the end of the horn. JPL measurement on bolomers showed that the differences between two PSB of the same pair could be in same case of the order of 15%.

On the other hand if the illustrated differences depends only on this cross section we could have:

$$\frac{\tau_{Tot}^{PSBa}/\tau_{Tot}^{PSBb}}{coup_{4K}^{PSBa}/coup_{4K}^{PSBb}} \sim 1 \tag{4.9}$$

In Fig 4.23 the results of this calculation are presented. We can conclude that the degree of polarised systematic of the optical change is not relevant.

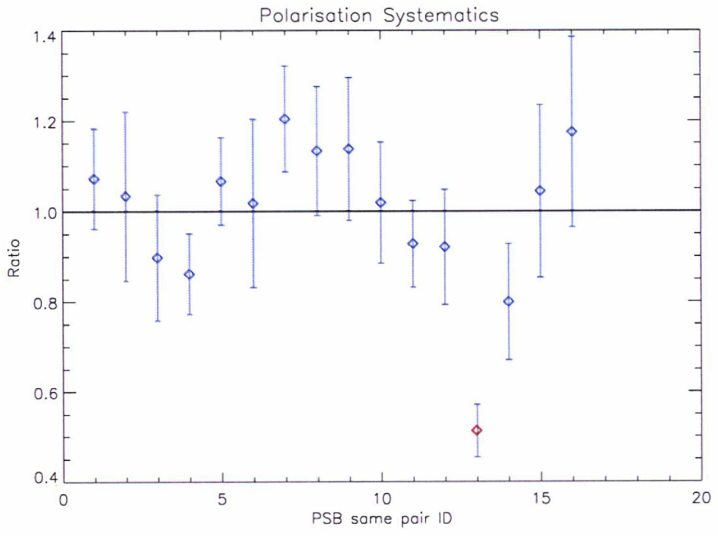

Figure 4.23: *Study of the degree of polarised systematics in the optical chain. The red point corresponds to a ratio between a pair of PSB in which the autobalance procedure did not work*

4.5 Steady State Response and Non-Linearities

The steady state (or static) response function is the relation between the incoming power (in watts) and the instrument output data in digital units (ADU), once all transients have died away.

It is expected to be non-linear because both the conductance between the bolometer and the heat sink and the bolometer impedance have a non-linear dependence with temperature (see model of bolometer in section 3.2.1).

We shall show that the non-linearities of the response curve is negligible for the signal from the CMB anisotropies, while this is not the case for strong source. Order of magnitude are given in table 4.5.

Let us define the instrument responsivity (ADU/Watt) as the derivative of the response function with respect to detected optical power:

$$S(G, R, I) = \frac{dDATA}{dW_{opt}} \tag{4.10}$$

In nominal condition, the background on HFI bolometers is much higher than the dipole signal which is not the case for bright sources like planets (Table 3.2.1). An experimental characterisation of static function is therefore very important to recover properly the optical power of the incoming signal. Since in case of HFI the experimental response is taken in digital units (ADU), we are interested to recover the static function binding ADU to optical power directly.

BOLO	*BACK* [*pWatt*]	DIP [*attoWatt*]	JUP [*pWatt*]	SAT [*pWatt*]	MARS [*pWatt*]
100-3a	0.33	360	0.17	0.03	0.01
143-3a	0.37	599	0.67	0.10	0.04
217-6a	0.43	350	1.58	0.25	0.09
353-5a	0.50	108	2.55	0.40	0.16
545-2	4.54	97.6	9.67	1.69	0.83
857-2	12.98	4.45	27.6	4.18	2.22

Table 4.5: *Typical incoming optical power on bolometers: background, dipole, Jupiter, Saturn and Mars. Optical power is calculated using optical parameters derived from calibration. The background is calculated when the all the source in integrating sphere are thermalized with the cavity at 3K.*

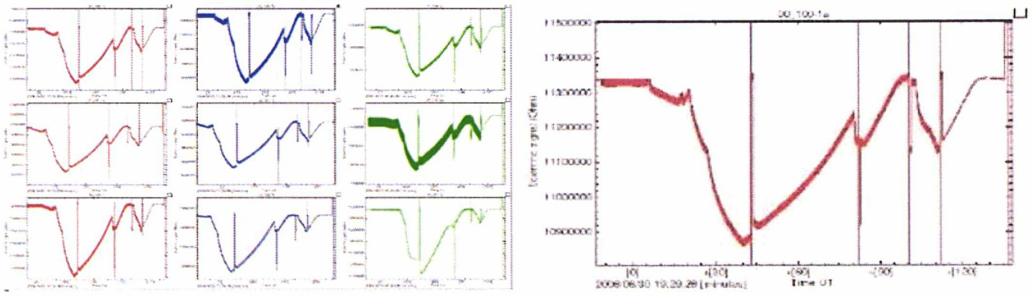

Figure 4.24: *EFF3-2 sequence (one bolometer for each freq) and detailed plot for 100GHz bc=00. The change of background is produced by CS1 source while the modulated signal is produced by the CSM carbon fiber source*

4.5.1 Measurements of the Response Function

The measurement of the response function consists in measuring the responsivity, that is the local derivative of the response function under a large range of background conditions. Practically, the responsivity is measured by illuminating all bolometers by the CSM carbon fibre source modulated at a frequency of about 1 Hertz. The average background power is explored by slowly changing the temperature of the CS1 source [61].

The amplitude of the modulated signal is:

$$Meas = S \cdot W_{fibre} \tag{4.11}$$

where S is the responsivity of the instrument and W_{fibre} the optical power of CSM.

An indefinite integration gives the integrated measure MI:

$$MI = \int \frac{dDATA}{meas} = \int \frac{1}{W_{fibre}} \frac{dW}{dDATA} dDATA = \frac{1}{W_{fibre}} W_{opt} + C \tag{4.12}$$

where C is a constant coming from the indefinite integration.

So we have:

$$W_{fibre} = \frac{W_{opt2} - W_{opt1}}{MI(DATA_2) - MI(DATA_1)} \tag{4.13}$$

and:

$$C = MI(ADU_1) - W_{opt1} \frac{MI(ADU_2) - MI(ADU_1)}{W_{opt2} - W_{opt1}} \tag{4.14}$$

The response function of the instrument derived with this procedure is presented in Fig(4.25).

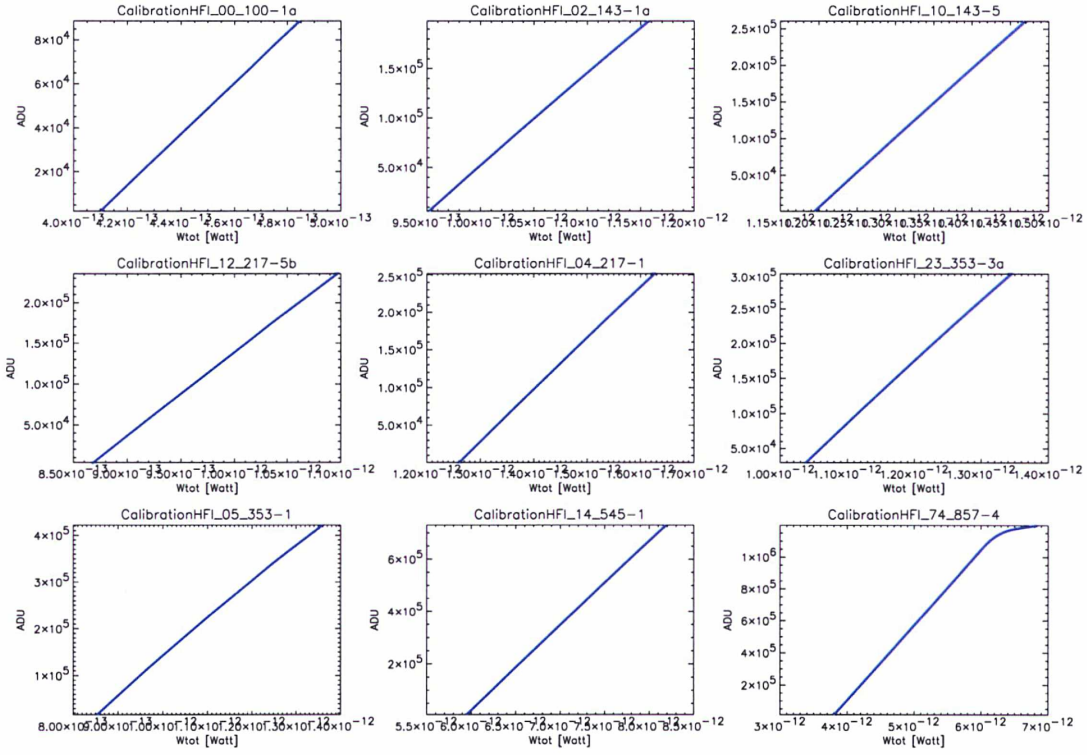

Figure 4.25: *Reponse function of the instrument for one bolometer of each kind. In the range of background examined the saturation occurs only in the 857GHz channels.*

The non-linearities of the instrument can be derived by a study of the deviation of this instrument function with respect to a linear one as shown in Fig (4.26).

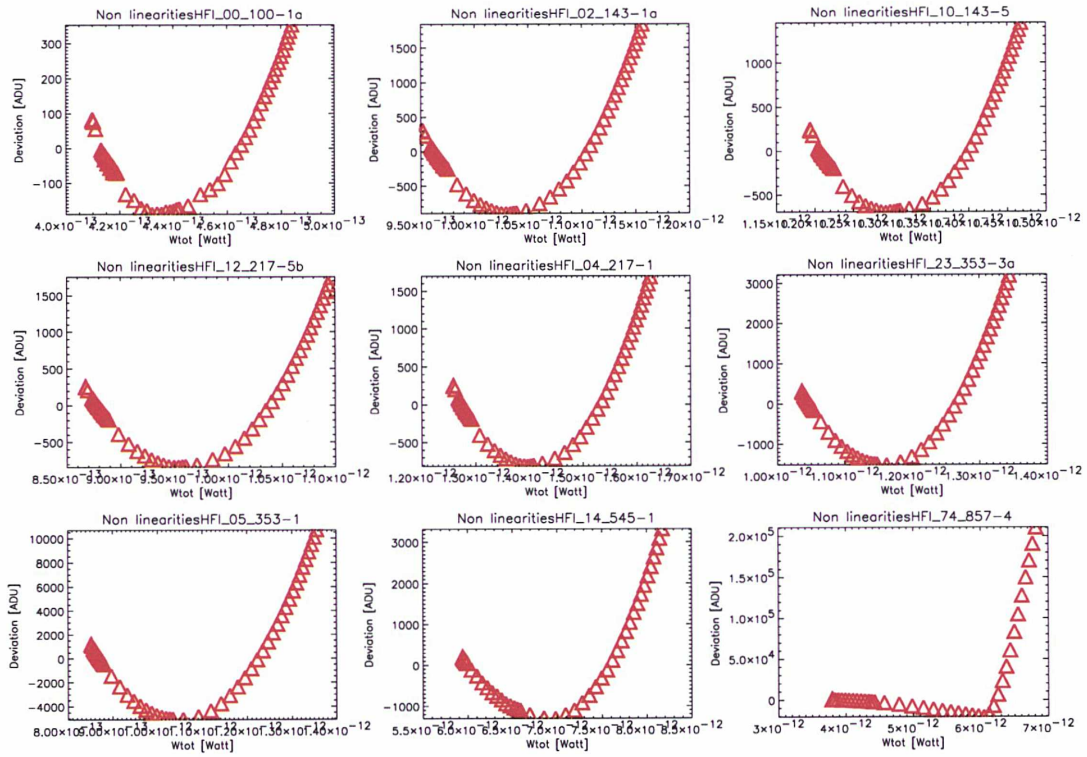

Figure 4.26: *Deviation from a linear response. The linearity of the bolometers in this range of background (except for 857GHz bolometers is that saturate less than 1%*

4.5.2 Discussion of results

By examining the results, we can conclude that the HFI bolometers are rather linear even for rather bright sources. The response curve departs from a linear one by a small amount (Fig 4.26). The typical level is of the order of per mil.

REU saturations has been observed on channel 857GHz. All the data are taken with a REU gain set to 1. Since during the sequence the background varied in a realistic range with respect the flight conditions with a gain set to 1 saturation occurs for bright source like Jupiter.

Let us extrapolate the measurement up to saturation limit.
We fit the experimental results with a two degree polynomial curve:

$$W_{opt} = W_0 + p_{lin} ADU + p_{n-lin} ADU^2 \tag{4.15}$$

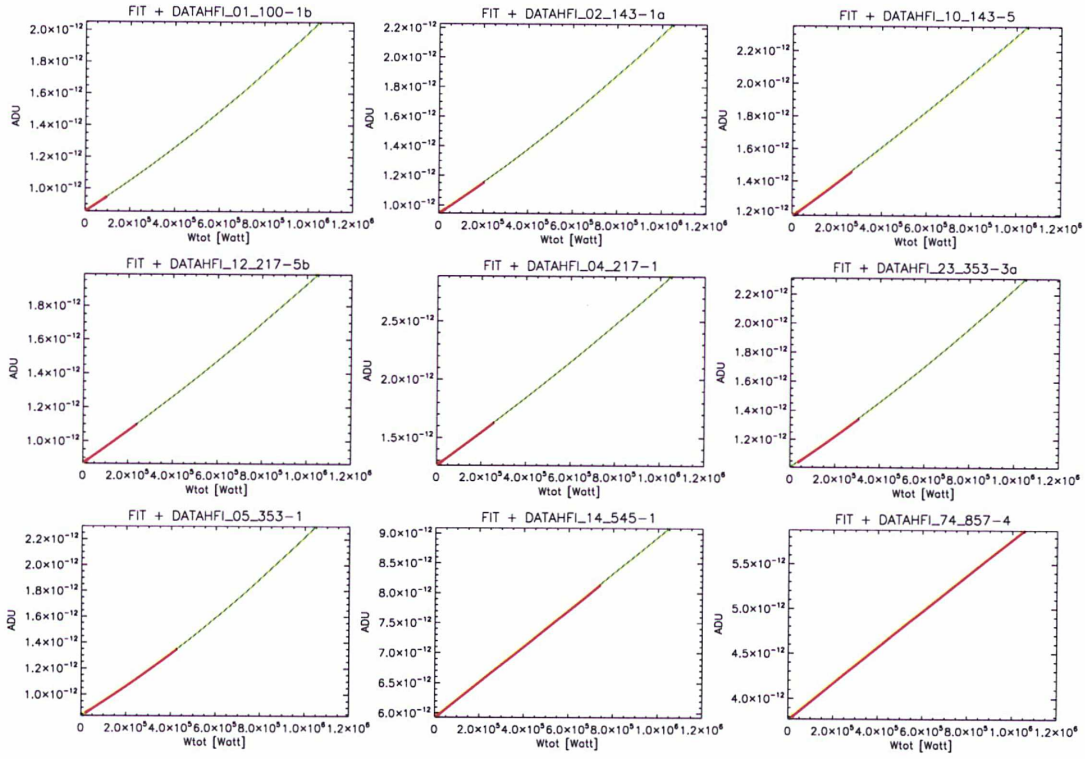

Figure 4.27: *Extrapolation of the response up to saturation. The range covered by Saturn is overplotted.*

In this way the linear and the non-linear contribution to the response of the instrument are well separated. In Fig 4.27 an overplot of the fit and the range of background covered by Saturn (second brightest source for Planck) is presented.

Now we can define for CMB channels a non-linearity parameter referred to the dipole signal as the relative deviation from a linear fit:

$$NL_{DIP} = \frac{DIPOLE_{lin}(ADU) - DIPOLE_{q}(ADU)}{DIPOLE_{lin}(ADU)} \tag{4.16}$$

Where the *lin* and the q subscript refer to a linear and second order fit respectively.

For high frequency channels we can define in the same way a non-linearity parameter referred to planets.

$$NL_{HFC} = \frac{PLANETS_{lin}(ADU) - PLANETS_{q}(ADU)}{PLANETS_{lin}(ADU)} \tag{4.17}$$

In the next table typical results of the non-linearity parameters for HFI are presented.

BOLO	NL_{DIP} [%]	NL_{Mars} [%]	W_0 [$pWatt$]	p_{lin} [$attoWatt/ADU$]	p_{n-lin} [$attoWatt/ADU^2$]
100-3a	0.39	-	0.70	0.90	2.5e-7
143-3a	0.50	-	0.81	1.07	2.23e-7
217-6a	0.71	-	0.51	0.90	1.68e-7
353-5a	0.72	-	0.82	0.89	1.81e-7
545-2	-	0.30	0.90	2.71	9.93e-8
857-2	-	0.6	4.78	2.63	1.75e-8

Table 4.6: *Non-Linearity summarizing table*

4.6 Time Response

As I showed in section 3.2.1, bolometers have not an instantaneous response. The effect on the response is a filtering of the high frequencies coming from the optical signals adding with respect the filtering effect due to the beam. In the HFI, the filtering due to the effect of bolometer has to be added to the integration of the modulated signal over a half-period and the presence of a stray capacitance. This makes a complex time response.

We have shown that the response of all channels is very linear for all the sky excepted for the brightest planets. Therefore the time response is well described in the Fourier domain by a pseudo transfer function, defined as the ratio of the Fourier function of the output in ADU to that of the optical input in Watt.

The measurement of the time response is an essential results for HFI scientific goals. For example the propagation of the flight calibration from the dipole to the higher order moments of the spherical harmonics depends strongly on the accuracy of the measurement (expected to be better than 0.2%). In addiction the time response is one of the most difficult quantities to measure in flight so a good characterisation on the ground was a key point during PFM ground calibrations.

4.6.1 Measurements of the Transfer Function

Three different sequences has been performed to measure the time response of HFI during PFM ground calibration:

TauELS (LERMA in charge) intends to measure the time response from

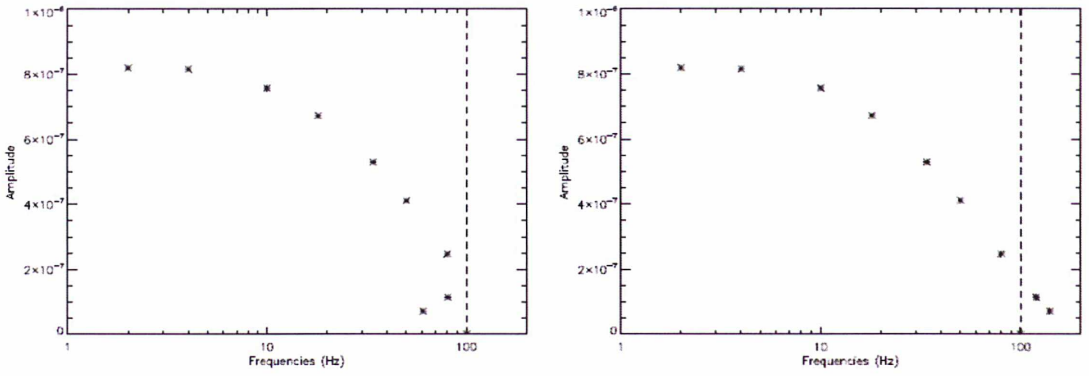

Figure 4.28: *Results of the analysis data from TauELS: the vertical dashed line is represents the modulation frequency of the measurement. Data with an mechanical frequency of the chopper faster than F_{mod} are aliased below F_{mod}. On the left results with aliasing. On the right results with a de-aliasing procedure trasposing the aliased results at frequencies above F_{mod}*[64]

2 to 100 Hz with the chopped external source (ELS). We performed these measurements with two different choppers: a 25%+25% blade chopper and a 10% blade chopper. This permits to insure a coverage in frequency down to the minimal frequency of the mechanical system.

FilterWheel (LERMA in charge) consists in using the response to large Heavyside-like steps produced by opening and closing the cryogenic filter wheel to explore low frequency responses.

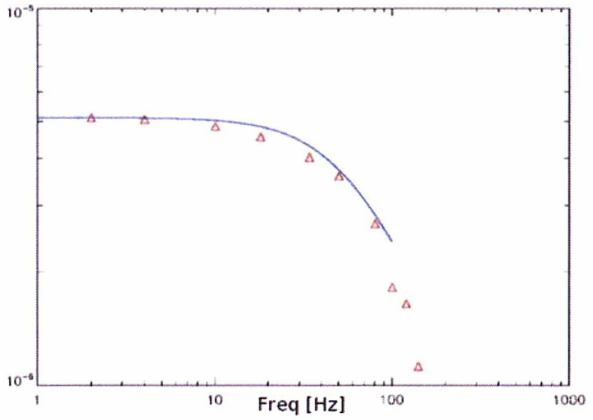

Figure 4.29: *Experimental data for a 353GHz bolometer. It cannot be properly fitted by a first order low pass filter expected from classical models.*

TauCSM (LAL) uses the CSM (carbon fibre source) to produce a nearly square modulation at about 1Hz.

Background conditions, readout frequencies, bolometer temperatures and bias currents have been explored in more than 50 runs of the sequences. The quasi-totality of the acquired data has been successfully reduced to recover the amplitude of the transfer function (see Fig 4.28).

The model of a DC biased bolometer is not able to fit properly results of the amplitude of the transfer function of HFI. It is necessary to develop a semi-empirical model to obtain a some better fit in the investigated range of frequency (see Fig 4.29).

The Semi-empirical model intends to fit experimental data with a transfer function of this form:

$$TF(f) = LP(f) \cdot H_{rej}(f) \cdot H_{res}(f) \tag{4.18}$$

Where $LP(f)$ is a first order low-pass filter due to the bolometer thermal time constant.

$H_{rej}(f)$ is a rejection filter (centred at modulation frequency) with a free parameter f_c related to the width of the filter itself. Such a rejection filtering centred on modulation frequency F_{mod} is expected due to the design of the filters in read out electronics.The filter has this form:

$$H_{rej} = \frac{1}{\sqrt{1 - \frac{f_c^2}{(f-f_{mod})^2}}} \tag{4.19}$$

$H_{res}(f)$ is a low-pass second order filter with a resonance centred on F_{mod}:

$$H_{res} = \frac{1}{\sqrt{1 + \frac{(f-f_{mod})^2}{(1+Q)f_{mod}^2}}} \tag{4.20}$$

Where Q represent a pseudo-quality parameter to fit with experimental data.

For a given set of environmental and REU parameters, the model has only 3 free parameters: time constant of the low-pass filter and the parameter coming from the rejection and resonant filters f_c and Q. Results of the fit are presented in Fig 4.30.

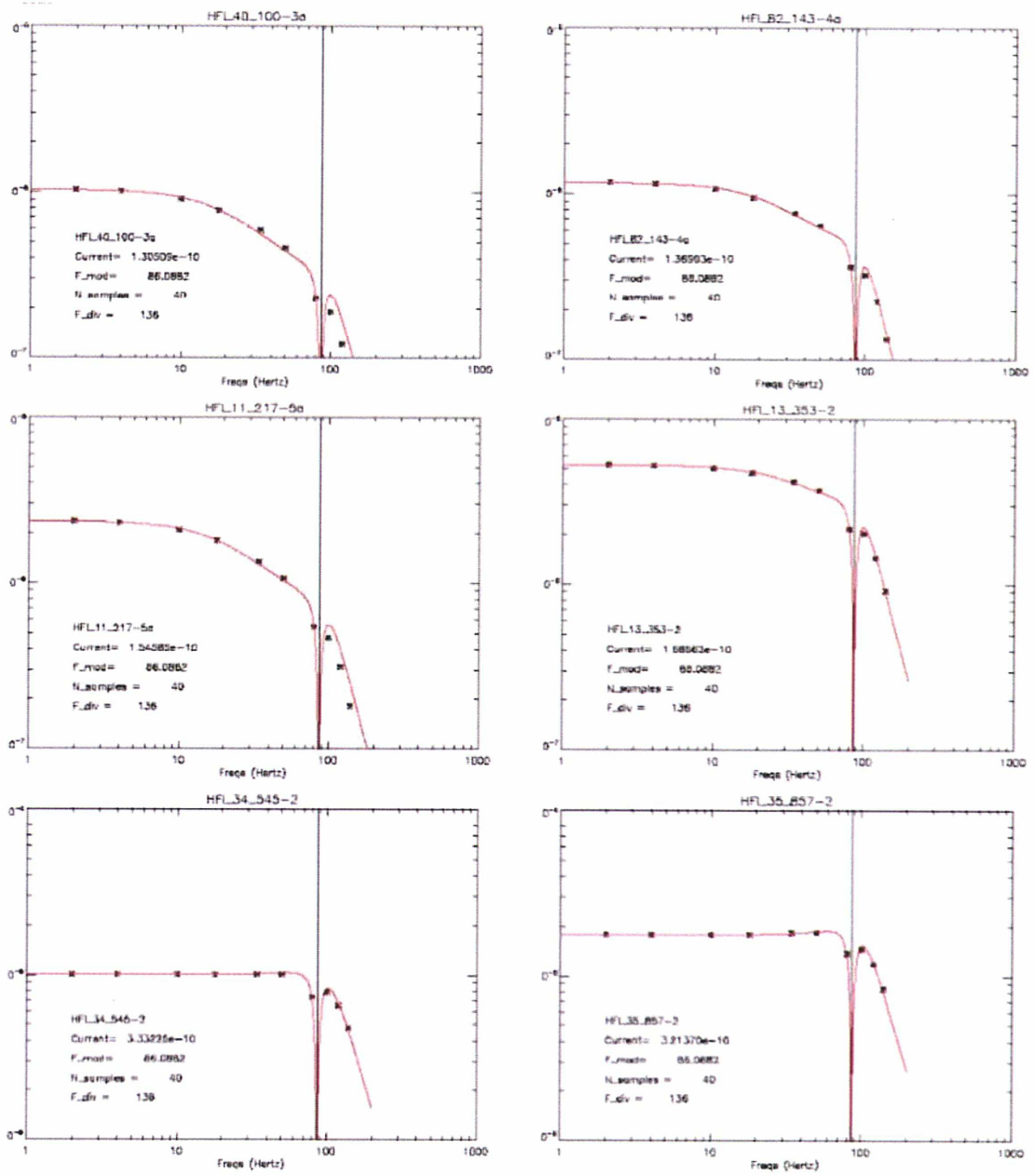

Figure 4.30: *The measures (points) and the semi-empirical model (red curves) for six different channels.*

4.6.2 Evidence of a low frequency excess response (LFER)

The preliminary data reduction from the TauCSM and TauELS tests clearly evidence a response enhancement at low frequencies for same bolometers

(Fig 4.31). This LFER concerns the range of frequencies less than a few Hz. Two bolometers (two PSB-b) show it at a high level on TauCSM. Some others show it clearly. For others it is small or not visible at first look. The measurements with the choppers also show an excess response at 1Hz and 2Hz on these bolometers (see Fig 4.31), which is consistent with the previous result.

Finally the *FilterWheel* data show that the signal takes more than one second to cover the last 2% and converge to its the asymptotic value (Fig 4.32).

The LFER is important because it change the response to the CMB dipole (a signal at 16mHz), which is the reference signal for in-flight calibration of the CMB channels.
During CSL calibration in Liege a sequence of time response measurements has been performed. The modulated source is a carbon fibre source inserted in a small central aperture in the cold load in front of the FPU. These measurements plus the use of semi-empirical models will give us a good knowledge of the transfer function in the whole frequency range of interest and in

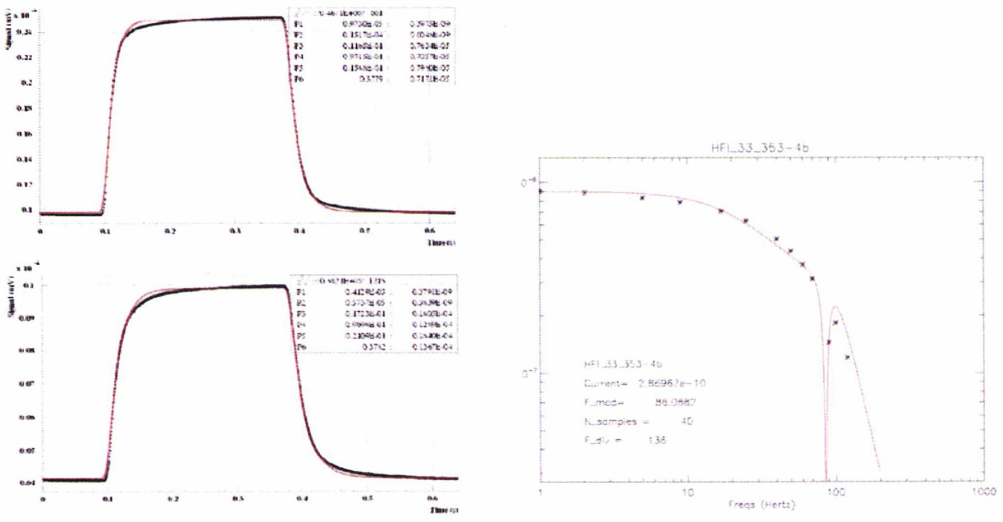

Figure 4.31: *On the left: response of bolometers 353-4b and 143-1b to the carbon fibre nearly square wave source (Black curves). The red curves represent the tentative to fit data with a first order model in the time domaine. On the right: Amplitude of the transfer function from Tau-ELS for the bolometer* $353-4b$*. The semi-empirical model does not fit with data because of an evidence of a low frequency excess response.*

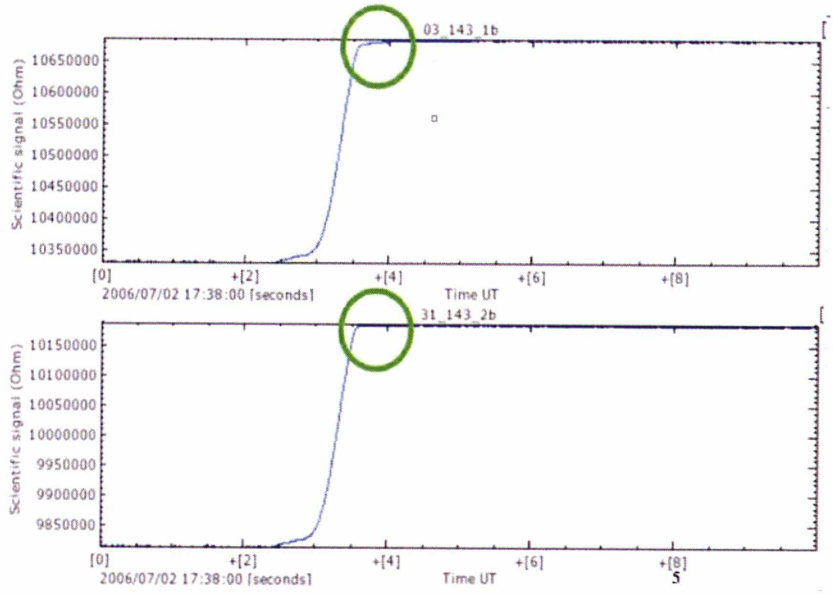

Figure 4.32: *Response to the closing of the filter wheel. The slow convergence towards the final value is the signature of an excess response at very low frequencies. LFER.*

different environmental conditions.

4.7 From Ground Calibrations to Calibration Performance Verification (CPV) Phase

CPV phase represents the final test and preparation activities before starting survey operations.

As showed in Fig 4.33, CPV phase will start about 50 days after launch after a first phase of *Commissioning* expected during the early days of the mission (from the launch to the 18th days) and during the cool-down of the instrument (from 18th to 50th day). Commissioning phase represents the complete checkout of spacecraft functions and the verification of all subsystem performances. In this period the instrument will be switched-on and all the functional checkout will be done in order to verify that the basic functions are available for the scientific operations.

The main goals of CPV phase are listed here:

- To check that performances of Planck payload are adequate to perform

the nominal mission.

• To obtain the in-orbit characterization of the instruments (LFI and HFI) in terms of all the tuning parameters.

• To characterise the instruments in the in-orbit conditions.

• To check the performance of spacecraft and payload subsystems which cannot be checked out during the commissioning phase.

Formally the calibration and performance verification (CPV) phase starts when the payload is at the nominal operational temperatures. Due to the complex cryogenic cooling system and the related operations, commissioning activities and calibration and test activities can be, and in several cases are, required to take place already in the cool-down period.

The timeline of the HFI tasks during CPV phase are listed in the next:

• Tuning: This stage involves the tuning and checkout of HFI subsystems and includes determination of the HFI thermal coupling parameters.

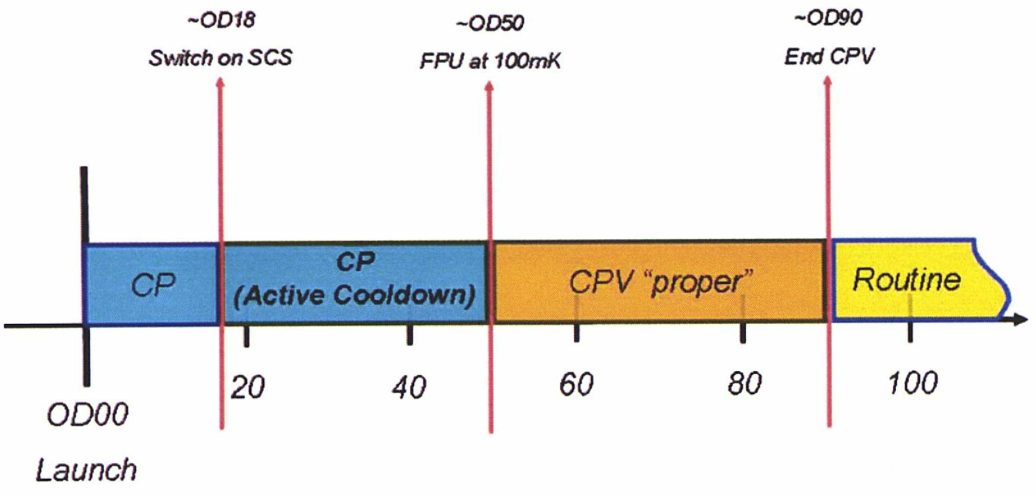

Figure 4.33: *Overview of the main periods before routine phase. The timeline is given in operational days (ODs) since launch. Both Commissioning and CPV activities take place during the active cooldown period. CPV proper starts around OD50.*

• Sensitivity: noise and compatibility tests are performed

• Final Tunings. The HFI will perform the final parameter adjustments assuming that the instrument sub-systems are sufficiently relaxed.

• HFI Optical Calibrations: This stage includes the activities which require the instruments to be operational for routine survey. The in flight optical calibration consists of all the activities not well ground-calibrated and all the optical health test.

In the next I will detail the activities related to CPV phase in which I am involved.

4.7.1 Checking for coupling parameters and Non-Linearities

In this test we measure the coupling parameters of cryogenics stages 4K and 1.6K. With the same data taken from this test we will be able to cover a small range of the static response curve of the HFI instrument. It allows us to reconstruct the whole static response function by merging data with the PFM ground calibrations. This is a good health test for HFI (2-level), indeed except for an evident problem in the instrument, expected results has to be a confirmation of PFM calibration. The test will be done with a strategy as close as possible to PFM tests.

The dipole will be the reference source during the sequences. Let's give a simplistic estimation of the signal to noise ratio not taking into account all the foregrounds in its estimation.

The dipole signal produces a sinusoidal fluctuation of the CMB of the order of 7 mK peak-peak. With a RMS estimation we can find a fluctuation of 3.5mK peak-peak.

The $NE\Delta T$ (Noise Equivalent Temperature Fluctuation) for a 100GHz HFI channel results from PFM calibration:

$$NE\Delta T \simeq 60\mu K \cdot s^{0.5} \tag{4.21}$$

The signal to noise ratio for an integration of 1 hour results:

$$\frac{S}{N} = \frac{Dipole}{NE\Delta T} \cdot \sqrt{t} = \frac{3.5 \cdot 10^{-3}}{60 \cdot 10^{-6}} \cdot \sqrt{3600} \sim 3500 \tag{4.22}$$

4K stage and checking non linearities

The test consists in measuring the optical coupling parameters for the 4K cryogenic stage with a check in parallel of the static function and its non-linearities. We want to perform a step in temperature of the stage of about

60mk (heating the 4K PID) and then come back to the original setup. After stabilisation in temperature we integrate the signal for about 2 hours in order to reach a good signal to noise ratio for the dipole. We repeat the sequence twice in order to reach a better signal to noise ratio and in order to have some redundancy in measures. The test duration is of the order of 10-12 hours.

The integration of the signal of about 2 hours means an over-integration for the coupling parameters recovering but is strictly sufficient for recovering data from non-linearities. The non-linearity test in fact, in accordance with PFM non-linearities calibration, consists in controlling the change in amplitude of a modulated source with a changing background. During CPV phase the candidate modulated source is dipole for CMB channels and Galaxy for high frequency channels. In this case the critical parameter is the signal to noise ratio for the dipole. From eq4.22 we obtain for a 100GHz channel, a signal to noise ratio of about 5000 for a 2 hours integrated dipole.

During the PFM ground calibrations we have estimated the non-linearities coefficients for low frequency bolometers in the case of dipole signal (see table 4.6). For a 100GHz PSB bolometer this coefficient is about 0.4%. This means that with 2 hours integrated dipole we can recover the non-linearities of 100GHz bolometers with a signal to noise ratio of about 20 which is a good trade-off.

1.6K stage

We perform a step in temperature of about 30mk (heating the 1.6K PID) and then come back to the original setup. we integrate signal after stabilisation of the cryogenic stage for 10m and repeat the sequence several times for redundancy. The test duration is estimated to be of the order of 8 hours.

Chapter 5

Elements for Measuring the HFI Beams with Planets

Introduction

A detailed and accurate beam knowledge is essential for science objectives of Planck because it determines the knowledge of the transfer function of the experiment in the domain of angular frequencies. The use of the planets for this goal is the most accurate way to measure the main beam.
Planets are point-like sources with a very good approximation when compared to FWHM of the HFI channels; furthermore, because their mm-wave brightness temperature is rather well known, observable planets are perfectly suitable for mapping the beam shape [20].
The differences of physical characteristics between giants planets and terrestrial planets (and asteroids), affect the variation of their brightness temperature versus frequency. While it is a good approximation to consider the temperature of Mars versus the frequency as a constant (in the HFI range) thanks to total or just about total absence of atmosphere, for Giants planets the situation is diametrically opposite; because of the absorption lines of the gas of which these planets are constituted, their brightness temperature measured in different bands, can strongly vary with frequency (up to 30%).
In the following section I will present the Signal to Noise Ratio for planets in all the HFI channels. In the section 5.6 a study on effect of under-sampling beams will be also presented.

Freq. [GHz]	100	143	217	353	545	857
MARS	206	206	206	206	206	206
JUPITER	173	176	179	178	133	145
SATURN	141	144	146	141	118	114
URANUS	120	120	120	120	120	120
NEPTUNE	117	117	117	117	117	117

Table 5.1: *Brightness Temperature of Planets and Ceres. [65], [66], [67], [68]*

5.1 Planets Suitability

We assume that the Planck mission will start to observe the sky on the 1-1-2009. It is possible compute the position of the planets with respect the Planck lines of sight (see table 5.2). The first problem is to establish how many times every planet is visible by the satellite; it is a fundamental information to know the suitability of a planet with respect the others. In the table 5.1 of brightness temperature of the plantes and the results of simulations are presented.

5.2 Simulated Beams

We are using beams computed with GRASP 9 at the central frequency with an ideal Planck telescope, i.e. a perfect implementation of the Planck design [69].

The horn field is generated using the scattering matrix (mode matching) approach. A corrugated horn is viewed as a succession of cylindrical waveguide segments with varying radii. Each junction has its own scattering matrix and the overall scattering matrix for the complete horn is calculated by cascading the matrices describing consecutive segments. This final matrix contains the reflection and transmission coefficients for the total system.

5.3 SNR on Planets

Planck will spin at $\sim 1rpm$ and every detector observes a *Circle* each turn. This is nearly a great circle, since the central point of the detector array

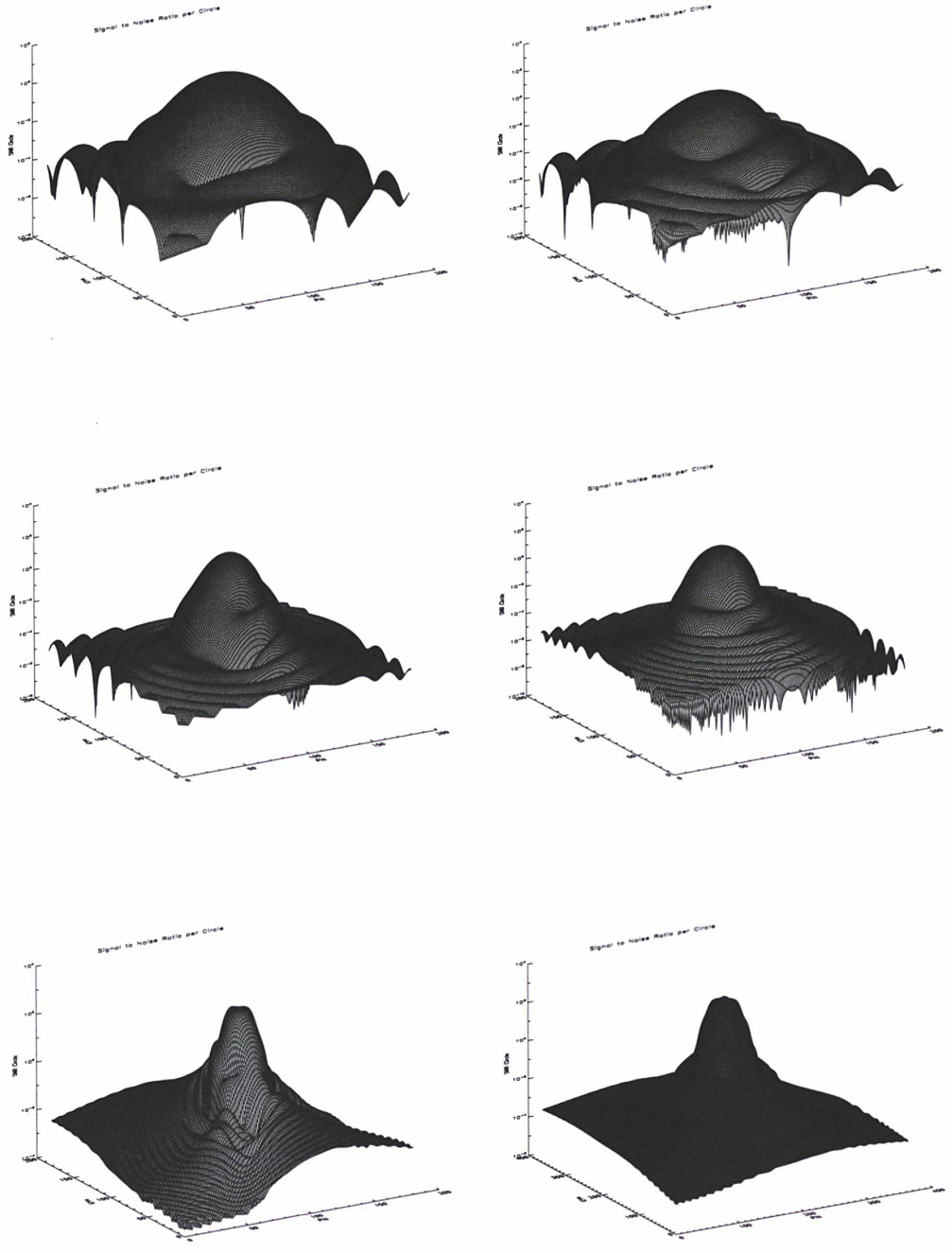

Figure 5.1: *SNR for a circle in case of Mars for a typical selection of HFI channels.*

Planet	Date	Angular diam [arcsec]	RA	Dec	Glon	Glat
Jupiter	10May09	39	327.6	-13.8	41.1	-45.8
Neptune	12May09	2.3	328.7	-13.1	42.7	-46.5
Saturn	11Jun09	18	167.2	7.8	-113.2	58.9
Uranus	12Jun09	3.5	357.0	-2.1	88.9	-60.7
Mars	20Oct09	7	124.9	20.8	202.7	28.3
Jupiter	16Nov09	39	321.5	-16.1	34.9	-41.4
Neptune	20Nov09	2.3	326.1	-14.1	39.9	-44.6
Uranus	19Dec09	3.5	353.6	-3.6	81.5	-60.1
Saturn	20Dec09	17	184.6	0.4	-74.9	62.2
Mars	13May10	7	140.2	17.4	212.8	40.6
Neptune	14May10	2.3	330.8	-12.4	45.0	-48.0
Uranus	16Jun10	3.5	0.6	-0.6	97.0	-60.9
Jupiter	17Jun10	40	1.8	-0.6	99.2	-61.4
Saturn	24Jun10	17	179.2	2.9	-87.6	62.5
Neptune	23Nov10	2.3	328.2	-13.4	42.1	-46.2
Jupiter	22Dec10	40	356.0	-3.1	86.1	-61.1
Uranus	23Dec10	3.5	357.2	-2.0	89.4	-60.7

Table 5.2: *Planets Suitability: a simple (non-cycloidal) scan is assumed.*

corresponds to a line of sight making an angle of 85 degrees with respect to the spin axis. We can defined also a *Ring* as the signal from circles of one bolometer 60 minutes of integration.

The Signal to Noise Ratio (SNR) related to planets on the HFI [70] channels per ring and per circle, is obtained using the following equations:

When a planet is at the main pointing position of the detector, the optical background coming from the planet on bolometer is equal to:

$$W_{Plan}(\vartheta,\varphi) = n_{modes}\lambda_0^2 PAR_{EFF}\frac{\Omega_{Plan}}{\Omega_{Beam}}\int_0^\infty \chi(\nu)BB_i(\nu,T_b)d\nu \qquad (5.1)$$

where n^i_{mode} correspond to the number of the modes of the horn for the i-th channel; chi_ν is the optical efficiency of the instrument and PAR_{EFF} (see table 4.3) is the normalisation factor associated to $\chi(\nu)$ for each channel measured from Calibration campaign. The factor $\frac{\Omega_{Plan}}{\Omega_{Beam}}$ is the *Dilution Factor* of the planet in the beam of HFI.

The SNR per circle for one sample is:

$$SNR_c = \frac{W_{plan}}{NEP_{tot} \cdot \sqrt{F_{mod}}} \tag{5.2}$$

where NEP_{tot} is the total noise equivalent power of the channel (from Table2.4) and F_{mod} is the modulation frequency of the REU, i.e. the effective band pass of the post-detection signal. For these simulations the F_{mod} has been set at 100Hz

Now, the SNR per ring results from integration in one hour of the SNR per ring as:

$$SNR_r = SNR_c \cdot \sqrt{60} \tag{5.3}$$

In the following are presented the nominal characteristic of the instrument and the evaluation of the SNR per circle and per ring for each planet visible from the satellite (except for Pluto), for each frequency.

BOLO	MARS	JUPITER	SATURN	URANUS	NEPTUNE
SNR 100-3a (per circle)	39.8	617.6	100.4	3.7	1.3
SNR 100-3a (per ring)	308.3	4783.7	777.8	28.7	10.6
SNR 143-3a (per circle)	121.3	1913.6	312.0	11.2	4.1
SNR 143-3a (per ring)	939.5	14823.2	2416.9	87.1	32.2
SNR 217-6a (per circle)	268.9	4311.1	699.0	24.7	9.1
SNR 217-6a (per ring)	2083.3	33393.5	5414.5	191.9	71.1
SNR 353-5a (per circle)	317.4	5045.2	789.5	28.9	10.6
SNR 353-5a (per ring)	2458.7	39080.0	6115.5	223.8	82.7
SNR 545-2 (per circle)	1752.6	20191.5	3537.8	156.7	57.9
SNR 545-2 (per ring)	13576	156403	27403.7	1214.4	448.6
SNR 857-2 (per circle)	2833.6	35324.3	5332.6	246.5	90.9
SNR 857-2 (per ring)	21948	273621	41306.4	1909.6	704.2

Table 5.3: *SNR per Ring and per Circle at the central point of the beam (in which the optical efficiency is assumed to be 0.3) for all the HFI channels.*

5.3.1 Discussion on SNR Results

Full beam reconstruction requires the observation of both a bright planet (Mars, Jupiter, Saturn) and of a fainter one (Uranus, Neptune) to check for non-linear model of the bolometers.

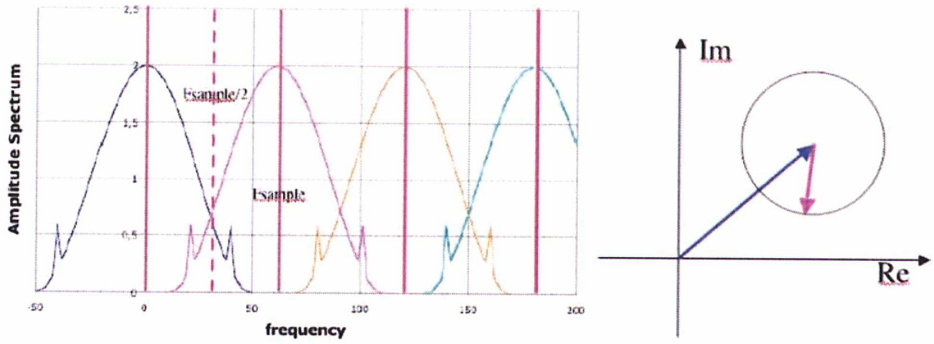

Figure 5.2: *Sampling in the time domain produces in the frequency domain the co-addition of the initial spectrum shifted by multiples of the sampling frequency fsample (right). This is often described as an aliasing of the initial spectrum about Fsample/2. The "aliased" part of the spectrum is added to the initial spectrum with a phase that depends on exact sampling times (right).*

The reconstruction of the far side lobes with the planets is not possible because for the all planets the SNR is less than 1 in this region of beams. Therefore, the reconstruction of the far side lobes has to perform with measurements using other sources (for instance with galactic centre) together with models.

5.4 Effect of Under-Sampling Beams

A de-pointing step of 2' is now considered in the Planck scanning strategy. The expected benefits are that maps reconstructed with a single detector should provide an acceptable sampling of the sky for all channels dedicated to CMB measurements. In this section I present in the Fourier domain the aliasing of the signal due to under-sampling.

This work is intended to estimate the errors made when measuring sources with HFI with respect to the separation between scans [71].

We compute the Fourier transform of the beams and evaluate the maximum error by integrating the module of the part that is aliased by under-sampling.

The aliased spectrum cannot be removed from the initial spectrum because its phase steeply depends on the exact position of the sampling, which can be considered as random for random sources on the sky (Fig 5.2). The

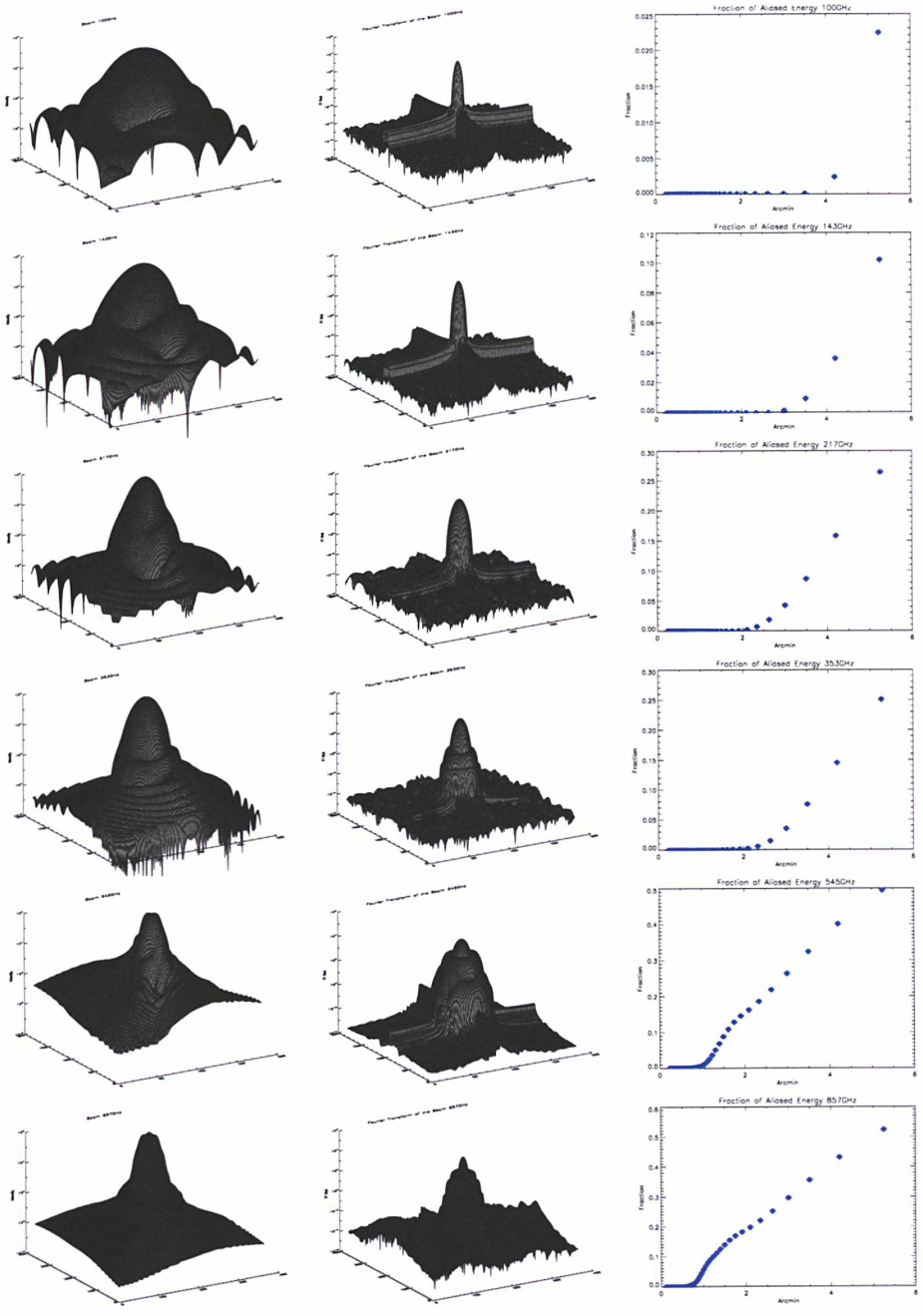

Figure 5.3: *Six HFI beams (one per frequency), their Fourier transform (module) and the aliased amplitude vs. the sampling interval (see next figure for details).*

integral of the module of the aliased spectrum tells what is the possible error

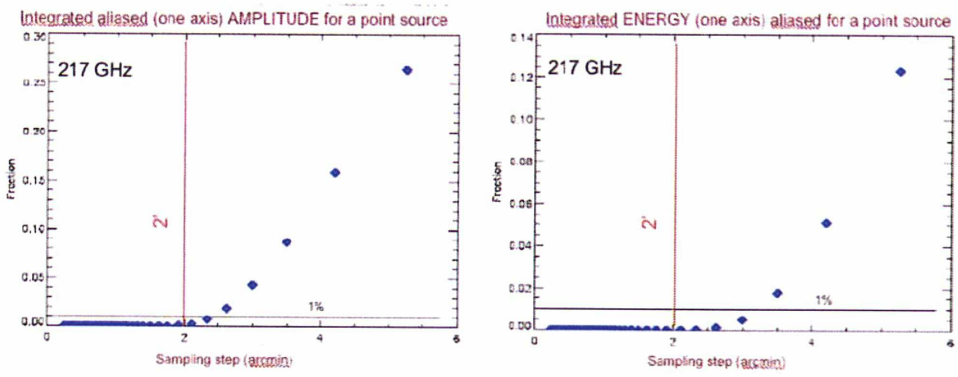

Figure 5.4: *Aliased amplitude (left) gives the maximum relative error produced by under-sampling while the integral of the square aliased spectrum provides an estimation of the second order statistics of the under-sampled map.*

produced by under-sampling. We have computed the module of the Fourier transform (Fig.5.3, middle) of the beam (Fig.5.3, left). Let us note here the effect of using a truncated beam that produces a low level cross-shaped feature in the Fourier domain. We have checked that this artefact has no impact on the results.

The integral along the cross scan direction of the aliased spectrum has been computed and renormalized by the integral of the whole spectrum. This quantity is the possible relative sampling error. The error increases as soon as the Nyquist criterion is not met. Applying the same procedure to the square of the module provides us with the error produced by under-sampling on the second order statistics of the maps (Fig.5.4, right), which is not essential here. This method has the advantage of requiring no assumption on the beam reconstruction process. It supposes that the module of the Fourier transform is a good estimator of the sampling error. Another prerequisite is that the source has a white spectrum, whether it is a point source or random source with white spectrum. If the source has a different spectrum (i.e. the interstellar medium) it has to be accounted for by weighting the FT by the source spectrum.

This process has been applied to six receivers of Planck-HFI, one per frequency. Fig.5.3 represents the beams, their Fourier transforms and the possible errors produced by aliasing. The 857GHz beam is the average of beams computed at three frequencies in the bandwidth of this channels, which somewhat compensates for the steep variation of the beam shape with

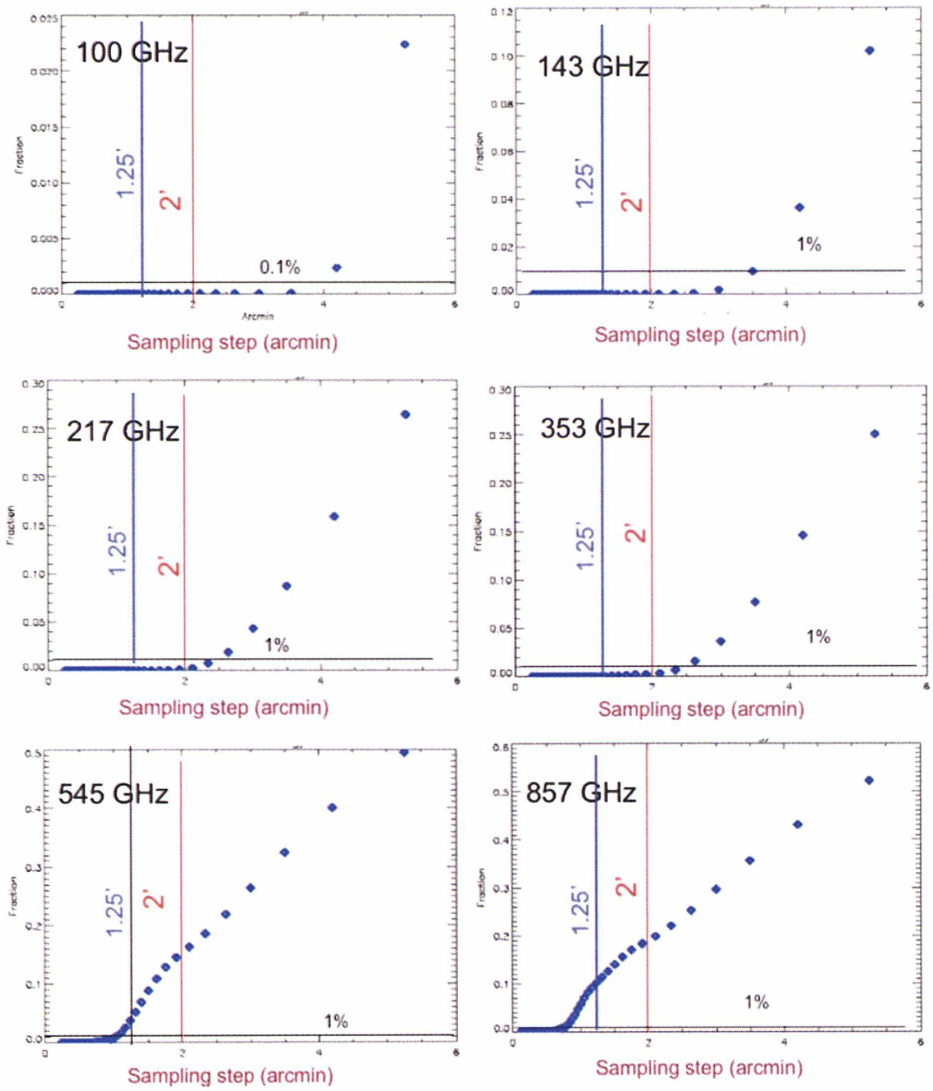

Figure 5.5: *Relative amplitude of aliased signal. The 2' and 1,25' sampling intervals represent the nominal pointing step and the staggering interval between horns at a same frequency.*

frequency. Other beams have been computed at the centre frequency only. All are the best available versions at the date of the edition of this thesis.

5.4.1 Consequences on Point Sources

The 2' sampling interval is good enough for the 100GHz and 143GHz channels. The aliasing error is less than 0.5% for the 217GHz and 353GHz beams,

which may be considered as acceptable for photometric calibration of any kind of source and for map reconstruction from individual bolometers. This would not the case with 2.5' intervals, that would make sampling errors larger than 1% RMS. The two multi-mode beams (545GHz and 857GHz) are strongly under-sampled at 2' and even 1.25' sampling intervals, which induces random errors up to 20%, and is probably not acceptable for most of the scientific applications. Fully solving this issue would imply using a scanning step of 0.8' or less. On the other hand the proper movement of mars (1.24 arcmin in one hour) will improve these results so that a greater scanning step can be used for high frequency channels too. Other methods, based on the accurate beam knowledge and/or on the use of the detailed features of the real scanning strategy can restore an acceptable accuracy to the measurement of point sources.

5.4.2 Consequences on Interstellar Medium

Measuring the interstellar medium is important both as a scientific object in itself and for component separation. Would it have a flat spectrum, the aliasing error made would have exceeded the acceptable error budget for component separation, even with the 1,25' sampling at 857GHz. We have taken an angular PSD with a power law of k-5/3 down to k = 1 per degree, and flat at lower angular frequencies. The estimated aliasing is less than 1% for 2' sampling steps and 0.2% to 0.3% for 1,25'.. This looks acceptable for ISM removal. Due to the rather simplistic estimate of this first approach both from the point of view of the method and of the representation of the ISM, we think that it would be profitable to revisit this aspect with realistic ISM templates and dedicated simulations in the image domain (instead of the Fourier domain).

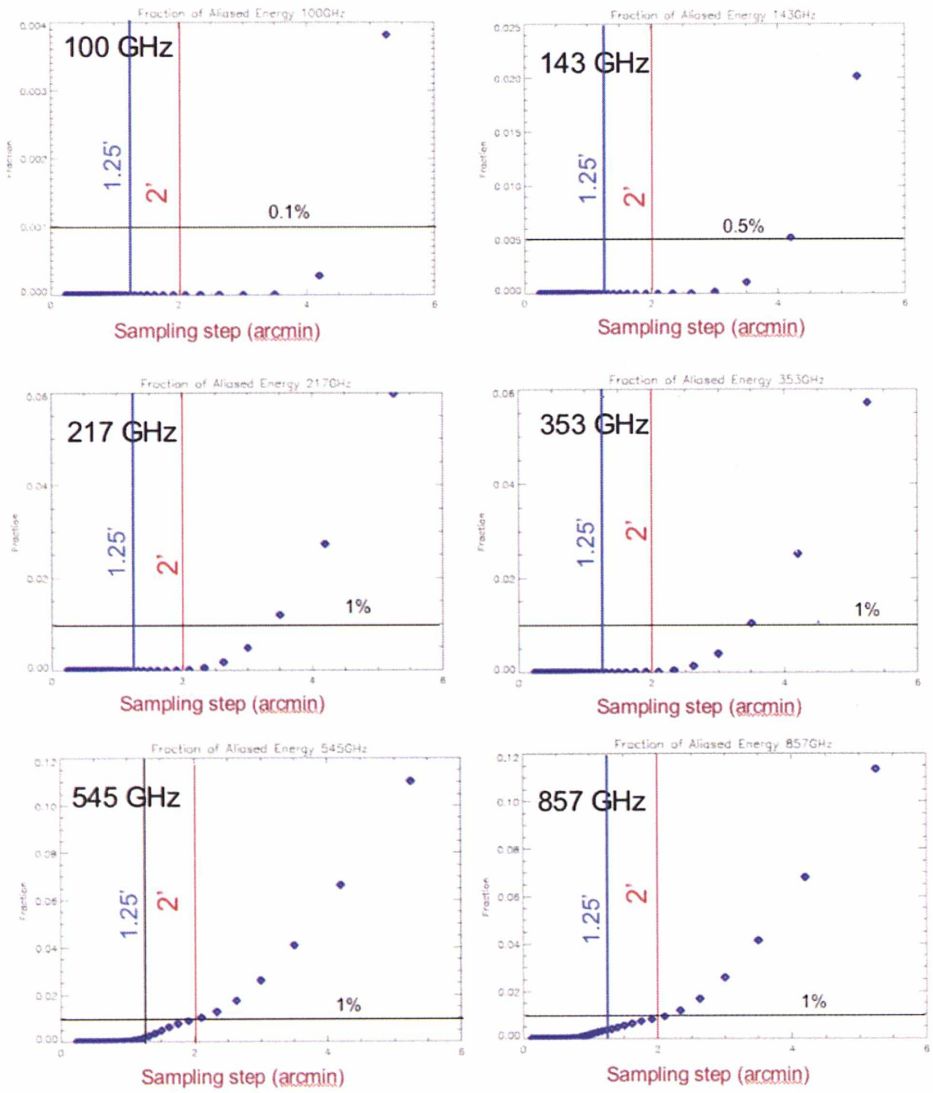

Figure 5.6: *Aliased amplitudes for a source with a spectrum inspired from that of the interstellar medium.*

Chapter 6

The impact of dust on the scaling properties of galaxy clusters

This chapter concerns the work I have done in the context of the evolution of clusters of galaxy. It is taken from the article accepted for publication arXiv0808.2313. My contribution in this work consists in analysing results of these digital simulations and in comparing the statistical properties (Lx-M, Y-M and S-M relations) of the cluster population for different models of structure formation (gravitation+radiative cooling and gravitation+ radiative cooling+ dust cooling models) (see section 6.4 and 6.5).

Introduction

From the first stages of star and galaxy formation, non-gravitational processes drive together with gravitation the formation and the evolution of structures. The complex physics they involve rule the baryonic component within clusters of galaxies, and in a more general context within the intergalactic medium (see the review [72]). The study of these processes is the key to our understanding of the formation and the evolution of large-scale structure of the Universe. Indeed, understanding how their heating and cooling abilities affect the thermodynamics of the IGM at large scales and high redshifts, and thus that of the intra-cluster medium (hereafter ICM) once the gas get accreted onto massive halos is a major question still to be answered. The continuous accretion and the merger events through which a halo assembled lead to a constant interaction of the IGM gas with the evolving galactic component. Within denser environments, like clusters, feedback provided by

AGN balances the gas cooling (see for instance [73, 74], and [75]). Also, from high redshift, the rate of supernovae drives the strength of the galactic winds and thus the amount of material that ends ejected within the IGM and the ICM ([76]). These ejecta are then mixed in the environment by the action of the surrounding gravitational potential and the dynamics of cluster galaxies within.

Since long, X-ray observations have shown the abundant presence of heavy elements within the ICM (see for instance review works [77, 78]). Physical processes like ram-pressure stripping, AGN interaction with the ICM, galaxy-galaxy interaction or mergers are scrutinized within analytical models and numerical simulations in order to explain the presence of metals (see for instance works by [79, 79, 80]). Moreover, it is obvious that the process of tearing of material from galaxies leads not only to the enrichment of the ICM/IGM in metal, but in gas, stars and dust as well. Recent work on numerical simulations [81, 82, 74] have stressed the role of hierarchical buiding of structures in enriching the ICM with stars in a consistent way with the observed amount of ICM globular clusters, and ICM light. Indeed, the overall light coming from stars in between cluster galaxies represent an important fraction of the total cluster light: for instance it has been measured [83] 6 to 22% from a sample of 10 clusters. The effect of a diffuse dust component within the IGM/ICM, and its effect is less known. A few observational studies with the ISO and the Spitzer satellites have tried without frank success to detect the signature of such a component [84, 85, 86, 87]. More successfully, [88] have obtained a statistical detection, via a stacking analysis, of the overall infrared emission coming from clusters of galaxies. However, they were not able to disentangle the IR signal from dusty cluster galaxies from a possible ICM dust component. On the other hand, from a theoretical point of view a few works have looked at the effect of dust on the ICM [89] or in conjunction with the enrichment of the ICM in metals [90]. However, the effect of dust on a ICM/IGM-type thermalized plasma has been formalized by Montier and Giard [91]. These authors have computed the cooling function of dust taking into account the energetic budget for dust. They have shown the ability of dust to be a non negligible cooling/heating vector depending on the physical properties of the environment.

Dust thus comes, within the ICM/IGM, as an added source of non-gravitational physics that can potentially influence the formation and the evolution of large scale structure in a significant way. Indeed, since redshift of $z \simeq 2-5$ during which the star formation activity reached its maximum in the cosmic history, large amounts of dust has been produced and thus ejected out of the galaxies due to violent galactic winds into the IGM [92]. As this material is then accreted by the forming halos, one can wonder about

the impact produced by dust on the overall properties of clusters of galaxies once assembled and thermalized. In a hierarchical Universe, the population of clusters is self-similar, thus is expected to present well defined structural and scaling properties. However, to date, it is common knowledge that the observed properties deviate form the prediction by a purely gravitational model (see [72, 78] for review works). It is thus important to address the issue of the impact of dust on the statistical properties of structures such as clusters of galaxies, the same way it is done for AGNs, supernovae, stripping or mergers.

In order to tackle this question, we have put into place the first N-body numerical simulations of hierarchical structure formation implementing the cooling effect of dust according to the dust nature and abundance. In this chapter, we present the first results of this work focusing at the scale of galaxy clusters, and more specifically on their scaling properties. The paper is organized as follows: we start by presenting the physical dust model and how it is implemented in the numerical simulation code. In Sec. 6.2, we describe the numerical simulations and the various runs (i.e. model) that have been tested. From these simulations our analysis concerns the galaxy cluster scale, and focus on the impact of the presence of dust on the scaling relation of clusters. In Sec. 6.3, we present our results on the $M-T$, the $S-T$, the $Y-T$ and the L_X-T relations. The derived results are presented in Sec. 6.4 and discussed in Sec.6.5.

6.1 The dust model

In our numerical simulations the implementation of the physical effect of dust grains is based on the computation by Montier and Giard [91] of the dust heating/cooling function. We decided to limit our implementation to the dust cooling effect only. Indeed the goal of this paper is to study the effect of dust at the galaxy cluster scales. The heating by dust grains is mainly effective at low temperatures (i.e $T_e < 10^5$ K) and is a localised effect strongly dependent of the UV radiation field. Our numerical simulations (see Sec. 6.2 and 6.5.2) do not directly implement this level of physics.

Dust grains in a thermal plasma with $10^6 < T < 10^9$ K are destroyed by thermal sputtering, which efficiency was quantified by [93]. The sputtering time depends on the column density and on the grain size. For grain sizes ranging form 0.001μm to 0.5μm, and an optically thin plasma ($n \sim 10^{-3}$ atom/cm^2), the dust lifetime spawns from 10^6 yr for small grains up to 10^9 yr for big grains. This lifetimes are therefore large enough for the cooling by dust in the IGM/ICM to be considered. Evidently, it is also

strongly linked to the injection rate of dust, thus to the physical mechanism that can bring and spread dust in the IGM/ICM.

Our implementation of the dust cooling power is based on the model by [91]. We recall bellow the main aspects of this model and describe the practical implementation within the N-body simulations.

6.1.1 The dust cooling function

Dust grains within a thermal gas such as the ICM or the IGM can either be a heating or a cooling vector depending on the physical state of the surrounding gas and on the radiative environment. Heating can occur via the photo-electric effect if the stellar radiation field (stars and/or QSOs) is strong enough ([93] and references therein). Indeed, the binding energies of electrons in dust grains are small, thus allowing electrons to be more easily photo-detached than in the case of a free atom or a molecule. On the other hand, the cooling by dust occurs through re-radiation in the IR of the collisional energy deposited on grains by impinging free electrons of the ICM/IGM [1].

Montier and Giard [91] have computed the balance of the heating and cooling by dust with respect to the dust abundance: cooling by dust dominates at high temperatures in the hot IGM of virialized structures (i.e clusters of galaxies), and heating by dust dominates in low temperature plasma under high radiation fluxes such as in the proximity of quasars. The details, of course, depend on the local physical parameters such as the grain size and the gas density.

Assuming local thermal equilibrium for the dust, the overall balance between heating and cooling in dust grains can be written as follows:

$$\Lambda^g(a, T_d) = H^g_{coll}(a, T_e, n_e), \tag{6.1}$$

with H_{coll} being the collisional heating function of the grain and Λ the cooling function due to thermal radiation of dust. a is the grain size, T_e and n_e are respectively the electronic temperature and density of the medium and T_d is the dust grain temperature.

The heating of the dust grain was taken from [94] and can be expressed in a general way as:

$$H^g_{coll}(a, T_e, n_e) \propto n_e\, a^\alpha\, T_e^\beta \tag{6.2}$$

where the values of α and β are dependent of the value of the ratio $a^{2/3}/T_e$.

The relevant dust parameters affecting the cooling function are the grain size and the metallicity. Indeed, the smaller the grains and the higher the

[1] In the galactic medium the cooling occurs through re-radiation of the power absorbed in the UV and visible range.

metallicity, the higher is the cooling power of the dust. Thus the total cooling function due to a population of dust grains can be expressed as a function of these two parameters as:

$$\Lambda(a, T_d) = \int\int\int \Lambda^g(a, T_d) \frac{\mathrm{d}N(a, Z, V)}{\mathrm{d}V\mathrm{d}a\mathrm{d}Z} \mathrm{d}V\mathrm{d}a\mathrm{d}Z \tag{6.3}$$

where $\mathrm{d}N(a, Z, V)/\mathrm{d}V\mathrm{d}a\mathrm{d}Z$ is the differential number of dust grains per size, metallicity and volume element.

Cooling by dust happens to increase with the square root of the gas density, whereas the heating by dust is proportional to the density. As stressed by Montier and Giard [91] the cooling by dust is more efficient within the temperature range of $10^6 < T < 10^8$ K (i.e $0.1 < kT < 10$ keV), which is typically the IGM and ICM thermal conditions.

6.1.2 The dust abundance

The abundance of dust is a key ingredient to properly weight in our implementation. Observations indicate that dust represents only a tiny fraction of the baryonic matter: $M_{dust}/M_{gas} \approx 0.01$ in our Milky Way, and this is possibly lower by a factor 100 to 1000 in the ICM: $M_{dust}/M_{gas} = 10^{-5} - 10^{-4}$ [89, 90]. We defined the abundance of dust as the ratio of the dust mass with respect to the gas mass:

$$Z_d = \frac{M_{dust}}{M_{gas}} = f_d \frac{Z}{Z_\odot} Z_{d\odot} \tag{6.4}$$

where Z is the metallicity in units of solar metallicity, $Z_{d\odot} = 0.0075$ is the solar dust abundance, i.e the dust-to-gas mass ratio in the solar vincinity, and f_d is the abundance of dust in the ICM in units of solar dust abundance.

Dust enrichment occurs via the feedback of galaxy formation and evolution in the ICM through interaction, stripping, mergers, galactic winds and AGNs outburst. At all redshifts, it is linked to the star formation rate (SFR) which drives the production of dust in cluster galaxies. However, in our hydrodynamic simulations (see Sect. 6.2) the SFR is not physically modeled, but it is inferred by the cooling state of the gas particles within the simulations: gas particles below a given threshold of temperature and above a given threshold of density are considered as colisionless matter, forming stars and galaxies (see Sec. 6.2). In order to tackle this problem, we choose to directly link the dust abundance to the metal abundance using Eq. (6.4). Therefore, the dust distribution in our simulations mimics the metal distribution.

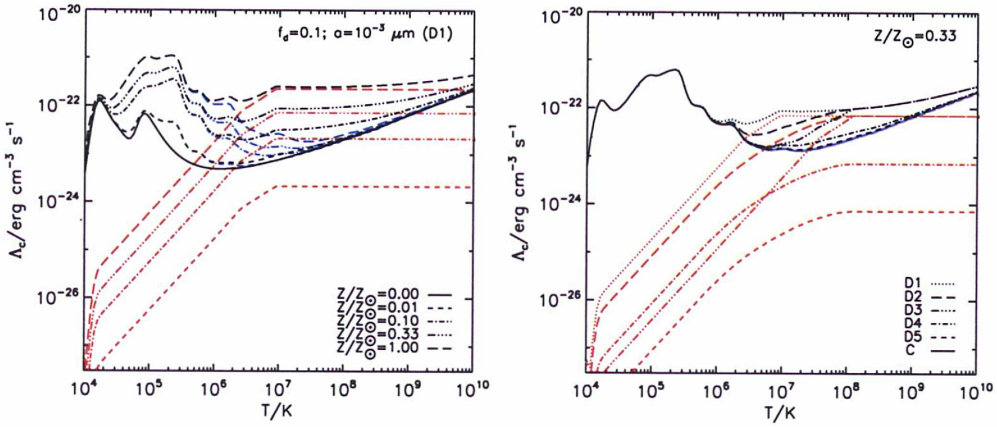

Figure 6.1: Cooling functions implemented in the numerical simulations. Panel on the left shows the dependence of dust model D1 ($f_d = 0.1$ and $a = 10^{-3}$ μm) with metallicity (and temperature) whereas the panel on the right shows different dust models at the same metallicity $Z/Z_\odot = 0.33$ (see text). Black, blue and red curves are the total cooling functions, radiative cooling of the gas from [95] and dust cooling functions, respectively.

6.1.3 Implementation in the N-body simulations

From the equations presented in the previous sections, we computed the dust cooling function according to the embedding medium temperature and (global) metallicity. In simulations, once the metallicity and temperature are known, a and f_d are the only two parameters driving the dust cooling rate (i.e $\Lambda(a, Z) = \Lambda(a, f_d)$). In the top panel of Fig. 6.1 we present dust cooling rates (red lines) for $f_d = 0.1$ and $a = 10^{-3}$ μm (model D1, see below) at different values of metallicity. The blue and black lines are the radiative cooling rates from [95] and the total (i.e radiative plus dust cooling) rate, respectively.

Together with an adiabatic run (i.e model A) and a "standard" radiative run (model C – see Sect. 6.2 for further details), we ran a total of five runs implementing various population of grains (i.e named D1 to D5) characterized by their sized and dust-to-metal mass ratio:

- We tested three types of sizes: two fixed grain sizes with $a = 10^{-3}$ μm and $a = 0.5$ μm), respectively labeled *small* and *big*. The third assumes for the IGM dust grains a distribution in sizes as defined by Mathis [96] for the galactic dust: $N(a) \propto a^{-3.5}$ within the size interval of $[0.001, 0.5]$ μm. It is hereafter referred as the 'MRN' distribution.

- We investigate three values of f_d: 0.001, 0.01 and 0.1. The two ex-

treme values roughly bracket the current theoretical and observational constraints on dust abundance in the ICM/IGM (i.e $10.^{-5}$ and 10^{-3} in terms of dust-to-gas mass ratio) [89, 97].

Tab. 6.1 lists code names and simulation details of all runs used in this work. In case of models D1 to D5, simulation cooling rates are given by the added effect of cooling due to dust and radiative gas cooling. Total cooling functions are displayed (non-coloured lines) in the bottom panel of Fig 6.1 for each of these models at $Z/Z_{\odot} = 0.33$. As the Figure indicates, the effect of dust cooling is stronger for models with higher dust-to-metal mass abundance parameters, f_d, and for smaller grain sizes (model D1). For low values of f_d the impact of dust cooling is significantly reduced. For example, in the case of model D5, the contribution of dust to the total cooling rate is negligible at $Z/Z_{\odot} = 0.33$ for all temperatures. Therefore we do not expect to obtain significant differences between simulations with these two models.

6.2 Numerical Simulations

6.2.1 Simulation description

Simulations were carried out with the public code package `Hydra`, [98], an adaptive particle-particle/particle-mesh (AP^3M), [99] gravity solver with a formulation of smoothed particle hydrodynamics (SPH), see [100], that conserves both entropy and energy. In simulations with cooling gas particles are allowed to cool using the method described in [101] and the cooling rates presented in previous section. At a given time step, gas particles with overdensities (relative to the critical density) larger than 10^4, and temperatures below 1.2×10^4K are converted into collisionless baryonic matter and no longer participate in the gas dynamical processes. The gas metallicity is assumed to be a global quantity that evolves with time as $Z = 0.3(t/t_0)Z_{\odot}$, where $Z_{\odot}$ is the solar metallicity and t/t_0 is the age of the universe in units of the current time.

All simulations were generated from the same initial conditions snapshot, at $z = 49$. The initial density field was constructed, using $N = 4,096,000$ particles of baryonic and dark matter, perturbed from a regular grid of fixed comoving size $L = 100\,h^{-1}$Mpc. We assumed a Λ-CDM cosmology with parameters, $\Omega = 0.3$, $\Omega_{\Lambda} = 0.7$, $\Omega_b = 0.0486$, $\sigma_8 = 0.9$, $h = 0.7$. The amplitude of the matter power spectrum was normalized using $\sigma_8 = 0.9$. The matter power spectrum transfer function was computed using the BBKS formula [102], with a shape parameter Γ given by the formula in [103]. With this choice of parameters, the dark matter and baryon particle masses are

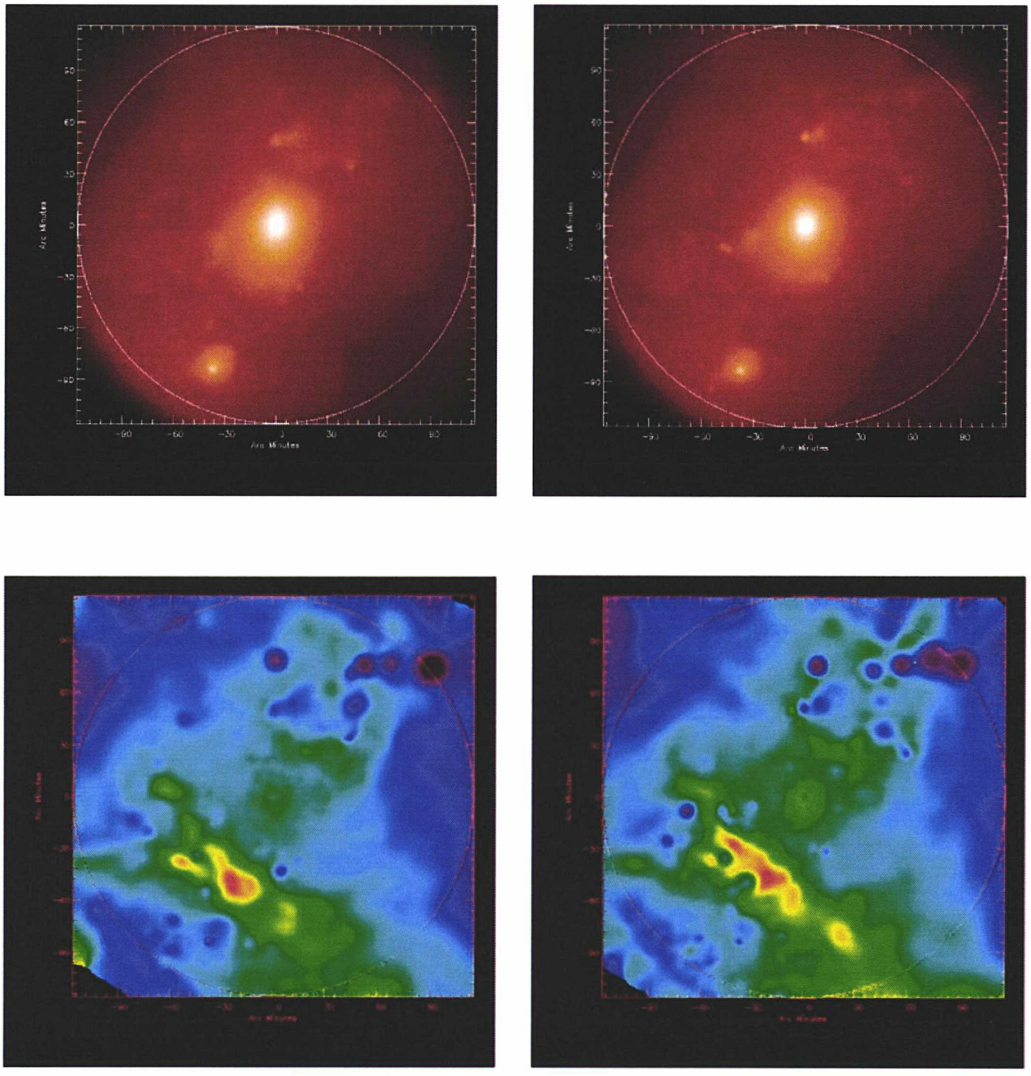

Figure 6.2: Density maps (on top) of the same cluster in the cooling (on the left) and cooling+dust (on the right) simulations. Emission weighted temperature maps (in the bottom) of the same cluster in the cooling (on the left) and cooling+dust (on the right) simulations.

Run	Physics	f_d	Grain size	$N_{\rm steps}$
A	adiabatic (no dust)	-	-	2569
C	cooling (no dust)	-	-	2633
D1	cooling with dust	0.100	small	2944
D2	cooling with dust	0.100	MRN	2920
D3	cooling with dust	0.100	big	2886
D4	cooling with dust	0.010	MRN	2698
D5	cooling with dust	0.001	MRN	2633

Table 6.1: Simulation parameters: f_d, dust-to-metal mass ratios (see Eq. 6.4), grain sizes, and number of timesteps taken by simulation runs to evolve from z=49 to z=0. Cosmological and simulation parameters were set the same in all simulation, as follows: $\Omega = 0.3$, $\Omega_\Lambda = 0.7$, $\Omega_b = 0.0486$, $\sigma_8 = 0.9$, $h = 0.7$, boxsize $L = 100\,h^{-1}$Mpc, and number of baryonic and dark mater particles, $N = 4,096,000$.

$2.1 \times 10^{10}\,h^{-1}\mathrm{M}_\odot$ and $2.6 \times 10^{9}\,h^{-1}\mathrm{M}_\odot$ respectively. The gravitational softening in physical coordinates was $25\,h^{-1}$kpc below $z = 1$ and above this redshift scaled as $50(1+z)^{-1}\,h^{-1}$kpc.

We generate a total of 7 simulation runs, listed in Table 6.1. The first two runs, which will be referred hereafter as 'adiabatic' (or model 'A') and 'cooling' (or model 'C') simulations, do not include dust. Simulations 3 to 7 differ only on the dust model parameters assumed in each case, and will be referred to as 'dust' runs, and are labeled as 'D1' to 'D5' models (see Sec. 6.1.3 for details on the dust models definition). This will allow us to investigate the effects of the dust model parameters on our results. The last column in the table gives the total number of timesteps required by each simulation to arrive to redshift zero. For each run we stored a total of 78 snapshots in the redshift range $0 < z < 23.4$. Individual snapshots were dump at redshift intervals that correspond to the light travel time through the simulation box, ie simulation outputs stack in redshift.

6.2.2 Catalogue construction

Cluster catalogues are generated from simulations using a modified version of the Sussex extraction software developed by Thomas and collaborators [104]. Briefly, the cluster identification process starts with the creation of a minimal-spanning tree of dark matter particles which is then split into clumps using a maximum linking length equal to $0.5\,\Delta_{\rm b}^{-1/3}$ times the mean

inter-particle separation. Here Δ_b the contrast predicted by the spherical collapse model of a virialized sphere [105]. A sphere is then grown around the densest dark matter particle in each clump until the enclosed mass verifies

$$M_\Delta(< R_\Delta) = \frac{4\pi}{3} R_\Delta^3 \, \Delta \, \rho_{\rm crit}(z). \tag{6.5}$$

where Δ is a fixed overdensity contrast, $\rho_{\rm crit}(z) = (3H_0^2/8\pi G)E^2(z)$ is the critical density and $E(z) = H(z)/H_0 = \sqrt{(\Omega(1+z)^3 + \Omega_\Lambda}$. Cluster properties are then computed in a sphere of radius R_{200}, ie with $\Delta = 200$, for all objects found with more than 500 particles of gas and dark matter. This means that our original catalogues are complete in mass down to $1.18 \times 10^{13} h^{-1} M_{sun}$. For the study presented in this paper we have trimmed our original catalogues to exclude galaxy groups with masses below $M_{\rm lim} = 5 \times 10^{13} h^{-1} M_{sun}$. In this way the less massive object considered in the analysis is resolved with a minimum of 2100 particles of both gas and dark mater. Our catalogues at z=0 have at least 60 clusters with masses above $M_{\rm lim}$. This number drops to about 20 clusters at z=1.

Cluster properties investigated here are the mass, M, mass-weighted temperature, $T_{\rm mw}$ and entropy, S (defined as $S = k_{\rm B} T / n^{-2/3}$), integrated Compton parameter, Y (i.e roughly the SZ signal times the square of the angular diameter distance to the cluster), and core excised (50 h^{-1}kpc) X-ray bolometric luminosity, $L_{\rm X}$. These were computed in the catalogues according to their usual definitions, see [106]:

$$M = \sum_k m_k, \tag{6.6}$$

$$T_{\rm mw} = \frac{\sum_i m_i \, T_i}{\sum_i m_i}, \tag{6.7}$$

$$S = \frac{\sum_i m_i \, k_{\rm B} T_i \, n_i^{2/3}}{\sum_i m_i}, \tag{6.8}$$

$$Y = \frac{k_{\rm B} \sigma_{\rm T}}{m_{\rm e} c^2} \frac{(1+X)}{2 m_{\rm H}} \sum_i m_i \, T_i, \tag{6.9}$$

$$L_{\rm X} = \sum_i \frac{m_i \, \rho_i \, \Lambda_{\rm bol}(T_i, Z)}{(\mu m_{\rm H})^2}, \tag{6.10}$$

where summations with the index i are over hot ($T_i > 10^5$K) gas particles and the summation with the index k is over all (baryon and dark matter) particles within R_{200}. Hot gas is assumed fully ionised. The quantities m_i, T_i, n_i and ρ_i are the mass, temperature, number density and mass density

of gas particles, respectively. $\Lambda_{\rm bol}$ is the bolometric cooling function in [107] and Z is the gas metallicity. Other quantities are the Boltzmann constant, $k_{\rm B}$, the Thomson cross-section, $\sigma_{\rm T}$, the electron mass at rest, $m_{\rm e}$, the speed of light c, the Hydrogen mass fraction, $X = 0.76$, the gas mean molecular weight, μ, and the Hydrogen atom mass, $m_{\rm H}$.

6.3 Scaling Relations

In this paper we investigate the scalings of mass-weighted temperature, $T_{\rm mw}$, entropy, S, integrated Compton parameter, Y and core excised X-ray bolometric luminosity, $L_{\rm X}$, with mass, M. Taking into account Eq. (6.5) these cluster scaling relations can be expressed as:

$$T_{\rm mw} = A_{\rm TM}\,(M/M_0)^{\alpha_{\rm TM}}\,(1+z)^{\beta_{\rm TM}}\,E(z)^{2/3}\,, \tag{6.11}$$

$$S = A_{\rm SM}\,(M/M_0)^{\alpha_{\rm YT}}\,(1+z)^{\beta_{\rm YT}}\,E(z)^{-2/3}\,, \tag{6.12}$$

$$Y = A_{\rm YT}\,(M/M_0)^{\alpha_{\rm YM}}\,(1+z)^{\beta_{\rm YM}}\,E(z)^{2/5}\,, \tag{6.13}$$

$$L_{\rm X} = A_{\rm LM}\,(M/M_0)^{\alpha_{\rm LM}}\,(1+z)^{\beta_{\rm LM}}\,E(z)^{7/3}\,, \tag{6.14}$$

where $M_0 = 10^{14}h^{-1}{\rm M}_\odot$ and the powers of the $E(z)$ give the predicted evolution, extrapolated from the self-similar model, [108], of the scalings in each case. The quantities, A, α, and β, are the scalings normalisation at $z = 0$; the power on the independent variable; and the departures from the expected self similar evolution with redshift.

These scalings can be expressed in a condensate form,

$$y\,f(z) = y_0(z)\,(x/x_0)^{\alpha}\,, \tag{6.15}$$

where y and x are cluster properties (e.g. $T_{\rm mw}$, M),

$$y_0(z) = A\,(1+z)^{\beta}\,, \tag{6.16}$$

and $f(z)$ is some fixed power of the cosmological factor $E(z)$. To determine A, α, and β for each scaling we use the method described in [106, 109]. To summarize, the method involves fitting the simulated cluster populations at each redshift with Eqs. (6.15) and (6.16) written in logarithmic form. First we fit the cluster distributions with a straight-line in logarithmic scale at all redshifts. If the logarithmic slope α remains approximately constant (i.e. shows no systematic variations) within the redshift range of interest, we then set α as the best fit value at $z = 0$. Next, we repeat the fitting procedure with α fixed to $\alpha(z = 0)$ to determine the scaling normalisation factors $y_0(z)$. This

avoids unwanted correlations between α and $y_0(z)$. The r.m.s. dispersion of the fit is also computed at each redshift according to the formula,

$$\sigma_{\log y'} = \sqrt{\frac{1}{N}\sum_i (\log(y'_i/y'))^2}\,, \tag{6.17}$$

where $y' = yf$ (see Eq. (6.15)) and y'_i are individual data points. Finally, we perform a linear fit of the normalisation factors with redshift in logarithmic scale, see Eq. (6.16), to determine the parameters A and β.

We note that above $z = 1.5$ the number of clusters in our catalogues decreases typically below 10, hence, we do not fit the scaling relations above this redshift value.

6.4 Results

6.4.1 Scaling relations at $z = 0$

In this section we present cluster scaling relations obtained from simulations at redshift zero. We investigate the four scalings presented in Section 6.3 for all models under investigation.

Figure 6.3 shows the $T_{\rm mw} - M$ (top left panel), $S_{\rm mw} - M$, (top right panel), $Y - M$ (bottom left panel), and $L_{\rm X} - M$ (bottom right panel) scalings, with all quantities computed within R_{200}. In each case, the main plot shows the cluster distributions for the C (triangles), D4 (diamonds), D2 (filled circles) and D1 (crosses) simulations, whereas the embedded plot presents the power law best fit lines (solid, triple dot-dashed, dashed and dot-dashed for C, D4, D2 and D1 models, respectively) obtained in each case, colour coded in the same way as the cluster distributions. Here we have chosen to display dust models that allow us to assess the effect of dust parameters individually. For example, the dust models in runs D4 and D2 only differ by the dust-to-metal mass ratio parameter, whereas models D2 and D1 have different grain sizes but the same f_d. The shaded gray areas in the embedded plots give the r.m.s. dispersion of the fit for cooling (C) model. The dispersions obtained for the other models have similar amplitudes to the C case. The scalings of entropy and X-ray luminosity with mass show larger dispersions because they are more sensitive to the gas physical properties (density and temperature) in the inner parts of clusters than the mass-weighted temperature and Y versus mass relations which are tightly correlated with mass.

An inspection of Fig. 6.3 allows us to conclude that the cluster scalings laws studied here are sensitive to the underlaying dust model, and in particular to models where the dust cooling is stronger (model D1 and D2).

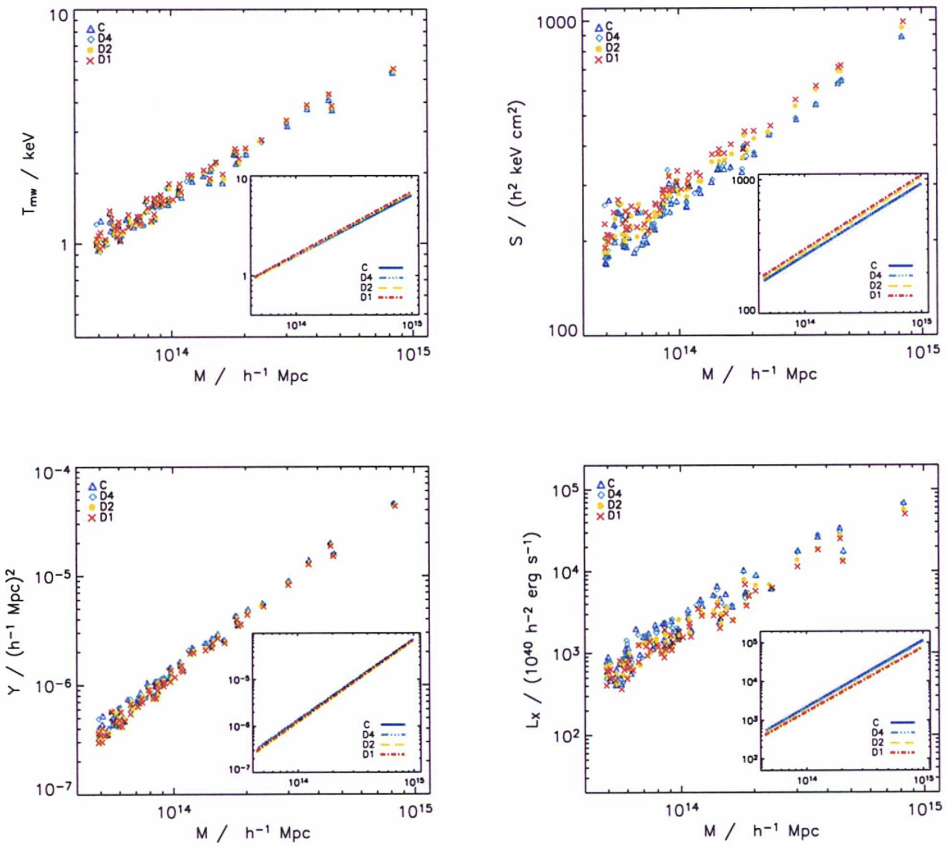

Figure 6.3: Cluster scalings at redshift zero for the $T_{\rm mw} - M$ (top left panel), $S - M$, (top right panel), $Y - M$ (bottom left panel), and $L_{\rm X} - M$ (bottom right panel). Displayed quantities are computed within R_{200}, the radius where the mean cluster density is 200 times larger than the critical density. Blue colour and triangles stand for the cooling (C) run, cyan and diamonds are for the D4 run, yellow and filled circles are for clusters in the D2 run, and red and crosses are for the D1 run. The lines in the embedded plots are the best-fit lines to the cluster distributions and the shaded areas are the fit r.m.s. dispersions for the C model, for each scaling.

The differences are more evident in the $S - M$ and $L_X - M$ scalings, but are also visible, to a lower extent, in the $T_{\rm mw} - M$ and $Y - M$ relations. Generally, the inclusion of dust tends to increase temperature and entropy because the additional cooling increases the formation of collisionless (star forming) material leaving the remaining particles in the gas phase with higher mean temperatures and entropies. The decrease of Y and X-ray luminosities reflects the effect of lowering the hot gas fraction and density due to dust cooling. These effects dominate over the effect of increasing the temperature.

In fact a closer inspection of Fig. 6.3 indicates that differences for the same cluster in different models (note that all simulations have the same initial conditions so a cluster-to-cluster comparison can be made), reflect the differences of intensity between cooling functions presented in Figure 6.1. For example, the differences between models D4 and C are clearly small as one would expect from the small differences between cooling functions displayed in the bottom panel of Figure 6.1. Another interesting example is that an increase of one order of magnitude in f_d from D4 to D2 seems to cause a stronger impact in the properties of the most massive clusters than the differences arising from changing the dust grain sizes from D2 to D1. Again this reflects the differences between cooling functions, which in the latter case are smaller at higher temperatures (see bottom panel of Figure 6.1).

A way of quantifying the effect of dust, is to look at the best fit slope, α, and normalisation, $\log A$, parameters of these scalings which are presented in Table 6.2 for all cooling models considered. We find that fitting parameters are quite similar for models C, D5, and D4 whereas models with high dust abundances provide the strongest variations of the fitting parameters, particularly for the normalisations. In several cases, differences are larger than the (statistical) best-fit errors, particularly for the D1 and D2 models. We also investigated scalings at redshift zero for the A (adiabatic) model and found they were consistent with self-similar predictions. As expected, the results obtained for the adiabatic and cooling models are in very good agreement with the findings of [106, 109] which use similar simulation parameters and cosmology.

6.4.2 Evolution of the scaling relations

We now turn to the discussion of the evolution of the cluster scaling laws in our simulations. Here we apply the fit to a power law procedure described in Section 6.3 to derive the logarithmic slope, β, of our fitting functions, Eqs. (6.11)-(6.14). As mentioned earlier, this quantity measures evolution departures relative to the self-similar expectations for each scaling.

In Figs. 6.4, 6.5, 6.6, and 6.7 we plot the redshift dependence of the power

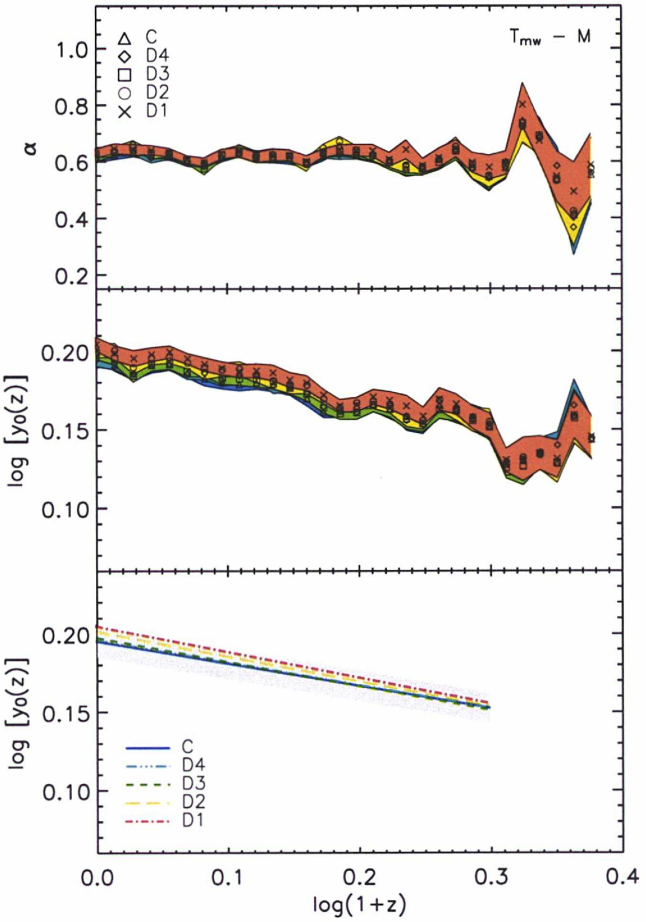

Figure 6.4: Evolution of the slope (top panel), normalisation (middle panel), and normalisation best fit lines (bottom panel) of the $T_{\rm mw} - M$ cluster scaling relation for the C (triangles, solid line), D4 (diamonds, triple-dot-dashed line), D3 (squares, short-dashed line), D2 (circles, dashed line) and D1 (crosses, dot-dashed line) simulation models. Colour bands are best fit errors to the cluster distributions at each redshift. The shaded area in the bottom panel is the rms dispersion of the normalisation fit for the cooling model.

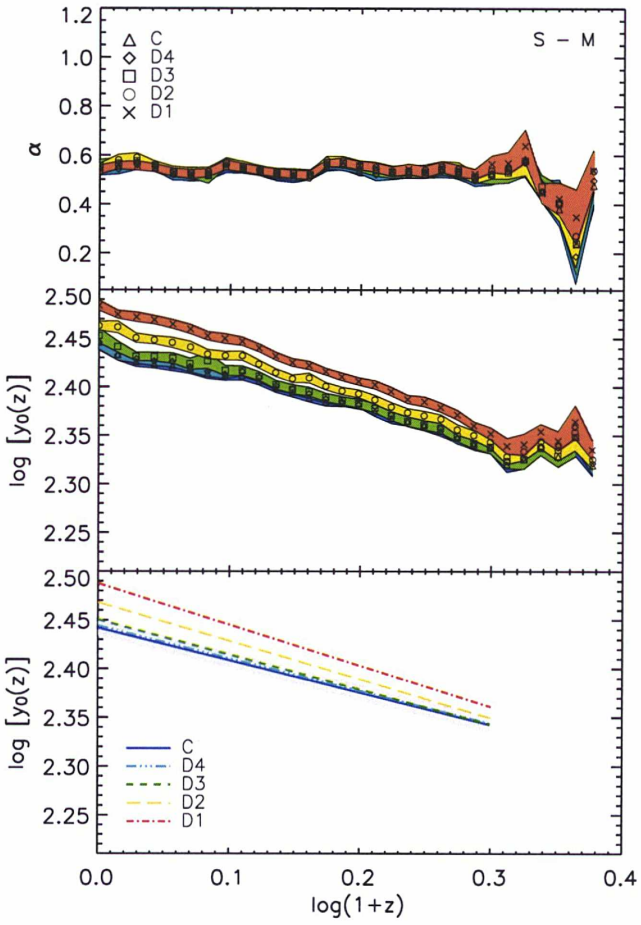

Figure 6.5: Evolution of the slope (top panel), normalisation (middle panel), and normalisation best fit lines (bottom panel) of the $S - M$ cluster scaling relation for the C, D4, D3, D2, D1 simulation models. Symbols, lines and colours are the same as in Fig 6.4.

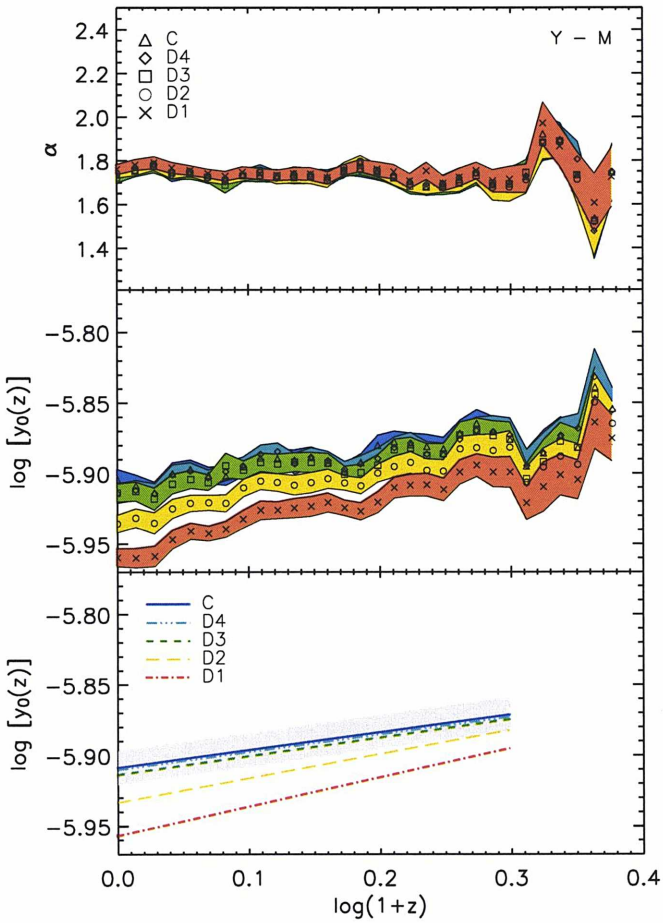

Figure 6.6: Evolution of the slope (top panel), normalisation (middle panel), and normalisation best fit lines (bottom panel) of the $Y - M$ cluster scaling relation for the C, D4, D3, D2, D1 simulation models. Symbols, lines and colours are the same as in Fig 6.4.

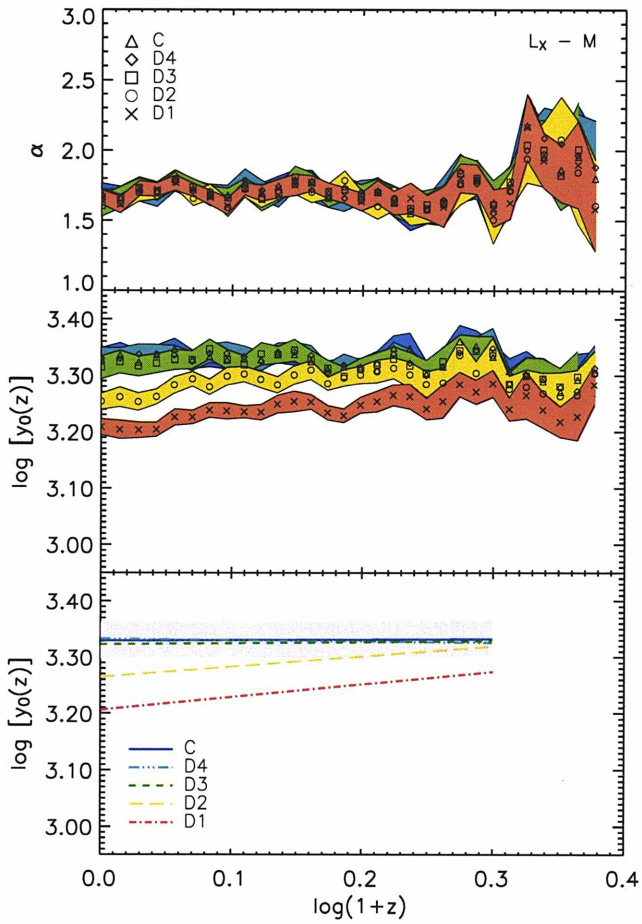

Figure 6.7: Evolution of the slope (top panel), normalisation (middle panel), and normalisation best fit lines (bottom panel) of the $L_X - M$ cluster scaling relation for the C, D4, D3, D2, D1 simulation models. Symbols, lines and colours are the same as in Fig 6.4.

law slopes, α, (top panels), and normalisations, $\log y_0$, (middle panels) for our $T_{\rm mw} - M$, $S - M$, $Y - M$, and $L_{\rm X} - M$ scalings, respectively. The bottom panels show straight lines best fits, up to z=1, to the data points in the middle panels of each Figure. The slopes of these lines are the β parameters in Eqs. (6.11)-(6.14). We decided not to include data points above z=1 in the computation of β because cluster numbers drop rapidly (below 20) which, in some cases, causes large oscillations in the computed normalizations. Moreover in the case of the $L_X - M$ relation, the evolution of $y_0(z)$ with redshift appears to deviate from a straight line above $z \simeq 1$. In Table 6.2 we provide a complete list of the $\log A$, β and α fitting parameters and associated statistical errors for all scalings and cooling models investigated. The displayed values are valid in the redshift range $0 < z < 1$. In the top and middle panels the coloured bands correspond to the $\pm 1\sigma$ envelope of the best fit errors obtained at each redshift for α, and $\log y_0$. The shaded area in the bottom panels are r.m.s. fit dispersions of the normalisations, $\log y_0$, computed for the cooling model using Eq. (6.17).

Results from different simulation runs are coded in the following way: triangles and solid lines stand for the cooling model, diamonds and triple-dot-dashed lines represent the D4 model, squares and short-dashed lines are for D3 model, circles and dashed lines for the D2 models and crosses and dot-dashed lines are for the D1 model. Here we have omitted the D5 model for clarity. It provides the same fitting results as the cooling model. This confirms expectations and the comments made in the last paragraph of Section 6.1.3.

The top panels of these Figures allow us to conclude that the α slopes of our scalings are fairly insensitive to dust cooling. These also show no evidence of systematic variations with redshift for all scalings, which is an important requirement when fitting the cluster distributions with power-laws of the form Eqs. (6.11)-(6.14). The redshift independence of the slopes with the dust model confirms our findings at redshift zero. The scatter (non-systematic "oscillations") at high redshift is caused by the decrease of the number of clusters with $M_{\rm lim} \geq 5 \times 10^{13} h^{-1} M_{sun}$, the sample selection used for all fits.

The main effect of cooling by dust is reflected in the changes it produces in the normalisations of the cluster scaling laws. Again, the the impact of dust is different depending on the scaling under consideration. For the $T_{\rm mw} - M$ scaling in Fig. 6.4 we see a sytematic variation with the dust model (ordered in the following way: C, D4, D3, D2, D1), but differences between models are within the errors and fit dispersions of each others. For the evolution of the normalisations of the $S - M$, $Y - M$, and $L_{\rm X} - M$ scalings (see Figs. 6.5, 6.6, and 6.7) we conclude that the inclusion of dust cooling causes significant

departures from the standard radiative cooling model depending on the dust model parameters. For example, this is clear from the non-overlapping errors and fit dispersions of the normalisations for the D2 and D1 models. For all scalings, the relative strength of the effect of dust follows the relative intensity of the cooling functions presented in Section 6.1.3. This orders the models in the following way: C, D4, D3, D2, D1 with increasing normalisations for the $T_{\rm mw} - M$ and $S - M$ scalings and decreasing normalisations for the $Y - M$ and $L_X - M$ relations.

We end this section by noting that we find positive evolution (relative to the expected self-similar evolution, i.e. for a given x in Eq (6.15) the property yf is higher at higher redshifts) for the $Y - M$ and $L_X - M$ (models D1 and D2 only) relations whereas the $T_{\rm mw} - M$, and $S - M$ relations show negative evolutions relative to the self-similar model. This is in line with the findings from simulations with radiative cooling of similar size and cosmology, (see [106, 109]).

6.5 discussion

6.5.1 Efficiency of the dust cooling

In agreement with the cooling functions of [91], the dust cooling is most effective in the cluster temperature regime. The relative importance of the dust cooling with respect to the gas radiative cooling is strongly dependent on the dust abundances and the intrinsic physical properties of the dust. This is clearly shown in our scaling relations results:

- the $T_{\rm mw} - M$ relation is almost unchanged when adding dust cooling to the radiative gas cooling (see Fig. 6.4). Our results show that the (mass weighted) temperature–mass relation within R_{200}, is essentially driven by the gravitational heating of the gas (due to its infall on the cluster potential well), and that the physics of baryons (at least for the physics implemented in the simulations presented in this paper) play very little role in the outer parts of halos which dominate the estimation of the mass-weighted temperature and integrated mass. Since gas cooling tends to disturb the dark matter distribution at the centre of clusters in high resolution simulations [110], the cooling by dust may amplify this effect, and thus modify scaling relations like the $T_{\rm mw} - M$. In the case of observationally derived quantities, scaling laws will be drawn from overall quantities that will proceed from mixed-projected information over a wide range of radii. If a gradient exist in the dust effect towards the cluster centre, an "overall" temperature might bear the signature of

the structural effect of dust. There is also no significant effect between the different dust models and the radiative case on the evolution of the slope and normalisation of the $T_{\rm mw} - M$ relation.

- On the other hand the other three scaling laws are deeply related to the clusters baryonic component. The clear effect on the $S - M$, $Y - M$, and $L_{\rm X} - M$ relations illustrates this fact (see Figs. 6.5, 6.6, and 6.7). We found that the slopes of these scalings remain fairly insensitive to dust, whereas normalisations show significant changes depending on the dust parameters. Relative changes in the normalisations at redshift zero and $M_0 = 10^{14} h^{-1} {\rm M}_\odot$ can be as high as 25% for $L_{\rm X} - M$ and 10% for the $S - M$, $Y - M$ relations for the D1 model. Models with lower dust abundances and MRN grain size distributions present smaller but systematic variations relative to the C model. As any other cooling process, the cooling due to dust tends to lower the normalisations of the $Y - M$, and $L_{\rm X} - M$ scalings due to the decrease of the hot gas fractions and densities which dominate the increase of temperature. The increase of normalisations for the $S - M$ and $T_{\rm mw} - M$ relations with added dust cooling is also in line with expectations because cooling converts cold, dense, gas into collisionless star forming material, which raises the mean temperature and entropy of the remaining gas.

- Our simulations allow us to quantify the relative impact of the dust parameters on the investigated cluster scalings (see Figs. 6.4 to 6.7 and Table 6.2). From one model to another one can identify two clear effects due to dust: (i) it shows the expected effect of the dust abundance, which from models D4 to D2 raise by a factor of 10, producing a change of normalisations relative to the purely radiative case (model C), from almost zero percent contribution to about 14%, 5% and 6% contributions for the $L_{\rm X} - M$, $Y - M$ and $S - M$ relations, respectively. (ii) Even more striking is the effect of the intrinsic dust grain physical properties. The variation of normalisations relative to the C model, change from a zero percent level for model D4 to about 25% ($L_{\rm X} - M$) and 10% ($Y - M$, and $S - M$) for the model D1 (ie the relative change from models D2 to D1 is about 13% and 5%, respectively). All these percentages were calculated using normalisations at redshift zero and $M_0 = 10^{14} h^{-1} {\rm M}_\odot$. Therefore the size of the grains comes to be an equally important parameter varying the efficiency of the dust cooling. The smaller the grain, the stronger the cooling.

- From Figs. 6.4, 6.5, 6.6, and 6.7 one finds that differences between normalisations become progressively important with decreasing red-

shift. This confirms expectations because metallicity was modelled in simulations as a linearly increasing function of time. Although our implementation of metallicity should only be regarded as a first order approximation to the modelling of more complex physical processes (acting on scales below the resolution scale of the present set simulations), it would be interesting to investigate whether a similar effect remains (ie the effects of dust become progressively important at low redshift) when such processes are taken into account throughout the formation history of galaxy clusters (see discussion below).

6.5.2 Limitation of the dust implementation

In order to implement the presence of dust in the numerical simulations, we chose a "zero order approach": we directly correlated the presence of dust with the presence of metals under the assumption that there is no segregation in the nature of the material withdrawn from galaxies and injected in the IGM/ICM (metals, gas, stars or dust). However, this assumption suffers from limitations linked to the dust lifetime. Indeed, dust grains strongly suffer of sputtering and within their lifetime they are depleted from metals which, contrary to dust grains, are not destroyed i.e. remain in the ICM/IGM. Therefore our whole analysis is to be considered within the framework of this assumption, and is to be understood as a basic implementation of the effects of dust with the objective of assessing whether dust has a significant impact on large scale structure formation, and consequently to quantify these effects at first order.

Moreover, our implementation is also *ad hoc*. Indeed, beside the cooling function of dust, our implementation is not a physical implementation. We did not deal *stricto senso* with the physics of the dust creation and dust destruction processes. However, making use of the cooling function by Montier and Giard [91], we have performed a fully self-consistent implementation of the effect of dust as a cooling vector of the ICM/IGM. Indeed, on the basis of the cooling function, the implementation encapsulates the major physical processes to which dust is subjected and acts as a non-gravitational process at the scale of the ICM and the IGM.

As already mentioned, we directly correlated the abundance of dust with metallicity, thus to the metallicity evolution, which chosen evolution law is quite drastic: $Z = 0.3(t/t_0)Z_\odot$. Indeed, if the metallicity at $z = 0$ is normalized to the value of $0.3Z_\odot$, it is lowered to ~ 0.2 at $z = 0.5$ and ~ 0.1 at $z = 1$. However, other numerical works based on simulations including physical implementation of metal enrichment processes but without dust agree

well with observational constraints (mainly provided by X-ray observations of the Fe-K line) which indicate high metalicity values, $Z \sim 0.3Z_{\odot}$, up to redshifts above 1.0 [111, 112]. This shows that, as for the stellar component which is already in place in galaxies when clusters form, the metal enrichment of the ICM/IGM has occured through the feedback of galaxy formation and evolution, and therefore it *de facto* strongly enriched the IGM/ICM bellow $z = 1$. It also might give hints that the high metallicity of clusters could be correlated to the dust enrichment of the IGM/ICM. Indeed, the amount of gaseous iron in galaxies such as the Milky Way is $\sim 0.01\mathrm{Z}_{\odot}$. An early enrichment of dust in the IGM and/or the ICM, which once sputtered will provide metals, could explain part of the iron abundances found in the ICM at low redshifts. This hypothesis seems to be consolidated by the few works that have investigated dust as a source for metals in the material stripped from galaxies via dynamical removal within already formed clusters [90] or via an early IGM enrichment at high redshift during the peak of star formation around $z = 3$ [113]. The latter work stressed that only big grains ($a > 0.1\mu$m) can be transported on a few 100kpc physical scale, however leading to a very inhomogenous spatial enrichment in metals once the dust grains are sputtered. For all these reasons, by underestimating the metallicity at high redshifts, we might have underestimated the amount of dust injected in the ICM at high redshift, and thus the efficiency of dust cooling when integrated from early epoch down to redshift zero.

6.6 Conclusion

As conclusion we can summarize our results as:

- The cooling due to dust is effective at the cluster regime and has a significant effect on the "baryon driven" statistical properties of cluster such as $L_{\mathrm{X}} - M$, $Y - M$,$S - M$ scaling relations. As an added non-gravitational cooling process dust changes the normalisation of these laws by a factor up to 27% for the $L_{\mathrm{X}} - M$ relation, and up to 10% for the $Y - M$ and $S - M$ relations. On the contrary, dust has almost no effect on a "dark matter driven" scaling relation such as the $T_{\mathrm{mw}} - M$ relation.

- The inclusion of cooling by dust does not change significantly the slopes of the cluster scaling laws investigated in this paper. They compare with the results obtained in the radiative cooling simulation model.

- Through the implementation of our different dust models, we have

demonstrated that the dust cooling effect at the scale of clusters depends strongly on the dust abundance in the ICM, but also on a similar proportion on the size distribution of dust grains. Therefore the dust efficiency is strongly dependent on the nature of the stripped and ejected galactic material, as well as the history of these injection and destruction processes along the cluster history. Indeed the early enrichment of dust might provide an already modified thermodynamical setup for the "to-be-accreted" gas at lower redshifts.

The setup of our simulations and the limitation of our dust implementation can be considered at a "zero order" test with which we demonstrated the active effect of dust on structure formation and especially at the cluster scale. In order to go one step further, a perspective of this work will be needed to couple the radiative cooling function of dust with a physical and dynamical implementation of the creation and destruction processes of dust in the IGM/ICM.

	Model C	Model D5	Model D4	Model D3	Model D2	Model D1
$T_{\rm mw} - M$						
$\alpha_{\rm TM}$	0.61 ± 0.02	0.61 ± 0.02	0.61 ± 0.02	0.62 ± 0.02	0.63 ± 0.02	0.63 ± 0.02
$\log A_{\rm TM}$	0.195 ± 0.002	0.195 ± 0.003	0.196 ± 0.002	0.197 ± 0.003	0.201 ± 0.002	0.204 ± 0.002
$\beta_{\rm TM}$	-0.14 ± 0.01	-0.14 ± 0.01	-0.14 ± 0.01	-0.15 ± 0.01	-0.16 ± 0.01	-0.16 ± 0.01
$S - M$						
$\alpha_{\rm SM}$	0.55 ± 0.03	0.54 ± 0.03	0.54 ± 0.03	0.56 ± 0.03	0.55 ± 0.02	0.54 ± 0.02
$\log A_{\rm SM}$	2.443 ± 0.002	2.444 ± 0.002	2.445 ± 0.002	2.451 ± 0.002	2.468 ± 0.002	2.488 ± 0.02
$\beta_{\rm SM}$	-0.33 ± 0.01	-0.34 ± 0.01	-0.34 ± 0.01	-0.36 ± 0.01	-0.40 ± 0.01	-0.42 ± 0.01
$Y - M$						
$\alpha_{\rm YM}$	1.74 ± 0.03	1.72 ± 0.03	1.73 ± 0.03	1.72 ± 0.02	1.74 ± 0.02	1.76 ± 0.02
$\log A_{\rm YM}$	-5.909 ± 0.002	-5.907 ± 0.002	-5.910 ± 0.002	-5.914 ± 0.002	-5.933 ± 0.002	-5.957 ± 0.002
$\beta_{\rm YM}$	0.12 ± 0.01	0.11 ± 0.01	0.13 ± 0.02	0.13 ± 0.01	0.17 ± 0.01	0.21 ± 0.01
$L_{\rm X} - M$						
$\alpha_{\rm LM}$	1.69 ± 0.07	1.68 ± 0.07	1.65 ± 0.07	1.61 ± 0.08	1.67 ± 0.05	1.67 ± 0.05
$\log A_{\rm LM}$	3.330 ± 0.006	3.334 ± 0.006	3.333 ± 0.005	3.323 ± 0.005	3.265 ± 0.005	3.207 ± 0.004
$\beta_{\rm LM}$	0.01 ± 0.03	-0.02 ± 0.03	-0.02 ± 0.03	0.02 ± 0.03	0.18 ± 0.03	0.23 ± 0.03

Table 6.2: Best fir values of the parameters α, $\log A$ and β as well as their respective 1σ errors. These values are valid within the redshift range $0 < z < 1$.

Acknowledgements

The first person I would like to thank is my tutor Jean-Michel Lamarre. His knowledge and instinct on research have deeply affected me. I hope I have stolen a bit of his nose. I thank Jean-Michel for his skills in exhorting and inciting me when facing scientific challenges. I'm really glad to have met Jean-Michel in my life.

I would like to thank my colleague Alain Coulais who kept an eye on the progress of my work and always was available when I needed his advises. Thank you to Etienne Pointecouteau, Ludovic Montier and Antonio da Silva who helped me to study the dust effect in the ICM and in general for their liking. I would like also to thank the other members of HFI core team who helped me to build a researcher profile.

Thank you Laurent, Eric and Annick of LERMA for teaching me this "strange" language which is French tongue and to be always available when needed. I am glad to be part of the 8th floor gang.

Energy and vitality during the past years was provided externally thanks to my friends in the cité universitaire where maybe I have found love (....who knows?). Thank you all Guys!

Facing problems with optimism inspired me to better understand my origins and the world. Thank you dad. You could not even realize how much I have learned from you. *Mamma*, you held me in your lap and then you kept my feet on the ground. I have always been crazy of you!

Andrea Catalano
Observatoire de Paris
November 4th 2008

Bibliography

[1] A. A. Friedmann. Uber die Krummung des Raumes. *Z. Phys*, 10:377–386, March 1922.

[2] E. Hubble. A relation between distance and radial velocity among exstra-galactic nebulae. *Astronomische Nachrichten*, 1924.

[3] G. Gamow. Expanding Universe and the Origin of Elements. *Physical Review*, 70:572–573, March 1946.

[4] Padmanabhan,T. *Structure formation in the universe.* Cambridge university press, 1993.

[5] A.H.Guth. *Inflazionary Universe: a possible solution to the horizon and flatness problems. Phys.Rev.*, 1980.

[6] A. A. Penzias and R. W. Wilson. A Measurement of Excess Antenna Temperature at 4080 Mc/s. *Astrophysical Journal*, 142:419–421, July 1965.

[7] D. J. Eisenstein, W. Hu, and M. Tegmark. Cosmic Complementarity: Joint Parameter Estimation from Cosmic Microwave Background Experiments and Redshift Surveys. *Astrophysical Journal*, 518:2–23, June 1999.

[8] L. Lamagna, E. S. Battistelli, S. de Gregori, M. de Petris, G. Luzzi, and G. Savini. S Z constraints on the dependence of the CMB temperature on redshift. *New Astronomy Review*, 51:381–384, March 2007.

[9] G.Smoot. Cobe observation and results. *astr-ph.*

[10] J. C. Mather, D. J. Fixsen, R. A. Shafer, C. Mosier, and D. T. Wilkinson. Calibrator Design for the COBE Far-Infrared Absolute Spectrophotometer (FIRAS). *Astrophysical Journal*, 512:511–520, February 1999.

[11] J. R. Bond, R. Crittenden, R. L. Davis, G. Efstathiou, and P. J. Steinhardt. Measuring cosmological parameters with cosmic microwave background experiments. *Physical Review Letters*, 72:13–16, January 1994.

[12] J. Chluba and R. A. Sunyaev. Superposition of blackbodies and the dipole anisotropy: A possibility to calibrate CMB experiments. *AAP*, 424, September 2004.

[13] M. Piat, G. Lagache, J. P. Bernard, M. Giard, and J. L. Puget. Cosmic background dipole measurements with the Planck-High Frequency Instrument. *AAP*, 393, October 2002.

[14] Hu,W. and White,M. A CMB Polarization Primer. *New Astronomy*, **2:323** , 1997.

[15] R. H. Hildebrand and M. Dragovan. The Shapes and Alignment Properties of Interstellar Dust Grains. *Astrophysical Journal*, 450:663–+, September 1995.

[16] J. Delabrouille and J. . Cardoso. Diffuse source separation in CMB observations. *ArXiv Astrophysics e-prints*, February 2007.

[17] J. C. Mather, E. S. Cheng, R. A. Shafer, E. L. Wright, S. S. Meyer, R. Weiss, D. J. Fixsen, R. E. Eplee, R. B. Isaacman, and S. M. Read. Spectra and Sky Maps from the COBE Far Infrared Spectraphotometer (FIRAS). In *Bulletin of the American Astronomical Society*, volume 22 of *Bulletin of the American Astronomical Society*, pages 1216–+, September 1990.

[18] D. J. Fixsen and J. C. Mather. The Spectral Results of the Far-Infrared Absolute Spectrophotometer Instrument on COBE. *Astrophysical Journal*, 581:817–822, December 2002.

[19] C. L. Bennett. The Microwave Anisotropy Probe (MAP) Mission. In *Bulletin of the American Astronomical Society*, volume 28 of *Bulletin of the American Astronomical Society*, pages 1391–+, December 1996.

[20] P. de Bernardis, P. A. R. Ade, J. J. Bock, J. R. Bond, J. Borrill, A. Boscaleri, K. Coble, B. P. Crill, G. De Gasperis, G. De Troia, P. C. Farese, P. G. Ferreira, K. Ganga, M. Giacometti, E. Hivon, V. V. Hristov, A. Iacoangeli, A. H. Jaffe, A. E. Lange, L. Martinis, S. Masi, P. Mason, P. D. Mauskopf, A. Melchiorri, L. Miglio, T. Montroy, C. B. Netterfield, E. Pascale, F. Piacentini, D. Pogosyan, F. Pongetti, S. Prunet,

S. Rao, G. Romeo, J. E. Ruhl, F. Scaramuzzi, D. Sforna, and N. Vittorio. Detection of anisotropy in the Cosmic Microwave Background at horizon and sub-horizon scales with the BOOMERanG experiment. *ArXiv Astrophysics e-prints*, November 2000.

[21] S. Hanany, P. Ade, A. Balbi, J. Bock, J. Borrill, A. Boscaleri, P. de Bernardis, P. G. Ferreira, V. V. Hristov, A. H. Jaffe, A. E. Lange, A. T. Lee, P. D. Mauskopf, C. B. Netterfield, S. Oh, E. Pascale, B. Rabii, P. L. Richards, G. F. Smoot, R. Stompor, C. D. Winant, and J. H. P. Wu. MAXIMA-1: A Measurement of the Cosmic Microwave Background Anisotropy on Angular Scales of 10-5deg. *Astrophysical Journal*, 545:L5–L9, December 2000.

[22] A. Benoît, P. Ade, A. Amblard, R. Ansari, É. Aubourg, S. Bargot, J. G. Bartlett, J.-P. Bernard, R. S. Bhatia, A. Blanchard, J. J. Bock, A. Boscaleri, F. R. Bouchet, A. Bourrachot, P. Camus, F. Couchot, P. de Bernardis, J. Delabrouille, F.-X. Désert, O. Doré, M. Douspis, L. Dumoulin, X. Dupac, P. Filliatre, P. Fosalba, K. Ganga, F. Gannaway, B. Gautier, M. Giard, Y. Giraud-Héraud, R. Gispert, L. Guglielmi, J.-C. Hamilton, S. Hanany, S. Henrot-Versillé, J. Kaplan, G. Lagache, J.-M. Lamarre, A. E. Lange, J. F. Macías-Pérez, K. Madet, B. Maffei, C. Magneville, D. P. Marrone, S. Masi, F. Mayet, A. Murphy, F. Naraghi, F. Nati, G. Patanchon, G. Perrin, M. Piat, N. Ponthieu, S. Prunet, J.-L. Puget, C. Renault, C. Rosset, D. Santos, A. Starobinsky, I. Strukov, R. V. Sudiwala, R. Teyssier, M. Tristram, C. Tucker, J.-C. Vanel, D. Vibert, E. Wakui, and D. Yvon. The cosmic microwave background anisotropy power spectrum measured by Archeops. *AAP*, 399:L19–L23, March 2003.

[23] T. J. Pearson, B. S. Mason, A. C. S. Readhead, M. C. Shepherd, J. L. Sievers, P. S. Udomprasert, J. K. Cartwright, A. J. Farmer, S. Padin, S. T. Myers, J. R. Bond, C. R. Contaldi, U.-L. Pen, S. Prunet, D. Pogosyan, J. E. Carlstrom, J. Kovac, E. M. Leitch, C. Pryke, N. W. Halverson, W. L. Holzapfel, P. Altamirano, L. Bronfman, S. Casassus, J. May, and M. Joy. The Anisotropy of the Microwave Background to l = 3500: Mosaic Observations with the Cosmic Background Imager. *Astrophysical Journal*, 591:556–574, July 2003.

[24] A. C. S. Readhead, S. T. Myers, T. J. Pearson, J. L. Sievers, B. S. Mason, C. R. Contaldi, J. R. Bond, R. Bustos, P. Altamirano, C. Achermann, L. Bronfman, J. E. Carlstrom, J. K. Cartwright, S. Casassus, C. Dickinson, W. L. Holzapfel, J. M. Kovac, E. M. Leitch, J. May,

S. Padin, D. Pogosyan, M. Pospieszalski, C. Pryke, R. Reeves, M. C. Shepherd, and S. Torres. Polarization Observations with the Cosmic Background Imager. *Science*, 306:836–844, October 2004.

[25] M. C. Runyan, P. A. R. Ade, R. S. Bhatia, J. J. Bock, M. D. Daub, J. H. Goldstein, C. V. Haynes, W. L. Holzapfel, C. L. Kuo, A. E. Lange, J. Leong, M. Lueker, M. Newcomb, J. B. Peterson, C. Reichardt, J. Ruhl, G. Sirbi, E. Torbet, C. Tucker, A. D. Turner, and D. Woolsey. ACBAR: The Arcminute Cosmology Bolometer Array Receiver. *Astrophysical Journal*, 149:265–287, December 2003.

[26] C. L. Kuo, P. A. R. Ade, J. J. Bock, C. Cantalupo, M. D. Daub, J. Goldstein, W. L. Holzapfel, A. E. Lange, M. Lueker, M. Newcomb, J. B. Peterson, J. Ruhl, M. C. Runyan, and E. Torbet. High-Resolution Observations of the Cosmic Microwave Background Power Spectrum with ACBAR. *Astrophysical Journal*, 600:32–51, January 2004.

[27] P. F. Scott, P. Carreira, K. Cleary, R. D. Davies, R. J. Davis, C. Dickinson, K. Grainge, C. M. Gutiérrez, M. P. Hobson, M. E. Jones, R. Kneissl, A. Lasenby, K. Maisinger, G. G. Pooley, R. Rebolo, J. A. Rubiño-Martin, P. J. Sosa Molina, B. Rusholme, R. D. E. Saunders, R. Savage, A. Slosar, A. C. Taylor, D. Titterington, E. Waldram, R. A. Watson, and A. Wilkinson. First results from the Very Small Array - III. The cosmic microwave background power spectrum. *MNRAS*, 341:1076–1083, June 2003.

[28] N. W. Halverson, E. M. Leitch, C. Pryke, J. Kovac, J. E. Carlstrom, W. L. Holzapfel, M. Dragovan, J. K. Cartwright, B. S. Mason, S. Padin, T. J. Pearson, A. C. S. Readhead, and M. C. Shepherd. Degree Angular Scale Interferometer First Results: A Measurement of the Cosmic Microwave Background Angular Power Spectrum. *Astrophysical Journal*, 568:38–45, March 2002.

[29] J. M. Lamarre, J. L. Puget, F. Bouchet, P. A. R. Ade, A. Benoit, J. P. Bernard, J. Bock, P. de Bernardis, J. Charra, F. Couchot, J. Delabrouille, G. Efstathiou, M. Giard, G. Guyot, A. Lange, B. Maffei, A. Murphy, F. Pajot, M. Piat, I. Ristorcelli, D. Santos, R. Sudiwala, J. F. Sygnet, J. P. Torre, V. Yurchenko, and D. Yvon. The Planck High Frequency Instrument, a third generation CMB experiment, and a full sky submillimeter survey. *New Astronomy Review*, 47:1017–1024, December 2003.

[30] J.-M. Lamarre, F.-X. Désert, and T. Kirchner. Background Limited Infrared and Submillimeter Instruments. *Space Science Reviews*, 74:27–36, October 1995.

[31] B. Maffei, P. A. Ade, J. J. Bock, J. Brossard, E. M. Gleeson, J.-M. Lamarre, A. E. Lange, Y.-Y. Longval, J. A. Murphy, G. Pisano, J.-L. Puget, I. Ristorcelli, R. V. Sudiwala, and V. B. Yurchenko. Planck-HFI focal plane concept. In J. C. Mather, editor, *Society of Photo-Optical Instrumentation Engineers (SPIE) Conference Series*, volume 5487 of *Society of Photo-Optical Instrumentation Engineers (SPIE) Conference Series*, pages 523–531, October 2004.

[32] J. A. Murphy, R. Colgan, E. Gleeson, B. Maffei, C. O'Sullivan, and P. A. R. Ade. Corrugated horn design for HFI on PLANCK. In M. de Petris and M. Gervasi, editors, *Experimental Cosmology at Millimetre Wavelengths*, volume 616 of *American Institute of Physics Conference Series*, pages 282–289, May 2002.

[33] G. Savini and F. Pajot. HFI Spectral Calibration report of the IAS measurements. *Planck HFI Calibration Report*, November 2006.

[34] P. A. R. Ade, G. Pisano, C. Tucker, and S. Weaver. A review of metal mesh filters. In *Society of Photo-Optical Instrumentation Engineers (SPIE) Conference Series*, volume 6275 of *Society of Photo-Optical Instrumentation Engineers (SPIE) Conference Series*, July 2006.

[35] J. M. Lamarre, P. R. Ade, A. Benoît, P. de Bernardis, J. Bock, F. Bouchet, T. Bradshaw, J. Charra, S. Church, F. Couchot, J. Delabrouille, G. Efstathiou, M. Giard, Y. Giraud-Héraud, R. Gispert, M. Griffin, A. Lange, A. Murphy, F. Pajot, J. L. Puget, and I. Ristorcelli. The High Frequency Instrument of Planck: Design and Performances. *Astrophysical Letters Communications*, 37:161–+, 2000.

[36] R. C. Jones. The general theory of bolometer performance. *Journal of the Optical Society of America (1917-1983)*, 43, January 1953.

[37] J. C. Mather. Bolometer noise: nonequilibrium theory. *AO*, 21:1125–1129, 1982.

[38] S. Gaertner, A. Benoit, J.-M. Lamarre, M. Giard, J.-L. Bret, J.-P. Chabaud, F.-X. Desert, J.-P. Faure, G. Jegoudez, J. Lande, J. Leblanc, J.-P. Lepeltier, J. Narbonne, M. Piat, R. Pons, G. Serra, and G. Simiand. A new readout system for bolometers with improved low frequency stability. *AAPS*, 126:151–160, November 1997.

[39] F. M. Rieke, Lange A., Beeman J. W., and Haller E. E. An AC bridge readout for bolometric detectors. *Nuclear Science, IEEE Transactions on*, 36:946–949, 1989.

[40] F. Pajot, J. M. Lamarre, J. L. Puget, and Calibration Team. HFI Calibration and Performances Document. *CA-PH412-600824-IAS*, March 2008.

[41] X. Desert. Private Communications.

[42] J. P. Torre, J. M. LAMARRE, and C. Doucerain. Background Limited bolometers for First and COBRAS/SAMBA. In *International Workshop on Bolometers for mm and sub-mm projects*, Lamarre Editor, pages 1391–+, June 1995.

[43] A. Benoît, M. Caussignac, and S. Pujol. New types of dilution refrigerator and space applications. *Physica B Condensed Matter*, 197:48–53, March 1994.

[44] A. Benoît, A. Sirbi, T. Bradshaw, A. Orlowska, J. J. Fourmond, J. M. Lamarre, C. Jewell, B. Pouilloux, and T. Maciaszek. Development of a 0.1 K cryocooler for space applications. In T.-D. Guyenne, editor, *Sixth European Symposium on Space Environmental Control Systems*, volume 400 of *ESA Special Publication*, pages 497–+, August 1997.

[45] T. W. Bradshaw and A. H. Orlowska. The Use of Closed Cycle Coolers on Space Based Observatories. *Space Science Reviews*, 74:205–213, October 1995.

[46] M. J. Griffin, B. M. Swinyard, and L. G. Vigroux. SPIRE instrument for FIRST. In J. B. Breckinridge and P. Jakobsen, editors, *Society of Photo-Optical Instrumentation Engineers (SPIE) Conference Series*, volume 4013 of *Presented at the Society of Photo-Optical Instrumentation Engineers (SPIE) Conference*, July 2000.

[47] W. S. Holland, W. D. Duncan, M. D. Audley, B. D. Kelly, T. Peacocke, M. MacIntosh, T. Hodson, K. D. Irwin, G. Hilton, A. Walton, A. Gundlach, P. A. R. Ade, and E. I. Robson. SCUBA-2: A new generation submillimeter imager for the James Clerk Maxwell Telescope. In *Bulletin of the American Astronomical Society*, volume 33 of *Bulletin of the American Astronomical Society*, December 2001.

[48] J.-M. Lamarre, J. L. Puget, M. Piat, P. A. R. Ade, A. E. Lange, A. Benoit, P. De Bernardis, F. R. Bouchet, J. J. Bock, F. X. Desert,

R. J. Emery, M. Giard, B. Maffei, J. A. Murphy, J.-P. Torre, R. Bhatia, R. V. Sudiwala, and V. Yourchenko. Planck high-frequency instrument. In J. C. Mather, editor, *Society of Photo-Optical Instrumentation Engineers (SPIE) Conference Series*, volume 4850 of *Presented at the Society of Photo-Optical Instrumentation Engineers (SPIE) Conference*, pages 730–739, March 2003.

[49] M. Piat, J.-P. Torre, E. Bréelle, A. Coulais, A. Woodcraft, W. Holmes, and R. Sudiwala. Modeling of Planck-high frequency instrument bolometers using non-linear effects in the thermometers. *Nuclear Instruments and Methods in Physics Research A*, 559:588–590, April 2006.

[50] M. Yun, J. W. Beeman, R. Bhatia, J. J. Bock, W. Holmes, L. Hustead, T. Koch, J. L. Mulder, A. E. Lange, A. D. Turner, and L. Wild. Bolometric detectors for the Planck surveyor. In T. G. Phillips and J. Zmuidzinas, editors, *Society of Photo-Optical Instrumentation Engineers (SPIE) Conference Series*, volume 4855 of *Presented at the Society of Photo-Optical Instrumentation Engineers (SPIE) Conference*, pages 136–147, February 2003.

[51] S. Lefranc, M. Piat, J.-P. Torre, E. Bréelle, B. Leriche, L. Dumoulin, L. Bergé, C. Evesque, and F. Pajot. Superconducting NbSi thermometers for use in TES devices. *Nuclear Instruments and Methods in Physics Research A*, 559:468–470, April 2006.

[52] M. Piat, C. Rosset, J. Bartlett, Y. Giraud-Héraud, E. Bréele, A. Maestrini, C. Tripon Canseliet, C. Algani, M. Girard, F. Pajot, S. Masi, P. de Bernardis, L. Piccirillo, B. Mafei, M. Jones, and A. Taylor. Precise measurement of CMB polarisation from Dome-C: the BRAIN and CLOVER experiments. In F. Combes, D. Barret, T. Contini, F. Meynadier, and L. Pagani, editors, *SF2A-2004: Semaine de l'Astrophysique Francaise*, pages 707–+, December 2004.

[53] S. Zwerdling. A fast, high-responsivity bolometer detector for the very-far infrared. *Infrared Physics*, 8:271–336, December 1968.

[54] J. M. Lamarre. Photon noise in photometric instruments at far-infrared and submillimeter wavelengths. *AO*, 25:870–876, 1986.

[55] R. V. Sudiwala, B. Maffei, M. J. Griffin, C. V. Haynes, P. A. R. Ade, R. S. Bhatia, A. D. Turner, J. J. Bock, A. E. Lange, and J. W. Beeman. Evaluation of prototype 100 mK bolometric detector for Planck

Surveyor. *Nuclear Instruments and Methods in Physics Research A*, 444:408–412, April 2000.

[56] E. Pointecouteau, L. Montier, and M. Giard. SEB Validation. December 2006.

[57] A. Catalano, A. Coulais, G. Recouvreur, and J. M. Lamarre. Optimal Bias Current for HFI GRound Calibrations. *Planck Report*, March 2006.

[58] A. Catalano, A. Coulais, G. Recouvreur, and J. M. Lamarre. Optimisation of Ibias and Sphase. *Planck Report*, November 2006.

[59] A. Catalano, A. Coulais, G. Recouvreur, and J. M. Lamarre. Fmod Sequence. *Planck Report*, November 2006.

[60] L. Montier, E. Pointecouteau, and M. Giard. RU Calibration PFM. *CA-PHCB450-500233-CESR*, March 2006.

[61] A. Catalano, A. Coulais, G. Recouvreur, and J. M. Lamarre. HFI Calibration Report - EFF Sequence. *Planck Report*, November 2006.

[62] F. Pajot, J. M. Lamarre, J. L. Puget, and Calibration Team. HFI CQM Calibration Report. *CA-PH440-500552-IAS*, July 2005.

[63] A. Catalano. Convertion Factor between the Cryogenic Stages and a RJ Source. *Planck Report*, February 2007.

[64] A. Coulais, J.-M. Lamarre, A. Catalano, and M. Bauchy. HFI PFM Ground Tau ELS Measurements. *Planck HFI Calibration Report*, November 2006.

[65] B. L. Ulich. Millimeter-wavelength continuum calibration sources. *AJ*, 86:1619–1626, November 1981.

[66] R. H. Hildebrand, R. F. Loewenstein, D. A. Harper, G. S. Orton, J. Keene, and S. E. Whitcomb. Far-infrared and submillimeter brightness temperatures of the giant planets. *Icarus*, 64:64–87, October 1985.

[67] P. Naselsky, D. Novikov, and J. Silk. A combined multifrequency map for point source subtraction. *MNRAS*, 335:550–554, September 2002.

[68] G. Lagache, M. Piat, J. L. Puget, and J. P. Bernard. Planck HFI L2 PHOTOMETRIC CALIBRATION Implementation Plan. *PL-HFI-IAS-PL-GPH427*, September 2002.

[69] F. Noviello. HFI Beams Patterns Archive. *Planck Report*, July 2007.

[70] A. Catalano, V. Yourchenko, and J. M. Lamarre. Beams Calibration Requirements for Planck HFI. *Planck Report*, February 2006.

[71] A. Catalano, F. Noviello, and J. M. Lamarre. Sampling HFI Beams. *Planck Report*, June 2008.

[72] G. M. Voit. Tracing cosmic evolution with clusters of galaxies. *Reviews of Modern Physics*, 77:207–258, April 2005.

[73] A. Cattaneo and R. Teyssier. AGN self-regulation in cooling flow clusters. *mnras*, 376:1547–1556, April 2007.

[74] C. Conroy and J. P. Ostriker. Thermal Balance in the Intracluster Medium: Is AGN Feedback Necessary? *ArXiv e-prints*, 712, December 2007.

[75] B. R. McNamara and P. E. J. Nulsen. Heating Hot Atmospheres with Active Galactic Nuclei. *ARAA*, 45:117–175, September 2007.

[76] M. Loewenstein. On Iron Enrichment, Star Formation, and Type Ia Supernovae in Galaxy Clusters. *Astrophysical Journal*, 648:230–249, September 2006.

[77] C. L. Sarazin. *X-ray emission from clusters of galaxies.* Cambridge Astrophysics Series, Cambridge: Cambridge University Press, 1988, 1988.

[78] M. Arnaud. X-ray observations of clusters of galaxies. In F. Melchiorri and Y. Rephaeli, editors, *Background Microwave Radiation and Intracluster Cosmology*, pages 77–+, 2005.

[79] W. Domainko, M. Mair, W. Kapferer, E. van Kampen, T. Kronberger, S. Schindler, S. Kimeswenger, M. Ruffert, and O. E. Mangete. Enrichment of the ICM of galaxy clusters due to ram-pressure stripping. *AAP*, 452:795–802, June 2006.

[80] R. Moll, S. Schindler, W. Domainko, W. Kapferer, M. Mair, E. van Kampen, T. Kronberger, S. Kimeswenger, and M. Ruffert. Simulations of metal enrichment in galaxy clusters by AGN outflows. *AAP*, 463:513–518, February 2007.

[81] G. Murante, M. Arnaboldi, O. Gerhard, S. Borgani, L. M. Cheng, A. Diaferio, K. Dolag, L. Moscardini, G. Tormen, L. Tornatore, and P. Tozzi. The Diffuse Light in Simulations of Galaxy Clusters. *Astrophysical Journal*, 607:L83–L86, June 2004.

[82] G. Murante, M. Giovalli, O. Gerhard, M. Arnaboldi, S. Borgani, and K. Dolag. The importance of mergers for the origin of intracluster stars in cosmological simulations of galaxy clusters. *mnras*, 377:2–16, May 2007.

[83] J. E. Krick and R. A. Bernstein. Diffuse Optical Light in Galaxy Clusters. II. Correlations with Cluster Properties. *Astronomical Journal*, 134:466–493, August 2007.

[84] M. Stickel, D. Lemke, K. Mattila, L. K. Haikala, and M. Haas. Far-infrared emission of intracluster dust in the Coma galaxy cluster. *AAP*, 329:55–60, January 1998.

[85] M. Stickel, U. Klaas, D. Lemke, and K. Mattila. Far-infrared emission from intracluster dust in Abell clusters. *AAP*, 383:367–383, January 2002.

[86] L. Bai, G. H. Rieke, M. J. Rieke, J. L. Hinz, D. M. Kelly, and M. Blaylock. Infrared Luminosity Function of the Coma Cluster. *Astrophysical Journal*, 639:827–837, March 2006.

[87] L. Bai, D. Marcillac, G. H. Rieke, M. J. Rieke, K.-V. H. Tran, J. L. Hinz, G. Rudnick, D. M. Kelly, and M. Blaylock. IR Observations of MS 1054-03: Star Formation and Its Evolution in Rich Galaxy Clusters. *Astrophysical Journal*, 664:181–197, July 2007.

[88] L. A. Montier and M. Giard. Dust emission from clusters of galaxies: statistical detection. *AAP*, 439:35–44, August 2005.

[89] C. C. Popescu, R. J. Tuffs, J. Fischera, and H. Völk. On the FIR emission from intracluster dust. *AAP*, 354:480–496, February 2000.

[90] A. Aguirre, L. Hernquist, J. Schaye, N. Katz, D. H. Weinberg, and J. Gardner. Metal Enrichment of the Intergalactic Medium in Cosmological Simulations. *Astrophysical Journal*, 561:521–549, November 2001.

[91] L. A. Montier and M. Giard. The importance of dust in cooling and heating the InterGalactic Medium. *AAP*, 417:401–409, April 2004.

[92] V. Springel and L. Hernquist. The history of star formation in a Λ cold dark matter universe. *mnras*, 339:312–334, February 2003.

[93] J. C. Weingartner, B. T. Draine, and D. K. Barr. Photoelectric Emission from Dust Grains Exposed to Extreme Ultraviolet and X-Ray Radiation. *Astrophysical Journal*, 645:1188–1197, July 2006.

[94] E. Dwek. Cooling and evolution of adiabatic blast waves in a dusty medium. *Astrophysical Journal*, 247:614–627, July 1981.

[95] R. S. Sutherland and M. A. Dopita. Cooling functions for low-density astrophysical plasmas. *Astrophysical Journal*, 88:253–327, September 1993.

[96] J. S. Mathis, W. Rumpl, and K. H. Nordsieck. *APJ*, 217:425–+, 1977.

[97] M. Giard, L. Montier, E. Pointecouteau, and E. Simmat. The Infrared Luminosity of Galaxy Clusters. *ArXiv e-prints*, 808, August 2008.

[98] H. M. P. Couchman, P. A. Thomas, and F. R. Pearce. Hydra: an Adaptive-Mesh Implementation of P 3M-SPH. *Astrophysical Journal*, 452:797–+, October 1995.

[99] H. M. P. Couchman. Mesh-refined P3M - A fast adaptive N-body algorithm. *Astrophysical Journal*, 368:L23–L26, February 1991.

[100] R. J. Thacker and H. M. P. Couchman. Implementing Feedback in Simulations of Galaxy Formation: A Survey of Methods. *Astrophysical Journal*, 545:728–752, December 2000.

[101] P. A. Thomas and H. M. P. Couchman. Simulating the formation of a cluster of galaxies. *mnras*, 257:11–31, July 1992.

[102] J. M. Bardeen, J. R. Bond, N. Kaiser, and A. S. Szalay. *APJ*, 304:15–+, 1986.

[103] N. Sugiyama. *APJS*, 100:281–+, 1995.

[104] V. Springel, S. D. M. White, J. M. Colberg, H. M. P. Couchman, G. P. Efstathiou, C. S. Frenk, A. R. Jenkins, F. R. Pearce, A. H. Nelson, J. A. Peacock, and P. A. Thomas. Genus statistics of the Virgo N-body simulations and the 1.2-Jy redshift survey. *MNRAS*, 298:1169–1188, August 1998.

[105] V. R. Eke, J. F. Navarro, and C. S. Frenk. The Evolution of X-Ray Clusters in a Low-Density Universe. *APJ*, 503:569–+, August 1998.

[106] A. C. da Silva, S. T. Kay, A. R. Liddle, and P. A. Thomas. Hydrodynamical simulations of the Sunyaev-Zel'dovich effect: cluster scaling relations and X-ray properties. *mnras*, 348:1401–1408, March 2004.

[107] R. S. Sutherland and M. A. Dopita. Cooling functions for low-density astrophysical plasmas. *APJS*, 88:253–327, September 1993.

[108] N. Kaiser. Evolution and clustering of rich clusters. *MNRAS*, 222:323–345, September 1986.

[109] N. Aghanim, A. C. da Silva, and N. J. Nunes. Cluster scaling relations from cosmological hydrodynamic simulations in dark energy dominated universe. *ArXiv e-prints*, August 2008.

[110] O. Y. Gnedin, A. V. Kravtsov, A. A. Klypin, and D. Nagai. Response of Dark Matter Halos to Condensation of Baryons: Cosmological Simulations and Improved Adiabatic Contraction Model. *APJ*, 616:16–26, November 2004.

[111] S. A. Cora, L. Tornatore, P. Tozzi, and K. Dolag. On the dynamical origin of the ICM metallicity evolution. *MNRAS*, 386:96–104, May 2008.

[112] S. Borgani, D. Fabjan, L. Tornatore, S. Schindler, K. Dolag, and A. Diaferio. The Chemical Enrichment of the ICM from Hydrodynamical Simulations. *Space Science Reviews*, 134:379–403, February 2008.

[113] S. Bianchi and A. Ferrara. Intergalactic medium metal enrichment through dust sputtering. *MNRAS*, 358:379–396, April 2005.

[114] P.De Bernardis et al. *A flat universefrom high-resolution maps of the cosmic microwave background radiation. Nature*, 404:995, 2000.

[115] M. Tegmark. How to measure CMB power spectra without losing information. *Physical Review D*, 55:5895–5907, May 1997.

[116] M. Tegmark. How to Make Maps from Cosmic Microwave Background Data without Losing Information. *Astrophysical Journal*, 480:L87+, May 1997.

[117] R. J. Laureijs. In-Orbit Test and Calibration Requirements. *Planck/PSO/2003-024*, September 2004.

[118] J. M. Bardeen, J. R. Bond, N. Kaiser, and A. S. Szalay. The statistics of peaks of Gaussian random fields. *Astrophysical Journal*, 304:15–61, May 1986.

[119] V. R. Eke, J. F. Navarro, and C. S. Frenk. The Evolution of X-Ray Clusters in a Low-Density Universe. *Astrophysical Journal*, 503:569–+, August 1998.

[120] N. Kaiser. Evolution and clustering of rich clusters. *mnras*, 222:323–345, September 1986.

[121] W. Kapferer, C. Ferrari, W. Domainko, M. Mair, T. Kronberger, S. Schindler, S. Kimeswenger, E. van Kampen, D. Breitschwerdt, and M. Ruffert. Simulations of galactic winds and starbursts in galaxy clusters. *AAP*, 447:827–842, March 2006.

[122] G. Lagache, J.-L. Puget, and H. Dole. Dusty Infrared Galaxies: Sources of the Cosmic Infrared Background. *ARAA*, 43:727–768, September 2005.

[123] J. S. Mathis, W. Rumpl, and K. H. Nordsieck. The size distribution of interstellar grains. *Astrophysical Journal*, 217:425–433, October 1977.

[124] O. Muanwong, P. A. Thomas, S. T. Kay, and F. R. Pearce. The effect of cooling and preheating on the X-ray properties of clusters of galaxies. *mnras*, 336:527–540, October 2002.

[125] F. R. Pearce and H. M. P. Couchman. Hydra: a parallel adaptive grid code. *New Astronomy*, 2:411–427, November 1997.

[126] N. Sugiyama. Cosmic Background Anisotropies in Cold Dark Matter Cosmology. *Astrophysical Journal*, 100:281–+, October 1995.